Tampere University

MINNA NIITTYMÄKI

Electrical Performance of Insulating Ceramic Coatings in Different Environmental Conditions

Tampere University Dissertations 689

Tampere University Dissertations 689

MINNA NIITTYMÄKI

Electrical Performance of Insulating Ceramic Coatings in Different Environmental Conditions

ACADEMIC DISSERTATION
To be presented, with the permission of
the Faculty of Information Technology and Communication Sciences
of Tampere University,
for public discussion in the auditorium TB109
of Tietotalo, Korkeakoulunkatu 1, Tampere,
on 18 November 2022, at 12 o'clock.

ACADEMIC DISSERTATION
Tampere University, Faculty of Information Technology and Communication Sciences
Finland

Responsible supervisor and Custos	Adjunct Professor Kari Lahti Tampere University Finland	
Pre-examiners	Professor Stanislaw Gubanski Chalmers University of Technology Sweden	D.Sc.(Tech.) Markus Takala ABB Finland
Opponent	Associate Professor Frank Mauseth NTNU, Norwegian University of Science and Technology Norway	

The originality of this thesis has been checked using the Turnitin OriginalityCheck service.

Cover design: Roihu Inc.

ISBN 978-952-03-2609-8 (print)
ISBN 978-952-03-2610-4 (pdf)
ISSN 2489-9860 (print)
ISSN 2490-0028 (pdf)
http://urn.fi/URN:ISBN:978-952-03-2610-4

Carbon dioxide emissions from printing Tampere University dissertations have been compensated.

PunaMusta Oy – Yliopistopaino
Joensuu 2022

Abstract

Thermally sprayed insulating ceramic coatings are typically utilized to protect material against hot corrosion or wear. However, the ceramic coatings are also used as an electrical insulation e.g. in applications where the operating conditions are demanding, e.g. very high temperatures or harsh environments. A coating is formed layer-by-layer within a process where a raw material, e.g. powder, is heated, accelerated and melted by high temperature and high-velocity gas stream towards a substrate. The layered microstructure of the coating differs strongly from the sintered bulk alumina, and thus their dielectric properties differs as well. Since the previous studies in the literature are typically focused on the dielectric properties of sintered alumina, there is a need to study dielectric properties of ceramic coatings comprehensively. This is also required to increase the use of alumina and spinel coatings as electrical insulation systems.

Atmospheric plasma spraying (APS) is a typical method to deposit oxide coatings, e.g. alumina and spinel coatings. However, a more dense and well-adhered coatings with better dielectric properties can be deposited by utilizing high-velocity oxygen fuel (HVOF) spray method, which makes this interesting method compared to traditional plasma spraying. In this thesis, most of the coatings were sprayed by utilizing HVOF method but some of the studied coatings were deposited by atmospheric plasma spraying or by rod flame spraying. Several different alumina and spinel raw materials were studied to form wide perspective of the coating properties.

This thesis focuses on the dielectric properties of the alumina and spinel coatings at different ambient conditions. In addition, suitable measurement methods for the dielectric characterization of ceramic coatings were studied and developed. The dielectric characterizations included following test series: i) short-term breakdown performance, ii) long-term breakdown performance, iii) DC resistivity at low and high electric fields, and v) relative permittivity and dielectric losses at low and high electric fields.

For all the studied coatings, a comprehensive dielectric characterization (short-term DC breakdown performance, DC resistivity, relative permittivity and dielectric loss) were made at controlled conditions (20 °C/RH 20%). According to the results, the HVOF sprayed coatings have superior dielectric properties in comparison to the rod flame sprayed coatings. HVOF spinel coatings have in general better performance than HVOF alumina coatings. The properties of the plasma sprayed coatings were at quite similar level with the HVOF coatings but the breakdown performance of the plasma coatings were lower. The differences between the different spray methods can be linked to different particle

velocities since the HVOF coatings have the highest particle velocity and thus more dense structure while in rod flame spray process the velocity is the lowest.

Due to the microstructural differences between a bulk and a ceramic coating, the DC resistivities of the studied coatings are similar with that of bulk alumina only at the lowest electric fields (typically below 0.5 V/µm). At higher electric fields, resistivity of the coatings decreases gradually indicating strong non-linear resistivity. According to the high field DC conductivity studies, it is proposed that the coatings follow only partly the space charge limited conduction (SCLC) theory as opposite to bulk alumina which has been reported following the SCLC theory fully. The difference in conduction behavior can be explained by the layered structure of coatings consisting of crystalline and amorphous regions which exhibit different conductivities resulting in uneven DC electric field distribution.

The role of microstructure can also be seen in the relative permittivity and dielectric losses of the coatings. At the highest frequencies, the relative permittivities of coatings are more or less constant being at similar level with bulk alumina. However, at the lowest frequencies the relative permittivity rapidly increases which most probably indicates interfacial polarization occurring at the crystalline-amorphous interfaces in the coating. Also, the role of microstructure can be seen in the dielectric losses since the losses of the coatings were higher than those of bulk ceramic. In addition, low-frequency dispersion/quasi-DC conduction contribution can be seen in the dielectric losses in the low frequency region which also can be linked to the layered microstructure.

The effect of temperature and humidity on the dielectric properties of HVOF, APS and rod flame sprayed alumina and spinel coatings was studied. The breakdown strength of HVOF sprayed alumina coating is at a similar level from 20 °C to 300 °C. From 300 °C to 800 °C the breakdown strength decreases gradually reaching a value which is only 14% of the breakdown strength at 20 °C. In addition, the results show that increasing humidity does not directly affect the DC breakdown strength but it decreases the DC resistivity several orders of magnitude and increases the relative permittivity and dielectric losses notably. The DC resistivities of alumina coatings increased more significantly with increasing humidity than those of spinel coatings. It can be concluded that both ceramic coating materials exhibit moisture sensitive nature which is in coherence with literature. In addition, this moisture sensitive nature of the coatings can be seen in the breakdown voltage measurements when the oil immersion was utilized since the breakdown strength in oil is in the order of two times higher than the breakdown strength without oil immersion.

In order to increase the use of thermally sprayed alumina and spinel coatings, their long-term reliability needs to be known. When the long-term performance is known, a possible service stress levels can be estimated. Long-term breakdown performance of HVOF sprayed spinel and alumina coatings were studied with a long 1000 h test and several shorter 168 h tests. According to the test series, a possible maximum service stress level for the studied coatings could be in the range of 10 V/µm which is approximately 25–30% of the short-term breakdown strength (Weibull α).

Preface

This dissertation work was carried out at the department of Electrical Engineering at Tampere University of Technology (TUT) during the years 2012–2018. The work was finalized in 2021–2022 at Tampere University which was formed in 2019 by merging of the two Tampere Universities. The research was conducted mainly under projects carried out in co-operation with VTT Technical Research Centre of Finland, ABB Motors and Generators, Millidyne Oy, Kuopion Konepaja, Saint-Gobain Coating Solutions, Wärtsilä Ecotech Oy and Aalto University. Additional funding in the form of personal grants from Ulla Tuominen foundation, Jenny and Antti Wihuri foundation and Walter Ahlström foundation are greatly appreciated.

Firstly, I want express my sincere gratitude to my supervisor Adjunct Professor Kari Lahti for his excellent guidance, encouragement and kindness during my academic years. I am privileged that I have had opportunity to work with such an experienced high-voltage engineer who always has time for discussions. I am also grateful to my pre-examiners, Prof. Stanislaw Gubanski and Dr. Markus Takala, for their valuable comments and suggestions. Furthermore, I am grateful to Prof. Frank Mauseth for agreeing to act as an opponent in the public defense of my thesis. I want to thank all my co-authors, M.Sc. Tomi Suhonen, M.Sc. Jarkko Metsäjoki and M.Sc Ulla Kanerva, for the enjoyable collaboration.

I am deeply grateful to my former high-voltage research group members, Dr. Ilkka Rytöluoto, Dr. Mikael Ritamäki and M.Sc. Hannes Ranta, for their valuable support and contributions during these years. The high team spirit and humor made my work days more enjoyable. I hope that our friendship will last for a lifetime. I want to thank all my present and former colleagues at the unit of Electrical Engineering for the enjoyable and warm working atmosphere. Especially, I am grateful to Dr. Heidi Krohns-Välimäki, Dr. Matias Berg and M.Sc. Antti Hildén for their support and friendship. I also want to thank Pentti Kivinen, Pekka Nousiainen and Hannu Nieminen for their craftsmanship for building test benches and setups.

My deepest thanks goes to my family and friends. I feel myself fortunate that I have so many good friends. I want to express my sincere gratitude to you all. Most of all, I am grateful to my friend who has always supported me through thick and thin. Thank you for everything, Tiina. Last but not least I want to thank Leevi who brings joy and happiness to my life.

Tampere, September 2022

Minna Niittymäki

Contents

Acronyms

Al_2O_3	Aluminum oxide, alumina
Al_2O_3–TiO2	Alumina-titania
APS	Atmospheric plasma spraying
BDS	Dielectric breakdown strength
Com.	Commercial
D-Gun	Detonation spray method
Exp.	Experimental
FS	Flame spraying
HICC	”Highly Insulating Ceramic Coatings” -project
HVAF	High-velocity air spraying
HVOF	High-velocity oxygen
LFD	Low-frequency dispersion
LPPS	Low pressure plasma spraying
$MgAl_2O_4$	Magnesium aluminate, spinel
LFD	Low-frequency dispersion
OM	Optical microscope
PD	Partial discharge
SEM/BSE	Scanning electron microscope using backscattered electron detector
SEM/SE	Scanning electron microscope using secondary electron detector
SCLC	Space charge limited conduction
TBC	Thermal barrier coating
TiO_2	Titanium oxide, titania
VPS	Vacuum plasma spraying
YSZ	Yttria-stabilized zirconia

Nomenclature

A_{RD}	Richardson-Dushman's constant
α	Weibull scale parameter
β	Weibull shape parameter
β_s	Schottky's constant
β_{PF}	Poole-Frenkel coefficient
C	Capacitance
C_e	Edge field correction
C_p	Parallel capacitance in the RC-model
d	Thickness of a dielectric
D	Electric flux density
E	Electric field
$E_{10\%}$	Breakdown field at the breakdown probability of 10%
$E_{63.2\%}$	Breakdown field at the breakdown probability of 63.2%
$E_{90\%}$	Breakdown field at the breakdown probability of 90%
E_{bd}	Breakdown field
E_{TFL}	Trap-filled limit electric field
E_{TR}	Transition electric field
$\varepsilon*$	Complex permittivity
ε_0	Permittivity in vacuum
$\varepsilon*_r$	Complex relative permittivity
ε_r	Relative permittivity
ε'_r	Real part of relative permittivity
ε''_r	Imaginary part of relative permittivity
ϕ_0	Effective work function
ϕ_{PF0}	Trap barrier height
J	Current density
J_0	Pre-exponential current density
k	Boltzmann's constant
L_f	Free-space length characterizing a crystalline domain
m	Slope
n	Free carrier density
ω	Angular frequency

q	Electronic charge
μ	Charge carrier mobility
R	Resistance
R_p	Parallel resistance in the RC-model
ρ	DC resistivity
σ	DC conductivity
T	Temperature
$\tan\delta$	Dissipation factor
U	Voltage
U_{bd}	Breakdown voltage

List of publications

This thesis is based on the following original publications which are referred to in the text as [P1]–[P8]:

[P1] M. Niittymäki, T. Suhonen, U. Kanerva, J. Metsäjoki and K. Lahti "Dielectric properties of HVOF sprayed ceramic coatings," *Proceedings of IEEE International Conference on Solid Dielectrics, ICSD*, pp. 389–392, 2013. DOI: 10.1109/ICSD.2013.6619769

[P2] M. Niittymäki, T. Suhonen, J. Metsäjoki and K. Lahti, "Influence of humidity and temperature on the dielectric properties of thermally sprayed ceramic $MgAl_2O_4$ coatings," in *2014 IEEE Conference on Electrical Insulation and Dielectric Phenomena (CEIDP)*, pp. 94-97, 2014. DOI: 10.1109/CEIDP.2014.6995894

[P3] M. Niittymäki, T. Suhonen, J. Metsäjoki and K. Lahti, "Dielectric breakdown strength of thermally sprayed ceramic coatings: effects of different test arrangements," in *Journal of Thermal Spray Technology*, vol. 24, no. 3, pp. 542–551, 2015. DOI: 10.1007/s11666-014-0211-1

[P4] M. Niittymäki, T. Suhonen, J. Metsäjoki and K. Lahti, "DC dielectric breakdown behavior of thermally sprayed ceramic coatings," in *24th Nordic Insulation Symposium (NORD-IS 15)*, pp. 499–510, 2015. DOI: 10.5324/nordis.v0i24.2289

[P5] M. Niittymäki, T. Suhonen, J. Metsäjoki and K. Lahti, "Electric field dependency of dielectric behavior of thermally sprayed ceramic coatings," in *IEEE International Conference on the Properties and Applications of Dielectric Materials (ICPADM)*, pp. 500–503, 2015. DOI: 10.1109/ICPADM.2015.7295318

[P6] M. Niittymäki, I. Rytöluoto, T. Suhonen, J. Metsäjoki and K. Lahti, "Role of microstructure in dielectric properties of thermally sprayed ceramic coatings," in *2016 IEEE International Conference on Dielectrics (ICD)*, pp. 500–503, 2015. DOI: 10.1109/ICD.2016.7547811

[P7] M. Niittymäki, T. Suhonen, J. Metsäjoki and K. Lahti, "DC conduction and breakdown behavior of thermally sprayed ceramic coatings," *IEEE Transactions on Dielectrics and Electrical Insulation*, vol. 24, no. 1, pp. 499–510, 2017. DOI: 10.1109/TDEI.2016.006156

[P8] M. Niittymäki, T. Suhonen, J. Metsäjoki and K. Lahti, "Effect of temperature and humidity on dielectric properties of thermally sprayed alumina coatings," *IEEE Transactions on Dielectrics and Electrical Insulation*, vol. 25, no. 3, pp.908–918, 2018. DOI: 10.1109/TDEI.2018.006892

Chapter 1

Introduction

Thermal spraying is a coating process in which finely divided metallic or non-metallic materials are deposited on the surface in a molten or semi-molten state to form a coating [1–4]. The spray technique is a way of generating a stream of such particles [1–4]. First thermal spraying techniques were developed to spray low-melting temperature materials (e.g. tin or lead) in 1910. In the 1960s, the thermal spray technologies started to develop rapidly since new materials were required in aeronautical and space industries [4]. Since then remarkable developments have been made in spray coating devices and processes, process diagnostics and controls, materials and new applications [4]. Nowadays, a wide range of materials (e.g. metals, alloys, cermets, ceramics) can be thermally sprayed on different surface materials utilizing different spray techniques [4–6]. The global market of thermal spraying (revenue consisting of material, equipment and coating manufacturing) was 9.8 billion US dollars in 2015 [7]. This is expected to grow at an annual growth rate of 2% reaching 10.7 billion US dollars by 2026 [7]. Aerospace and industrial gas turbine applications are about 60% of the overall global thermal spray market including materials, equipment, consumables and coating services [5, 7]. The remaining 40% is distributed over a large number of applications in oil and gas, biomedical, pulp and paper, and electronics industries [5].

Thermal spraying is an effective and a rather low cost method in producing a protective or an insulating layer on a component surface [8–12]. The method enables a tight deposition on different substrate materials (e.g. metals, alloys, glass, etc.) which can have challenging geometries. Typically, thermally sprayed coatings are utilized as heat or wear resistant coatings since corrosion and wear problems are of great importance in several industrial applications, e.g. in metal working industries many parts are coated against severe wear and corrosion problems [3, 4, 6, 8, 13]. In an aircraft engine, several parts can be coated against fretting wear, friction, or utilized for clearance control [3, 4]. The coatings can also be utilized to restore worn or poorly machined parts to their original dimensions and specifications [8].

In high temperature applications, the hot corrosion degradation of metals and alloys is a serious problem in aggressive environment, e.g. in boilers, internal combustion engines,

gas turbines [2, 4, 5], fluidized bed combustion, and industrial waste incinerators [3]. Since thermally sprayed oxide coatings endure heat and harsh environments very well, a ceramic coating (a thickness of 100–2000 µm) can be deposited on component surface to protect the component against the hot corrosion [2, 4]. In gas turbine components or aero-engine parts, thermal barrier coatings (TBCs) are used to insulate the components which operate at very high temperatures [2–6]. The coatings have low thermal conductivity which enables them to act as a thermal barrier, thus decreasing the surface temperature of a metal component [14]. In particular, oxide coatings like yttria-stabilized zirconia (YSZ) or alumina (Al_2O_3) are the most suitable materials as a thermal barrier coating [2, 4, 5, 15–17]. The YSZ is the most widely used material in TBCs since it has excellent thermo-mechanical properties (i.e. good thermal stability, low thermal conductivity, high coefficient of thermal expansion) [16, 17].

Alumina (Al_2O_3) is a widely used electrical insulation material in high temperature applications because it exhibits high hardness and refractory nature [18]. Thermally sprayed alumina coatings are well suitable for industrial applications due to their high hardness, elastic modulus, and good electrical performance [12]. In particular, alumina based coatings (e.g. Al_2O_3-TiO_2) are utilized as wear resistant coatings in industrial applications [6, 13, 19, 20]. Low amount of titania (e.g. 13 wt.-%) is sometimes mixed with alumina in order to improve the mechanical properties [19]. Alumina coatings can be utilized as an electrical insulation in several industrial applications, which are e.g. solid oxide fuel cells (operating temperatures 500-800 °C) [6, 21, 22], electrostatic chucks utilized in semiconductor wafer processing [10, 23], power electronic circuit boards [11], corona-discharge devices (e.g. corona rolls in printing industry) [2, 23], ozonizer tubes [2, 23], or in general in electronic devices [23, 24]. An alternative to alumina is magnesium aluminate spinel (hereafter termed spinel), $MgAl_2O_4$, which in general has as good electrical performance as alumina coatings or sometimes slightly better [23]. Spinel coatings are utilized as an electrical insulation layer in solid oxide fuel cells, in particular on metallic interconnects [10, 25, 26] or in multilayer electronic circuits [24], or utilized as ceramic humidity sensors [27]. The use of alumina and spinel coatings as electrical insulation is significantly lower than the use against hot corrosion or wear. However, the utilization of the coatings as electrical insulation is estimated to increase in the future since they are well applicable for very high operating temperatures or for harsh environment applications. Furthermore, an insulating coating can be sprayed tightly on the object surface which has challenging geometries.

Although numerous applications exist for thermally sprayed alumina and spinel coating insulations, relatively few studies on the electrical performance of these coatings can be found in literature. Furthermore most of these studies are focused only on the short-term dielectric breakdown strength studies [9, 12, 23, 28–32]. In comparison to the alumina coatings, the dielectric breakdown strength of bulk alumina is reported quite comprehensively in the literature [33–42]. However, the microstructure of these two material types differs significantly, and consequently also their electrical performance.

In order to design electrical insulation systems based on thermally sprayed ceramics, the electrical performance of these materials needs to be known comprehensively. The performance is defined by dielectric parameters (e.g. permittivity, $\tan\delta$, DC resistivity and breakdown strength). However, these are not constant values but differ depending on the form of electrical stress (e.g. DC, AC, frequency of AC, transients) and ambient conditions. In addition, the long-term performance needs to be known in order to use an insulating coating reliably in real applications since the long-term performance finally defines the operating regions of an insulating system. Partial discharge (PD) measurements is also a typical characterization method for insulation systems. Preliminary surface discharge measurements showed that ceramic coatings withstood the discharges well, at least in comparison to certain filled polymer materials. However, thorough surface discharge tests would have required special test samples with ground and polished surfaces. Thus, it was decided not to go on this and to leave this aspect outside the scope of this thesis. In this thesis, the dielectric characterization of the studied coatings are performed as-sprayed coatings without grinding, polishing or sealing. The focus of this thesis will be in the short- and long-term breakdown performance, DC resistivity as well as permittivity and dielectric loss.

Several different thermal spray methods exist but a common method to deposit insulating alumina coatings is atmospheric plasma spraying (APS) while high-velocity oxygen (HVOF) method is a more common method for the deposition of metals and cermets [2, 4, 15]. However, several studies [9, 23, 43, 44] have shown that HVOF process can be utilized to deposit alumina-based ceramics to produce dense and well-adhered coatings. The dielectric properties of HVOF alumina coatings have been reported to be even better than those of APS alumina coatings [23]. Due to aforementioned reasons, the studied thermally sprayed coatings in this thesis are mainly deposited utilizing HVOF method. In addition, the dielectric properties of APS and rod flame sprayed ceramic coatings are studied in order to distinguish possible differences between the coatings deposited by utilizing different spray methods.

1.1 Objectives of the thesis

The main objectives of the thesis can be summarized as:

- Development and evaluation of measurement methods and setups for dielectric characterization (dielectric breakdown strength, DC resistivity, relative permittivity and dielectric losses) of thermally sprayed ceramic coatings.
- Study and analysis of short-term and long-term breakdown performance as well as the DC conductivity, relative permittivity and dielectric losses at low and high electric fields for thermally sprayed ceramic coatings.
- Analysis of the role of microstructure on the dielectric properties of thermally sprayed alumina and spinel coatings.

- Analysis and development of suitable conduction models for thermally sprayed alumina and spinel coatings.

- Study and analysis of the effect of temperature and humidity on the dielectric properties of thermally sprayed alumina and spinel coatings.

1.2 Publications and author contributions

This thesis is written in the form of compilation dissertation based on the publications [P1]–[P8] and other additional material. Dielectric characterization in [P1]–[P8] included DC resistivity, DC breakdown voltage, relative permittivity and dielectric loss measurements for all the studied materials at controlled ambient conditions. In addition to these, following aspects are discussed. In [P3], different breakdown voltage test arrangements were studied and suitable breakdown voltage measurement method was developed for ceramic coatings. Publications [P1, P4, P7] discuss mainly the DC conduction behavior of thermally sprayed alumina and spinel coatings at low and high electric fields. In [P5] the role of electric field on relative permittivity and dielectric losses is discussed. Publications [P2, P8] focus on the effect of temperature and humidity on thermally sprayed alumina and spinel coatings. The role of microstructure on the dielectric properties is discussed in all publications [P1]–[P8] but in detail this is done for one test series in [P6].

The author was the main author in all the associated publications [P1]–[P8] under the supervision of Adjunct Professor Kari Lahti who has contributed to the publications through guidance during the research work and by commenting on the publications prior to the publishing. The author developed suitable measurement methods for ceramic coatings, made the sample preparation tasks for dielectric characterization, performed the measurements of dielectric properties (DC resistivity, breakdown voltage, relative permittivity and dielectric losses), analyzed the results and wrote all the manuscripts. Contributions from the other authors or organizations were as follows:

- All the studied HVOF coatings were manufactured by VTT Technical Research Centre of Finland for the purposes of the HICC project. The studied atmospheric air plasma sprayed and rod flame sprayed coatings were manufactured by Saint-Gobain Coating Solutions also for the purposes of the HICC project.

- M.Sc.(Tech.) Ulla Kanerva developed and manufactured the experimental $MgAl_2O_4$ powder utilized in the HVOF coating studied in [P1, P2].

- The HVOF coatings were sprayed under the supervision of M.Sc.(Tech.) Tomi Suhonen at VTT in [P1]–[P8]. The material characterization [P1] was written by M.Sc.(Tech.) Tomi Suhonen and later edited by the author. Optical and scanning electron microscope (SEM) cross-sectional images were made by VTT. M.Sc.(Tech.) Jarkko Metsäjoki made the material characterization for the studied coatings which

includes the determination of the porosity from the cross-sectional images and gas permeability measurements in [P1]–[P8].

- M.Sc.(Tech.) Tomi Suhonen and M.Sc.(Tech.) Jarkko Metsäjoki commented on the publications [P1]–[P8] prior to the publishing.
- D.Sc.(Tech.) Ilkka Rytöluoto performed the structural analysis from the cross-sectional images and wrote the analysis of that in the manuscript [P6]. In addition, D.Sc.(Tech.) Ilkka Rytöluoto commented on the manuscript [P6] prior to the publishing.

1.3 Structure of the thesis

This thesis is written as in the form of compilation dissertation based on the aforementioned publications and other additional material. The thesis is structured as follows. Chapter 2 presents the background of the thesis giving a brief introduction to thermal spray methods and material properties of alumina based coatings but the main focus is on the dielectric properties of thermally sprayed alumina based coatings. Chapter 3 presents the material characterization methods, the material properties of the studied coatings, and the experimental of dielectric characterization methods. Three following chapters focus on the results of the dielectric properties of thermally sprayed alumina and spinel coatings and the affecting factors. Chapter 4 presents results and discussion on the short-term and long-term breakdown performance of the studied alumina and spinel coatings. Chapter 5 gives an overview of the DC resistivity of all the studied coatings at low electric fields. In addition, a comprehensive study of DC conductivity up to breakdown fields was made for selected coatings. Chapter 6 presents results and discussion on the relative permittivity and dielectric losses for all studied coatings at low electric fields, and for selected coatings the electric field dependency of these properties is discussed. Chapter 7 gives the concluding discussion of the thesis topic and some future research topics are proposed.

Chapter 2

Background: Thermal spray methods, microstructure and dielectric properties of ceramic coatings

This chapter introduces the fundamentals of thermal spray process of a ceramic coating and the lamellar microstructure of ceramic coatings which differs significantly from the structure of sintered bulk ceramic materials commonly utilized in electrical insulation applications. Figure 2.1 presents the various factors which affect the properties of thermally sprayed ceramic coatings. Furthermore, this chapter presents the current state-of-art of the dielectric properties of the electrically insulating ceramic coatings focusing on alumina and magnesium aluminate (spinel) coatings.

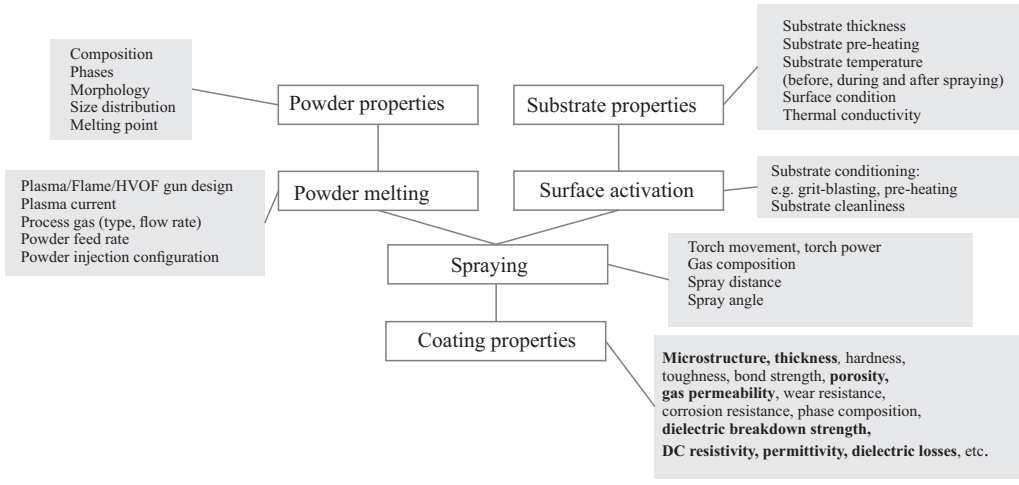

Figure 2.1: The schematic presentation of factors which affect the properties of thermally sprayed ceramic coatings. The highlighted properties (in bold) are studied in this thesis. The figure is revised from [32].

2.1 Thermal spray methods

Thermal spray processes generally involve complete or partial melting of a coating material. Although several thermal spray technologies exist, the basic principle of the coating formation is similar in all the methods. In the thermal spray process, a torch has a significant role since it converts the supplied thermal energy (chemical energy for combustion processes or electrical energy for plasma based processes) into a stream of heated gases and accelerates the particles. The spray torch is typically controlled by a robot. Figure 2.2 presents the schematic idea of a thermal spray process and a coating formation. The coating material is heated, melted and accelerated by the formed high-temperature, high-velocity gas stream towards a substrate (e.g. grit-blasted steel plate) or a coating surface. The particle or droplet deforms to generate a splat. Multiple layered splats form a coating layer-by-layer as shown in Figure 2.2. The droplets may be generated either by melting powder particles or by melting ceramic rods using high-energy gas stream. The ceramic powders can be manufactured by several methods of which so-called fused and crushed -method is the most typical technique. In addition to that method, agglomerated and sintered powders can be utilized. However, the latter technique produces more porous particles than the fused and crushed method although the agglomerated and sintered powder particles have finer structure. As a result of the coating formation, a dense and strongly adhered coating is formed by the rapid solidification of splats when the heat from the hot particles is transferred to cooler substrate material. However, a successful application of thermally sprayed coatings to engineering usage strongly depends on the quality of the adhesion between the coating and the substrate or the previously sprayed layers. Surface roughening improves the adhesion because the adhesion is mechanically enhanced by shrinking of the splats around the peaks of the roughened substrate. According to Amada and Hirose [45], the adhesion strength of plasma sprayed alumina coatings can vary from 15.2 MPa to 18.8 MPa depending on the grit-blasting angle. [1–4, 8, 10, 17, 18, 45–52]

As mentioned before, the thermal and kinetic energy of the flame can be produced either by the burning mixtures of fuel gas and oxygen, or by using an electrical power source. Thus, thermal spray methods can be divided into a few main groups based on the energy sources [2–4, 44, 46, 48, 52]. The groups are plasma spray methods (atmospheric plasma APS, vacuum plasma VPS, and low pressure plasma LPPS), combustion flame spray methods, high velocity oxygen- or air-fuel methods (HVOF/HVAF), electrical arc methods, detonation methods (D-Gun), and cold gas methods [2–4, 44, 46, 48, 52]. The main differences between the different thermal spray techniques are the different flame temperatures and particle velocities [4, 14, 18, 44, 48] presented in Figure 2.3. Because a coating is formed of flattened and fast solidified droplets, the particle velocity affects the obtained density of the lamellar microstructure of the coating significantly [44]. The flame temperature determines which materials can be sprayed by certain thermal spray technique, and due to the high flame temperature of atmospheric plasma spraying, ceramic

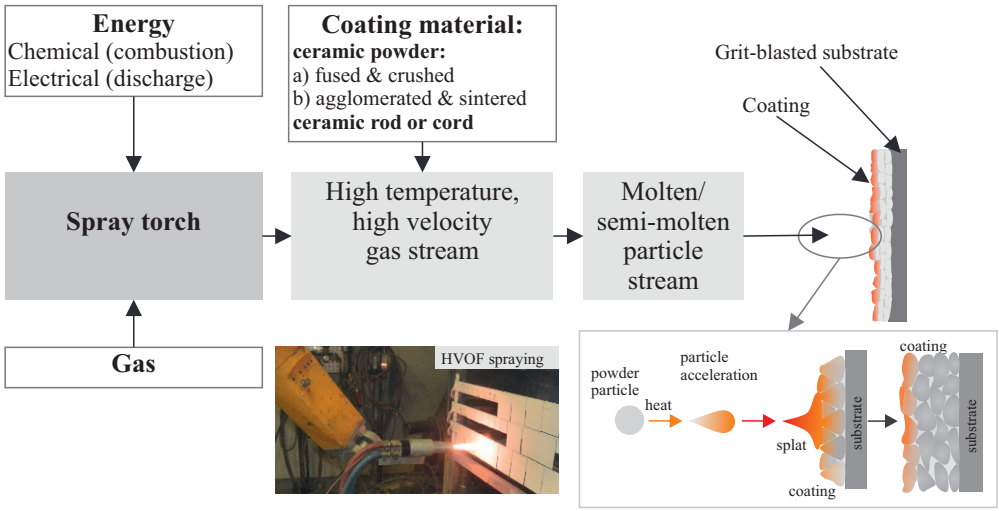

Figure 2.2: The schematic principle of a thermal spray process of the ceramics is in the top and a schematic idea of the coating formation from a powder particle to a droplet and finally to the coating is in the middle right. The schematic figures are revised from [4, 48]. In the photograph, alumina coatings are deposited by utilizing high-velocity oxygen (HVOF) thermal spray process.

coatings are mainly deposited utilizing this technique [2, 4, 44]. In this thesis, the studied ceramic coatings are sprayed by utilizing rod flame spraying, atmospheric plasma spraying (APS) and high-velocity oxygen fuel (HVOF) spraying. The basic principles of these techniques are presented in the following.

2.1.1 Atmospheric plasma spraying

The first plasma torches were developed in the mid 1950s forming the basis of the plasma torches used today [4]. The conventional plasma spray method is atmospheric plasma spraying (APS), where the plasma jet exits the torch in atmospheric environment [4, 18, 48]. An electric arc generates plasma within the plasma torch. The electric arc is burned between a rod-type cathode and a cylindrical anode nozzle [2, 4, 17, 18, 47, 52]. The arc ionizes the flowing process gasses (argon, hydrogen, nitrogen or helium) into the plasma state [2, 4, 8, 15, 17, 18, 47, 52, 53]. Due to the high temperature of the plasma jet (temperatures over 8000 °C), the plasma spray method is widely used to produce ceramic and metal coatings [8, 15]. In particular, APS is a very suitable method for producing oxide coatings due to the high melting points of oxides [2, 4, 15].

The plasma jet exits the nozzle at very high temperature which can be even from 12 000 °C to 16 000 °C at its highest and the maximum plasma jet velocity can be from 250 m/s to 500 m/s depending on torch design, plasma gases, and operating parameters [2, 4, 15, 18, 52]. The plasma temperature decreases rapidly after exiting the nozzle [18, 47]. Therefore, the ceramic powder particles are injected radially by carrier gas into the

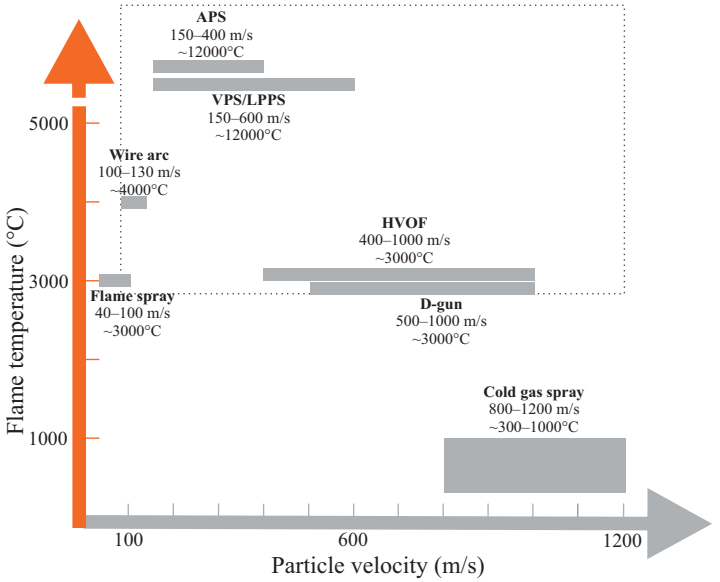

Figure 2.3: The flame temperatures of thermal spray processes presented as a function of particle velocity. The dashed line presents the operation temperatures of the processes suitable for spraying ceramic materials. The data is adapted from publications [4, 14, 18, 44, 48].

hottest part of the plasma jet where the particles are heated, melted, or partially melted, and accelerated, before they hit on the substrate, flatten and solidify [2, 4, 8, 17, 52]. Finally, a coating forms from several splats [2, 4, 8, 17, 52]. Thus, this process results in the deformation of the particles which spread like pan cakes or so-called splats [8, 17]. Figure 2.4 presents a schematic figure of a typical atmospheric plasma spray gun. The coating is formed layer-by-layer by several passes of the plasma/particle jet over the substrate [2, 4, 8, 17, 52]. The temperature of the substrate determines the cooling rates of the splats [17]. In order to achieve a good quality coating, the careful optimization of the spray parameters is essential. These parameters are the thermal properties of the material, the morphology and size distribution of powder particles, substrate pre-heating (achieved with the plasma jet), spray distance, powder feeder and injector, coating surface temperature control [8, 17, 54]. Furthermore, the movement of the torch affects the structure and the final properties of a coating since the relative motion of the torch over substrate controls the coating thickness per pass and partially also the heat transferred to coating and substrate [54, 55]. Due to this, the deposition of coatings on complex geometries requires the designing of an optimized movement with a defined torch velocity [54].

Plasma spraying is a very rapid process. Ctibor *et al.* [56] studied that there are approximately 6×10^5 powder particles in a volume of $1\,\mathrm{cm}^3$ of plasma jet traveling towards the substrate surface with a velocity of tens to hundreds of m/s. The particle

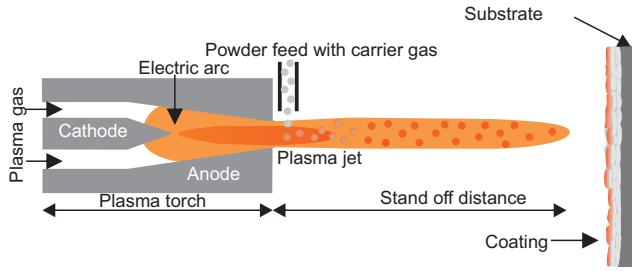

Figure 2.4: The schematic figure of the atmospheric plasma spray gun. The data is adapted from publications [4, 8, 17].

velocity can vary from 30 m/s to 600 m/s in the conventional plasma spraying [8, 18, 47, 48, 50]. The obtained particle velocities of plasma methods are higher than those of flame spraying, and this process results in coatings which are denser and have finer as-sprayed surface roughness [52, 57]. Furthermore, the microstructure of plasma sprayed coating is typically fine-grained [18]. However, the spray process is complex (e.g. electrode degradation, the flowability of powders, etc.) which can cause difficulties making similar deposition even with the same process parameters [4, 18].

2.1.2 Flame spraying

The flame spraying is chronologically the first spray technique, which was developed by a Swiss engineer Maximilian Schoop in 1910 in order to work with low-melting temperature metals, e.g. tin or lead [2, 4, 53]. The method was later extended to refractory metals and ceramics with special arrangements [2, 48]. In the flame spray method, the chemical energy of fuel gas and oxygen is released in a combustion process to generate the high-temperature flame [2, 4, 48, 52]. The common fuel gases are propane, hydrogen and acetylene but the oxygen-acetylene torches are the most commonly used [2, 4, 52].

The typical flame temperature is 3000 °C to 3350 °C [2, 15, 18, 50] and the flame velocities are in the range of 80–100 m/s [2, 15]. Typically a coating material is melted and the droplets or semi-molten particles are accelerated towards the substrate by the expanding hot gas flow and air jets [4]. The flame length is limited and the particle velocity is only in the range of 30–100 m/s [2, 4, 48, 50]. Due to these factors, after the flight the maximum temperature of the particles is only 70% –80% of the gas temperature (typically ∼2300 °C) which is too low to melt ceramic materials [4]. However, the ceramic cord or rod can be introduced in the flame in such a way that only the very tip of a rod or cord is melted and then atomized by atomizing gas (typically air) [4, 52]. This leads to higher material temperatures, even 95% of the gas temperature, which is enough to melt ceramic materials [4, 52]. In addition, the velocity of the droplets atomized by air jets is slightly higher (∼150 m/s) [4, 50, 52]. The schematic idea of the rod or cord flame spraying is presented in Figure 2.5. Typically, powders, rods or cords are introduced axially through the rear of the nozzle into the flame burning at the nozzle exit of the torch

[2, 4, 52, 57] but powders can also be introduced perpendicularly to the flame [2]. The rod or cord is pushed through the nozzle at controlled velocity [4]. The feedstock materials are melted and the particles or droplets are accelerated towards substrate surface by expanding hot gas flame and air jets [4, 57]. Figure 2.5 presents the schematic idea of the rod flame spraying. In order to deposit a good quality coating, uniform motion of cord or rod, adapted gas compostion, flow rate and the cord or rod diameter and composition play a key role [4].

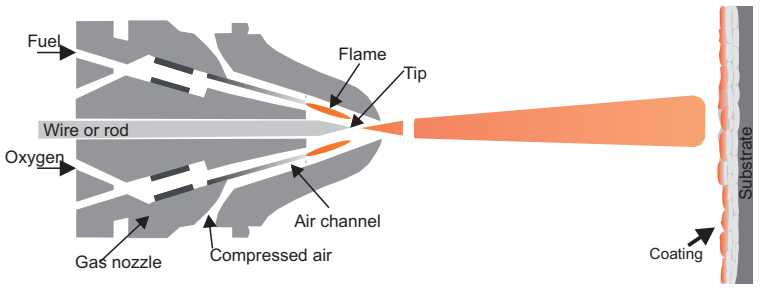

Figure 2.5: The schematic principle of a rod or wire flame spraying. The figure is revised from [4, 18].

From all the spray processes, atmospheric plasma spraying is the most well-established method of producing ceramic coatings. However, plasma spraying is a rather expensive method [4, 18, 52, 57], and due to this less expensive flame spray method utilizing a ceramic rod can be an interesting alternative to produce ceramic coatings [57]. Costil *et al.* [57] reported that the plasma sprayed alumina coatings exhibited denser structure with thinner splats in comparison to rod flame sprayed alumina coatings and thus their mechanical and thermal properties differ which can be advantageous depending on the applications. However, the limitation of rod flame spraying is the relatively low velocity of sprayed particles which results in more porous coatings [4, 15, 52]. Furthermore, oxidation inclusions are also present because of the high degree of interaction between fully molten droplets and the surrounding atmosphere which can reduce the quality of a coating [4, 48, 52].

2.1.3 High-velocity oxygen fuel spraying

The high-velocity oxygen fuel (HVOF) -torch was developed in 1958 but it was commercialized at the beginning of the 1980s [1, 2, 4, 48]. The principle of this technique is very similar to the Detonation gun -process (D-gun) developed in 1955 but the burning of the fuel in oxygen is continuous in HVOF while it is repetitive in D-gun process [2, 4, 44]. The flame temperature in HVOF process is similar to the temperature of flame spray processes (Figure 2.3), and due to this the HVOF process is typically utilized to spray composites with carbide reinforcements and metal or alloy matrices [2]. However, in the HVOF top gun system, where the spray powder is injected axially and centrally into the combustion

chamber, high particle temperatures can be achieved, and thus ceramic coatings (e.g. Al_2O_3) can be successfully deposited with this method [9, 15, 23, 29, 43, 44, 47, 58].

In HVOF spraying, a fuel gas (e.g. hydrogen, propane, propylene) with oxygen are injected into the combustion chamber of the torch where the gases are combusted continuously [2, 44, 48, 51, 52]. Figure 2.6 presents the schematic figure of one type of HVOF gun. The combustion of the gases produces a high temperature and pressure (from 3 bar to 10 bar) in the chamber, and this causes a supersonic flow of the gases through the nozzle [2, 15, 44]. Due to high back-pressures created by the combustion process, a pressurized powder feeder is required [2, 18]. Thus, the powder material is injected via a carrier gas (e.g. N_2, He, or Ar) into the combustion chamber [2, 18, 44]. The powder with carrier gas is introduced axially (e.g. Praxair HV-2000 torch) or radially into the jet of expanding hot gases where they are propelled forward, heated, and accelerated onto a surface to form a coating [2, 52]. The particles melt completely or only partially, depending on the flame temperature, particles dwell time, material melting point and thermal conductivity [44].

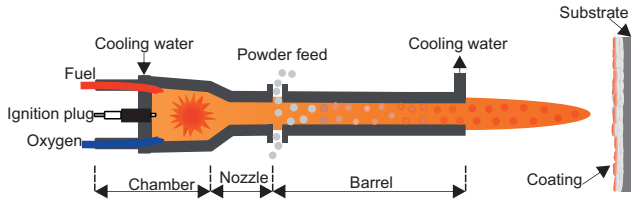

Figure 2.6: The schematic figure of the HVOF spray gun where the powder particles are introduced radially into the jet. The figure is revised from [51].

The typical flame temperature of HVOF process is 2500 °C to 3200 °C depending on the fuel, the fuel gas/oxygen ratio and the gas pressure [2, 18, 44, 50, 52] while the flame velocity is 1500 m/s to 2000 m/s [2, 18]. Due to the high temperatures, the combustion chamber, nozzle, and barrel are cooled by water [2, 47]. According to Sobolev [50], Basu *et al.* [18] and Dorfman [14] particle velocity can be up to 800 m/s in HVOF process while Oksa *et al.* [44] reported that particle velocity can vary from 400 m/s to 1000 m/s depending on the utilized nozzle type. The particle velocities are significantly higher in HVOF process than in flame or atmospheric plasma spraying, and thus very dense and well-adhered coatings can be achieved [4, 15, 18, 43, 47, 52]. In addition, the microstructure of the deposited coatings is often very fine-grained [18]. Accordingly, the abrasion wear resistance of HVOF sprayed alumina-titania coating is significantly higher in comparison to the plasma sprayed coatings [59].

The HVOF spraying is a very complex process which has several variables affecting the coating formation and thus the coating properties [44, 58]. These variables are hardware characteristics (e.g. nozzle geometry and spray distance) and process parameters (e.g. fuel gas, gas flow density, and powder feedstock) [44, 58]. During the spraying, the powder particles experience very high velocity (supersonic velocities) with fast heating up to the

melting point of a material or above it [43, 44]. The high temperature may cause the evaporation of the powder or some components of it, dissolution, in-flight oxidation of particles and phase transformations (alumina coatings) [4, 18, 44].

2.2 Coating formation and the microstructure of thermally sprayed ceramic coatings

The microstructure of thermally sprayed ceramic coatings is rather complex consisting of lamellar structure as well as defects such as pores, cracks and unmelted particles [2, 4, 28, 48, 60], see Figure 2.7. The coating microstructure strongly depends on several spray parameters which need to be optimized carefully in order to achieve a good quality coating [2, 4, 44]. The main spray parameters are i) the working parameters of the utilized process (e.g. torch design, the shape and dimension of nozzle, mass flow rates, the compositions and pressure of spray gases, gas consumption rates, etc), ii) powder, rod or cord composition, particle size distribution, particle morphologies, and post-treatment, iii) powder injection (axial or radial, injector position and orientation, internal diameter, carrier gas flow rate, the deposition rate (combination of feed rate and robot speed), the atomization gas flow rate for cord or rod, etc.), iv) spray distance and pattern, v) the temperature control of substrate and coating during the pre-heating, spraying, and cooling phases, and vi) substrate shape, size, thickness and surface preparation [4, 8, 17, 44, 48, 54].

Although several parameters affect the formed coating, all of the aforementioned aspects are not discussed in detail in this thesis, as the main focus of this thesis is not on the spray technique. In the following, the coating formation is briefly discussed and the formed microstructure is presented. The powder composition and particle morphologies have an important role in the coating formation [4, 48]. Depending on the manufacturing process, the powder particles can have angular shape (made by fused and crushed -method)

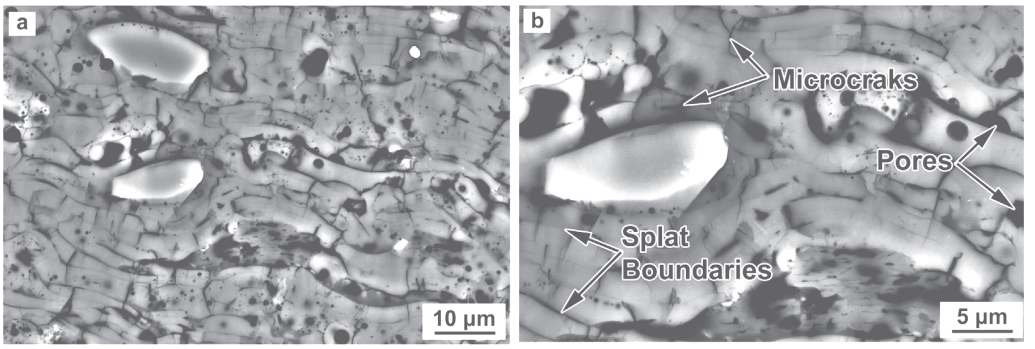

Figure 2.7: The cross-sectional SEM micrographs of APS alumina coating showing the typical lamellar microstructure of thermally sprayed coatings as well as the pores and microcracks of a coating [61].

or spherical shape (made by agglomerated and sintered -method) [4, 23, 25, 48, 62]. The particle shape affects the aerodynamic behavior and furthermore the powder flowability and powder feed rate [62]. If the flowability is poor, fluctuations exist at the powder feed rate, which results in an inhomogeneous coating structure [62].

As discussed previously, the utilized spray technique affects the temperature and velocities of powder particles, and consequently the formed microstructure. In addition, the relative velocity of the particles versus surrounding environment (plasma or flame and air) is not constant [56]. The temperatures and velocities of the powder particles depend on the particle size distribution and morphology as well as their injection conditions [4, 62]. The particle size distribution should be as narrow as possible in order to limit the particle trajectory dispersion which can cause particles impacting with different velocities, impact angles, and temperatures [4, 48, 54]. In HVOF process, the typical size distribution of alumina powder particles is from 5 µm to 25 µm [9, 23, 43] while in the plasma process it is slightly higher being from 10 µm to 45 µm [4, 23, 47, 53, 61]. Smaller particle size is required in HVOF process than in APS process in order to ensure sufficient heating and melting of the powder particles and efficient coating deposition [43]. In order to reduce the porosity, large unmelted particles (sufficiently heated to adhere) or partially melted particles must be avoided which can be made by choosing optimal the particle size distribution and optimizing the particle injection carefully [4].

During the spraying, the powder particles are heated, melted (totally or partially) and accelerated before impacting onto the surface of substrate at a high speed [2, 4, 17, 62]. The phenomena occurring at this stage determine the adhesion between a coating and a substrate [2, 54]. The molten particles deform and spread like pancakes forming so-called splats, which typically have thickness in the range of 0.5–5 µm [2, 17, 43, 63] and a diameter of 200–400 µm [17]. This spreading process of droplets is presented in Figure 2.8a where the lamellar microstructure of an alumina coating can be seen [64]. Heat from hot particles is transferred to a cooler substrate causing the splats solidify rapidly and shrink [17, 48]. The melting occurs in a few milliseconds and the solidification occurs even faster within a few microseconds with strong temperature gradients and cooling rates in the range of 1×10^6–$1 \times 10^9\,\mathrm{K\,s^{-1}}$ resulting in sometimes metastable crystalline phases, amorphous or partly amorphous phases [47, 48, 54, 62, 63, 65]. The lower surfaces of the splats cool down faster than the internal parts. Due to this, the surfaces are normally more amorphous while the internal parts are typically crystalline [2, 31, 66] which can be seen in Figure 2.8b–c. The thickness of the final coating is reached in a few tens to a hundreds of passes of the torch over substrate [2, 56].

In addition to the splats, the coating exhibits some unmelted powder particles, voids and often also some cracks [2, 17, 18, 48]. Since the contact between layered splats or between the first splats and the substrate can be imperfect, inter-lamellar pores or sometimes called inter-lamellar cracks can be formed [4, 17, 54]. These inter-lamellar pores are thin voids (the thickness of 0.01–0.1 µm [67]) which are formed between splats and are a part of coating porosity [4]. The splat boundaries and pores of an APS alumina

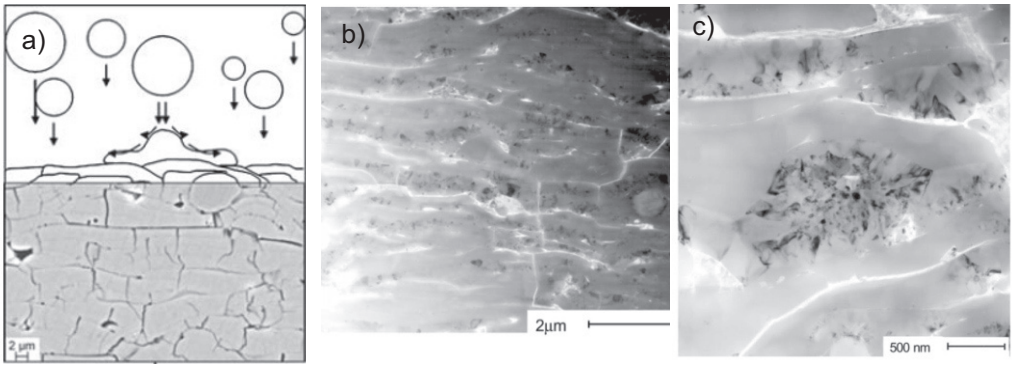

Figure 2.8: a) Cumulative process of spreading droplets on coating surface and the SEM image of cross-section of alumina coating [64]. b) TEM image of low-pressure plasma sprayed alumina coating which presents the layered splat-structure [31]. c) The close-up TEM image presents the internal structure of splat with polycrystalline interior and surrounding amorphous region [31].

coating can be seen in Figure 2.7. During the coating deposition voids, which are called globular pores, are formed due to an imperfect contact between different splat layers [4, 17, 64, 68]. The globular pores are distributed more or less homogeneously, and their potential to worsen the coating properties is proportional to their size, amount, distribution and inter-connections [4, 56, 68].

The rapid cooling and the shrinking of a splat leads to the generation of residual stresses which can cause different cracks in the coating, see Figure 2.7 [2, 4]. Due to the hindered contraction of the splats on the substrate or on the previously sprayed coating layer, tensile quenching stresses arise within the splats during the solidification and are mainly relaxed by micro-cracking (orthogonal to the splat) [2, 4, 17, 54]. Furthermore, macro-cracks can be formed which are running through layered splats in particular at their interfaces [4, 17, 54]. However, the spray pattern, the spray distance, the control of the temperature of substrate before and during the spraying, and the temperature control of coating allow tailoring the different residual stresses and their relaxation in the coating and substrate [62].

Due to the process-dependent defects described above, thermally sprayed coatings always have some degree of porosity [4, 43, 48, 63, 68, 69]. Porosity can be described as a distribution of voids of two different kind: globular pores and micro-cracks, see Figure 2.7 [61, 64]. The determination of the porosity can be made by using several methods. The typical method is image analysis which is made by utilizing cross-sectional micrographs taken by optical or scanning electron microscopes (SEM) [12, 23, 56, 60, 68–70]. Although the image analysis gives a good estimation about the porosity [69], the defined value does not represent the volumetric porosity of a coating which would take into consideration the unique shape of the voids and their connectivity between each others [60, 68]. However, the shape and orientation of the pores can be defined by using three-dimensional images

instead of the 2D images [56, 56, 64, 71, 72]. The 3D analyzing methods are not as widely used as the methods based on the 2D images since the 3D imaging is more difficult task, rather time-consuming and more expensive [64].

The porosity of HVOF sprayed alumina coatings is typically reported to be from 4% to 10% [11, 23, 73], while for plasma sprayed alumina coatings it is from 2% to 9% [4, 12, 23, 28, 32, 73, 74]. However, Dong *et al.* [75] noticed that the porosity of plasma sprayed alumina coatings increased (from 6.9% to 15.8%) with the increasing thickness (154–546 µm) since more pores are distributed in thicker coatings. Kulkarni *et al.* [73] noticed that plasma alumina coatings have large globular pores, inter-lamellar pores and cracks, while HVOF coatings have well-adhered splats with finer porosity. Kulkarni *et al.* [73] also noticed that the porosity of plasma sprayed alumina coatings increased from 8.4% to 23.8% with the increasing powder particle size due to the reduced melting efficiency of coarser particles in the plasma flame and due to the larger overall splat thickness.

Porosity affects a wide range of coating properties, e.g. elastic modulus, thermal conductivity, and dielectric properties [28, 69, 76]. The high porosity can be even beneficial if the coating is utilized as a thermal barrier coating since the high porosity decreases the thermal conductivity of a coating [43, 63]. In wear and corrosion protection, high porosity is commonly very harmful feature [43]. Due to this, the alumina coatings in these applications are typically sealed using either organic (e.g. polyurethane- or epoxy-based) or inorganic (e.g. aluminum phosphates) sealants [4, 13, 77]. However, high porosity has been suggested to decrease the dielectric breakdown strength of alumina coatings [23, 28, 76] but it has also been reported that porosity does not clearly affect the breakdown strength of alumina coatings [12, 31]. Although porosity is one of the key structural parameters to determine the microstructure of the ceramic coatings, also other material properties need to consider in a comprehensive coating property analysis.

2.3 Phase transitions in thermally sprayed alumina coatings

Naturally, alumina normally occurs in its crystalline α-phase which is thermodynamically the only stable form of alumina [63, 65, 78, 79]. Also, the powders utilized in thermal spraying consist of mainly stable α-Al_2O_3 [23, 43, 65, 78, 80]. However, due to the rapid solidification of a splat during the spray process, the coating consists of metastable Al_2O_3 phases, i.e. γ, δ, and θ, and some amorphous regions [2, 43, 81–83]. Typically, thermally sprayed alumina coating consists of metastable γ-Al_2O_3 as the main phase and stable α-Al_2O_3 as the minor phase [4, 12, 23, 28, 43, 53, 65, 70, 74, 75, 78, 80, 82–93]. In HVOF sprayed alumina coating the amount of γ-Al_2O_3 has been reported to be 75% [43], 79% [23], 85% with high particle velocity [58] and 96% with low particle velocity [58]. In plasma sprayed alumina coatings, the amount of γ-phase is almost similar level with HVOF coatings being 56% [90] and 65% [83].

The phase transformation occurs since during the solidification process the γ-Al_2O_3 is more easily and rapidly nucleated from the melt than α-Al_2O_3 because of its lower

critical free energy for nucleation [53, 65, 84]. The nucleation energy depends on the temperature and the size of the splat [2]. Typically, γ-Al_2O_3 nucleates first from the melt and the cooling rate after solidification is sufficiently rapid to prevent transformation to δ-Al_2O_3 or α-Al_2O_3, and thus the main phase in the alumina coatings is γ-Al_2O_3 [53, 65]. The alumina coatings commonly consist of some amount of α-Al_2O_3 [12, 23, 28, 43, 63, 74, 80, 83, 84, 90, 92]. This amount of α-Al_2O_3 can originate from the unmelted original powder particles or particles which are melted only a little on the outer surface of the powder particle [65, 83, 84]. However, Damani *et al.* [83] proposed that only a little of the total amount of α-Al_2O_3 in the material is originated from unmelted original powder particles and major part of α-Al_2O_3 is nucleated directly from the melt.

Thermally sprayed coatings are manufactured with phase transformation being either ignored or accepted [79]. Although the phase transformation occurs, the alumina coatings are well acceptable for many applications [79, 80]. However, it needs to be emphasized that the physical properties of γ-Al_2O_3 are generally inferior to those of α-Al_2O_3 [65, 85]. For example, the γ-Al_2O_3 is highly hygroscopic which can cause problems in the applications utilized at high humidity conditions [2, 28, 29, 79]. The high amount of γ-Al_2O_3 in alumina coatings is reported to increase significantly the relative permittivity and dielectric loss of the coatings with increasing humidity [24, 28, 85].

2.4 Dielectric properties of thermally sprayed alumina based coatings

In the present literature, studies on the electrical performance of thermally sprayed alumina and spinel coatings are mainly focused on the dielectric breakdown strength at room temperature conditions. DC resistivity, relative permittivity and dielectric loss of the coatings are not widely studied and in particular studies of the long-term properties or degradation of coatings are not much reported. The following sub-chapters present the current state-of-the-art of the dielectric properties of thermally sprayed alumina based coatings. Although the microstructure of alumina coatings differs from the structure of bulk alumina, the dielectric properties of bulk alumina are discussed as a reference to the alumina coatings.

2.4.1 Breakdown strength of thermally sprayed alumina coatings

One of the main dielectric parameters is the dielectric breakdown strength (BDS) and the previous studies of the dielectric properties of thermally sprayed alumina and spinel coatings are mainly focused on the breakdown strength at room temperature conditions. In the breakdown voltage measurements, a sample is placed between the electrodes and the voltage is increased either by a linear ramp or by step-wisely until a breakdown voltage is reached. When the breakdown voltage is reached, a local narrow conducting path forms which connects the electrodes of the dielectric material, and thus the material

loses its insulating state and converts to a conducting state. For solid dielectrics, the breakdown causes a permanent failure into the material.

Several theoretical breakdown models can be found in literature and some of them are briefly discussed here. More information of the models can be found for example in [94–100]. Breakdown mechanisms can be categorized according to the process which leads to final breakdown [94, 96]. The breakdown mechanisms can be divided as follows:

- *Thermal breakdown mechanism*: when an insulation material is stressed, conduction current and dielectric loss generate heat into the material. The process is balanced through heat dissipation in accordance with the thermal properties of the material. When the rate of heating exceeds the rate of cooling, unstable situation occurs which leads to thermal runaway, and eventually the material breaks down. At high temperatures, the electrical conductivity increases rapidly, and due to this the breakdown at high temperatures usually occurs according to thermal mechanism [97, 101, 102].

- *In electronic breakdown mechanism*, the charge carrier multiplication is due to electronic processes. One of electronic breakdown mechanism is intrinsic breakdown which is purely electronic since it occurs very rapidly (1×10^{-8} to 1×10^{-7} s) and depends only on temperature [96, 99, 100]. The breakdown strength according to this mechanism occurs at higher fields than thermal breakdown.

- *Electro-mechanical breakdown mechanism*, where the breakdown occurs when mechanical stress (the electrostatic attraction of the electrodes) exceeds a critical value which cannot be balanced by the elasticity of the dielectric (Young's modulus). When this high field is maintained, the field increases because of the decrease in thickness and furthermore increasing the electrode attraction further. Local heating and consequent softening or cracking causes the final dielectric collapse or fracture.

- *Partial-discharge breakdown mechanism*: solid insulation materials often have some voids or cavities filled with gas, e.g. air. Since the permittivity of air is lower than that of solid insulation, the electric stress in the void (air) is higher than in the solid. When the applied voltage is increased, at certain level the inception voltage of partial discharges can be exceeded. These discharges starts to degrade the material and can eventually cause breakdown.

Although several breakdown mechanisms are presented in literature, the final breakdown is rarely caused by only one mechanism. Additionally, it needs to be emphasized that breakdown strengths are higher than the operating electric fields under service conditions. During a long time, material degradation can occur at the operating fields which can start weakening the insulation properties eventually leading to a breakdown. Due to this, applied electric field, operating conditions, and history affects a real breakdown mechanism. In addition, one breakdown mechanism can take over from the other over the time or the

actual breakdown can be a combination of two or several mechanism. Owate [33, 103] noticed that the latter one can occur for bulk alumina because the proposed breakdown mechanism was a combination of thermal and electro-mechanical processes. However, Owate [33] emphasized that the rate of voltage rise, current-voltage characteristic, the fracture patterns, micro- or macro cracks, the presence of melt, and the recrystallization structures have decreasing effect on breakdown strength. In addition, Carabajar [104] noticed that the microstructure of bulk alumina affects notably the breakdown strength since the smaller grain size material had higher breakdown strength although the elastic modulus, permittivity and toughness between the materials were similar.

According to literature [23, 29, 75], the presence of defects (voids, cracks, etc.) can enable the dielectric breakdown of thermally sprayed alumina and spinel coatings at lower fields. In addition, it has been proposed that the breakdown performance of the coating was more related to the microstructure than to phase composition [9, 23, 29, 75]. In particular, vertical cracks in coating microstructure enables the formation of critical failure path and lower breakdown strength [29]. The breakdown mechanism of alumina coatings was considered to occur according to thermal mechanism [23] or discharges/partial discharges [9, 30] or as a combination of these two mechanisms [30, 75]. These observations are in coherence with Moulson & Herbert [100] since they proposed that one possible breakdown mechanism for ceramics is partial discharge mechanism due to the inhomogeneous and porous nature of ceramics. As it has been discussed before, the partial discharges can be formed in the voids and thus progressively deteriorate the insulation material, eventually causing the material break down.

Figure 2.9 gives an overview of DC and AC breakdown strengths of bulk aluminas and thermally sprayed Al_2O_3-, Al_2O_3-TiO_2 and $MgAl_2O_4$ coatings from literature at room temperature conditions [9, 12, 23, 28–36, 38–42, 75, 76, 102–109]. The breakdown strengths of ceramic coatings are at a similar level with bulk aluminas. The very high AC and DC breakdown strengths of alumina coatings in Figure 2.9 may be explained by the insulation oil immersion utilized in the measurements [31, 75] since the breakdown strengths of the alumina coatings measured without oil immersion are clearly lower [12, 23, 28, 29, 32]. The insulation oil can easily penetrate into the porous and moisture sensitive coatings, and thus enhances the breakdown strength of a coating. However, the utilization of insulation oil in breakdown voltage measurements has not been observed to affect the breakdown strength of sintered alumina [33–42, 102, 103, 105–108] since sintered alumina exhibits dense and fully crystalline structure. Sometimes the measurement arrangements or results are reported insufficiently in the literature, e.g. exact sample thickness values are not given [37, 110] or the sample thickness is only given as a range, e.g. 200-300 µm [76]. Although sample thickness was not reported [37, 110], the breakdown field of bulk alumina were given (E_{bd}=15 V/µm). These results are not presented in Figure 2.9 due to the lack of exact thickness info but the obtained breakdown fields are at similar level with the other bulk aluminas presented in Figure 2.9.

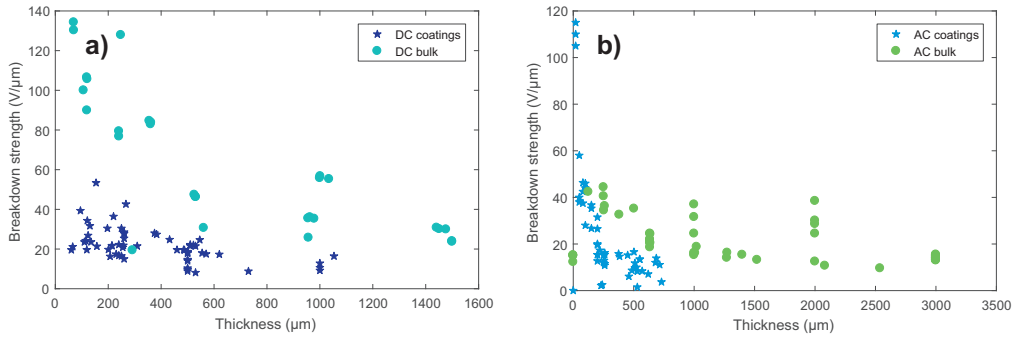

Figure 2.9: **a**) DC breakdown strength of thermally sprayed Al_2O_3-, Al_2O_3-TiO_2 and $MgAl_2O_4$ coatings [23, 28–30, 32, 75] and bulk Al_2O_3 [40, 41, 102, 104–106] as a function of thickness at room temperature conditions. **b**) AC breakdown strength of thermally sprayed Al_2O_3-, Al_2O_3-TiO_2- and Al_2O_3-MgO coatings [9, 12, 31, 32, 75, 76] and bulk Al_2O_3 [33–36, 38, 39, 42, 103, 107–109] as a function of thickness at room temperature conditions. The presented AC breakdown fields are assumed to be RMS values although this was not always reported in the literature.

2.4.2 DC resistivity/conductivity

Real insulation materials are never ideal and some conduction current always exists although the conductivity of the material is very low or the resistivity is very high. The DC resistivity of bulk alumina has been reported be high $>1 \times 10^{12}\,\Omega\,\mathrm{m}$ [34, 36, 42, 111]. However, the DC resistivity of thermally sprayed alumina coatings has been reported varying from 1×10^{6} to $1 \times 10^{11}\,\Omega\,\mathrm{m}$ [11, 23, 28] and that of spinel coatings from 1×10^{7} to $3 \times 10^{11}\,\Omega\,\mathrm{m}$ [11, 23]. Pawlowski [28] noticed that the DC resistivity of plasma sprayed alumina coatings increased 2–4 orders of magnitude when the coatings were heat-treated 1–3 days at 120 °C. After such heat-treatment, the resistivities of alumina coatings varied from 2×10^{11} to $6 \times 10^{12}\,\Omega\,\mathrm{m}$ being at a similar level with the resistivity of bulk alumina [28].

At low electric fields, the voltage-current relation is linear and the conductivity of most insulation materials is thus ohmic [94, 98]. This ohmic conduction is due to the thermally generated charge carriers [94]. However, when the applied field is increased to a high level, the conductivity is usually field-dependent [98]. If the field is increased further and unstable situation occurs, the irreversible breakdown takes place [94, 98].

At high fields, the DC conduction behavior of solid insulation materials can be explained by theoretical conduction mechanisms [94, 95]. Charge injection from electrodes can be described either by Schottky or Fowler-Nordheim injection mechanisms [94, 112]. The latter one describes how the electrons can tunnel from the metal electrode into dielectric due to the strong electric field when the potential barrier between a metal electrode and a dielectric becomes very low [94, 98]. Typically, the Fowler-Nordheim mechanism occurs at very high fields which are close to the intrinsic breakdown field [94, 112].

At slightly lower electric fields, another electrode-limited conduction mechanism called Schottky injection can occur [94]. In Schottky emission, a barrier between a metal electrode and a dielectric is formed due to the electrostatic attraction [94, 98]. This attraction changes the barrier slowly due to the potential energy of the electron [94]. The charge injection over the metal-dielectric barrier (Schottky) results in current density which can be defined as:

$$J = A_{RD}T^2 exp\left(-\frac{\phi_0 - \beta_s\sqrt{E}}{kT}\right) \tag{2.1}$$

$$\beta_s = \sqrt{\frac{q^3}{4\pi\varepsilon_r\varepsilon_0}} \tag{2.2}$$

$$ln(J) = \frac{\beta_s}{kT}\sqrt{E} + \left(2ln(A_{RD}T - \frac{\phi_0}{kT}\right) \tag{2.3}$$

where the A_{RD} is the Richardson-Dushman's constant, k is the Boltzmann's constant, β_s is the Schottky's constant, ε_r and ε_0 are the relative and vacuum permittivity respectively, q is the electronic charge and ϕ_0 is the effective work function as well as the height of the barrier [95, 99]. In order to validate if the Schottky mechanism is involved in the conduction process, the measured data can be plotted as $ln(J)$ versus $E^{1/2}$ (Schottky plot), which should result in a straight line with a slope (β_s/kT) in the case of Schottky emission [94]. This relation can be seen in Equation 2.3 which is a rewritten form of the equation 2.1. However, at low field strengths space charges and surface inhomogeneities typically causes deviations [94]. The theoretical value of the real part of relative permittivity can be evaluated from the slope using Equation 2.2, and thus a comparison between a theoretical and a measured high frequency permittivity can be made.

At high electric fields, one of the bulk-limited conduction mechanisms is Poole-Frenkel which is a bulk-limited analogue to Schottky mechanism [94, 96, 98]. At low fields, the charge carriers are trapped in potential wells [94–96]. When the electric field is increased, the field lowers the potential barrier and the trapped electron can escape from neutral donor and acceptor levels to localized energy states [94, 96, 112]. The current density of Poole-Frenkel conduction mechanism in a dielectric containing shallow traps is defined as:

$$J = J_0 exp\left(-\frac{\phi_{PF0} - \beta_{PF}\sqrt{E}}{kT}\right) \tag{2.4}$$

$$\beta_{PF} = \sqrt{\frac{q^3}{\pi\varepsilon_r\varepsilon_0}} = 2\beta_s \tag{2.5}$$

where the J_0 is the pre-exponential current density, ϕ_{PF0} is the trap barrier height when $E = 0$ and β_{PF} is Poole-Frenkel coefficient which is defined in Equation 2.5 and it is twice that of the Schottky coefficient [96, 112]. The theoretical relative permittivity can be defined from the slope (β_{PF}/kT) of the Schottky plot ($ln(J)$ versus $E^{1/2}$) and this can be

compared with the measured real part of relative permittivity. The physical base of Poole-Frenkel model is very simplified and the analysis must be made as an-order-of-magnitude calculation [94, 98, 112].

Space charge limited current (SCLC) -mechanism is another bulk limited conduction mechanism and it describes how the conduction current behavior changes with an increasing applied electric field [94, 112]. In order to validate this mechanism, experimental J–E data can be plotted in a double logarithmic scale in order to obtain different conduction regions which are presented in Figure 2.10 [94, 112]. According to this mechanism, at low field strengths (field below the transition field, E_{TR}), the voltage-current relation is linear due to the thermally generated charge carriers [94, 112]. The current density of ohmic conduction for dielectric with a thickness, d, is defined as:

$$J = qn\mu\frac{U}{d} \tag{2.6}$$

where q is the electronic charge, n is free charge carrier density, μ is the charge carrier mobility, and U is voltage applied over the dielectric [94, 96]. Thus, the current density is directly proportional to the voltage [94]. Correspondingly, the slope is unity in a plot of $logJ - logE$ (see Figure 2.10) [94, 112].

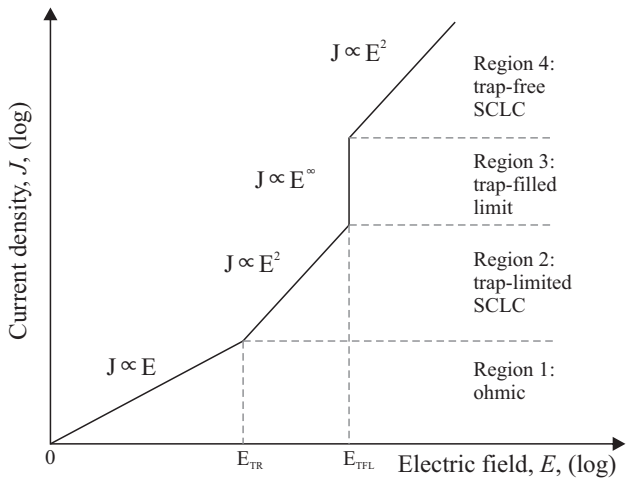

Figure 2.10: Relationship between electric field and current in accordance with the space charge limited current –theory. The figure is revised from [94].

At higher fields (Region 2 in Figure 2.10), the conduction is no longer ohmic because a charge can inject from the electrode into the bulk but the charge has difficulties moving further through the material [94, 112]. Thus, a space charge is formed in the vicinity of the electrodes and throughout the bulk and this charge will limit the further movement of charges which is known as SCLC [94, 112]. When the applied field has reached the level of E_{TR} (see Figure 2.10), the space charge limited current dominates over the ohmic component [94, 112]. In a simple case of one carrier injection and transport, the current

density of space charge limited injection can be defined as:

$$J = \frac{9}{8}\varepsilon_0\varepsilon_r\mu\frac{U^2}{d^3} \tag{2.7}$$

where ε_0 is permittivity in vacuum and ε_r relative permittivity of a dielectric. Thus, the current is proportional to the square of electric field and the slope is two in a plot of $logJ - logE$ (Figure 2.10) [94, 96]. When the applied field has reached the trap-filled limit field, E_{TFL}, all traps in the dielectric are filled and the slope increases from two (see Region 3 in Figure 2.10). At the fields above E_{TFL}, the trap-free space charge conduction might take place and the slope is two (Region 4 in Figure 2.10) if the breakdown did not occur before this region was reached [94].

Talbi *et al.* [107] and Neusel *et al.* [111] made comprehensive studies in order to define a suitable conduction mechanism for bulk alumina. They concluded that the DC conductivity of bulk alumina follows the SCLC mechanism [107, 111]. In addition to these studies, conduction mechanism studies were performed on porous alumina thin films and the material followed SCLC mechanism [113]. However, similar conductivity studies have not been conducted for thermally sprayed alumina based coatings and thus one aim of this thesis is to find suitable conduction mechanism for the coatings.

2.4.3 Permittivity and dielectric loss

All real dielectric materials contain some mobile charge carriers and the conductivity is proportional to the number of charge carriers. The electrical behavior of such dielectric can be modeled for example as an RC parallel circuit which is presented in Figure 2.11. One way to characterize an electric insulation is to measure the capacitance and the dielectric loss of the material. Dielectric loss can be defined by the energy dissipated in a dielectric under certain electrification. The dielectric loss is due to various polarization mechanisms related losses (like molecular friction) and due to conduction [96]. When AC field is applied across the parallel plate capacitor, where the distance between the plates is d, the total current density can be expressed as:

$$J_T = J + \frac{dD}{dt} = J + \varepsilon^*\frac{dE}{dt} \tag{2.8}$$

where J is conduction current density, D is electric flux density, E is electric field, and ε^* is complex permittivity [96, 114]. Complex permittivity is commonly expressed as relative permittivity ε_r^*, which can be given by:

$$\varepsilon_r^* = \left(\varepsilon_r^{'} + j\varepsilon_r^{''}\right) \tag{2.9}$$

where $\varepsilon_r^{'}$ is the is real part of the relative permittivity (sometimes called dielectric constant), $\varepsilon_r^{''}$ is the loss factor [96, 114].

When the DC conductivity of a material is very low, the complex relative permittivity of the material can be defined by using Equation 2.9. However, the conductivity of

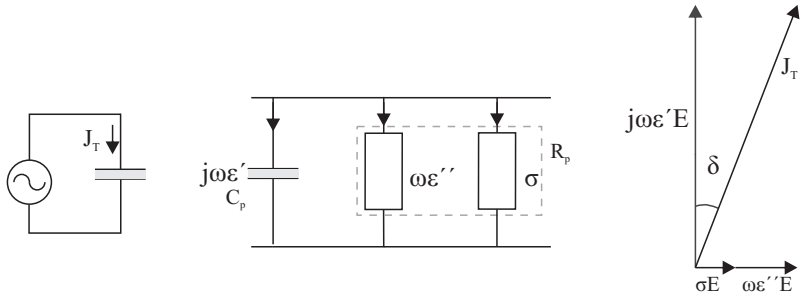

Figure 2.11: Parallel plate capacitor under AC field and its equivalent circuit when DC conductivity will contribute to the imaginary part of the relative permittivity. The dashed square presents resistance, R_p, in the RC-model. The figure is revised from [96, 114].

thermally sprayed insulating coatings can vary significantly and compared with a typical high voltage insulation material it is not very low. When the DC conductivity is high, the conductivity σ will notably contribute to the imaginary part of the complex permittivity [96]. Thus, σ will contribute to R_p in the equivalent circuit which can be seen in Figure 2.11. Then, the complex relative permittivity can be expressed as:

$$\varepsilon_r^* = \varepsilon_r^{'} - j\left(\varepsilon_r^{''} + \frac{\sigma}{\omega\varepsilon_0}\right) \tag{2.10}$$

where $\varepsilon_r^{'}$ is the real part of the permittivity and the corresponding capacitance, C_p, in the equivalent circuit represents the capacitance per unit area of the material [96, 114]. $\varepsilon_r^{''}$ is the loss term due to polarization, σ is DC conductivity, ω is the angular frequency and ε_0 is vacuum permittivity [96, 114]. Any dielectric measurement result always includes both loss components caused by both polarization and conduction.

Figure 2.11 also gives the vector presentation of the total current density passing through the dielectric under AC field. When the real and imaginary parts of the permittivity and conductivity are placed in Equation 2.8 the total current density is given as:

$$J_T(\omega) = j\omega\varepsilon_0\left[\varepsilon^{'}(\omega) - j\left(\varepsilon''(\omega) + \frac{\sigma}{\omega\varepsilon_0}\right)\right]E \tag{2.11}$$

where the first term is a capacitive current due to the polarization processes [96]. The second term is a resistive current due to polarization losses and the third term is a resistive current due to the conduction losses [96]. For typical high voltage insulation materials e.g. dielectric polymers, the σ is extremely small and the last term in Equation 2.11 can be neglected but this cannot be made for thermally sprayed coatings.

The real and imaginary parts of the permittivity can be linked together by using the dissipation factor, $\tan\delta$ [96, 99, 114]. It can be defined as:

$$\tan\delta = \frac{\varepsilon_r'' + \sigma/\omega\varepsilon_0}{\varepsilon_r'} \tag{2.12}$$

This loss tangent can also be seen in Figure 2.11. The dissipation factor defines how much the dielectric differs from an ideal one. As it can be noticed from Equation 2.12, in

dissipation factor the losses of the material are related to the real part of the permittivity. If both real and imaginary parts of the permittivity change remarkably with the frequency, the evaluation of the losses over frequencies using $\tan\delta$ is challenging. Due to this, the loss values in this thesis are presented as the imaginary part of the complex relative permittivity.

Notable differences between the real part of relative permittivity of bulk alumina and thermally sprayed alumina coating cannot be noticed in the literature which can be seen in Table 2.1. In addition, no significant difference can be seen between the relative permittivity of plasma and HVOF sprayed alumina coatings. However, the measuring frequencies were quite high, and thus the microstructural differences between bulk and coating in the referred literature cannot be seen as clearly as they may be noticed in the DC conductivity or in the slow charging or polarization phenomena at lower frequencies. In this thesis, the real part of relative permittivity and the dielectric loss are measured as a function of frequency in order to distinguish the low frequency polarization mechanisms, e.g. interfacial polarization.

Table 2.1: The relative permittivities, ε'_r, from literature measured at room temperature.

Material	ε'_r [a)]	Measuring frequency (Hz)	Reference
Bulk alumina	9–10	1×10^6	[36, 100, 107]
Bulk alumina	7	1×10^3	[41, 105]
Bulk spinel	8–8.5	1×10^6	[115]
APS spinel	11.4	100	[85]
APS spinel	8.4	1×10^6	[85]
APS alumina	6–8	1×10^3	[28]
APS alumina	11–23	1×10^3	[85]
APS alumina	5–8.7	10×10^6	[73]
APS alumina	9.2	10×10^3	[47]
APS alumina	7.8	1×10^6–1.8×10^9	[64]
APS alumina[b)]	8.5	0.1×10^3	[90]
APS alumina[b)]	7.65	1×10^3	[90]
APS alumina[c)]	10.5	0.1×10^3	[90]
APS alumina[c)]	8.8	1×10^3	[90]
HVOF alumina	6–8	10×10^3	[9]
HVOF alumina	7.9	10×10^6	[73]
HVOF alumina	7.8	1×10^6	[47]

a) The term is also called dielectric constant in the literature.
b) During the spraying, the plasma arc current was 300 A.
c) During the spraying, the plasma arc current was 600 A.

Although the relative permittivities of aluminas are not reported as a function of frequency, other aspects have been noticed to affect the permittivity of bulk alumina. Moulson *et al.* [100] noticed that the lower purity alumina (85%) had lower relative permittivity (ε'_r=8.2) and the higher purity alumina (99.9%) has higher permittivity (ε'_r=9.8–10.1). However, Malec *et al.* [38] reported the highest relative permittivity (10.5) was observed for the lowest purity alumina (92%) and the lowest permittivity (9.5) was

for 96% alumina while the relative permittivity of 99.9% alumina was in between the aforementioned two values being 10. Due to this, it can be concluded that the relative permittivity of bulk alumina is not always linearly dependent on the purity.

Gao *et al.* [90] noticed that spraying parameters affect the microstructure of plasma sprayed alumina and consequently the relative permittivity. When the plasma arc current was lower (300 A), the alumina coating mainly consisted of α-Al_2O_3 and the relative permittivity was lower than when using higher plasma arc current (600 A) [90]. The high plasma arc current coating consisted mainly of γ-Al_2O_3 which explained the higher relative permittivity [90]. Brown *et al.* [85] noticed also that the plasma sprayed alumina coating consisting mostly of α-phase exhibited lower relative permittivity than the coating with a high amount of γ-phase.

2.4.4 Effect of humidity on the resistivity and the relative permittivity of alumina coatings

The sintered bulk alumina and alumina powder utilized in thermal spray consist of thermodynamically stable α-Al_2O_3 as the main crystalline phase but due to the rapid solidification during the spraying the alumina coatings exhibit metastable γ-phases as a main phase [12, 23, 28, 43, 63, 70, 74, 75, 84, 90, 91]. This γ-Al_2O_3 is highly hygroscopic [23, 28, 85] which can be one reason for the significant increase of the relative permittivities and losses of the coatings with increasing humidity [28, 47, 85]. However, the high amount of γ-phase in alumina coating cannot only explain the moisture sensitivity since the DC resistivity of $MgAl_2O_4$ coatings, which have stable crystalline phases, decreased several orders of magnitude with increasing humidity as well as the resistivity of the studied HVOF alumina coatings [23]. Thus, it may be hypothesized that the special microstructure with pores, voids, different interfaces, etc. together with the hygroscopic nature of the materials can explain the moisture sensitive nature of the alumina and spinel coatings. However, the effect of humidity and temperature on the DC resistivity, permittivity and dielectric loss of thermally sprayed alumina or spinel coatings is not comprehensively studied. Due to this, one aim of this thesis is to study the effect of temperature (20–60 °C) and relative humidity (20–90%) on the DC resistivity, permittivity and dielectric loss of thermally sprayed alumina and spinel coatings.

Chapter 3

Experimental: Material and dielectric characterization of the studied coatings

This chapter presents the studied coating materials and the experimental measurement methods which have been utilized in the experiments made for the associated publications [P1]–[P8]. The dielectric characterization was made for as-sprayed coatings. This characterization includes the following measurements:

- Breakdown strength measurements which are made by linearly ramped DC & AC voltage and step-wisely increased DC voltage. In addition, voltage endurance tests are performed.
- DC conductivity measurements at low and high electric fields.
- Relative permittivity and dielectric loss measurements at low and high electric fields.

3.1 Studied materials and material characterization

Table 3.1 presents the detailed material information of the studied coatings. The experimental powders utilized in HVOF coatings were manufactured by VTT Technical Research Centre of Finland. The commercial alumina and spinel powders utilized in HVOF coatings were from different suppliers (Praxair, Fujimi, Mesoscribe, Millidyne). Figure 3.1 presents the SEM images of the powders of $MgAl_2O_4$ coating (HVOF4) and Al_2O_3-MgO coating (HVOF8). The studied HVOF coatings were deposited by VTT. Since the main objective of this thesis is to study the dielectric properties of the coatings, the spray parameter optimization was done by VTT's thermal spray experts. The chosen parameters represent current state-of-the-art. The atmospheric plasma sprayed and flame sprayed coatings were manufactured by Saint-Gobain Coating Solutions as well as the raw materials utilized in these coatings. The process parameters were also optimized at Saint-Gobain. The coatings were deposited on 2.5 mm thick stainless steel substrates (100 mm×100 mm) which were grit-blasted before coating deposition. However, one type

Table 3.1: The studied materials of this thesis. HVOF6A and HVOF6B coatings are deposited from the same commercial alumina powder. Plasma samples are deposited by utilizing atmospheric plasma spraying. Flame sprayed coatings are deposited from a cord.

Name	Powder	Method[a)]	p_{OM}[b)] (%)	p_{SE}[c)] (%)	p_{BSE}[d)] (%)	GP[e)] (nm^2)	d_{OM}[f)] (µm)	d_m[g)] (µm)	Publication
HVOF1	experimental Al_2O_3–MgO[h)]	a&s	0.9	0.6	1.4	3.0	–	130 ± 3.1	[P5]
HVOF2	commercial Al_2O_3	–	1.9	1.0	1.9	5.7	209	208 ± 3.9	[P5]
HVOF3	commercial Al_2O_3	–	1.7	1.0	3.0	19.2	288	281 ± 9.1	[P5]
HVOF4	commercial $MgAl_2O_4$	f&c	1.3	1.3	2.4	3.2	195	196 ± 3.4	[P5]
HVOF5	commercial Al_2O_3	a&s	6.0	1.7	3.7	11.1	215	228 ± 6.2	[P4, P7]
HVOF6A	commercial Al_2O_3	f&c	1.4	1.1	2.2	–	115	114 ± 3.9	[P3]
HVOF6B	commercial Al_2O_3	f&c	1.4	1.4	1.4	3.2	333	307 ± 6.1	[P7, P8]
HVOF7	experimental 100% Al_2O_3	a&s	2.9	1.0	2.6	7.7	255	237 ± 10.2	[P6, P7]
HVOF8	90% Al_2O_3–10% MgO	a&s	3.0	1.2	3.1	4.8	195	193 ± 8.0	[P6, P7]
HVOF9	75% Al_2O_3–25% MgO	a&s	2.5	1.2	3.1	3.9	190	184 ± 7.9	[P6, P7]
HVOF10	60% Al_2O_3–40% MgO	a&s	3.1	1.1	3.0	13.3	235	241 ± 13.8	[P6]
HVOF11	50% Al_2O_3–50% MgO	a&s	2.4	1.1	3.8	6.3	257	215 ± 2.4	[P6, P7]
HVOF12	35% Al_2O_3–65% MgO	a&s	2.3	1.6	3.8	15.5	191	234 ± 10.0	[P6]
HVOF13	experimental $MgAl_2O_4$	a&s	0.3	0.6	1.7	5.9	342	362 ± 10.0	[P1, P2]
PlasmaA	commercial Al_2O_3	f&c	2.3	2.4	3.6	–	245	271 ± 11.4	[P7, P8]
PlasmaB	experimental $MgAl_2O_4$	f&c	1.7	–	–	13.1	–	333 ± 10.8	[P2]
FlameA	commercial Al_2O_3	cord	2.7	3.8	4.8	–	235	225 ± 4.4	[P8]
FlameB	commercial $MgAl_2O_4$	cord	–	–	–	19.9	–	360 ± 8.1	[P2]

[a)] Powder manufacturing process, a&s is agglomerated and sintered, and f&c is fused and crushed.

[b)] p_{OM} is porosity defined from cross-sectional images taken by optical microscope (OM).

[c)] p_{SE} is porosity defined from cross-sectional images taken by SEM using secondary electron detector (SE).

[d)] p_{BSE} is porosity defined from cross-sectional images taken by SEM using backscattered electron detector (BSE).

[e)] GP is gas permeability.

[f)] d_{OM} is coating thickness determined by using cross-section images taken by OM.

[g)] d_m is coating thickness determined by utilizing magnetic measuring device followed by standard deviation of the measuring results.

[h)] Composite powder which formed into a spinel during the spraying process.

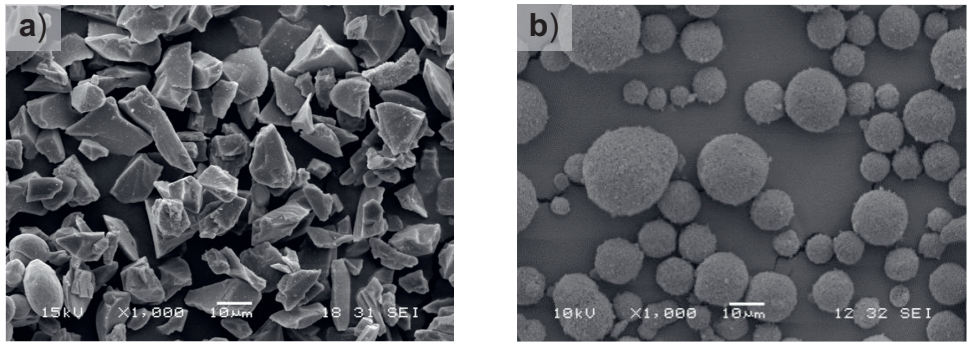

Figure 3.1: The SEM images of differently manufactured powders with a magnification of ×1000 **a**) Fused and crushed $MgAl_2O_4$ (coating HVOF4), **b**) agglomerated and sintered 10% MgO–90% Al_2O_3 (coating HVOF8).

of HVOF sprayed alumina coating (HVOF6A) was sprayed on grit-blasted carbon steel substrates. Grit-blasting ensures a good adhesion between the ceramic coating and the steel substrate.

The microstructural characterization of the coatings was made utilizing the image analysis of cross-sectional micrographs. The porosities of the coatings were determined by analyzing cross-sectional micrographs taken by optical microscopy (OM, 320× magnification) and by scanning electron microscope (SEM, 1000× magnification) using both secondary electron detector (SE) and backscattered electron detector (BSE), see Table 3.1. The porosities were determined as the ratio of total area of voids to the total image area. Figure 3.2 shows the steps of image analysis for porosity evaluation from SEM images.

In addition to the image analysis, the gas (nitrogen) permeability (GP) was measured for the coatings, providing an indirect measure of the porosity since higher gas permeability indicates higher porosity. For the test, a coating was deposited on a standardized porous round AISI 316 substrate with the diameter of 25.4 mm and the thickness of 3.2 mm. Practically, the porous substrates have zero resistance to the gas flow. In the test, the specimen was placed in a test cell where the gas pressure was increased in steps [4]. The

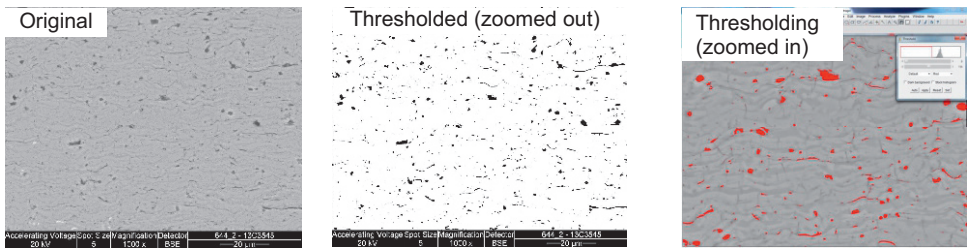

Figure 3.2: **a**) The original SEM/BSE cross-section image of HVOF sprayed alumina coating (HVOF6A), **b**) the porosity determined by contrast difference, and **c**) the zoomed-in image for more detailed adjustment of threshold values.

volumetric gas flow through the specimen was measured by a flow meter, and thus the viscous gas permeability coefficient can be calculated [4].

Although image analysis is widely used tool for porosity determination, it is not an exact determination method since the recognition parameters are defined more or less manually. Due to this, the analyses made at different laboratories do not give exactly same result. Also, one SEM image covers only a quite small section of the coating and does not reflect the possible variation in the microstructure of a coating with a thickness of several hundreds of micrometers. Due to the aforementioned aspects, porosity is also determined by using other methods. Gas permeability values can give a more realistic view of the actual porosity of the material. However, sometimes high gas permeability can indicate that large number of long vertical cracks exist in the coating (HVOF3, HVOF10, HVOF12) which are not necessarily noticed in the porosity determinations and can only be observed by eye [P5, P6]. In addition to the GP measurements, it is valuable to perform image analysis visually as well as computationally by PC.

For the studied coatings, the thickness was determined either by using magnetic measuring device (Elcometer 456B) or from cross-sectional images taken by optical microscopy (Table 3.1). The high standard deviation in thickness is partly due to the grit-blasting made for the steel substrates in order to ensure good adhesion between the ceramic and the steel. This effect can be seen clearly in Figure 3.3 where the cross-section image of HVOF6A is presented.

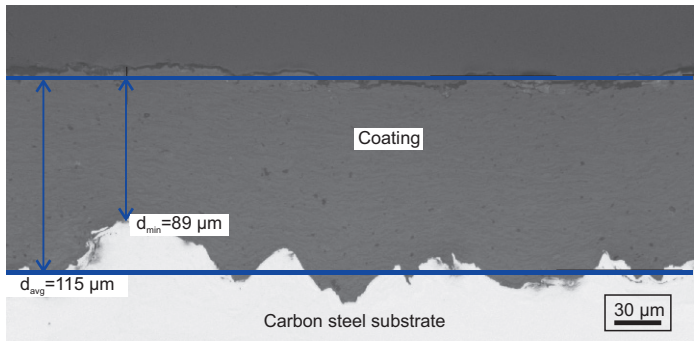

Figure 3.3: The cross-section image of HVOF sprayed alumina coating (HVOF6A) taken by optical microscope presenting the thickness variation of the coating [P3].

3.2 Sample preparation and measurement conditions

For permittivity and DC resistivity/conductivity (below 1 kV) measurements, a round electrode (⌀=50 mm) was painted on the sample surface using a silver paint (SPI High Purity Silver paint). In addition, a shield electrode was painted around the measuring electrode to prevent possible surface currents, see Figure 3.4a). At high field DC conductivity measurements, smaller silver painted electrodes (⌀=11 mm) were prepared on the

sample surface without guard rings. Breakdown measurements were performed both with silver painted electrodes and in certain cases without any embedded electrodes. When the silver painted electrodes were utilized, the diameter of the electrode was 11 mm and a guard ring was not utilized, see Figure 3.4b. According to experiments, the surface currents were minimal in comparison to the current through the sample and the variation between the parallel samples.

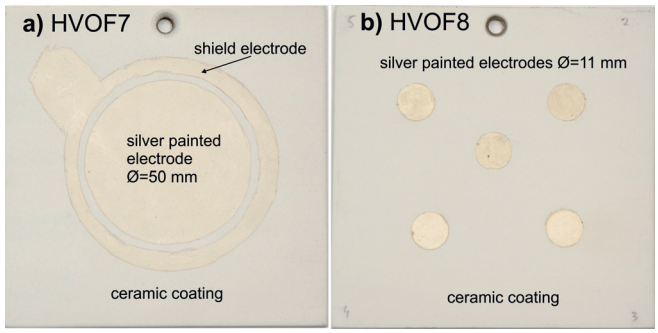

Figure 3.4: Photographs of the electrode arrangements utilized **a**) in DC conductivity below 1 kV voltage levels and permittivity measurements, and **b**) in breakdown and DC conductivity above 1 kV voltage levels. The photographs are taken after the measurements. [P7]

After painting the electrodes, the samples were at first dried at room temperature for ∼30 min followed by a heat-treatment at 120 °C for two hours. After the heat-treatment, the samples were conditioned in a climate room at the conditions of 20 °C, RH 20% for at least 12 h before the measurements. All the measurements were also carried out at controlled conditions in the climate room. The ambient condition of 20 °C, RH 20% was chosen the so-called basic measurement condition where most of the measurements were made.

In the beginning of this thesis project, silver paint penetration into the coating was studied from cross-sectional images taken by optical microscope, and it was observed that the utilized silver paint did not penetrate into the coating. However, preliminary voltage endurance tests showed that silver as an electrode material might be problematic due to its slightly reactive nature compared to e.g gold which is an inert metal [116]. According to literature [117–121], in favorable conditions silver ions may form and these ions may migrate into a porous material (a phenomenon called silver migration). These redeposited silvers can form paths (dendrites) and thus help a breakdown to occur [117–121]. A potential dielectric material for silver migration is a material which absorb moisture and dust particles [117]. Silver migration needs to be considered when i) DC field is applied so that positive electrode is placed against a silver electrode (silver ions are positive), ii) either temperature is high (above 250 °C) or humidity is high (RH 80% to 90%), or iii) stress duration is long enough (depending on the utilized environmental conditions (high temperature or humidity) and/or the applied electric field) [117–126].

The migration of silver ions from positive to negative electrode, especially the rate, is dependent upon the DC field, quality of the dielectric material (porous or non-porous), moisture content of dielectric material, hygroscopic nature of the dielectric, and diffusivity of silver ions on the dielectric [118, 120, 127]. According to Manepalli [118], the failure rate due to the silver migration is very low, typically years, under normal operation conditions and thus most of the migration studies are made at accelerated conditions (e.g. 85 °C/RH 85%) [118, 128]. Thus, it can be concluded that when a positive DC voltage is applied to a some other electrode materials, e.g. steel, and the negative electrode is silver, positive silver ions cannot penetrate into the material and thus the silver migration is not possible. Additionally, it can be concluded that in short-term DC measurements silver electrodes can be utilized if the temperature and humidity are not too high since silver is thermodynamically stable at temperatures below 250 °C [124]. A possibility to silver migration increases when the relative humidity is above 30% [127] but typically the humidity needs to be 80–90% [117–121]. However, in long-term measurements utilization of silver electrodes can cause problems and other electrode materials are most probably better solution.

Due to the aforementioned reasons, for the long-term voltage endurance tests gold electrodes (⌀=11 mm) were evaporated on the sample surface. The electrodes were deposited using a custom-built e-beam evaporator (Instrumentti Mattila) inside an ISO 14644-1 class 6 clean room facility. High vacuum (pressure $<1 \times 10^{-6}$ mbar) and low deposition rate (0.20 nm/s) were maintained during the evaporation process. The evaporated gold layer was 200 nm.

The effect of temperature and humidity on the dielectric properties of alumina (HVOF6B, PlasmaA and FlameA) and spinel (HVOF13, PlasmaB and FlameB) coatings was studied in the publications [P2, P8]. From 20 °C to 60 °C, the measurements were performed inside a climate room where the temperature and relative humidity were controlled. The DC resistivity, relative permittivity and dielectric losses of the $MgAl_2O_4$ coatings were studied at 20 °C, 40 °C and at 60 °C when the relative humidity was 20% or 45% [P2]. However, the DC breakdown voltage measurements of the spinel coatings were performed at 20 °C/RH 20% [P2]. The Al_2O_3 coatings were studied in more detail and the measurement conditions are given in Table 3.2 [P8]. In addition, DC breakdown voltage measurements for all the alumina coating types were made at 120 °C and at 180 °C [P8]. The high-temperature DC breakdown performance of HVOF sprayed alumina coating (HVOF6B) was studied more and the measurements were made at 200 °C, 300 °C, 350 °C, 400 °C, 600 °C and 800 °C [P8].

When the effects of temperature and humidity were studied [P2, P8], the spinel and alumina coating samples were stabilized at the measurement conditions in the climate room for three hours before the resistivity, permittivity or breakdown measurements. In all the high temperature measurements, the alumina coatings were placed in the oven at room temperature after which the temperature was slowly increased to the set value. In the breakdown measurements made at 120 °C, the stabilization period was one hour while

at 180 °C it was two hours. At the high temperatures (200–800 °C), the temperature was increased with a ramp of 25 °C/min to the set point. After the steel substrate reached the set temperature, one hour was waited until the first breakdown measurement was started. After the measurements, the oven was switched off and the samples were left in the oven to slowly cool down to the temperature of ∼20 °C.

Table 3.2: Measurement temperatures, relative humidities and the corresponding absolute humidities for the resistivity and permittivity measurements of HVOF6B, PlasmaA, and FlameA. The breakdown measurement conditions are in bold.

Temperature (°C)	RH (%)	Absolute humidity (g/m^3)
20	**20**	**3.5**
20	**45**	**7.8**
20	70	12.2
20	90	15.6
40	**20**	**10.3**
40	**45**	**23.1**
40	70	35.9
60	20	26.1
60	**45**	**58.7**
60	70	91.3

3.3 Breakdown voltage measurements

3.3.1 Short-term progressive breakdown voltage measurements

In the breakdown voltage tests at 20–180 °C, a stainless steel rod electrode (⌀=11 mm, edge rounding of 1 mm), was placed on the top of a coating surface while the steel substrate of the sample acted as the other electrode. Schematic figure of the measurement bench utilized in the measurements performed at 20–180 °C is shown in Figure 3.5b). In the high temperature measurements (200–800 °C), the rod electrode (⌀=9 mm) was made a nickel-chromium based alloy which was placed on the sample surface while the other arrangements were as in the low temperature tests.

In order to determine a suitable breakdown voltage test setup for thermally sprayed alumina based coatings, three different electrode arrangements were studied [P3]. In addition, the suitability of insulation oil was tested and evaluation of the suitability of the test arrangements at AC and DC were made [P3]. Based on the results obtained in [P3], the breakdown measurements of the coatings in the associated publications [P2, P5, P4, P6, P7, P8] were made with silver-painted electrodes on coating surfaces without oil immersion. Despite obvious edge field enhancement at the edges of the painted electrodes, the breakdown locations were distributed reasonably well along the electrode area. Since the oil immersion cannot be utilized to prevent surface flashovers at the highest test voltages (at 20 to 60 °C), a plastic cylinder with an O-ring seal was placed towards the coating and the O-ring was clamped on the coating surface around the

measuring electrode (⌀=11 mm) to extend the creepage distance over the solid insulation when needed [P6, P7, P8].

DC breakdown voltage measurements were performed by utilizing linearly increased DC voltage (ramp rate of 100 V/s throughout the test). In addition, a higher ramp rate (1000 V/s) was utilized for a HVOF sprayed alumina coating (HVOF5) [P4]. In the measurements made in insulation oil, the ramping of the voltage was started 30 s after the sample was placed in the oil bath (Shell Diala oil DX Dried) [P3]. The voltage source control and data recording was performed using a LabVIEW-based software. The voltage source was Spellman SL1200 (U_{max}=20 kV) and the voltage was measured using a resistive voltage divider (Spellman HVD-100-1, divider ratio 10000:1). The measurement circuit is presented in Figure 3.5a).

AC breakdown voltage measurements were performed by utilizing linearly increased AC voltage with a ramp rate of 100 V/s throughout the test. The voltage source was Hipotronics test transformer ($U_{max,rms}$=50 kV) and the measured voltage was recorded using LabVIEW-based software. [P3]

In DC tests, dielectric breakdown strength (BDS) of a coating was calculated by dividing the breakdown voltage by the corresponding coating thickness at the painted electrode (⌀=11 mm) location [P2, P3, P4, P5, P7, P8]. In the high temperature measurements (200 to 800 °C), the thickness was measured near the breakdown point after the measurement [P8]. In the AC tests, the dielectric breakdown strength was calculated by dividing the measured peak value of the AC voltage by the thickness of the measurement point [P3].

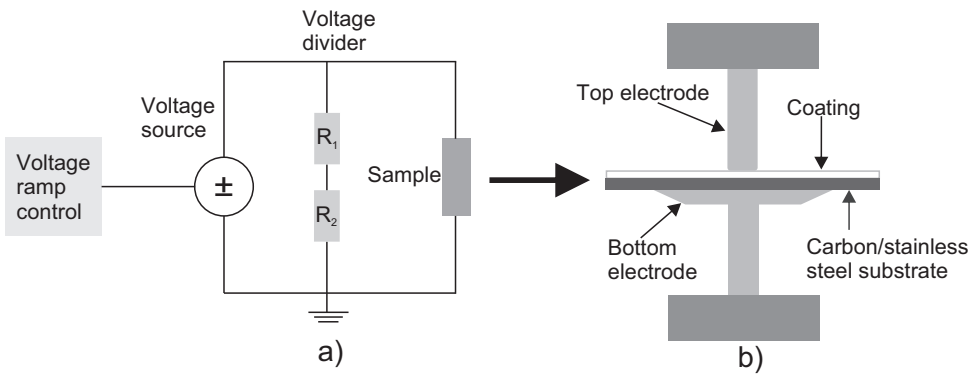

Figure 3.5: **a**) The measurement circuit for the breakdown measurements performed with linear ramp rate and **b**) the schematic figure of a measurement bench utilized in the breakdown measurements. In the DC tests, a positive voltage was applied to the rod electrode placed on the top of the coating surface while the steel substrate was the negative electrode.

3.3.2 Statistical analysis of breakdown data

Typically, the dielectric breakdown strength of solid materials is Weibull distributed and due to this the results were fitted in this distribution. The cumulative distribution function (CDF) of a two-parameter Weibull distribution is:

$$F(x) = 1 - \exp\left\{-\left(\frac{x}{\alpha}\right)^{\beta}\right\}, x \geq 0, \tag{3.1}$$

where *F(x)* is the breakdown probability, x is the measured variable, e.g. breakdown strength (V/µm), α is the scale parameter (V/µm) and β is the shape parameter [129, 130]. The scale parameter represents the breakdown strength at the 63.2% failure probability and the shape parameter indicates the slope of the theoretical distribution [129, 130]. The statistical analysis was performed using Weibull++ software. In [P2, P3, P4, P5, P6, P7] Maximum Likelihood method was used in the parameter estimation and in [P8] the least-square regression method was used in parameter estimation. However, the utilized parameter estimation method has no significant effect on the estimated Weibull parameters.

3.3.3 Stepwise breakdown voltage measurements

The breakdown strength was also studied by increasing the voltage step-wisely until breakdown occurred. During the measurement, the current of a sample was also measured but this method is described in Sub-chapter 3.4. Three different step durations (6 min, 10 min and 60 min) were utilized for a HVOF sprayed alumina coatings (HVOF5) [P4, P7]. The 10 min step duration was selected to study the conduction behavior of different coatings (HVOF5–9, HVOF11 and PlasmaA) [P7]. The 6 min and 10 min step tests were started at the voltage level of 250 V which was also the step size [P4, P7]. The 60 min step measurements were started at the voltage of 4000 V (∼18.6 V/µm) using a step voltage of 500 V [P4]. The schematic figure of the measurement circuit is presented in Figure 3.7. The voltage source control and data recording was performed using LabVIEW-based software. The voltage source was Keithley 2290-10 power supply (U_{max}=10 kV).

3.3.4 Voltage endurance tests

Voltage endurance tests were made for selected ceramic coatings in order to evaluate the long-term breakdown performance of the coatings. The tests were performed at room temperature conditions. The test series was started with an electric field of 10 V/µm and with a duration of 1000 h (41.7 days). During this test, no remarkable changes were noticed in the measured currents. Thus, the test was continued by increasing the test field to 15 V/µm for for seven days (168 h). As no remarkable current changes were noticed, the test was continued by increasing the test field in 2.5 V/µm steps so that the test fields were 17.5 V/µm, 20 V/µm, 22.5 V/µm, and 25 V/µm. The test duration of each of these fields was seven days (168 h).

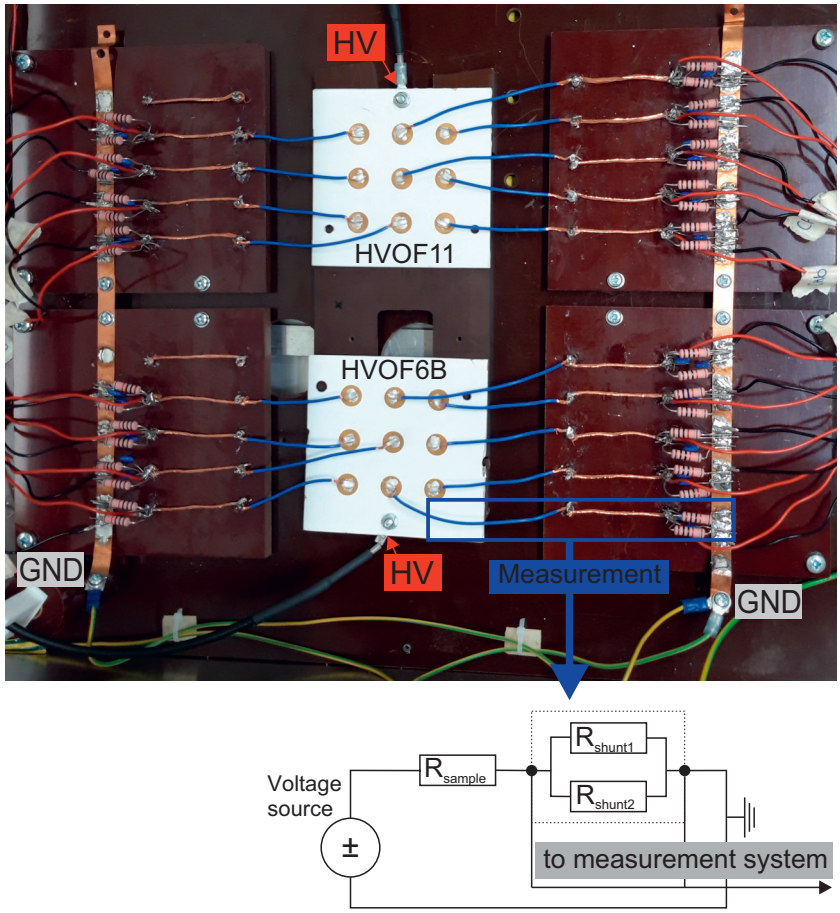

Figure 3.6: A photograph presents the measurement arrangement built for voltage endurance tests. Positive DC voltage is applied to the bottom of the coating sample which is made from stainless steel and thus acting as the other electrode. The current measurement is made from the top of the coating plates. Nine gold electrodes are evaporated on the top of each coating plate forming thus nine separate samples of each material. Each sample has its own current measurement circuit consisting of two resistors connected in parallel. The circuit is highlighted in blue in the photograph and the circuit diagram is shown below the photograph. In order to connect the measurement circuit to the gold electrodes, a high purity silver paint was utilized as a 'glue' to attach the wire on the electrode area.

The test was made by applying constant electric field to the coatings (alumina coating HVOF6B and spinel coating HVOF11). The utilized power supply was Keithley 2290E-5 power supply (U_{max}=5 kV) and for higher electric fields Keithley 2290-10 power supply (U_{max}=10 kV). In order to apply same electric field to the studied coatings with different thicknesses, both coating plates had their own power supply. During the test, the voltage was applied to the bottom of the coating plates and the current measurement was made from the top of the coatings, see Figure 3.6.

The current was measured by utilizing Keithley 2700 digital multimeter equipped with data acquisition multiplexer module (Keithley 7700) and utilizing shunt resistors. Keithley Kickstart software was utilized in the multimeter control and the data recording. Both coating plates (HVOF6B and HVOF11) have nine evaporated gold electrodes, and thus own current measurement circuit was built for each sample, see Figure 3.6. The measurement circuit consists of two resistors (R_{shunt}=10 kΩ) placed in parallel and two varistors for over-voltage protection (clamping voltages, $V_{c,max}$, are 93 V and 135 V). The circuit diagram of this system is presented in Figure 3.6.

3.4 DC resistivity/conductivity measurements

DC conductivity/resistivity as a function of the electric field of 0.1–∼4 V/µm was measured for all coatings which are listed in Table 3.1 at 20 °C/RH 20%. When the effect of temperature and humidity on DC resistivity was studied [P2, P8], the electric field was varied from 0.1 V/µm to 2.5 V/µm. DC conduction current measurements were performed using Keithley 6517B electrometer (U_{max}=1 kV). During these measurements, a stainless steel electrode (⌀=50 mm) was placed on the top of the silver painted area (⌀=50 mm) on the coating sample while the stainless steel substrate of the sample acted as the other electrode.

The measurement period for each voltage level was 1000 s when the measurements were performed at 20 °C/RH 20% [P1, P4, P5, P6, P7]. When the temperature or humidity was higher, the measurement period was lower being 300 s [P2, P8]. Depending on the test condition, the DC resistivity was determined from the average of the stabilized DC current measured over 990–1000 s or 290–300 s after the voltage application. All the measuring arrangements were in accordance with the standards IEC 60093 and ASTM D257-07 [131, 132].

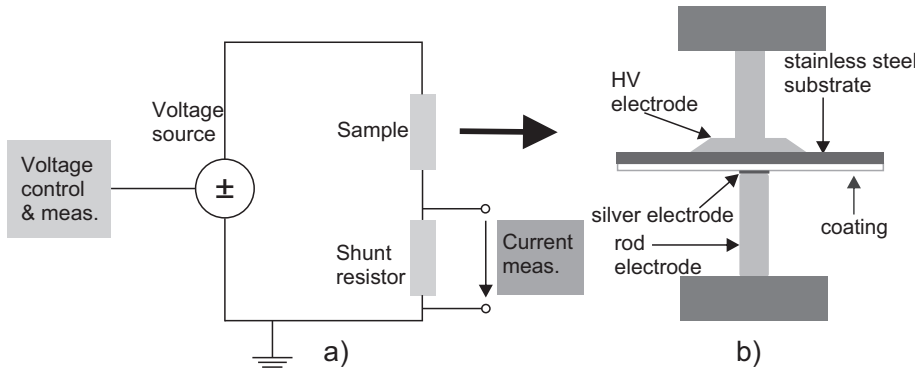

Figure 3.7: Schematic figure of the measurement circuit and test bench utilized in DC conductivity measurements above 1 kV [P4, P7]. A positive DC voltage was applied to the bottom of the coating (steel substrate), while the silver painted electrode was the negative electrode.

The DC conductivity/resistivity of alumina and spinel coatings (HVOF5, HVOF6B, HVOF7–9, HVOF11 and PlasmaA) was measured using two different measurement setups due to the wide measurement range ($U_{meas} = 10 - 10\,000$ V) and sensitivity required for the leakage current measurements [P7]. Below 1 kV, the DC conductivity was measured with the aforementioned measurement setup. Above 1 kV, the DC conductivity was studied during the stepwise breakdown tests with a step voltages of 250 V [P4, P7]. The step duration was 6 min in [P4] and 10 min in [P7]. The voltage control and monitoring are the same which were utilized in step-breakdown tests and are described in Sub-chapter 3.3. The schematic figure of the measurement circuit as well as the test bench are presented in Figure 3.7. The sample current was measured throughout the tests using shunt resistor (1 MΩ or 10 kΩ depending on the signal level) and Keithley 2001 digital multimeter. The voltage source control and data recording were made using LabVIEW-based software. The voltage source was Keithley 2290-10 power supply (U_{max}=10 kV).

3.5 Permittivity and loss measurements

Relative permittivity and total power dissipation of the materials were studied by utilizing an insulation diagnosis analyzer device (IDA 200, U_{max}=200 V_{peak}) using the same sample holder as in the resistivity measurements. During the measurements, a sinusoidal voltage of 0.1 Hz–1 kHz was applied over the sample. The measuring voltage was 200 V_{peak} (corresponding to the electric field of 0.55-1.5 V_{peak}/µm) when the measurements were made at 20 °C/RH 20% [P1, P3, P4, P6]. When the effect of temperature and humidity was studied, the electric field strength was 0.3 V_{peak}/µm [P2, P8]. All the tests were performed in accordance with the IEC standard 60250 [133].

In addition, the electric field dependency of the relative permittivity and dielectric losses of alumina and spinel coatings (HVOF1–4) were studied utilizing the high voltage unit of IDA device (IDA HV unit, U_{max}=30 kV_{peak}) [P5]. The frequency range was 0.1 Hz–100 Hz. The electric field was limited to quite low levels (0.1–5 V/µm) corresponding possible service stress levels to ensure that samples will not break down during the measurements.

At all measuring voltages, the complex impedance of a sample determined from the measured test voltage and the current through a sample was calculated by IDA device and expressed as the values of the equivalent parallel RC circuit model (see Figure 2.11). The real part of the relative permittivity ($\varepsilon_r^{'}$) is defined as:

$$\mathrm{Re}\{\varepsilon_r^*\} = \varepsilon_r' = \frac{C_p}{C_0} - \frac{C_e}{C_0} \tag{3.2}$$

where C_p is measured parallel capacitance of the equivalent circuit. C_0 is the so-called geometric capacitance of the test sample (vacuum in place of the insulation) and ω is the angular frequency. The edge field correction (C_e) was not used since a shield electrode was utilized in the measurements. As indicated by Equation 2.10, the conductivity of a

material will also contribute to the relative permittivity ($|\varepsilon_r^*|$). However, in this thesis ε_r' values are reported, which better reflect the dielectric behavior of the materials.

Imaginary part of the relative permittivity indicates the total losses of a material, both polarization and conduction losses. It can be defined as:

$$\mathrm{Im}\{\varepsilon_r^*\} = \varepsilon_r'' + \frac{\sigma}{\omega\varepsilon_0} = \frac{1}{\omega R_p C_0} \tag{3.3}$$

where R_p is the parallel resistance of the equivalent circuit, see Figure 2.11. In this thesis, the total loss contribution is expressed for the coatings. The conductivity related component can be estimated by using the measured conductivities but since the conductivity is later shown to be dependent on several factors (e.g. field), it is not possible to give exact values for the different loss components with the available data.

Chapter 4

Dielectric breakdown strength

Breakdown strength is one of the main properties of an insulation material. In this chapter, the effects of different test arrangements, spray method, microstructure, and ambient conditions on short-term dielectric breakdown strength of alumina and spinel coatings are studied. Additionally, the influence of voltage form, the rate-of-raise of voltage, and long-term voltage stress on breakdown strength of ceramic coatings are studied.

4.1 Short-term breakdown strength of alumina and spinel coatings

4.1.1 Effect of different test arrangements

In order to determine a suitable short-term breakdown voltage measurement method for thermally sprayed ceramic coatings and in order to verify the differences caused by certain test arrangements utilized in the literature, a test series was carried out utilizing six different test arrangements for HVOF sprayed alumina coating (HVOF6A) at 20 °C, RH 45% [P3]. In all the arrangements, 15 parallel samples were tested and the voltage was increased linearly with the ramp rate of 100 V/s. The measurement arrangements were:

1. DC test in air without oil immersion or embedded electrodes on the coating surface.
2. DC test in oil immersion without embedded electrodes on the coating surface.
3. DC test in air with embedded electrodes (⌀=11 mm) on the coating surface.
4. DC test in air with graphite disk (⌀=11 mm, thickness of 0.8 mm) placed between the rod electrode and the coating surface.
5. DC test in oil with embedded electrodes (⌀=11 mm) on the coating surface.
6. AC test (50 Hz) in air without embedded electrodes on the coating surface.

Figure 4.1a) presents the breakdown strength of alumina coating (HVOF6A) with the aforementioned test arrangements. The Weibull β values are presented in Figure 4.1b). The deviation between the parallel measurements were quite high. However, the results present well that chosen measurement method affect breakdown strength significantly since the BDS values differs remarkably between the different test methods.

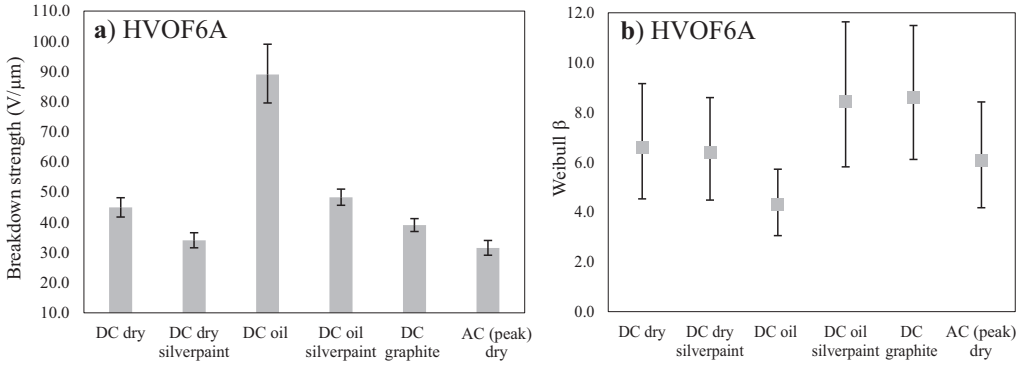

Figure 4.1: **a**) Breakdown strength (Weibull α) of HVOF alumina coating (HVOF6A) and **b**) Weibull β utilizing different measurement arrangements. The error bars present the range of the 90% confidence bounds. [P3]

Oil immersion is a typical method to prevent surface flashovers during breakdown testing. In literature, this method has been utilized successfully in the breakdown voltage measurements of several bulk alumina materials since due to the dense crystalline microstructure with low porosity and gas permeability insulation oil have only minor effects on the breakdown strength [33, 35–42, 102, 104–106, 108, 110]. However, the microstructure of thermally sprayed ceramic coating is moisture sensitive. According to literature [12, 23, 29–31, 75, 76], the BDS of the coatings measured in oil immersion is significantly higher than it has been reported without oil immersion. However, a comprehensive comparison between different test methods has not been made before [P3].

As it can be seen from Figure 4.1a), the highest breakdown strength of HVOF6A (89.0 V/µm) is measured in oil immersion when no embedded electrodes were used. This is almost two times higher than BDS was without oil immersion (DC BDS in dry conditions is 44.9 V/µm). In addition, the lowest Weibull β (4.3) is obtained indicating the highest deviation in breakdown strength distribution. Oil immersion increases the BDS remarkably since the oil can easily penetrate into a moisture sensitive coating. When silver electrodes were added on the coating surface and the sample was placed in the insulation oil bath, the BDS of HVOF6A (48.3 V/µm) increases 42% in comparison to the BDS without oil immersion. The remarkable increase in both oil immersion tests can be explained by the oil penetration since the coatings are quite porous, and thus the oil can fill the voids and pores of the coating rapidly. It may be speculated that the breakdown path develops in dry conditions partly through air filled pores and voids. When those voids are filled with highly insulating oil (BDS is ∼100 V/µm [99, 134]), the breakdown strength of the oil

impregnated coating increases.

Electrode size, shape and material can affect the breakdown strength. The breakdown testing standard ASTM D149-09(2013) [135] emphasizes that painted electrodes can be utilized but the painting may affect the results. These aspects can be well observed from Figure 4.1a) where the results of different electrode arrangements are presented. In the DC tests, the lowest value (34 V/µm) was obtained when silver electrodes were painted on the coating surface. This is well understandable since with this arrangements a good contact to the whole test area is ensured, including also the deepest points of the coating surface, and thus the whole electrode area is tested.

When the breakdown voltage is measured without any embedded electrodes on the coating surface, the situation is different. The electrode will contact only some of the highest points on the sample surface and tested area is energized either through these contact points or through possible discharges occurring in between the rod electrode and the sample surface. Figure 4.2 shows the formed air gap between the rod electrode and the coating surface. It can also be noticed that the coating surface is not smooth which furthermore affects the size of the air gap. The surface roughness of the studied alumina coating (HVOF6A) is 2.7±0.7 µm which is a typical value for HVOF sprayed alumina coating. The formed air gap can be problematic because in accordance with the Paschen's law after a certain inception voltage is reached partial discharges can occur in the air gap and bombard the surface. From Paschen's curve, the breakdown voltage of the air gap with the thickness of 15 µm is determined to be 450 V at the temperature of 20 °C and at normal air pressure. Under AC field, partial discharge activity is rather high and the discharges can bombard the sample surface quite intensively and at the same time the discharges are electrically connecting the corresponding surface spots to the test electrode. Thus, the AC breakdown strength of the HVOF6A is the lowest one (31.5 V/µm) and it is very close to the DC breakdown strength measured with silver electrodes (34 V/µm). According to literature [99, 136] and our own experiments, under DC fields the repetition rate of partial discharges is much lower than under AC. Due to this, the effective electrode area is smaller under DC when embedded electrodes are not used, and thus the DC breakdown strength is higher (44.9 V/µm) than the AC BDS or DC BDS with embedded electrodes.

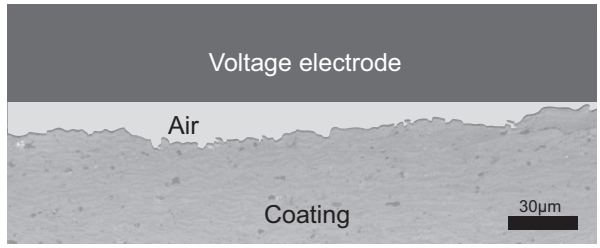

Figure 4.2: Formed air gap between the top electrode and the tested coating during the breakdown voltage measurements [P3].

As it can be seen from Figure 4.1, when a graphite felt disk was placed (⌀=11 mm) between steel electrode and sample surface, the breakdown strength is a bit higher (Weibull α is 39.1 V/µm) than it was with silver electrodes. The graphite felt is a slightly soft allowing better contact but the contact is still only to the highest points of a coating, and thus the contact is not as good as it is with painted electrodes. In addition, the effective test area is not large as it was with painted electrodes.

The aforementioned results presented originally in [P3] supported the idea that the breakdown voltage measurements are better to make with silver painted electrodes. This way the test arrangements can be homogenized. In addition, the weakest point over the test area (ca. 1 cm^2) will be directly measured and the comparisons between materials can be made more reliable. Due to this, the breakdown measurements in the associated publications [P2, P4, P5, P6, P7, P8] were performed utilizing silver painted electrodes on the coating surface. However, when a comparison of different electrode arrangements are made for large amount of different materials, the difference between with and without silver painted electrodes can be opposite to that observed in [P3] and the difference can be quite small, see Figure 4.3. Only three materials (HVOF1, HVOF2, HVOF13) have lower BDS with silver painted electrodes like it was reported for HVOF6A in [P3]. However, for some materials (HVOF3, HVOF5, PlasmaB, FlameB, HVOF4) the difference between the electrode arrangements can be quite small being within the deviation of parallel breakdown tests (in between the confidence bounds of the Weibull distributions).

Interestingly, the breakdown strengths of HVOF7–12 with silver painted electrodes

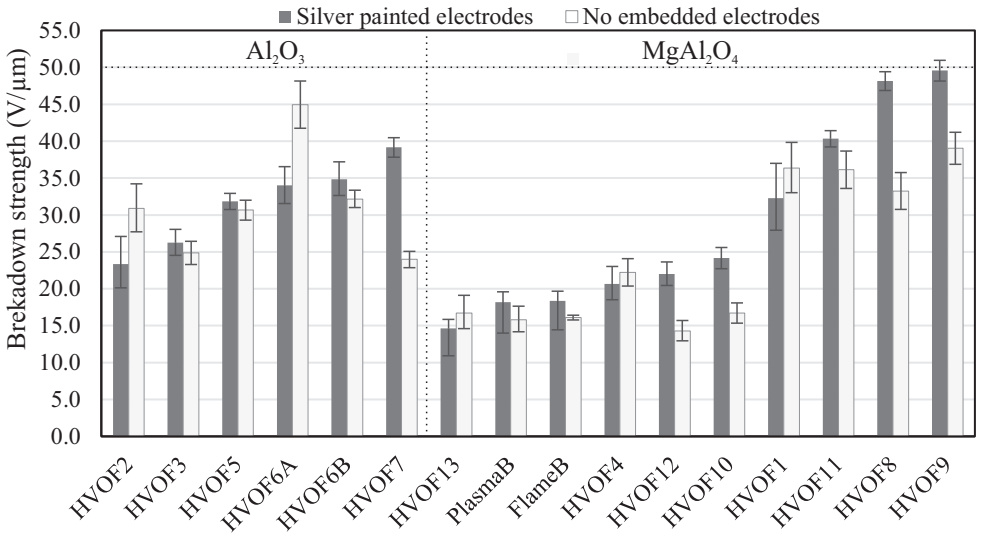

Figure 4.3: Breakdown strength (Weibull α) of the studied coatings with and without embedded electrodes. The presented Weibull parameters are based on 5-15 parallel breakdown tests with silver electrodes and 5-10 parallel results without silver electrodes. The error bars present the range of the 90% confidence bounds. The measurements were performed at 20 °C, RH 20%, except the results of HVOF6A (made at 20 °C, RH 45%).

are significantly higher than the BDS without embedded electrodes. These HVOF7–12 coatings are part of experimental test series where the powders of Al_2O_3 and MgO were same but the amount of MgO varied (0–65%). Otherwise the coatings are deposited similarly as the other HVOF sprayed coatings and their microstructural features are quite similar level with the other coatings. Thus, no clear material difference have noticed for this test series. It may be speculated that the tolerance to endure partial discharges on the coating surface is lower for the coatings HVOF7–12 which could explain the low BDS results without silver electrodes but this is difficult to understand for short-term tests made for ceramics which typically endure surface discharges quite well. All in all, no clear explanation for the results obtained for HVOF7–12 can be found and due to this, a possibility of silver paint penetration is also discussed.

As it was already mentioned earlier, even the breakdown testing standards emphasizes that painted electrodes can affect the results. Unfortunately, the effect of paint is not always similar for the studied coatings which of course raises questions, which method is the most suitable and if the silver paint penetrate too much into the coating and affects this way the BDS results. In fact, silver is a slightly reactive metal, positive silver ions may form and the ions may penetrate into a material under suitable direction (positive to negative electrode) of DC field in certain ambient conditions [116–119, 121, 123–128]. However, this silver migration occurs either at high humidity (RH 80% – 100%) and elevated temperature (above 80 °C) or at high temperature (above 250 °C) [117–119, 122–128]. Typically, also notable time (hours or more) is required for the migration to occur [116, 118]. Since the measurements are performed at quite dry conditions (20 °C, RH 20%) and the breakdowns occur in minutes (ramp rate was 100 V/s), most probably silver migration does not occur in these short-term breakdown voltage measurements. If the silver migration would occur, the breakdown strength should be evidently lower with silver painted electrodes. However, an opposite effect was observed for the coatings HVOF7–12.

As a conclusion it can be said that the effect of silver paint on the breakdown strength is quite minor if the test series HVOF7–12 is not considered. Breakdown strengths of HVOF7–12 made with embedded silver electrodes, except HVOF11, need be considered with a special attention since the silver painted results are 27%–63% higher than the results without silver painted electrodes. For the other coating materials, the difference is typically below 10% or slightly higher. In general as it was already mentioned, the silver paint improves the contact between steel electrode and coating, and the effective test area is larger with painted electrodes.

4.1.2 Overview of the breakdown strength

An overview of the short-term DC breakdown strengths of the studied alumina and spinel coatings is given in Figure 4.4a) and in Table A.1. The voltage was increased with a linear ramp rate of 100 V/s and the silver painted electrodes were embedded on the coating

surface. The results are based on 5–15 parallel samples of each coating type. The obtained DC breakdown fields are at similar level with the fields obtained in the literature when the insulation oil immersion was not utilized [23, 28–32]. The breakdown strengths of spinel coatings are slightly higher than those of alumina coatings which is well in line with the observations made by Toma *et al.* [23]. Figure 4.4b) presents the Weibull β for the studied coatings. In general, a quite high deviation can be seen between the parallel breakdown events for some of the coatings, e.g. PlasmaA. Then Weibull β is remarkably low indicating a high deviation in the breakdown strength distribution. However for some materials, e.g. FlameA, the Weibull β is high indicating high material homogeneity.

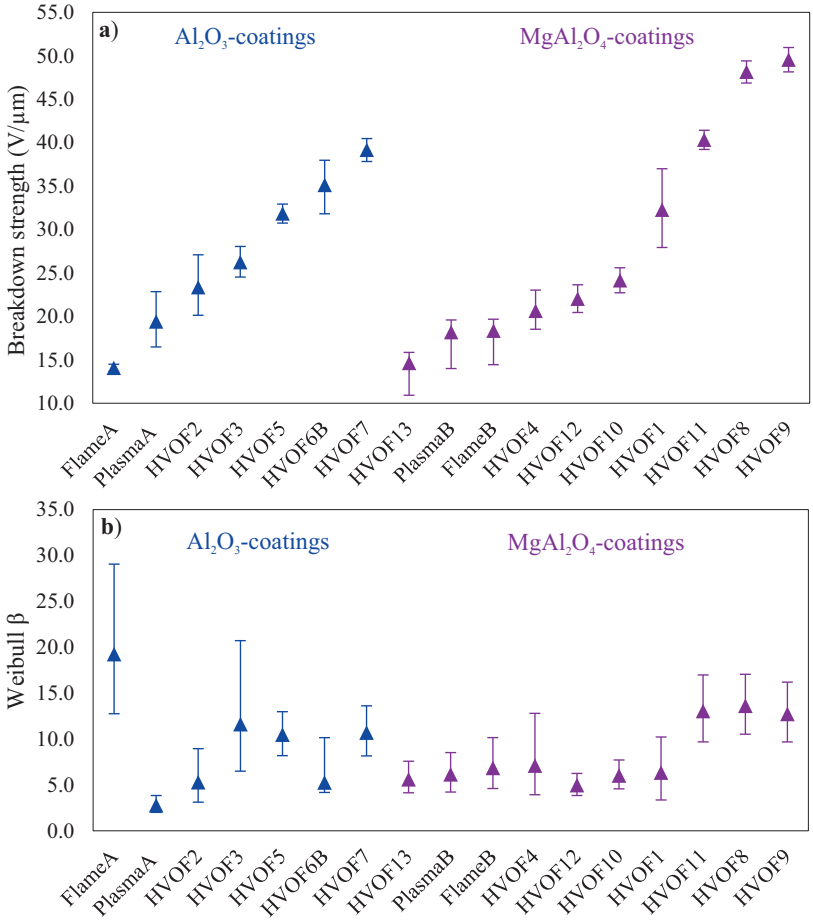

Figure 4.4: **a**) DC breakdown strength (Weibull α) and **b**) Weibull β of studied alumina and spinel coatings at 20 °C/RH 20%. The error bars in both figures present the range of 90% confidence bounds. The results are presented as they were presented in the publications. Due to this, some results are calculated utilizing MLE parameter estimation [P2, P4, P5, P6, P7] and some utilizing RRX [P8] but the parameter estimation method has only a little effect on the results.

The differences in the breakdown strength results between the studied coatings can be linked to their different microstructural features. The microstructure of a coating is very process-dependent as it was discussed in Sub-chapter 2.2. In particular, the spray temperature, the particle velocity and size distribution of the particles affect the formed coating structure remarkably [2, 4, 43, 44]. The chosen spray method determines the particle velocity, and consequently has the greatest influence on the coating structure. This effect on breakdown strength can be noticed since the studied HVOF coatings have higher dielectric breakdown strength than the rod flame or atmospheric plasma sprayed coatings. Since the particle velocity is very high in HVOF process, the HVOF coatings have very dense structure in comparison to APS and FS coatings [4, 15, 18, 43, 47, 52]. The lowest particle velocity is in rod flame spray process, and according to Costil *et al.* [57] rod flame sprayed alumina coatings have less dense structure than plasma sprayed coating. Similar microstructural differences have been obtained in this thesis, which can be seen in detail from the cross-sectional micrographs of the studied coatings (Figure 5.2).

In addition to the spray process, the spray distance (stand off distance) affects the melting capability of the powder particles. Due to this, increasing the spray distance increases the amount of unmelted particles and porosity of APS and HVOF sprayed alumina coatings [11, 137]. Kotlan *et al.* [12] noticed that the breakdown strength of APS alumina coating was the highest (17 V/µm) with a low spray distance (100 mm) while increasing the distance to 150 mm or 200 mm decreased the BDS sligthly (14 V/µm) but the difference cannot be thought being significant. In APS process, the spray distance is typically lower (100–120 mm) than in HVOF spraying (150 mm) [4, 9, 23, 43]. In this thesis, the utilized spray distances were close to the literature values, i.e. 170 mm in HVOF spraying and 110 mm in APS process.

4.1.3 Relationship between porosity and breakdown strength

The porosities of thermally sprayed ceramic coatings are determined from the cross-sectional micrographs. Figure 4.5 presents well that the porosity of a coating differs depending on the utilized determination technique (optical microscopy, SEM/SE or SEM/BSE). In addition, the determined porosity value depends on the magnification of the image, which regions in the figure are included in the porosity calculations, the utilized program etc. Although the methods are automatized quite well, the human decisions made during the evaluation process affect significantly the determined porosity values as well.

Rather low porosities were determined for the studied coatings from cross-sectional micrographs, the values being typically below 4 vol.%, see Figure 4.5 and Table 3.1. Again differences can be seen between different spray methods since the porosity of flame sprayed alumina coating (FlameA) is higher than that of HVOF and APS sprayed materials. Furthermore, FlameA has lower BDS in comparison to the BDS of HVOF and APS coatings. Some minor differences can be seen in the porosities of HVOF sprayed coatings,

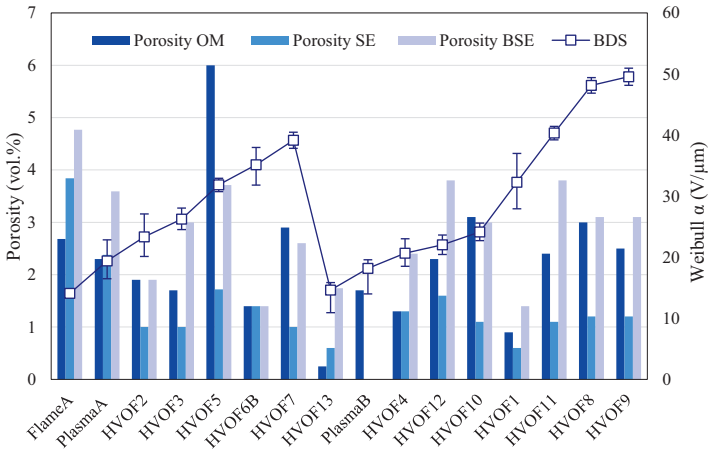

Figure 4.5: The relationship between the porosities determined from cross-sectional micrographs and the dielectric breakdown strengths of the studied coatings. Differences in the porosities of the studied coatings determined from cross-sectional micrographs taken by an optical microscope (OM), a SEM using either secondary electron (SE) or backscattered electron detector (BSE) are presented in columns. The breakdown strength (Weibull α) is presented as a line plot in secondary y-axis. The error bars of the line plot present the range of 90% confidence bounds of Weibull α.

e.g. alumina coating (HVOF5) has higher OM porosity than the other HVOF coatings. As it can be noted from the Figure 4.5, no clear correlation can be found between the porosity and the breakdown strength. This is opposite to the results obtained in the literature [28] where breakdown strength of APS alumina coatings decreased with increasing porosity. Toma *et al.* [23] also reported that lower breakdown strength of APS alumina and spinel coatings can be explained by the higher porosity of APS coatings. However, the porosity differences cannot alone explain the differences between the breakdown strengths of HVOF and APS coatings.

The effect of porosity on the breakdown strength has also been studied for bulk aluminas. According to Liebault *et al.* [35], the porosity has a minor effect on the breakdown strength of bulk alumina when the porosity is below 5%. Touzin *et al.* [138] made similar observations since they noticed that breakdown strength of bulk alumina decreased when the porosity was higher than 4.5%. However, Neusel *et al.* [106] obtained that the porosity has decreasing effect on the BDS of bulk alumina also below 5% values. Porosities of the studied ceramic coatings are below 5% in this thesis, and thus the results can be thought to be in coherence with the results obtained by Liebault *et al.* [35].

While the porosities determined from the cross-sectional micrographs were found to be relatively similar to all the coatings, the gas permeability (GP) measurements indicated differences between the coatings, see Table 3.1 and Figure 4.6. This is most likely due to the fact that gas permeability provides a more accurate estimate for the volumetric porosity and the amount of vertical voids and cracks than a porosity value determined from

a single cross-sectional micrograph. It can be noted that the gas permeabilities of APS and flame sprayed spinel coatings are higher than the general GP level of HVOF coatings, which can be linked to the denser structures of HVOF coatings. However, some of the HVOF coatings (HVOF3, HVOF10 & HVOF12) have very high gas permeabilities since the coatings exhibit long vertical cracks observed from the cross-sectional micrographs.

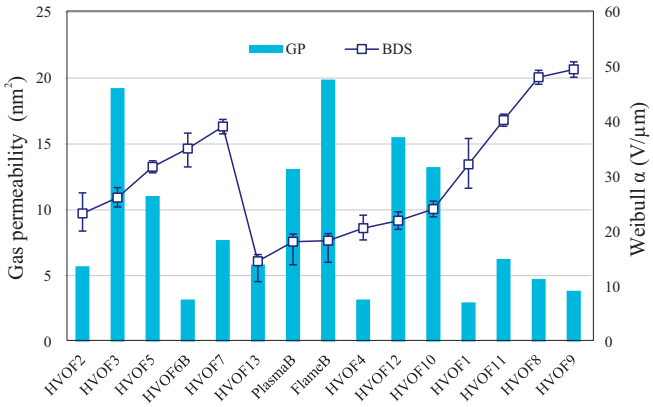

Figure 4.6: The relationship between the gas permeability and the breakdown strengths of the studied coatings. The breakdown strength (Weibull α) is presented as a line plot in secondary y-axis. The error bars present the range of 90% confidence bounds of Weibull α.

In [P6], the effect of gas permeability on the breakdown strength was studied for HVOF coatings (HVOF7–12) with varying amount of MgO (0% to 65%). In this test series higher gas permeability correlate with lower breakdown strength since the highest breakdown strength was obtained for HVOF9 (GP 3.9 nm^2) and the lowest for HVOF7 (GP 7.7 nm^2), see Figure 4.7. In addition, a coating with a high GP value shows lower shape parameter (Weibull β). However, the effect of gas permeability is not as explicit when the results of all different test series are compared since other factors affect the BDS as well due to the complexity of the coating formation, see Figure 4.6. The excellent correlation between gas permeability and breakdown performance of HVOF7–12 can be due to the fact that the base material of HVOF coatings is same and only the amount of MgO is varied, the coatings are manufactured at same time, and thus most of the properties of these coatings are very similar. In addition to the porosity, also other material properties affect the breakdown strength. Coating formation is a very sensitive process where even minor changes during the manufacturing process can cause variation in the material properties between different test series which can furthermore hide some of the effects presented in Figure 4.6. Based on the results of HVOF7–12, it may be concluded that higher gas permeability correlate with lower breakdown strength if the study is made for one test series. Although gas permeability is a good indicator to distinguish possible faults in the coatings, it needs to be emphasized that cross-sectional images, porosity determination, and gas permeability all together need to be determined

in order to analyze the role of microstructure on the dielectric properties, e.g. breakdown performance, thoroughly.

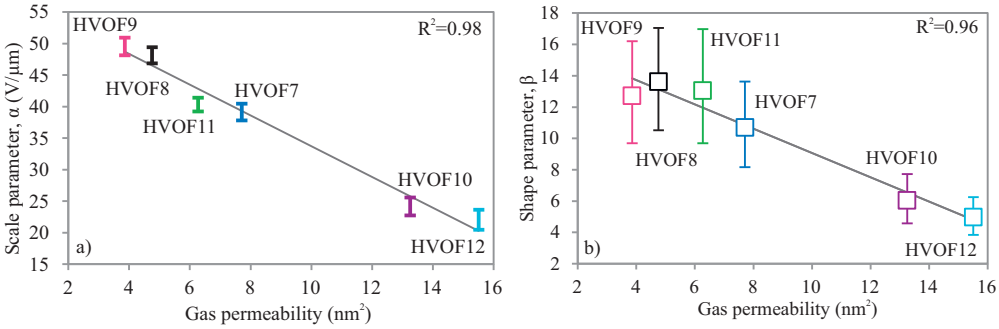

Figure 4.7: Weibull parameters α (a) and β (b) as a function of gas permeability where the error bars present the range of 90% confidence bounds for the parameters. [P6]

4.1.4 Role of lamellae size and the amount of MgO

The idea of manufacturing the test series of HVOF7–HVOF12 was to keep the base material the same and vary the amount of MgO from 0% to 65%. Effect of the size of lamellae on the breakdown strength of these coatings was studied in [P6]. In order to analyze the lamellar morphologies, the SEM/BSE images were converted into binary pixel matrices corresponding to the crystalline and amorphous areas and analyzed quantitatively in MATLAB. In accordance with the free-space length method developed by Khare & Burris [139], quantitative determination of the characteristic size of a morphological domain of interest provides means to relate structural features and material properties. In [P6], the free-space length method, was utilized to characterize the size of the crystalline domains of the coatings L_f. Free-space length can be defined as the size of the largest randomly placed box for which the most probable number of intersecting pixels corresponding to amorphous regions is zero. The MATLAB code, retrieved and used according to the literature [139, 140], iterates to box size by Monte Carlo approach–a more thorough description of the method is presented in [139, 140].

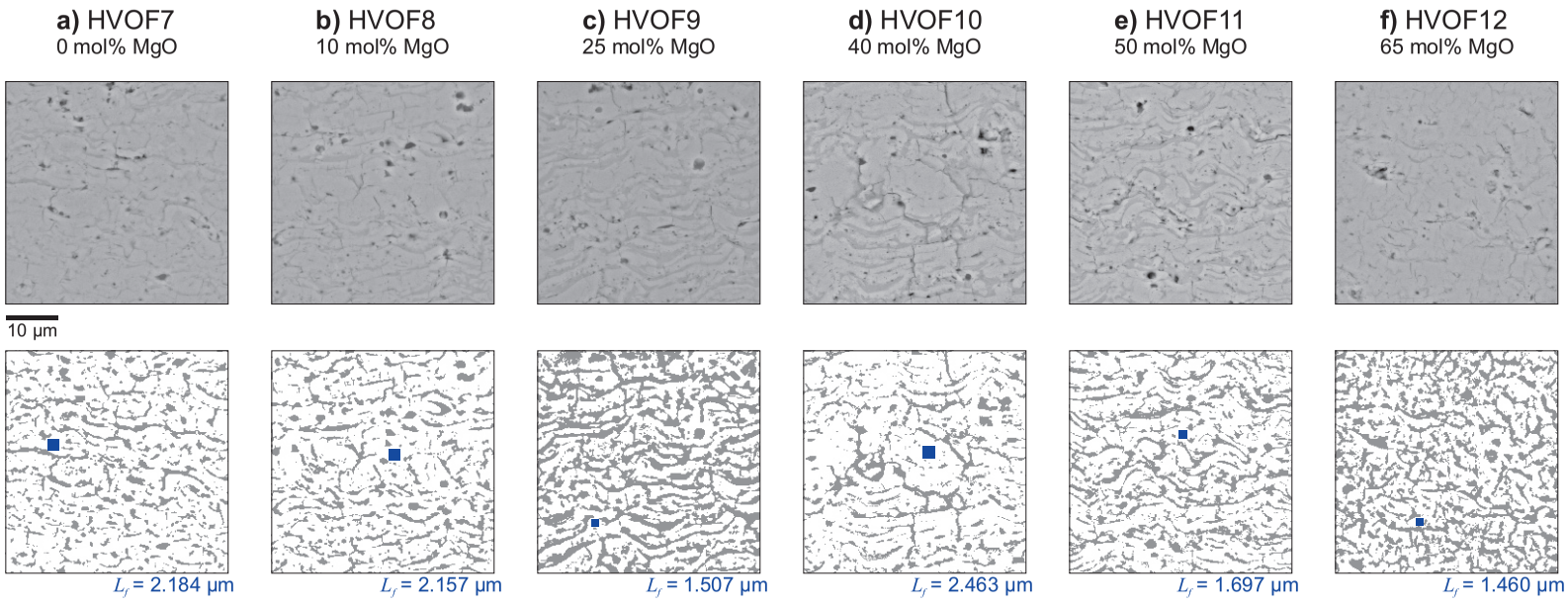

Figure 4.8: Zoomed-in portions of the SEM/BSE cross-sectional images of the studied coatings at 1000× magnification. The total studied image areas were $121 \times 98\,\mu m^2$. The top row presents the original SEM images, with light gray, dark gray and black image regions corresponding to the crystalline, amorphous and void (porosity) regions. The bottom row presents the corresponding binary images utilized for the quantitative structural analysis. The free-space length, L_f, characterizing the size of the crystalline domain is presented in each figure. Free-space length determination was performed iteratively in MATLAB (in manual mode) by gradually increasing the amount of random tests up to 100,000 in order to obtain high statistical accuracy. [P6]

Exemplifying SEM/BSE cross-sectional morphologies are presented in Figure 4.8, showing the porous nature and the lamellar crystal structure of the coatings. It is noted that the varying amount of small vertical cracks visible in the cross-sectional images likely contribute to porosity and gas permeability, with this being the most prominent for HVOF10 which exhibited particularly long vertical cracks (see Figure 4.8). Figure 4.8 also presents the corresponding binary images utilized for quantitative determination of the characteristic crystalline domain size and the calculated free-space lengths. While HVOF9 and HVOF12 were found to exhibit slightly more compact amorphous–crystalline regions, the overall differences remained small and showed no clear correlation with the MgO-content.

The breakdown strengths of the coatings (HVOF7–12) are presented in Figure 4.9. The highest breakdown strengths were obtained for HVOF9 (25% MgO) and HVOF8 (10% MgO) while the lowest breakdown strengths were measured for HVOF12 (65% MgO) and HVOF10 (40% MgO). Interestingly, the breakdown strength of the alumina coating (HVOF7, 0% MgO) and spinel coating (HVOF11, 50% MgO) is very similar although typically the HVOF spinel coatings exhibit higher breakdown strength than the HVOF alumina coatings [23, P5].

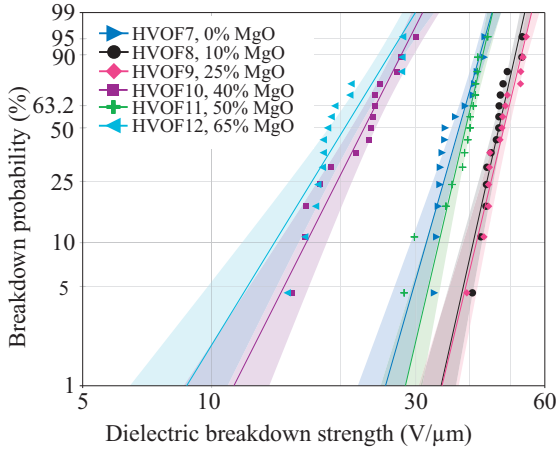

Figure 4.9: Weibull distributions of DC breakdown strength of the coatings (HVOF7–HVOF12) in Weibull probability plot where the shaded areas present 90% confidence bounds. [P6]

The significant difference between the lowest and the highest BDS of HVOF7–HVOF12 can partly be explained by the differences in gas permeabilities, see Figure 4.7. However, the amount of MgO changes in this test series, which has also some effect on the breakdown strength. On the other hand, the characteristic crystalline domain sizes showed no clear correlation with the breakdown performance, which suggests that the porosity and the vertical cracks (structural defects) play a more determining role in the BDS of the coating than the crystalline–amorphous morphology, which is in coherence with [23, 28]. It is also

remarked that the observed long vertical cracks, particularly in HVOF10, likely affect the BDS.

Obviously, the amount of MgO affects the breakdown strength. However, this effect is difficult to obtain explicitly comparing the breakdown strength results because HVOF10 (40% MgO) exhibit long vertical cracks and high GP in comparison to the HVOF9 (25% MgO) and HVOF11 (50% MgO). In addition, rather high deviation between parallel breakdown results makes it difficult to distinguish the exact effect of MgO content on the breakdown strengths. However, it can be noticed that the optimal composition of MgO in Al_2O_3 powder seems to be in the range of 10–25%. However, the breakdown strengths of HVOF7 and HVOF11 (39.2 V/µm and 40.3 V/µm, respectively) are in coherence with the results presented in Figure 4.4 and reported in literature [23].

4.1.5 Effect of ambient conditions

The effect of temperature and humidity on the DC breakdown performance was studied for alumina coatings (HVOF6B, PlasmaA and FlameA) [P8]. The DC breakdown strengths (BDS) of the studied alumina coatings at 20–180 °C are presented in Table 4.1, where the results are based on 10–15 parallel breakdown measurements. The highest BDS is obtained for HVOF6B at all the ambient conditions and the lowest one for FlameA.

Figure 4.10 shows the Weibull distributions of the coatings at all the studied ambient conditions. The lowest Weibull β values in Table 4.1 are obtained for PlasmaA indicating the highest deviation in the breakdown distribution. Below 200 °C, the temperature does not affect the breakdown strength of ceramic coatings notably since only some minor differences can be seen. The obtained results are in coherence with results obtained by Dutarde *et al.* [34] since they noticed that increasing temperature from ∼20 °C to 80 °C has no influence on the BDS of bulk alumina. Although the higher absolute humidity conditions seemed to decrease the BDS of HVOF6B alumina, similar effect is not seen

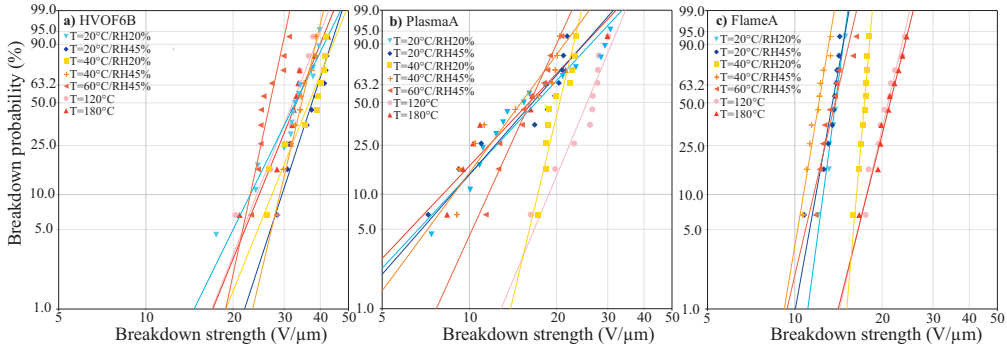

Figure 4.10: Weibull distributions of HVOF6B, PlasmaA and FlameA coatings at 20–180 °C. In order to ensure a visually good figure, the confidence bounds are not presented. The breakdown fields at various breakdown probabilities and Weibull β are presented in Table 4.1.

Table 4.1: The breakdown fields of the alumina coatings at the breakdown probabilities of 10%, 63.2% and 90% at 20–180 °C and Weibull β. The statistical analysis of the breakdown data was performed using Weibull++ software and the least-square regression method was used in parameter estimation. The goodness of the fit results can be expressed by correlation coefficient, λ. The closer to 1 λ is, the better the fit is. λ was 0.91–0.97 for HVOF6B, 0.93–0.98 for PlasmaA and 0.93–0.98 for FlameA. [P8]

	BDS of HVOF6B ($\mathrm{V\,\mu m^{-1}}$)				BDS of PlasmaA ($\mathrm{V\,\mu m^{-1}}$)				BDS of FlameA ($\mathrm{V\,\mu m^{-1}}$)			
	$E_{10\%}$	α, $E_{63.2\%}$	$E_{90\%}$	β	$E_{10\%}$	α, $E_{63.2\%}$	$E_{90\%}$	β	$E_{10\%}$	α, $E_{63.2\%}$	$E_{90\%}$	β
20 °C/RH 20%	22.9	35.1	41.2	5.3	8.6	19.4	26.2	2.8	12.5	14.1	14.7	19.3
20 °C/RH 45%	29.5	39.2	43.5	7.9	8.7	18.7	24.8	3.0	11.8	13.8	14.7	14.3
40 °C/RH 20%	27.2	38.7	44.1	6.4	17.2	21.2	22.9	10.8	16.3	17.6	18.1	30.2
40 °C/RH 45%	29.0	35.6	38.5	10.9	8.8	16.8	21.3	3.5	10.7	12.4	13.1	15.4
60 °C/RH 45%	22.9	27.6	29.6	12.0	11.6	17.3	20.0	5.7	11.6	14.2	15.3	11.1
120 °C	24.1	33.9	38.5	6.6	18.8	27.0	30.9	6.2	17.7	21.7	23.4	11.0
180 °C	24.6	35.0	39.9	6.4	8.1	18.4	24.9	2.7	17.7	22.1	24.0	10.3

for other coatings, and it may be concluded that humidity did not directly affect the breakdown strength.

At 120 °C and 180 °C, the breakdown strength of FlameA is higher than the BDS at the low temperatures. It is rather obvious particularly for FlameA that at the higher temperatures (120 °C and 180 °C) moisture is partially escaped from the porous coating, and thus the BDS increases in comparison to the 20–60 °C results. Pawlowski [28] noticed that the relative permittivity of plasma sprayed alumina coating decreased after a long period (48 h) at 120 °C which was linked to the hygroscopic nature of the coatings which enables the moisture to penetrate into the coating easily. Although the samples were in an oven for a shorter period (1–2 h) than in [28], the heat treatment most probably removed part of the moisture from the porous coating in this study, too. This may explain the higher breakdown strengths of FlameA at 120 °C and 180 °C.

Since the ceramic coating may also be used at notably higher temperatures than 180 °C, the breakdown measurements were extended to higher temperatures (200–800 °C). Figure 4.11 presents the breakdown strength of the HVOF alumina coating (HVOF6B) as a function of temperature. The BDS is at a quite similar level from 20 °C to 200 °C although the deviation between the parallel samples is quite large in many cases. Interestingly, the deviation between parallel samples is remarkably lower at higher temperatures (above 350 °C) which can be seen as a high β in Figure 4.11. Above 300 °C the breakdown strength starts to decrease reaching the value of 5.2 V/µm at 800 °C which is 14% of the BDS at 20 °C/RH 20%. Yoshimura and Bowen [102] made almost similar observation for polycrystalline alumina since the breakdown strength decreased gradually from room temperature (90–100 V/µm) to 900 °C (∼25 V/µm). Above 900 °C, the BDS of alumina decreased at much higher rate and it was only 2 V/µm at 1400 °C [102].

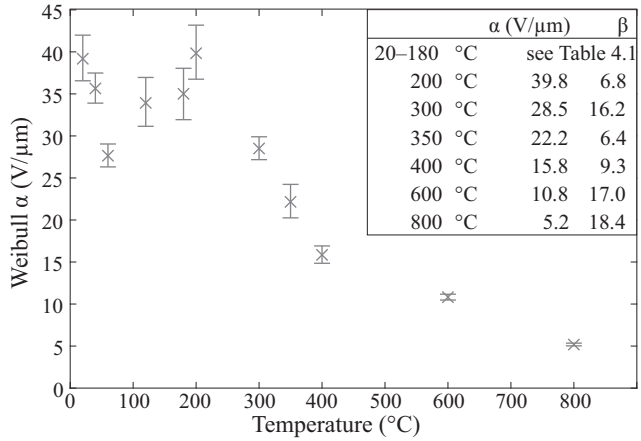

Figure 4.11: The breakdown strength of HVOF6B at 200–800 °C. The breakdown strength of HVOF6B (Weibull α) and Weibull β at 20–180 °C are presented in Table 4.1. [P8]

4.1.6 Effect of ramp rate on the breakdown strength

Possible ramp-rate-effect was studied in [P4] by utilizing two different ramp rates for HVOF sprayed alumina coating (HVOF5). In literature [141, 142], the ramp rate is found to affect the breakdown strength of certain insulation materials, with a higher ramp rate giving higher breakdown strength for the material due to the space charge phenomena. At the ramp rate of 100 V/s, the breakdown strength is 31.8 V/µm and Weibull β is 10.5. At 10 times higher ramp rate (1000 V/s), the breakdown strength is 32.1 V/µm and Weibull β is 14.7. As the breakdown strength distributions of different ramp rates are practically the same (see Figure 4.12), the ramp rate does not affect the breakdown strength, and thus the effects due to space charge accumulation cannot be noticed. Owate & Freer [103] observed similar behavior for bulk alumina since the breakdown strength was noticed to be independent of the rate of voltage rise.

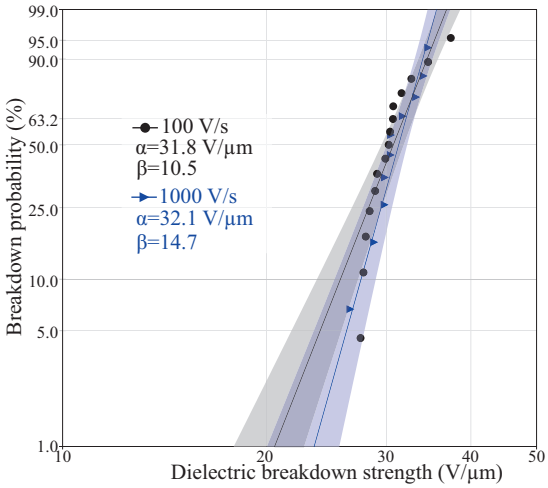

Figure 4.12: The breakown strength of the alumina coating (HVOF5) with two different ramp rates in Weibull plot. The shaded areas present the 90% confidence bounds [P4].

4.2 Step-by-step increased breakdown strength of alumina and spinel coatings

In addition to linearly ramped breakdown tests, the breakdown tests were also performed increasing the DC voltage step-by-step. In [P4], the step-by-step tests were carried out with step durations of 6 min and 60 min for HVOF alumina coating (HVOF5). The 6 min step tests were started at the voltage of 250 V (E=1.2 V/µm) which was the step size as well. The 60 min step measurements were started at the voltage of 4000 V (E=∼18.6 V/µm) with the step size of 500 V.

Since the step voltage was two times higher in the 60 min tests than in the 6 min tests, the test "resolution" in the 60 min tests decrease to some extent. In the 60 min tests, the

times to breakdown varied from 100 min to 236 min. In the 6 min tests, this variation was from 121 min to 159 min. Thus, the total duration was at a quite similar level in both test types. The mean breakdown strength was 23.9 V/µm in the 60 min tests and 27.2 V/µm in the 6 min. Hence, only a minor difference can be seen since the standard deviation was 2 V/µm in both tests.

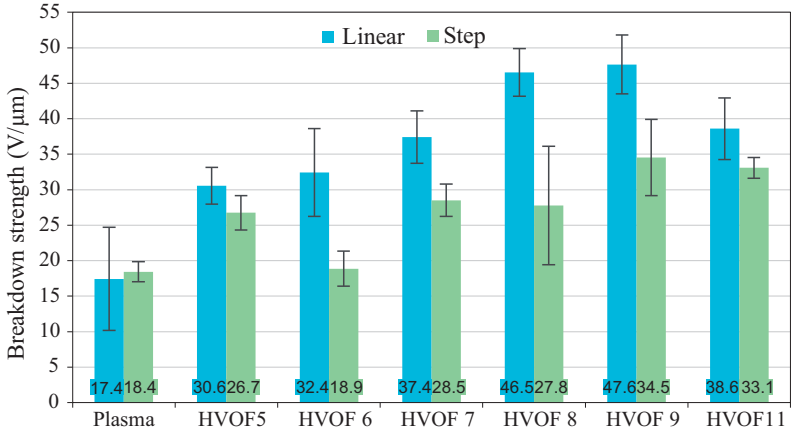

Figure 4.13: Mean DC breakdown strengths of the coatings from the linear ramp rate and from the step measurements (250 V/ 10 min). The error bars present the experimental standard deviations of parallel measurements (15 tests in linear ramp tests and two or five tests in step tests). [P7]

In [P7], the step-by-step increased breakdown voltage tests were made for several HVOF coatings (HVOF5, HVO6B, HVOF7–9 & HVOF11) and one plasma sprayed alumina coating (PlasmaA). In these tests, the step duration was 10 min and the starting voltage was 250 V which also was the step size. Figure 4.13 presents the mean breakdown strengths of the coatings when the voltage was increased either linearly or step-wisely. For plasma sprayed alumina coating (PlasmaA), the deviation between parallel samples in linear ramp tests is remarkably higher and due to this the breakdown strength is practically the same in step-test and ramp-test. For HVOF coatings, the step-test breakdown strengths are lower than the ramp-test breakdown strengths. The difference is from 3.9 V/µm (HVOF5) to 18.7 V/µm (HVOF8). The step-test breakdown strength is lower than the ramped one due to the clearly longer stress durations in the step tests. The differences thus give an estimation of the effects of electric stress duration and possible time dependent degradation of the coatings.

4.3 Long-term breakdown performance of alumina and spinel coatings

In order to evaluate long-term breakdown performance of ceramic coatings, DC voltage endurance tests were performed for one alumina coating (HVOF6B) and one spinel coating

(HVOF11) at room temperature conditions. The test was started with a constant electric field of 10 V/µm and a duration of 1000 h. Since remarkable changes in the sample currents were not observed or breakdowns did not occur, the electric field was increased to 15 V/µm for seven days (168 h). After this test, no remarkable changes were noticed and the test was continued with following procedure: the test field was increased in the steps of 2.5 V/µm until 25 V/µm so that the duration of each test field was 168 h. Thus, the total test duration was 1840 h.

Figure 4.14 presents the measured currents of the whole test period for the alumina coating (HVOF6B) as well as the breakdown events. Figure 4.15 presents the measured currents and the breakdown events for the spinel coating (HVOF11). As it can be observed from the figures, the measured leakage currents varied to some extent which can be linked to the small changes in the air humidity since the measurements were performed at room temperature where the air humidity varied some amount. The observed relationship between leakage currents and air humidity is understandable since the coatings have moisture sensitive nature when they are tested as-sprayed. This relationship between the leakage currents and air humidity will be discussed in detail afterwards in this sub-chapter.

As it was mentioned earlier, at 10 V/µm no breakdowns occurred but at the higher fields three breakdowns occurred for both materials. The detailed times to breakdown are presented in Table 4.2. As it can be seen from Figure 4.14, the breakdowns of the alumina coating, HVOF6B, at 15 V/µm and at 22.5 V/µm occurred almost immediately after the voltage was increased. At 25 V/µm, the breakdown occurred in the end of the test period. All the breakdowns of HVOF6B occurred quite suddenly and no slow current increase was seen before the breakdown or no high variation in the leakage currents was observed. Thus, no clear degradation process was noticed by leakage current and the observed breakdowns of HVOF6B can be thought to be weak-points of the material. Six samples out of the nine withstood the whole test period without any significant changes in the currents.

Table 4.2: Breakdown events during the voltage endurance test.

Material	Breakdown events		
HVOF6B	1001 h, 15 V/µm	1506 h, 22.5 V/µm	1825 h, 25 V/µm
HVOF11	1328 h, 17.5 V/µm	1336 h, 20 V/µm	1419 h, 20 V/µm

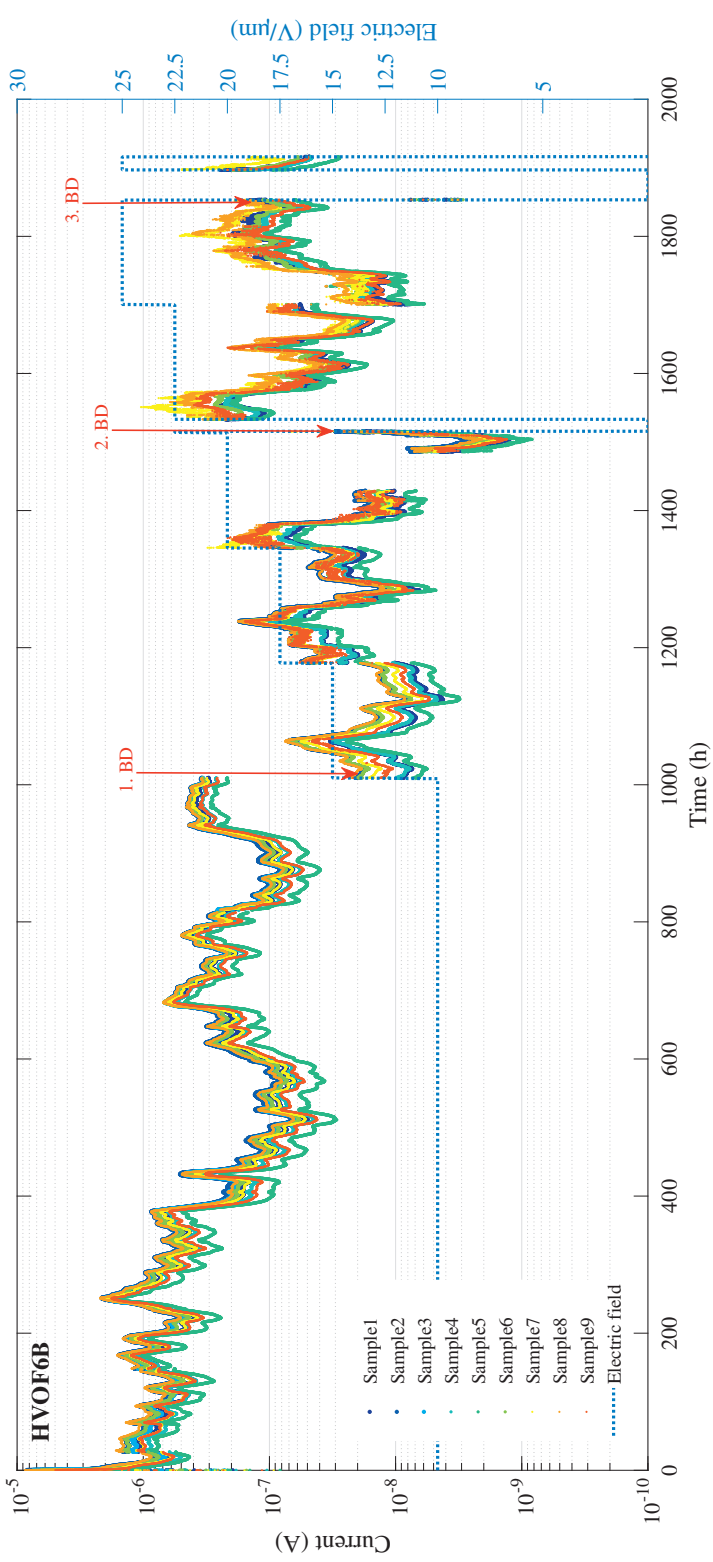

Figure 4.14: The measured leakage currents of the samples of the alumina coating (HVOF6B) during the whole test time presented in the left side y-axis and the electric field is in right y-axis. The red arrows show the breakdown events. After the 1st breakdown, the voltage was increased back to the set value without a long break but after the 2nd and 3rd breakdowns a longer breaks occurred which can be seen in the figure. After these longer breaks, the test duration was extended so that the 168 h was gathered totally. At 20 V/µm, the current measurement was off for some time due to a breakdown in the other material (HVOF11) which caused an error in the current measurement system and the data was not recorded.

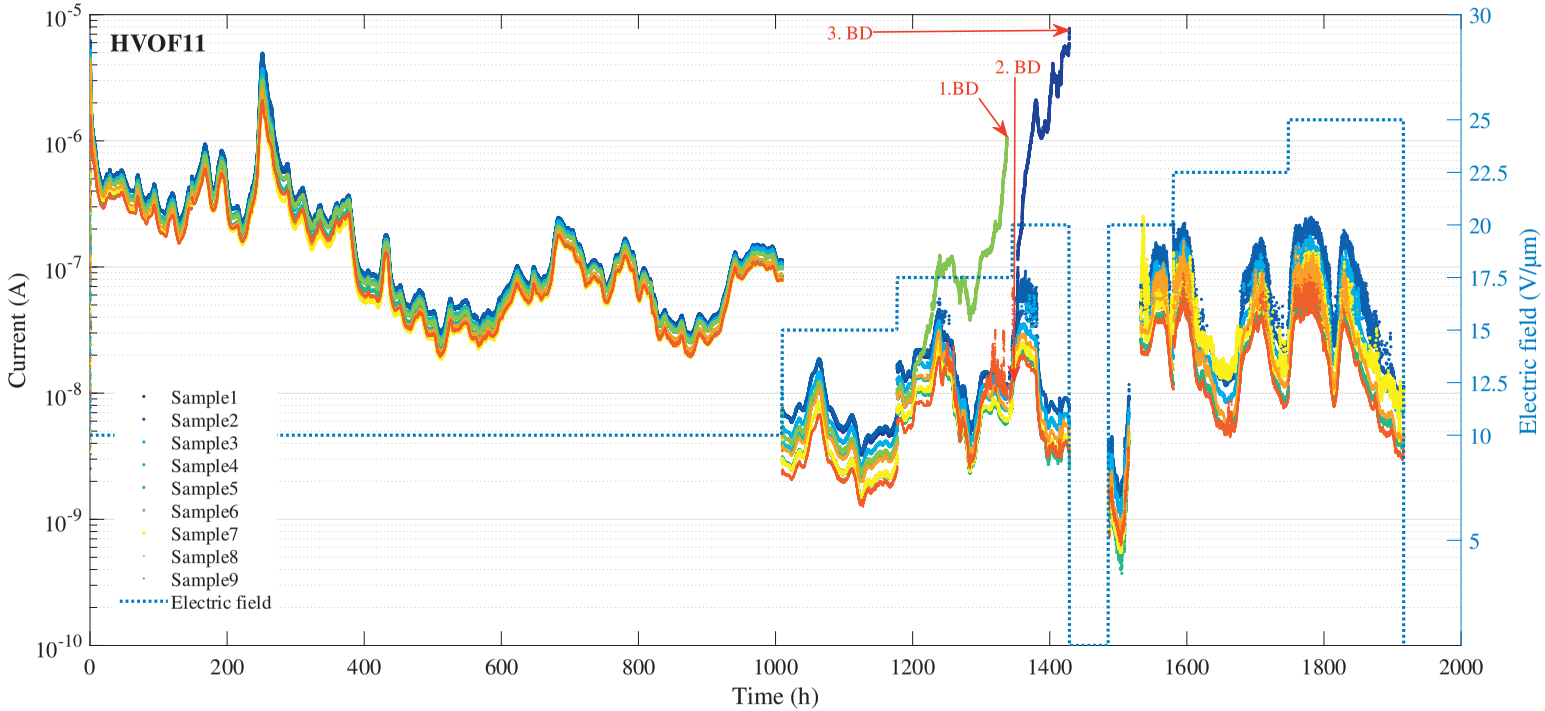

Figure 4.15: The measured leakage currents of the samples of the spinel coating (HVOF11) during the whole test time presented in the left side y-axis and electric field is in right y-axis. The red arrows show the breakdown events. After the 1st and 2nd breakdowns, the voltage was increased back the set value quite rapidly and thus no long breaks can be seen in current measurements. However, the 3rd breakdown occurred during a weekend which caused a longer break in the test but this break was compensated by extending the test so that the 168 h was gathered totally.

For the spinel coating (HVOF11), the first breakdown at 20 V/µm occurred also suddenly just few minutes after the voltage was increased without any slow current increase indicating most probably a weak-point of the material. However, two other breakdowns of the spinel coating occurred differently since the current started to increase slowly before the breakdown occurred, see Figure 4.15. At 17.5 V/µm, the current increased for 126 h before breakdown and the increase was almost two decades just before the breakdown. In the second breakdown at 20 V/µm, the increase lasted 84 h and the current increased almost three decades before the breakdown. This kind of current behavior can indicate a material degradation process. However, six samples out of the nine withstood the whole test period without significant changes in the currents.

In general, the current levels were at quite similar level during the whole test, and thus no clear aging can be noticed. Interestingly, it can be seen from Figures 4.14 and 4.15 that after the first 1000 h, the current decreased although the electric field increased. The measurements were made at room temperature conditions, not at controlled conditions, which most probably explain the difference between the current values. The first test at 10 V/µm was made during summer time while the higher field tests (15–25 V/µm) were performed during winter time i.e. four months after the first test period was ended. In Finland the air humidity is typically much higher in the summer time than it is in the winter time when the air humidity is low due to the cold period.

At the higher field tests, the temperature and relative humidity was recorded with Vaisala Humicap hand-held humidity and temperature meter HM70. Figures 4.16 and 4.17 present the measured currents at 15 V/µm and 17.5 V/µm together with the measured relative humidity. It can be observed clearly that the measured leakage currents follow the air humidity. This similar trend in the currents are also seen at the higher fields (20–25 V/µm). Previous short-term studies [P2, P8] have shown that the air humidity affects the dielectric properties since the ceramic coatings have moisture sensitive nature. However, when the long-term measurement procedure was defined, it was thought that at room temperature conditions small air humidity variations would affect only a little the measured leakage currents. As the results showed, the humidity affects the currents quite remarkably although the relative humidity was only 10–30% in the higher field tests. However, when the measurements were made at slightly varying room temperature conditions instead of utilization controlled conditions, e.g. 20 °C, 20%, the test conditions reflect the variation of realistic ambient conditions and thus also the possible stresses on the specimens.

Although the general current levels for both materials were at quite similar level, at the higher test fields (above 17.5 V/µm) for some of the samples partial charges (PD) occurred at the edges of the embedded electrodes on the coating surfaces, see Figures 4.14 and 4.15. Especially, PDs occurred on the samples of the spinel coating (HVOF11) particularly at the fields of 22.5 V/µm and 25 V/µm but the PD activity started for some of the samples at 17.5 V/µm. However, these PDs did not cause breakdowns. Some amount of PDs was also observed for the alumina coating but the activity not as high as

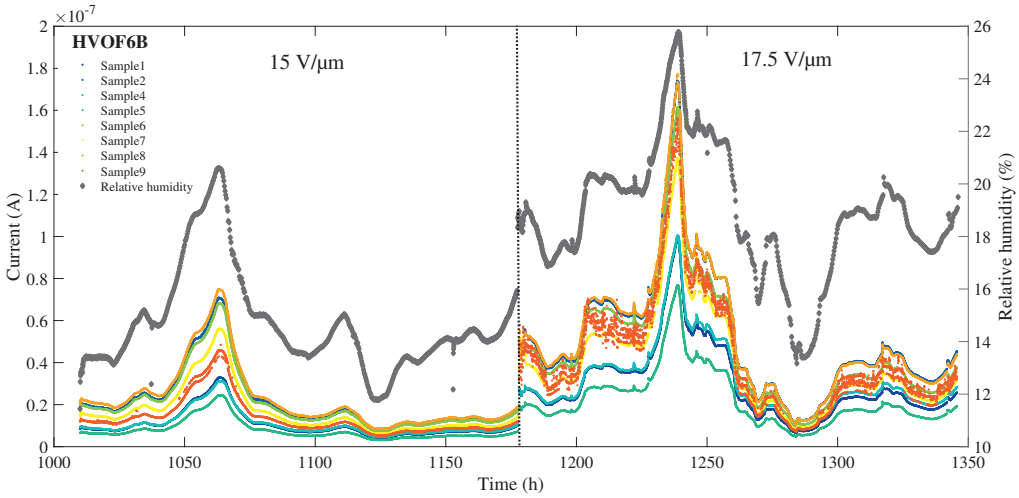

Figure 4.16: The measured currents of the alumina coating (HVOF6B) at the electric fields of 15 V/µm and 17.5 V/µm as a function of time as well as the measured relative humidity (marked as dark gray) during the same time period. Current data for Sample 3 is not shown since the sample broke down right after the field was increased to 15 V/µm.

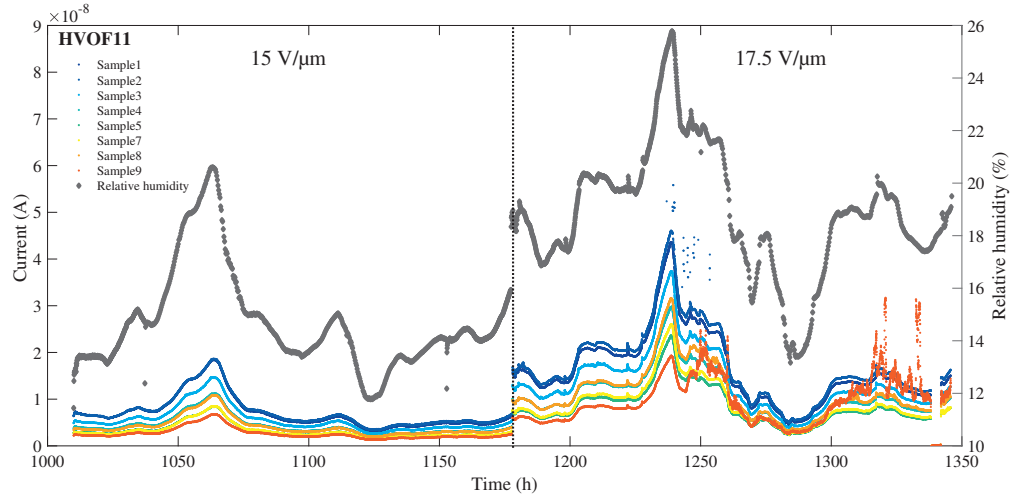

Figure 4.17: The measured currents of the spinel coating (HVOF11) at the electric fields of 15 V/µm and 17.5 V/µm as a function of time as well as the measured relative humidity (marked as dark gray) during the same time period. In order to help a reader to distinguish the the relationship between current and humidity well, the current data of Sample 6 is not presented since the material degradation/slow current increase started at 17.5 V/µm.

it was for the spinel coating. Some PD activity was noticed already at 17.5 V/µm and 20 V/µm for some of the samples but at 25 V/µm the increased amount of PDs caused eventually a breakdown for one sample of HVOF6B. As a conclusion, it can be said that the both materials withstood well the surface discharges and only one sample of the alumina coating broke down after the increased amount of surface discharges.

According to the long-term test, a possible service stress field can be estimated. Since the total tested area was quite small being approximately 9 cm^2 per material, breakdowns are not allowed when determining the possible service field. Thus, for both coating materials the safest choice as possible maximum service field at normal ambient conditions can be evaluated to be approximately 10 V/µm. This evaluation is based on the fact that the lowest breakdown fields were roughly two times higher. For the spinel coating, a slightly higher field (15 V/µm) might be still possible at normal ambient conditions, at least for shorted periods since the first breakdown occurred at the field of 17.5 V/µm. However, for the alumina coating the field of 15 V/µm is most probably too high because the first breakdown occurred at this field. Although that breakdown may have been an exceptionally weak point, it also introduces a true risk of breakdowns. At the higher fields, more breakdowns occurred for both materials which can indicate that these kind of stress levels already may introduce an increased breakdown possibility. In this instance, it shall be reminded that for final service stress decisions larger amount of tests for the specific coatings are required. The performed tests mainly serve as an overall evaluation of possible service field range at normal operating conditions. Naturally, also the planned life-time of the insulation plays a key role in this kind of decisions.

When a consideration of the possible service stress field is made, a following comparison

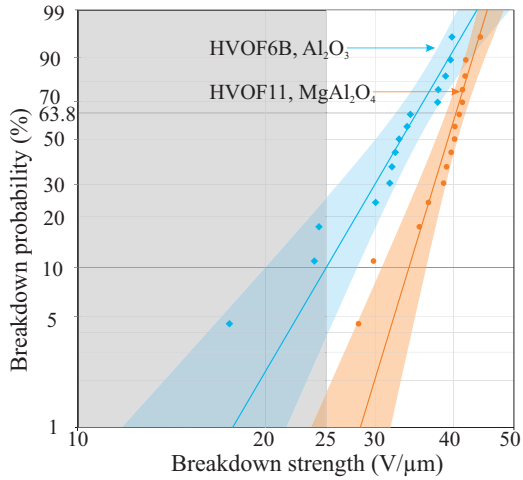

Figure 4.18: Short-term DC breakdown strengths of the alumina coating (HVOF6B) and the spinel coating (HVOF11) presented in Weibull plot where the shaded areas present 90% confidence bounds. The gray rectangle shows the stress region where the long-term breakdown tests were made.

between the short-term and long-term breakdown performance can also be made. Figure 4.18 presents the short-term breakdown strengths in a Weibull plot where the long-term test range is presented together with the short-term distributions. It can be observed that the short-term Weibull distribution of the spinel coating is out of the electric field region where the long-term tests were made. However, for the alumina coating the situation is different. When the short-term breakdown probability of the alumina coating is below 10%, this is in the electric field range of 17.5–25 V/µm. This strengthens the fact that the suitable maximum service stress level for the alumina coating is 10 V/µm. This electric field of 10 V/µm is 29% of the short-term Weibull α of the alumina coating and 25% of the short-term Weibull α of the spinel coating.

Finally, a comparison between different materials can be discussed. Almost all the short-term measurements have shown that the HVOF sprayed spinel coatings exhibit better dielectric performance than HVOF sprayed alumina coatings. According to this long-term test, this kind of clear difference cannot be seen although the first breakdown of the alumina coating occurred at the lower field strength. At high humidity conditions spinel coatings might be slightly better material choice due to their stable thermodynamic properties which furthermore affects their dielectric performance [P2, P8]. However, both coating materials are moisture sensitive at high humidity. All in all, the differences between the tested coating materials can be thought to be quite small.

4.4 Considerations and implications

In this chapter, a suitable breakdown voltage measurement method was determined for thermally sprayed ceramic coatings. The suitable method is a test with a silver electrode embedded on a coating surface and no oil immersion was utilized. According to the short-term breakdown strength results (voltage ramped linearly), following concluding discussion can be made:

- In general, spinel coatings have higher breakdown strength than alumina coatings. In addition, the HVOF sprayed coatings are more promising alternative due to the higher breakdown strength than APS and flame sprayed coatings.

- The porosities defined from cross-sectional micrographic images are rather similar between different coating materials, and due to this no clear correlation between porosity and breakdown strength can be observed. In some test series, high gas permeability (volumetric porosity) can explain the lower breakdown strength of those coatings but this correlation cannot be seen for all coatings. The observations emphasize that the coating structure is complex and it is difficult to find clear correlations between one specific material property and breakdown performance.

- Increasing the relative humidity has no significant effect on breakdown strength of ceramic coatings.

- In the temperature range of 20–180 °C, temperature has only a minor effect on the breakdown strength of alumina coatings but in the range of 300–800 °C the breakdown strength of alumina coating decreases gradually being only 14% of the value obtained at 20 °C/RH 20%.

According to the long-term breakdown performance test, a suitable maximum service stress level for the tested HVOF alumina and spinel coatings can be in the range of 10 V/µm which is approximately 25–30% of the short-term breakdown strength (Weibull α) since at this electric field the coatings withstood 1000 h without any breakdowns. At the higher electric fields (15–25 V/µm), some breakdowns occurred but neither of the tested coating materials was destroyed completely during the test. According to the long-term test, it cannot be said that either of the studied materials had evidently better performance. Finally, the operation environment and the planned life-time of an application determines the chosen material and service field.

Chapter 5

DC conductivity/resistivity

In addition to the breakdown performance, DC resistivity is one of the main dielectric properties for insulating materials. Typically, DC resistivity of thermally sprayed alumina and spinel coatings are measured only at low electric fields, and a detailed study of possible conduction mechanisms are not conducted for the coatings, only for bulk alumina. In this chapter, an overview of the DC resistivity of various thermally sprayed ceramic coatings at low and high electric fields are given. The role of microstructure and ambient conditions on the DC resistivity of various ceramic coatings are discussed, and a detailed conduction mechanism study is performed in order to define a suitable conduction mechanism for ceramic coatings.

5.1 DC resistivity of alumina and spinel coatings at low electric fields

Figure 5.1 presents the DC resistivity of thermally sprayed alumina and spinel coatings at 20 °C/RH 20%. The resistivities of the ceramic coatings are ohmic only at low electric fields, and at higher electric fields the resistivity decreases rapidly indicating non-linear conductivity. According to author's knowledge, similar non-linear conduction behavior has not been reported for ceramic coatings in literature prior to [P1] where the non-ohmic conduction behavior of HVOF sprayed $MgAl_2O_4$ coating (HVOF13) was reported. As Figure 5.1 indicates this behavior exists for almost all the studied coatings in the studied electric field range (0.1–5 V/µm) [P2, P4, P5, P6, P7, P8].

As it can be seen from Figure 5.1a–b, DC resistivity of HVOF and plasma sprayed Al_2O_3 and $MgAl_2O_4$ coatings are ohmic in the electric field range of 0.1–0.5 V/µm. In this field range, the obtained resistivities are $\sim 1 \times 10^{12}\,\Omega\,\mathrm{m}$ being in coherence with the resistivities reported in literature for bulk aluminas [34, 36] and for APS and HVOF sprayed Al_2O_3 and $MgAl_2O_4$ coatings [23, 28, 29]. In the non-ohmic region (0.5–5 V/µm), the resistivity decreases 1–2 orders of magnitude depending on the material. In general, the DC resistivities of spinel coatings are slightly higher than the resistivities of alumina coatings which is in coherence with the results reported by Toma *et al.* [23].

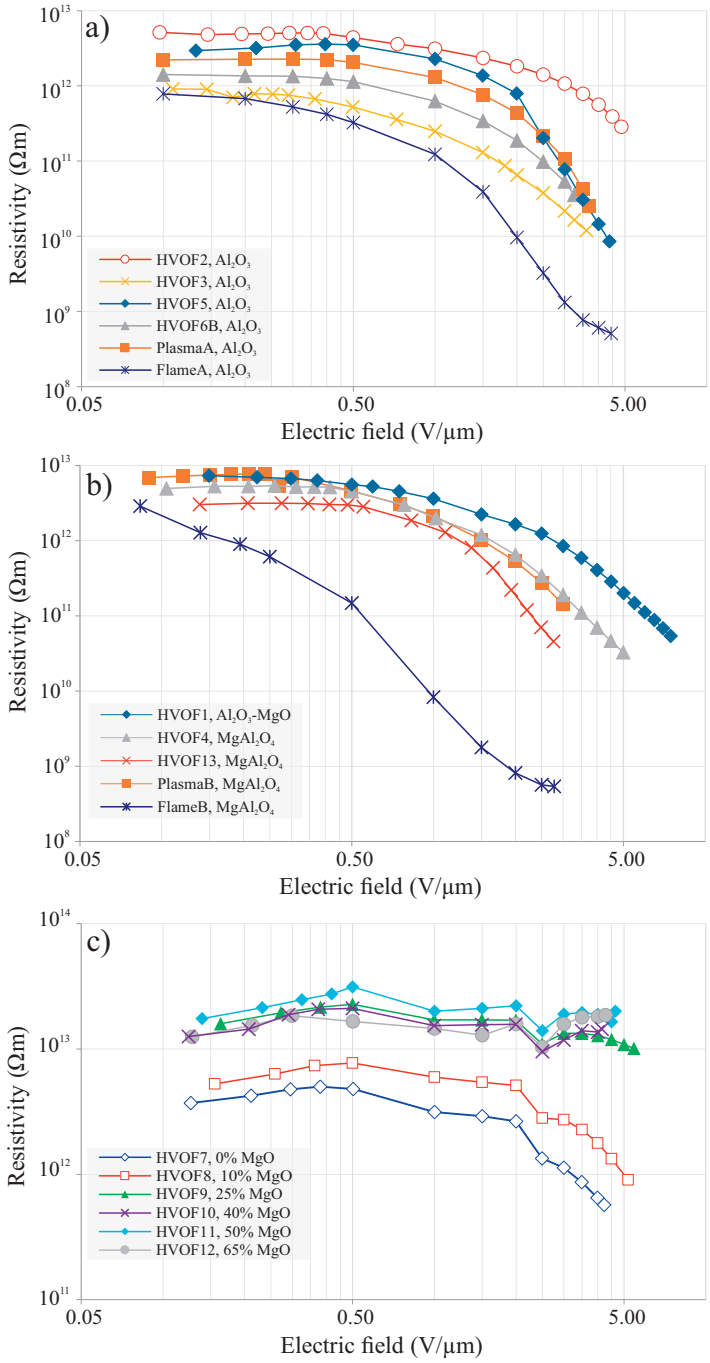

Figure 5.1: DC resistivity of the studied coatings as a function of electric field (log-log scale) at 20 °C/RH 20%: a) Al_2O_3 coatings [P4, P5, P7, P8], b) $MgAl_2O_4$ [P1, P2, P5], and c) Al_2O_3-MgO coatings [P6, P7]. Resistivity values at the electric fields of 0.5 V/µm and 2 V/µm are also given in Table A.1.

The rod flame sprayed alumina coating (FlameA) is ohmic below 0.5 V/µm being at similar level with HVOF and APS alumina coatings. However, the spinel coating (FlameB) is non-linear during the whole measuring electric field range being clearly lower in comparison to the resistivities of HVOF and APS spinel coatings. When the electric field increases from 0.1 to 2.8 V/µm, the resistivity of FlameB decreases approximately four decades being thus very non-linear. Almost similar decrease in the resistivity can be noticed for flame sprayed alumina coating (FlameA) in the non-linear region (0.5–4.4 V/µm).

Figure 5.1c) shows the DC resistivities of HVOF sprayed Al_2O_3–MgO coatings (HVOF7–12). In this test series, the Al_2O_3 powder was similar and the amount of MgO was varied (0–65%). Although the resistivity of HVOF7 (100% Al_2O_3) is the lowest one of the test series HVOF7–12, it is at a similar level with the resistivity of alumina coating HVOF2 which exhibits the highest resistivity of all the studied alumina coatings. Adding MgO in the Al_2O_3 powder increases the resistivity of the coatings because the resistivity of HVOF8 (10% MgO) is slightly higher than the resistivity of HVOF7 (0% MgO). When the amount of MgO is from 25% to 65% (HVOF9–HVOF12), the DC resistivity is even higher, being approximately at the level of $1.5 \times 10^{13}\,\Omega\,\mathrm{m}$, for all these compositions. These coatings exhibit the highest resistivities of all the coatings in this thesis and in literature [11, 23, 28, 29]. Furthermore, the non-ohmic behavior cannot be seen for these coatings (HVOF9–HVOF12) at the studied field strengths. However, the coatings with low amount of MgO (HVOF7 & HVOF8) exhibit similar non-ohmic resistivity as the other studied coatings (Figure 5.1a–b) when the electric field is above 2 V/µm. Thus, it can be concluded that adding MgO 25% or more into Al_2O_3 powder improves the DC resistivity of HVOF sprayed coating at low electric field strengths.

5.1.1 Role of microstructure

Thermal spray method yields to a special layered microstructure. SEM/BSE cross-sectional morphologies are presented in Figure 4.8 and in Figure 5.2 showing the lamellar microstructure of the coatings and the porous nature. Additionally, the crystalline and amorphous regions formed during the rapid solidification of the splats which can be observed in the figures. As it was discussed previously, the porosities determined from the cross-sectional micrographs were found to be relatively similar to all the coatings and more significant differences can only be seen in the gas permeabilities (Table 3.1). This can be linked to the fact that gas permeability provides a more accurate estimate for the volumetric porosity than the porosity determined from a single cross-sectional micrograph.

The coatings always exhibit some number of vertical cracks but long cracks can be problematic for an insulating coating. For some coatings, it is noticed that the high gas permeability can indicate high amount of long vertical cracks which can be observed from the cross-sectional micrographs, e.g. HVOF3, HVOF10 & HVOF12, see Figure 4.8

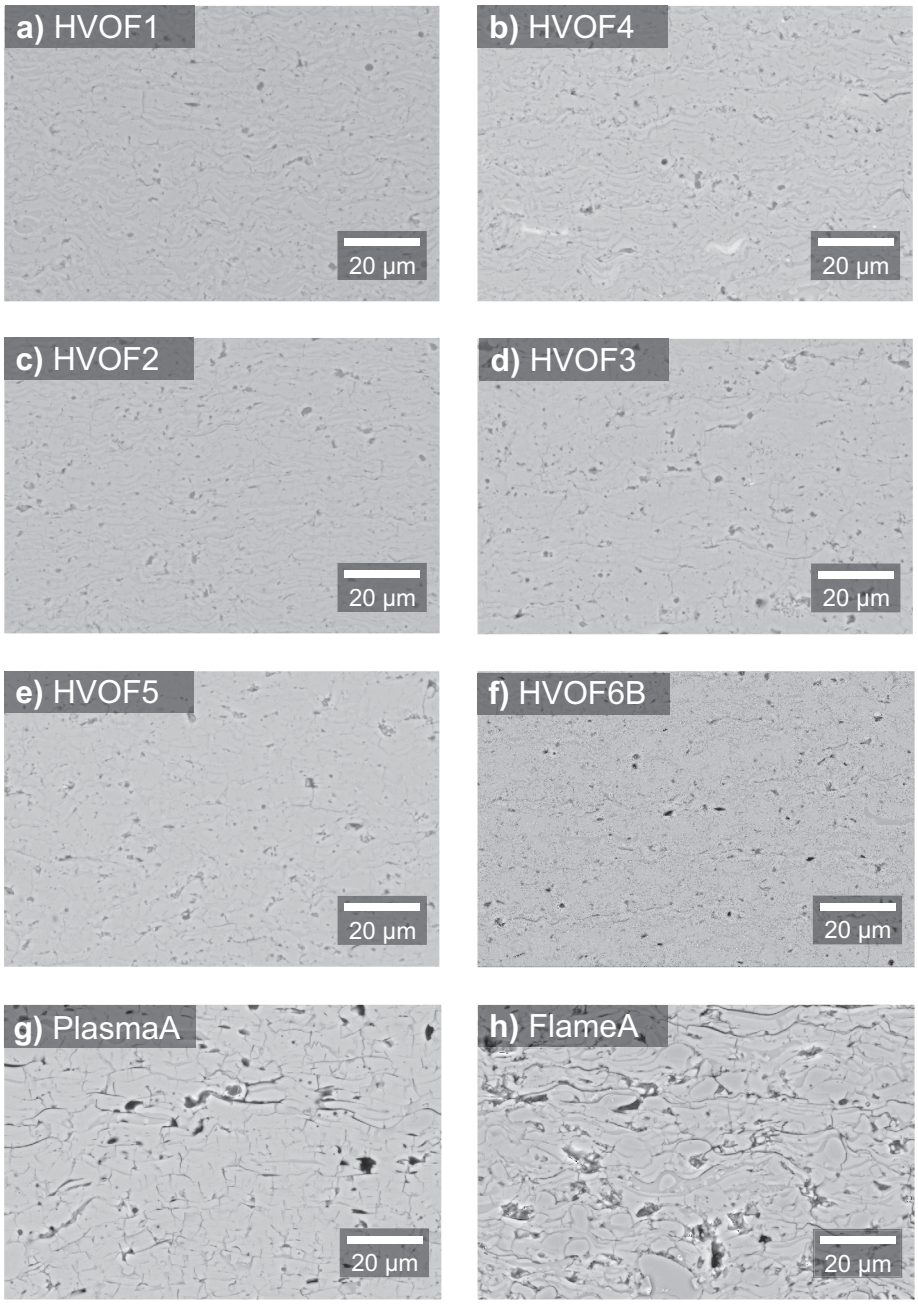

Figure 5.2: The SEM/BSE cross-sectional figures of thermally sprayed spinel coatings (a–b) and alumina coatings (c–h) at the 1000× magnification. Black image regions correspond to void type imperfections, while in general the light gray regions indicate crystalline material and slightly darker gray correspond to amorphous regions. h) Unmelted regions can be seen mainly for rod flame sprayed alumina coating. [P5, P4, P7, P8]

and Figure 5.2. For HVOF10 and HVOF12, these cracks have been found to decrease the breakdown strengths but similar decrease cannot be seen in the DC resistivity [P6]. However, for the alumina coating HVOF3 high gas permeability and high amount of vertical cracks are most probably reasons for the lower DC resistivity in comparison to that of alumina coating (HVOF2) [P5]. HVOF2 and HVOF3 were deposited of otherwise similar powder but the powder particle size of HVOF2 was lower (2–10 µm) than that of HVOF3 (5–25 µm) [P5].

It was also noticed in [P5] that utilizing smaller particle size can cause thinner lamellae in a coating which can further cause higher DC resistivity of HVOF2. Similar observation was also made for the studied spinel coatings (HVOF1 & HVOF4) although the coatings were deposited from different $MgAl_2O_4$ powders [P5]. However, the difference in the DC resistivity is smaller in the spinel coatings than in the alumina coatings, which emphasizes the fact that several microstructural features together affect the DC resistivity. Thus, it is difficult to distinguish exactly the effect of one feature or parameter, particularly, because it is often impossible to change only one property of a coating.

The studies in [P5] showed that the thicknesses of crystalline and amorphous lamellae have some effect on the DC resistivity. In order to study this more, a detailed analysis of the lamellar morphologies was done for one test series (HVOF7–HVOF12) [P6]. The idea of the test series (HVOF7–12) was to vary the amount of MgO (0%–65%) and keep the other parameters the same. The analysis was done by converting the SEM/BSE images into binary pixel matrices corresponding to the crystalline and amorphous areas, see Figure 4.8. Additionally, Figure 4.8 presents the calculated crystalline domain sizes of the coatings. While HVOF9 (25% MgO) and HVOF12 (65% MgO) were found to exhibit slightly more compact amorphous–crystalline regions, the overall differences remained small and showed no clear correlation with the MgO-content or DC resistivity at the studied low electric fields.

The rod flame sprayed coatings have remarkably lower resistivity than HVOF and APS coatings which can be linked to their different microstructures. Due to the lower particle velocities in rod flame spraying, the microstructure of rod flame sprayed alumina coating differs from HVOF and APS sprayed alumina coatings, see Figure 5.2 [P8]. Furthermore, the flame sprayed alumina coating, FlameA, has slightly higher porosity than the HVOF and APS alumina coatings, see Table 3.1. Similar trend can be seen for the spinel coatings since the flame sprayed spinel coating, FlameB, has the highest gas permeability in comparison to HVOF (HVOF13) and APS coatings (PlasmaB) (Table 3.1) [P2].

5.1.2 Effect of temperature and humidity

The effect of temperature and humidity on the DC resistivity was studied for HVOF, APS and rod flame sprayed sprayed Al_2O_3 and $MgAl_2O_4$ coatings [P2, P8]. The temperature range was 20–60 °C while the relative humidity was varied from 20% to 90%. The studied alumina coatings were HVOF6B, PlasmaA and FlameA [P8] and the spinel coatings

were HVOF13, PlasmaB and FlameB [P2]. In order to stabilize the coating to the measurement condition, the samples were kept for three hours in the climate room before the measurements. Since the coatings have non-ohmic conductivity starting from quite low electric fields, the resistivity was measured as a function of electric field (0.1–2.5 V/µm).

Figure 5.3 presents the DC resistivity of the Al_2O_3 and $MgAl_2O_4$ coatings as a function of electric field at the studied ambient conditions. In addition, Table 5.1 shows the DC resistivities at the electric field of 0.3 V/µm. It can be noted that at 20 °C/RH 20% the resistivities of all the coatings are at quite similar level ($\sim 1 \times 10^{12}\,\Omega\,\mathrm{m}$) at the lowest electric fields. However, at higher humidities and temperatures more differences can be seen, in particular, for the alumina coatings.

At 20 °C/RH 20%, the resistivities may be analyzed to be ohmic at the lowest electric fields. Roughly above the electric field of 0.5 V/µm, non-linear conductivity can be generally observed for all coating types, except for flame sprayed coatings, which showed non-linear behavior throughout the measurement range. Interestingly, the non-ohmic behavior cannot be seen for the flame sprayed alumina (FlameA) when the temperature and humidity increased above 20 °C/RH 20%. For HVOF and APS alumina coatings (HVOF6B and PlasmaA), the non-ohmic conductivity can be seen at 20 °C/RH 45% and 40 °C/RH 20% but not at higher temperatures or humidities. The conductivity caused by observed moisture most probably overruns the non-ohmic behavior of the alumina coatings at high absolute humidities. For the spinel coatings above-mentioned behavior cannot be seen. The resistivities of HVOF and APS $MgAl_2O_4$ coatings are decreasing with increasing temperature and humidity but at least some non-ohmic behavior can be noted in all results. However, flame sprayed $MgAl_2O_4$ coating exhibits similar behavior with alumina coatings at the highest absolute humidities but the resistivities are at higher

Table 5.1: DC resistivity of the alumina and spinel coatings at different ambient conditions at electric field of 0.3 V/µm. [P2, P8]

		HVOF6B	HVOF13	PlasmaA	PlasmaB	FlameA	FlameB
T (°C)	RH (%)	ρ ($\Omega\,\mathrm{m}$)	ρ ($\Omega\,\mathrm{m}$)	ρ ($\Omega\,\mathrm{m}$)	ρ ($\Omega\,\mathrm{m}$)	ρ ($\Omega\,\mathrm{m}$)	ρ ($\Omega\,\mathrm{m}$)
20	20	1.3×10^{12}	2.0×10^{12}	2.3×10^{12}	4.3×10^{12}	5.3×10^{11}	6.2×10^{11}
20	45	3.2×10^{10}	1.0×10^{12}	2.4×10^{10}	1.7×10^{12}	2.9×10^{7}	2.5×10^{11}
20	70	5.9×10^{9}		1.1×10^{8}		8.2×10^{6}	
20	90	1.8×10^{7}		1.2×10^{7}		5.6×10^{6}	
40	20	2.4×10^{10}	6.8×10^{11}	2.1×10^{10}	1.3×10^{12}	4.9×10^{8}	1.2×10^{11}
40	45	5.8×10^{7}	1.6×10^{11}	4.3×10^{7}	2.0×10^{11}	5.6×10^{6}	2.3×10^{9}
40	70	1.7×10^{7}		1.3×10^{7}		5.4×10^{6}	
60	20	1.0×10^{9}	1.9×10^{11}	7.1×10^{8}	3.2×10^{11}	1.9×10^{8}	5.6×10^{9}
60	45	4.1×10^{7}	1.5×10^{10}	3.8×10^{7}	1.0×10^{10}	5.0×10^{6}	1.1×10^{8}
60	70	5.9×10^{6}		6.0×10^{6}		3.5×10^{6}	

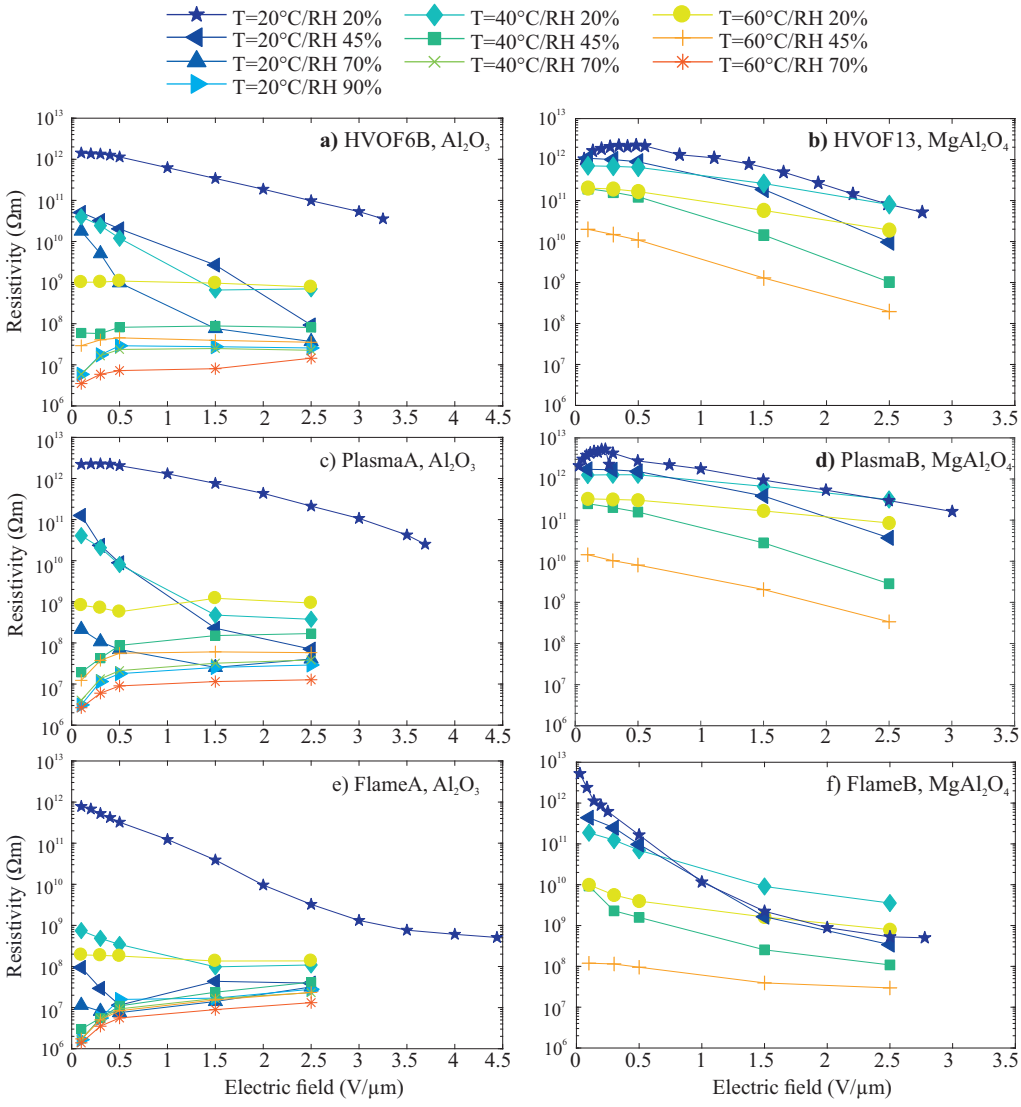

Figure 5.3: DC resistivity of the HVOF, plasma and rod flame sprayed Al_2O_3 [P8] and $MgAl_2O_4$ [P2] coatings as a function of electric field at different ambient conditions. Y-axis is logarithmic.

level than flame sprayed alumina coating.

When the temperature or humidity was increased above 20 °C/RH 20%, the resistivities of the alumina coatings decreased more than those of spinel coatings, see Figure 5.3. This observation is well in line with literature since according to Toma *et al.*[23], the HVOF and plasma sprayed spinel coatings exhibit higher resistivities at RH 30% and RH 95% in comparison to the alumina coatings. It can be speculated that the alumina together with water may form to aluminum hydroxide which can have a decreasing effect on the resistivity [P8].

Increasing the relative humidity from 20% to 90% decreased the DC resistivity of the alumina coatings five orders of magnitude at 0.3 V/µm, see Table 5.1 [P8]. Similar decrease can be seen for HVOF sprayed Al_2O_3–MgO coatings (HVOF7–HVOF12) [P6] but the DC resistivities of the Al_2O_3-MgO coatings (HVOF7–HVOF12) were at a higher level at 20 °C/RH 20% than the resistivities of Al_2O_3 coatings (HVOF6B, PlasmaA and FlameA), see Figure 5.1 [P6, P8]. Toma *et al.* made similar observation in [23] when increasing the relative humidity from 30% to 95% decreased the DC resistivity of HVOF sprayed alumina coating from $1 \times 10^{11}\,\Omega\,\mathrm{m}$ to $3 \times 10^{5}\,\Omega\,\mathrm{m}$ but for HVOF spinel coating the decrease was from $2.6 \times 10^{11}\,\Omega\,\mathrm{m}$ to $5.6 \times 10^{5}\,\Omega\,\mathrm{m}$. For the plasma sprayed (APS) alumina coating the decrease was from $3 \times 10^{11}\,\Omega\,\mathrm{m}$ to $2 \times 10^{4}\,\Omega\,\mathrm{m}$ while for APS spinel coating the decrease was lower being from $3.6 \times 10^{11}\,\Omega\,\mathrm{m}$ to $3.2 \times 10^{5}\,\Omega\,\mathrm{m}$ [23]. Luth *et al.* [11] noted also that the DC resistivity of HVOF sprayed alumina and spinel coatings decreased with increasing humidity (RH 43% to RH 75%) but the decrease was approximately 0.5–1 order of magnitude. However, at RH 43% the DC resistivities were significantly lower than in here (approx. $1 \times 10^{6}\,\Omega\,\mathrm{m}$ for alumina coating and 1.5×10^{5}–$1 \times 10^{7}\,\Omega\,\mathrm{m}$ for spinel coating)[11].

Porosity partly affects the DC resistivity since the highest porosity alumina and spinel coatings (FlameA & FlameB) exhibit the lowest resistivities at all conditions while HVOF coatings (HVOF6B & HVOF13) exhibit the highest resistivities and correspondingly the lowest porosities. Plasma sprayed coatings (PlasmaA & PlasmaB) have slightly lower resistivity and higher porosity than HVOF coatings. Pawlowski [28] noticed that the most porous plasma sprayed alumina coating exhibited the lowest DC resistivity which is well in line with the results of alumina coatings (HVOF6B, PlasmaA & FlameA). However, the high porosity (as indicated by relatively high gas permeability) did not affect the DC resistivity of HVOF coatings (HVOF7–12) although the humidity increased from 20% to 90% [P6]. It may be concluded that high porosity of a coating does not automatically decrease the DC resistivity.

As it was discussed in [23] and as the resistivity results indicate, the thermally sprayed alumina and spinel coatings exhibit sensitivity to moisture absorption due to the nature of the coating, the microstructure, and the phase composition of alumina coatings. However, as indicated by the above analysis, it is very difficult to clearly distinguish between the exact effects of any individual microstructural or other detail on the resistivity with increasing humidity. Due to this, only above-mentioned speculations

can be made. However, all the coatings can absorb notable amount of moisture which can significantly decrease the resistivity. The alumina coatings are stabilizing to the range of 1×10^7–$1 \times 10^8\,\Omega\,\mathrm{m}$ at high humidity and the resistivity seems to turn from originally field dependent behavior to linear behavior [P8]. Interestingly, the spinel coatings are in the range of 1×10^8–$1 \times 10^{10}\,\Omega\,\mathrm{m}$ even at the highest absolute humidities and the resistivity is still non-linear, except for rod flame sprayed coating [P2]. Thus, it can be concluded that in comparison to alumina coating spinel coating is more resistant to the resistivity decrease at humid conditions.

5.2 DC conductivity of alumina and spinel coatings at high electric fields

The low field DC resistivity measurements presented in Sub-chapter 5.1 were performed with utilizing Keithley electrometer. However, the maximum voltage of the power supply in Keithley electrometer is 1 kV limiting the measuring field to ∼5 V/µm for typical coating samples. In order to measure the DC conduction behavior at higher fields, a new measurement setup was developed in [P4] enabling resistivity measurements during the step-wisely breakdown tests.

5.2.1 General behavior of DC conduction currents

In [P4], the conduction current of HVOF sprayed alumina coating (HVOF5) was measured when the voltage was increased step-wisely until a breakdown with two different step durations and voltages (250 V/6 min & 500 V/60 min). In [P7], the same measurement setup was utilized to perform conduction current studies for several different coating types (HVOF5, HVOF6B, PlasmaA, HVOF7–9 & HVOF11) with one step duration and voltage (250 V/10 min).

Figure 5.4a) presents the measured currents of the HVOF alumina coating (HVOF5) as a function of time when the test was started at the voltage of 4000 V with a step voltage of 500 V and a step duration of 60 min [P4]. In this test, three parallel samples of HVOF5 were tested (L2, L3 and L5). The conduction behavior of the samples L2 and L5 are very similar since the conduction currents stabilize during the last full steps, 4.5 kV and 5.0 kV, respectively. The conduction currents are stable until the current start to increase just two minutes before the breakdown indicating some degradation (for L2 U_b=5.0 kV and for L5 U_b=5.5 kV). The conduction current of L3 starts to slightly increase already in the middle of the first voltage step (4 kV) and the increase continued at the second voltage step (4.5 kV). This behavior indicates that a material degradation process starts already at the first voltage step (4.0 kV). Before the final breakdown, the current of L3 increases similarly as the currents of the two other samples.

Figure 5.4b) presents the current data from the 250 V/6 min test performed for five parallel samples of HVOF5 (S1–S5) [P4]. During the first step (∼1 V/µm), the currents

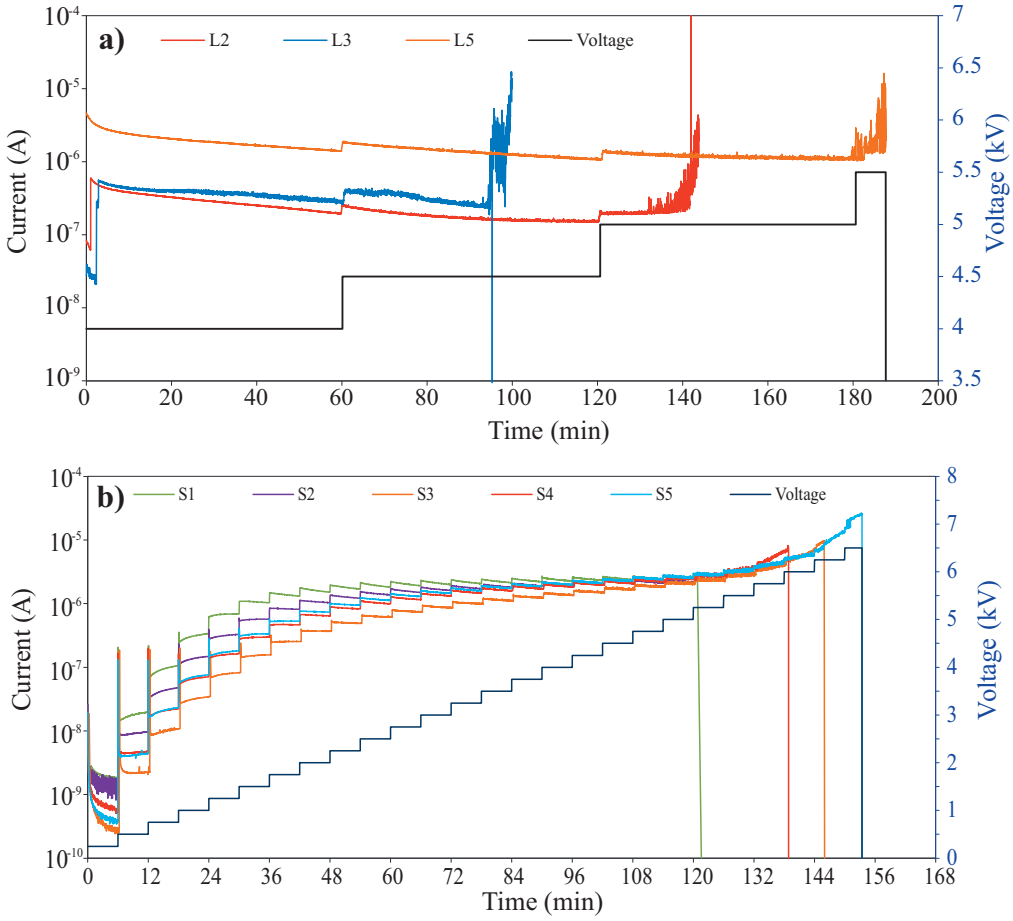

Figure 5.4: **a)** Measured DC current of three HVOF alumina coating samples (HVOF5) as well as the step-by-step voltage as a function of time when the step duration was 60 min and a step voltage of 500 V. The test was started at the voltage of 4 kV. **b)** Measured DC currents of five HVOF5 samples as a function of time in 6 min/250 V step tests when the test was started at voltage of 250 V.

stabilized quite well by the end of the measurement period although the values vary to some extent. At the second step (∼2 V/µm), the currents of samples S3 and S4 stabilize while the currents of the other samples start to gradually increase with time. At the higher voltage levels, all the currents do not stabilize during the measurement periods indicating that the material is in the non-ohmic conduction region. When the applied field is 8–12 V/µm (1750–2750 V), the currents of parallel samples stabilize at quite similar level. At 25 V/µm (5500 V), the currents of samples S3-S5 start to gradually increase indicating some degradation of the material. The degradation process cannot be seen for samples S1 and S2 since they broke down suddenly at this voltage level. Actually, these two samples had higher current levels than the other samples during the whole test duration.

In [P7], the DC conduction currents of several different HVOF coatings (HVOF5, HVO6B, HVOF7–9 & HVOF11) and APS alumina coating (PlasmaA) were studied in 250 V/10 min steps. Figure 5.5a)–g) presents the measured currents for each sample of these coatings as a function of time when the voltage was increased step-wisely until a breakdown. In addition, the breakdown strengths defined from these measurements are presented in Figure 5.5h). It can be noticed that the coatings exhibit strong non-linear voltage–current relationship and a quite large deviation in breakdown results as well as in the conduction currents between the parallel samples. It can be observed from Figure 5.5 that the coatings exhibit a "transition-field" region where highly non-ohmic conductivity is increasing to a new current level until breakdown occurs which is well in line with the measurements made with the steps of 250 V/6 min & 500 V/60 min for HVOF5 in [P4], see Figure 5.4.

In [P7], the focus was to compare the DC conductivities of the different coating materials in a more general sense rather than to determine the DC conductivity of only one type of coating material in detail using a very large number of parallel samples. The conduction current behaviors of the HVOF coatings sprayed using commercial alumina powders (HVOF5 and HVOF6B) are quite similar although the absolute current values differ. In addition, it can be noted that one of the samples of HVOF5 coating differs significantly from the other four samples. The conductivity of plasma sprayed alumina (PlasmaA) is generally at a similar level with the alumina coating HVOF6B. However, in "the transition field" region with non-ohmic conduction the current of plasma coating changes more rapidly than the currents of HVOF coatings. The conduction current behavior of HVOF7 and HVOF8 is very similar which is understandable due to the similar amounts of MgO (HVOF7 0%, HVOF8 10%) added in the same Al_2O_3 powder. The conductivity of HVOF9 (25% MgO) is very similar with alumina HVOF5 although the actual current level of HVOF9 is lower than the current of HVOF5. Three of five parallel samples of HVOF11 (50% MgO) did not break down until the maximum voltage of the power supply was reached. In addition, the current levels of those three samples were significantly lower than the currents of the samples which broke down. Although there are clear general differences between the materials, the typical current levels just prior the breakdown events were approximately at a level of $\sim 1 \times 10^6$ A for all the coatings.

5.2.2 High field DC resistivity of coating

From the step wisely increased voltage and current data, an estimation of DC resistivity can be made at higher electric fields [P4]. It is considered as estimation because the DC current did not fully stabilize during the 6 min measurement periods [P4]. However, the estimations are rather good (i.e. currents were close to the stabilized levels). The resistivities were defined at the end of each voltage step.

The DC resistivity of HVOF sprayed alumina coating (HVOF5) as a function of electric field is presented in Figure 5.6 where it can be seen that the resistivity can be divided

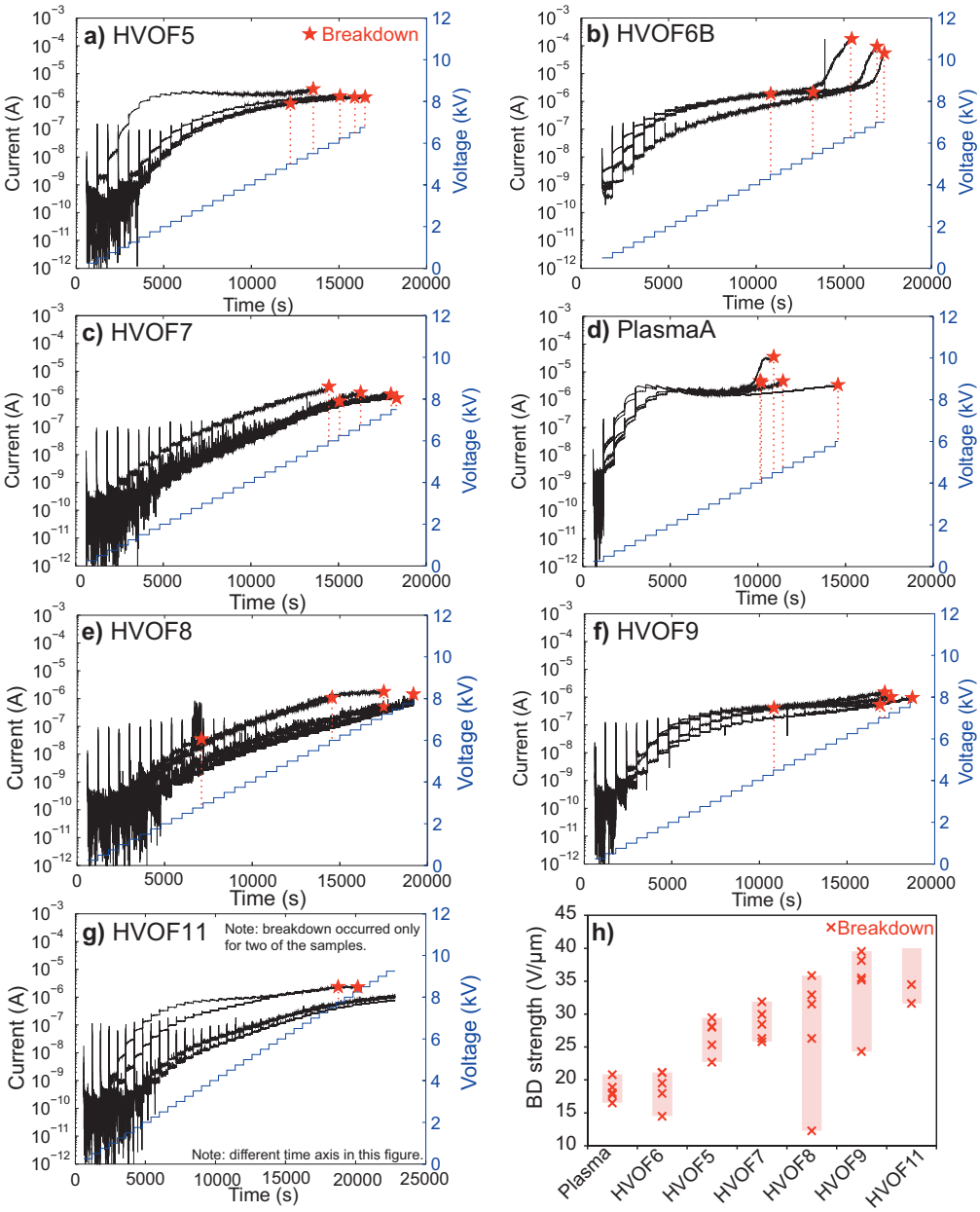

Figure 5.5: **a–g)** The measured DC currents of the studied materials as a function of time. The start voltage was 250 V which corresponds the electric field of ∼1 V/µm. The red stars and the dashed lines indicate the occurrence of a breakdown (current and voltage, respectively). It should be underlined that breakdown occurred only for two out of five samples for HVOF11 since the maximum voltage level of power supply was reached. **h)** The breakdown strengths of the studied coatings where the cross presents the individual breakdown event and the bar indicates the deviation between the minimum and maximum breakdown fields. For HVOF11, the upper limit of the bar presents the maximum electric field reached for the samples which did not break down during the tests. [P7]

in four operating regions. Below 0.5 V/µm, the resistivity is ohmic being $\sim 1 \times 10^{12}\,\Omega\,\mathrm{m}$. From 0.5 V/µm to 8–12 V/µm, the resistivity is non-ohmic and decreases approximately three decades reaching a new level. From 8–12 V/µm to 25 V/µm, the resistivity is again ohmic being $\sim 1 \times 10^{9}\,\Omega\,\mathrm{m}$ (except one sample, S3). The resistivity of the other HVOF alumina coating (HVOF6B) is quite similar. However, the actual resistivity values of HVOF6B are approximately one order of magnitude lower than the resistivity of HVOF5 and the transition electric fields of HVOF6B are slightly lower in comparison to the fields of HVOF5. According to Luth *et al.* [11], the resistivity of a ceramic coating needs to higher than $1 \times 10^{8}\,\Omega\,\mathrm{m}$ in power electronic applications, and thus the resistivity obtained in here is still at a suitable level. When the applied field is close to the breakdown field, the resistivity starts to slightly decrease. This decrease indicates an initiation of degradation/pre-breakdown process starting for HVOF5 approximately from 25 V/µm and for HVOF6B from 19 V/µm.

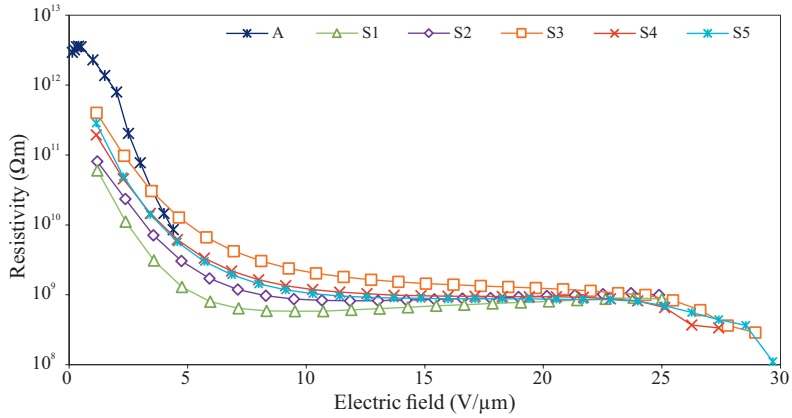

Figure 5.6: DC resistivity of HVOF alumina coating (HVOF5) as a function of electric field. The resistivity of sample A was measured by utilizing Keithley electrometer (U_{max}=1 kV) and the resistivity of samples S1–5 was measured by utilizing the high field measurement setup developed in this thesis. [P4]

5.2.3 Analysis of the conduction currents versus electric field

In order to evaluate the conduction processes of the coatings in detail, the current densities of the coatings (HVOF5, HVO6B, PlasmaA, HVOF7–9 & HVOF11) were determined as a function of applied electric field [P7]. Although the steady–state current level was not fully reached at each applied voltage level (this can be particularly seen in the "transition field" region, see Figure 5.5), the current densities of the materials were defined from the mean values of the current at the end of each voltage step (550–580 s). It should be emphasized that in "the transition fields" the defined current densities do not thus represent DC conductivity implicitly. Figure 5.7 presents the defined current densities of five parallel samples of each coating as a function of the applied electric field. In addition,

the mean current densities of the five parallel samples are presented. However, for HVOF5 the mean current density was defined only from four samples because one of the five samples exhibited totally different conduction behavior and are thus excluded from the analysis.

As it can be noticed from Figure 5.7, the current densities measured using the low (L1)

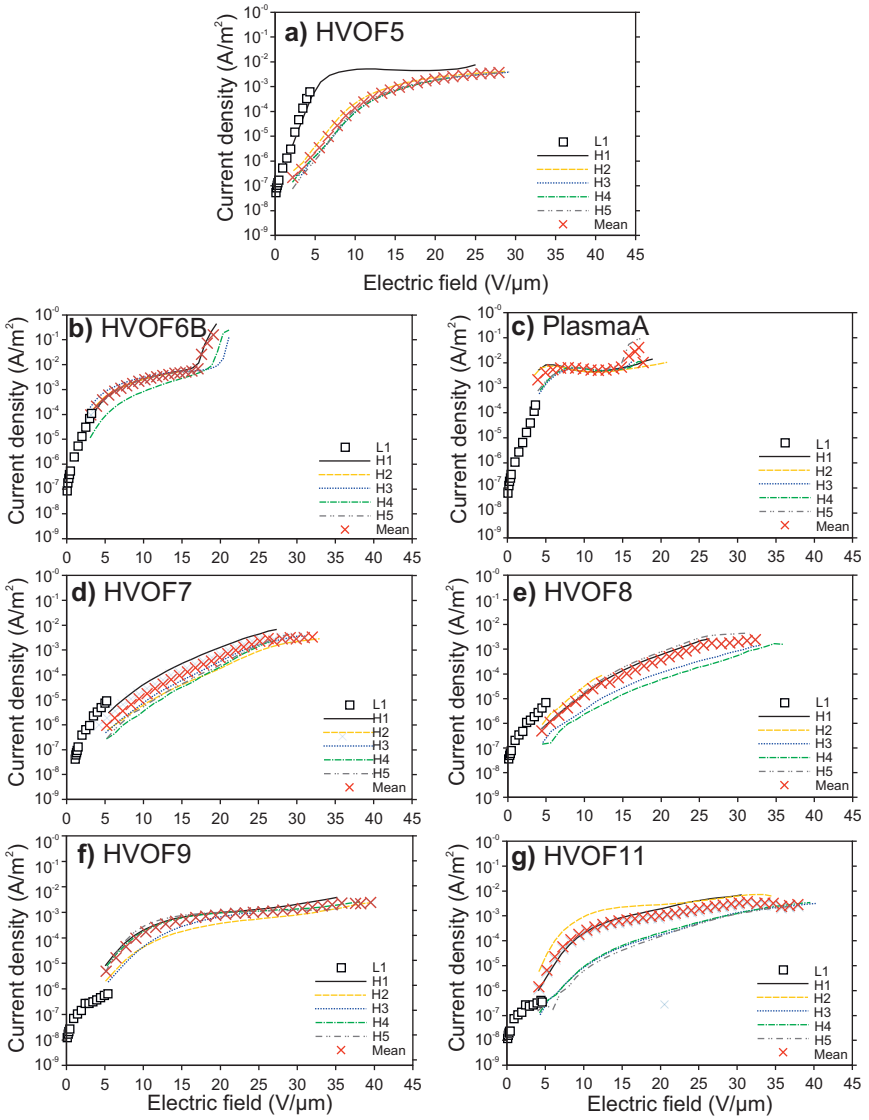

Figure 5.7: DC conduction currents as a function of the applied electric field. The squares (L1) present the currents measured using Keithley electrometer and the lines (H1–H5) present the conduction currents recorded using the measurement setup developed above 1 kV voltages. The crosses present the mean current densities defined from the five parallel conductivity measurements made until a breakdown, except for HVOF5 the mean current density is defined from four parallel measurements. [P7]

and high (H1–H5) field measurement setups differed to some extent. This most probably occurs since the sensitivity of the high field measurement setup was insufficient at the lowest test fields (see the high noise in the lowest test voltages in Figure 5.5). Separate samples were utilized at low and high field measurements. Quite large deviation between the parallel samples (H1–H5) can be seen which can further explain the difference. As it was discussed previously, the materials are also in a "transition field" region with non-ohmic conduction when the results from the high and low field setup overlap. In this region, the currents did not fully reach the steady-state level during the test period of 10 min, and thus the defined values give only an estimation for DC conductivity.

In order to further study the differences between the materials, the experimental data was plotted as log (J) versus log (E) where approximately straight lines with different slopes at different regions of field strengths may be obtained. Least-square technique was utilized to define the best fits for the conduction currents, and thus to define the slopes for each region. Table 5.2 presents the defined slopes of the mean current densities in different regions and the estimated transition electric fields between the different regions.

At the low field levels (Region 1), all the studied coatings are obviously ohmic because the defined slopes are close to unity indicating that electric field/voltage is directly proportional to the current. The estimated transition field to non-ohmic region varies between the materials. The lowest transition field (∼0.5 V/µm) is noticed for the alumina coatings HVOF6B and Plasma. Slightly higher transition field (1 V/µm) can be observed for the other commercial powder deposited HVOF sprayed alumina (HVOF5) but the highest transition field of the alumina coatings (2 V/µm) is obtained for alumina coating, HVOF7, deposited from experimental powder. The transition field of HVOF8 is the same as it is for HVOF7 probably due to the almost similar powder composition (10% MgO versus 0% MgO). The highest transition field (4 V/µm) is noted for the coatings with higher amount of MgO which are HVOF9 (25% MgO) and HVOF11 (50% MgO).

In the next region (Region 2), the conductivities of the coatings are highly non-ohmic since the defined slopes vary from 2.8 to 6.2. In this "transition field" region the currents

Table 5.2: The estimated transition electric fields and the corresponding slopes, m, of the mean current densities (log–log scale) for the studied materials. [P7]

Sample	Region 1		Region 2		Region 3		Region 4	
	E (V/µm)	m	E (V/µm)	m	E (V/µm)	m	E (V/µm)	m
HVOF5	0–1.0	1.1	1.0–16.6	5.7	16.6–28	2.2	–	–
HVOF6B	0–0.5	1.1	0.5–8.6	3.4	8.6–17.1	1.8	17.1–	21.7
HVOF7	0–2.9	1.2	2.0–10.5	2.8	10.5–24.1	5.3	24.1–	1.3
PlasmaA	0–0.5	1.0	0.5–5.9	4.3	5.9–13.9	-0.3	13.9–	12.2
HVOF8	0–2.0	1.1	2.0–7.8	2.8	7.8–26.6	4.9	26.6–	2.6
HVOF9	0–3.9	1.2	3.9–10.3	4.5	10.3–37.6	1.6	–	–
HVOF11	0–4.1	1.1	4.1–9.4	6.2	9.4–26.1	2.1	26.1–	1.1

did not fully stabilize during the DC step–stress periods (10 min), instead they were still increasing at the end of the periods. Thus, the real levels of stabilized DC current would have been slightly higher than the reported values and the above-mentioned slopes would have been correspondingly higher as well. All in all, it can be concluded that a considerable transition from a ohmic conduction state to another state occurs in this region. The transition field of HVOF coatings from Region 2 to Region 3 is ∼10 V/µm. However, the transition field of HVOF5 is higher (17 V/µm) but in the 250 V/6 min tests the transition is lower (10.5 V/µm) [P4]. This indicates that the conductivities of the parallel samples of a coating material deviate notably. The lowest transition field is noted for plasma sprayed alumina coating (5.9 V/µm). The differences in conductivities and breakdown strengths between HVOF and APS coatings may be linked to their different microstructure caused by the different spraying temperatures and powder particle velocities in the spray processes.

In Region 3, the defined slopes are approximately two indicating that the current density is proportional to the square of the electric field. However, HVOF7 and HVOF8 exhibit similar but clearly higher slopes (∼5) than the other HVOF coatings, and thus these two coatings exhibit similar behavior as the other coatings in the previous region. In addition, the conductivity of PlasmaA differs from that of the HVOF coatings because PlasmaA reaches an ohmic level in this region. However, this may be noticed only by visual evaluation because the obtained slope has negative value due to differences between the parallel current density values of PlasmaA.

Breakdowns occurred for the alumina coating (HVOF5) and the spinel coating (HVOF9) in Region 3 but for the rest of the materials the breakdowns occur in Region 4. Although a rapid current increase before the breakdown was observed for the alumina coating HVOF5 in Figure 5.4 [P4], no such increase in the conduction current is observed for HVOF5 when step duration was 10 min instead of 6 min. However, a similar rapid current increase can be seen for some of the samples of the alumina coatings (HVOF6B & PlasmaA) since the obtained slopes in Region 4 are very high, see Figures 5.5 and 5.7.

Throughout the tests, the conduction behavior of the coating HVOF8 (10% MgO) is very similar to the alumina HVOF7 (0% MgO) but in Region 4 the conductivity of HVOF7 is ohmic (slope ∼1) while the conductivity of HVOF8 is equal to the square of electric field (slope ∼2). Thus, it may be concluded that adding 10% MgO to the Al_2O_3 has only effect when the applied electric field is above 25 V/µm. The conduction behavior of the other two spinel coatings (HVOF9, 25% MgO and HVOF11, 50% MgO) is very similar throughout Regions 1–3. However, a breakdown occurred for HVOF9 in Region 3 while the breakdowns of HVOF11 occurred in Region 4 where HVOF11 exhibits ohmic conduction behavior (slope ∼1). Thus, it seems that the amount of MgO (25 or 50%) has influence on the conduction behavior only when the field is above ∼26 V/µm.

5.2.4 Material degradation during the conduction current measurements

Since it may be considered that the presented non-linear conductivity ranges are actually representing irreversible material degradation processes, this aspect was further studied. In [P1], the DC resistivity of HVOF sprayed $MgAl_2O_4$ coating (HVOF13) decreased remarkably when the resistivity measurements with varying electric field (0.1 to 3 V/µm) was repeated. Thus, in [P7] the conductivity measurements performed with the 1 kV test setup were repeated for some of the coating types (two alumina coatings: HVOF5 and HVOF7, and one spinel coating: HVOF11) in order to identify possible permanent changes at low electric fields. The selected coatings represent the conduction behavior of the coatings in a general manner.

Figure 5.8 presents the original DC conduction currents of the aforementioned coatings as a function of electric field together with the results of repeated measurements made later on. The time between the measurements was several months and during that time the samples were kept in a desiccator at room temperature/low relative humidity to avoid ageing. Already at low electric fields some permanent changes can be seen occurring for the alumina coating (HVOF7), which was deposited from the experimental powder, since the conductivity increases remarkably during the second measurement period. The conductivity of the alumina coating (HVOF5) made from commercial powder also increased slightly during the second measurement time but the difference is not so significant. No permanent changes occurred for the spinel coating (HVOF11).

Because these permanent changes occur already at very low electric fields, it is evident that it is not meaningful to perform conduction mechanism analysis for all the studied materials. In order to carry out the conduction mechanism study for HVOF5 and

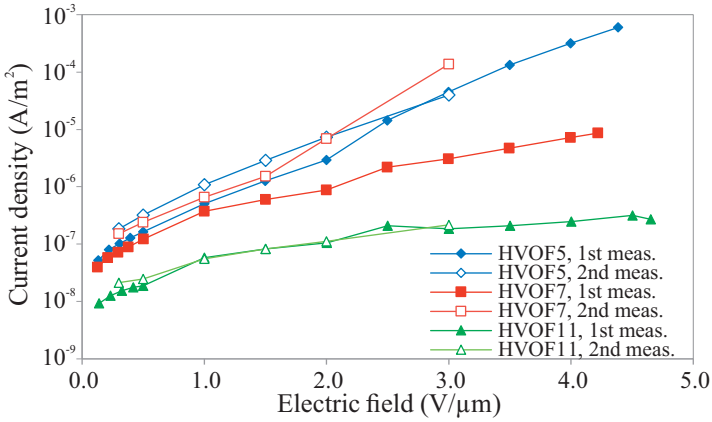

Figure 5.8: DC conduction currents as a function of electric field for two alumina coatings (HVOF5 & HVOF7) and one spinel coatings (HVOF11). The data of 1st measurement is the same as it has been shown in Figure 5.7. [P7]

HVOF11, the conductivity measurements were also repeated at high fields to ensure that no permanent changes/degradation occur in the materials. Three more samples of alumina HVOF5 were prepared and conductivity measurements were made for these samples with steps of 500 V/10 min until the voltage level of 3500 V was reached. The voltage corresponds to the electric field of ∼15 V/µm which is approximately half of the short-term breakdown strength of the HVOF5. The measurements showed that no permanent changes occurred for the samples of HVOF5. The procedure of conductivity measurements for HVOF11 was similar but the measurements were performed until the voltage level of 5500 V was reached. This level corresponds to the field of ∼22 V/µm which is again roughly half of the breakdown strength of HVOF11. The measurements were performed for the samples that did not break down in the step tests with the steps of 250 V/10 min. These measurements indicate that the current densities are at similar levels when the measurements were repeated two or three times (500 V/10 min). Based on the results, it may be concluded that although some material degradation can take place at the studied field range, generally the conduction behaviors presented in this Chapter represent the stable and repeatable behavior of the coatings.

5.2.5 Conduction mechanism studies

In order to evaluate the dominant conduction mechanism of thermally sprayed ceramic coatings, the measured conductivity data are analyzed in accordance with several theoretical conduction mechanisms despite the fact that the steady-state current level was not reached at each voltage level, particularly in the "transition field" region. Because the possible dominating conduction mechanism of thermally sprayed ceramics is not so evident, all theoretical conduction mechanisms are discussed even though some of the mechanisms take place only at very high electric fields often for other materials such as polymers [94], and are thus not relevant to thermally sprayed ceramic coatings. The conduction mechanism study is only carried out for alumina coating HVOF5 and spinel coating HVOF11 since it was verified that no material degradation occurred in those and thus the measured conduction behavior can be considered stable.

Charge injection from electrodes can be described either by Schottky or Fowler-Nordheim injection mechanisms which both occur at very high fields for polymers, e.g. the latter takes places $\sim 1 \times 10^9\,\mathrm{V\,m^{-1}}$ and the former one occurs at slightly lower fields [94, 112]. Although thermally sprayed ceramic coatings exhibit significantly lower breakdown strengths than polymers, the Fowler-Nordheim plots ($\log(J/E^2)$ versus $1/E$) were made for HVOF5 and HVOF11 [98, 143]. The obtained plots indicate that Fowler-Nordheim tunneling can be excluded from the dominating conduction mechanism for the studied thermally sprayed ceramic coatings. The slopes differed clearly from those reported in [98, 143] where the Fowler-Nordheim tunneling occurred.

In the Schottky analysis, the measured data is plotted as $\ln(J)$ versus $E^{1/2}$ (Schottky plot) which should result in a straight line where the theoretical value of relative per-

mittivity can be evaluated. Thus, the comparison between the theoretical and measured high frequency permittivities can be made. For both coatings (HVOF5, HVOF11) the relative permittivities defined from the Schottky plot are ∼70% smaller than the measured permittivities at the frequency of 1 kHz, and thus the pure Schottky injection can also be excluded from the dominating conduction mechanism.

At high electric fields, one of the bulk-limited conduction mechanisms is Poole-Frenkel where the theoretical relative permittivity can be defined from the slope of the Schottky plot (ln (J) versus $E^{1/2}$). The physical base of Poole-Frenkel model is very simplified and the analysis must be done as an-order-of-magnitude calculation [94]. Although this consideration is made, the defined theoretical values are ∼95% smaller than the measured ones. Thus, it can be concluded that the Poole-Frenkel conduction mechanism is not the dominating one for the ceramic coatings.

Space charge limited current (SCLC) mechanism is one of the bulk limited conduction mechanisms and it describes how the conduction current behavior changes with the increasing applied electric field [94, 112]. In order to validate this mechanism, experimental J–E data can be plotted in a double logarithmic scale (see Figure 2.10) [94, 112]. According to this theory, at low field strengths (field below the transition field, E_{TR}) the voltage-current relation is ohmic [94, 112]. The current density is thus directly proportional to the voltage and the slope is unity in a plot of log (J)–log (E) [94, 112].

At higher fields (Region 2), the conduction is no longer ohmic because charge can inject from the electrode into the bulk and it has difficulties moving further through the material [94, 112]. When the applied field has reached the level of E_{TR} (see Figure 2.10), the space charge limited current dominates over the ohmic component [94, 112]. The current is thus proportional to the square of the electric field and the slope is two in a plot of log (J)–log (E) (Figure 2.10). When the applied field has reached the trap-filled limit field, E_{TFL}, all the traps in the dielectric are filled causing current to increase and correspondingly the slope increase, too. Theoretically, the slope increases from two to infinity (see Region 3 in Figure 2.10). At the fields above E_{TFL}, the trap-free space charge conduction might take place and the slope is two (Region 4 in Figure 2.10) if the breakdown have not already occurred before this region was reached [94].

It has been reported in [107, 111] that a bulk alumina ceramic follows the SCLC mechanism. However, the conductivities of alumina HVOF5 and spinel HVOF11 coatings do not fully follow the SCLC theory since after the initial ohmic region (Region 1 in Table 5.2) the conductivity is not proportional to the square of the electric field as indicated by the calculated slope of ∼6 (Table 5.2). After this region, the slope should be higher than two in accordance with the SCLC theory (Region 3 in Figure 2.10) but the slopes of coatings are ∼2. According to the SCLC theory, the slope should be two again in the last region (Region 4 in Figure 2.10) but the slope of HVOF11 is ∼1 in Region 4 indicating ohmic type of conduction behavior. It can be concluded that the studied thermally sprayed ceramic coatings either do not follow or follow only partly the SCLC theory unlike the sintered alumina [107, 111]. The difference in the conduction

behaviors of the bulk and the thermally sprayed alumina is most probably due to their different crystalline structures and microstructures. Bulk alumina exhibits fully crystalline structure while the thermally sprayed coatings have lamellar structure consisting of both amorphous and crystalline areas as well as voids and defects. Due to above-mentioned facts, the coatings most probably exhibit a variety of trap levels which partly explains the deviation of the performance from the ideal SCLC theory.

A thermally sprayed coating should be considered as an insulation system consisting of different regions which exhibit different dielectric properties. It is probable, that the amorphous regions probably have higher conductivity than the crystalline regions. The differences in conductivity and the resulting uneven field distribution together with the above-mentioned trap level distribution might be the reason why the coatings followed the SCLC theory only partly. Although there are many uncertainties, thermally sprayed coatings could follow the SCLC theory as follows:

- At low electric fields (Region 1), the conductivity is clearly ohmic. Since the amorphous regions most probably exhibit higher conductivity than the crystalline regions, the electric field concentrates on the crystalline regions. Thus, the conduction behavior of a coating is dominated by the conductivity of the crystalline regions.

- At higher electric fields, charges start to collect into the interfacial areas and traps forming space charge. When a certain transition electric field, E_{TR}, is reached, the space charge limited current dominates over the ohmic component in the crystalline-amorphous interfaces of a coating. Theoretically, the current density is proportional to the square of the electric field when there is only one trap depth in the material. In the coatings, the microstructure varies along the material and due to this the E_{TR} and the current density changes are not as ideal, instead the changes take place "smoothly".

- When the conductivity increases in the crystalline regions, this also changes/equalizes the electric field distribution between the crystalline and amorphous regions at the same time. Due to this, at first the current is limited and is increasing with a slope lower than two but after a while the electric field is more concentrated on the amorphous regions, and thus the current is increasing strongly with a slope higher than two. This can occur since the transition field (E_{TR}) of amorphous regions is expected to be lower than the transition field of the crystalline regions due to their different conductivities.

- After this transition field range where a new electric field distribution is formed for a coating by the SCLC currents of amorphous and crystalline regions, the current of a coating system is increasing with a slope of $\sim$2.

At higher test voltages prior to breakdowns, partial breakdowns of certain regions are suggested to occur. Just before breakdowns, a rapid current increase was measured

for certain coatings (HVOF6B, PlasmaA). This is most probably caused by partial breakdowns e.g. in the amorphous regions and/or at the interfaces between the splats which may take place because the trap filled limit (E_{TFL}) of that region is reached. According to the SCLC theory, a sudden fast current increase occurs, when the E_{TFL} is reached. However, this current increase should lead to the breakdown very rapidly (within a few seconds) [94]. As the current increase of the coatings did not occur as rapidly, it is suggested that the breakdown for some of the coatings proceeded partially, and this way the breakdown process was delayed.

5.3 Considerations and implications

HVOF sprayed alumina and spinel coatings exhibit the highest DC resistivity in comparison to the APS and rod flame coatings most probably due to the denser microstructures of HVOF coatings. However, the resistivity of the ceramic coatings is ohmic only at very low electric fields (typically below 1 V/µm) and at higher fields the resistivity has non-linear behavior unlike bulk ceramics. This unique conduction behavior of the coatings is due to a layered microstructure of ceramic coatings consisting crystalline and amorphous regions as well as voids and cracks. The layered microstructure results in uneven electric field distribution, and thus the coatings follow only partly SCLC conduction theory unlike the bulk alumina ceramics which are reported to follow SCLC theory fully in literature.

Temperature and particularly humidity affect the DC resistivity of thermally sprayed alumina and spinel coatings significantly. At high humidities (RH 90%), the resistivity of both coating materials decreased approximately five orders of magnitude in comparison to the results at low humidity (RH 20%). However, low humidities (RH 20% and RH 45%) have minor influence on the DC resistivity of spinel coatings with increasing temperature. It is proposed that the layered microstructure and hygroscopic nature of ceramic coatings can explain the major decrease in the resistivities with increasing humidity.

Chapter 6

Relative permittivity and dielectric loss

The third main dielectric property of an insulation material is relative permittivity and dielectric loss. This chapter presents the results and analysis of the relative permittivity and dielectric loss of the studied coatings as a function of frequency. The role of microstructure, the effect of ambient conditions and the electric field dependency on the relative permittivity and dielectric loss are discussed.

6.1 Relative permittivity and dielectric loss at low electric field

Figure 6.1 presents the relative permittivities and total loss contributions of the studied Al_2O_3, $MgAl_2O_4$ and Al_2O_3–MgO coatings as a function of frequency at 20 °C/RH 20%. The given permittivity values are the real parts of the complex permittivity, and thus includes only the real polarizability related component. As it is mentioned in Section 3.5, the permittivity results are presented without edge field corrections presented in IEC standard 60250 [133] since a guard ring was utilized around a measuring electrode during the measurements.

The real part of relative permittivity for HVOF and APS sprayed alumina and spinel coatings are at similar level (ε'_r=8–12) in the frequency range 50 Hz to 1 kHz, see Figure 6.1a–b. These obtained values of HVOF and APS coatings are quite similar with the values reported in literature [9, 28, 47, 64, 73, 85, 90], see Table 2.1. In addition, in the frequency range of 50 Hz to 1 kHz the relative permittivity of rod flame sprayed alumina, FlameA, is at very similar level to the APS alumina coating. However, the rod flame sprayed spinel coating, FlameB, exhibits remarkably higher permittivity in the whole frequency range, e.g. at 1 kHz the ε'_r of FlameB is 12.6 while it is in the range of 8.3–10.4 for the other coatings. At the lowest frequencies, the relative permittivities of all coatings are increasing quite strongly which may be due to the hypothesized interfacial polarization due to the coating microstructure with varying conductivities. Similar behavior is reported by Brown *et al.* [85] for the relative permittivity of plasma sprayed alumina coatings.

As it can be seen from Figure 6.1d–e, the total loss contributions of Al_2O_3 and $MgAl_2O_4$ coatings are quite similar in the highest frequencies (100–1000 Hz). At the

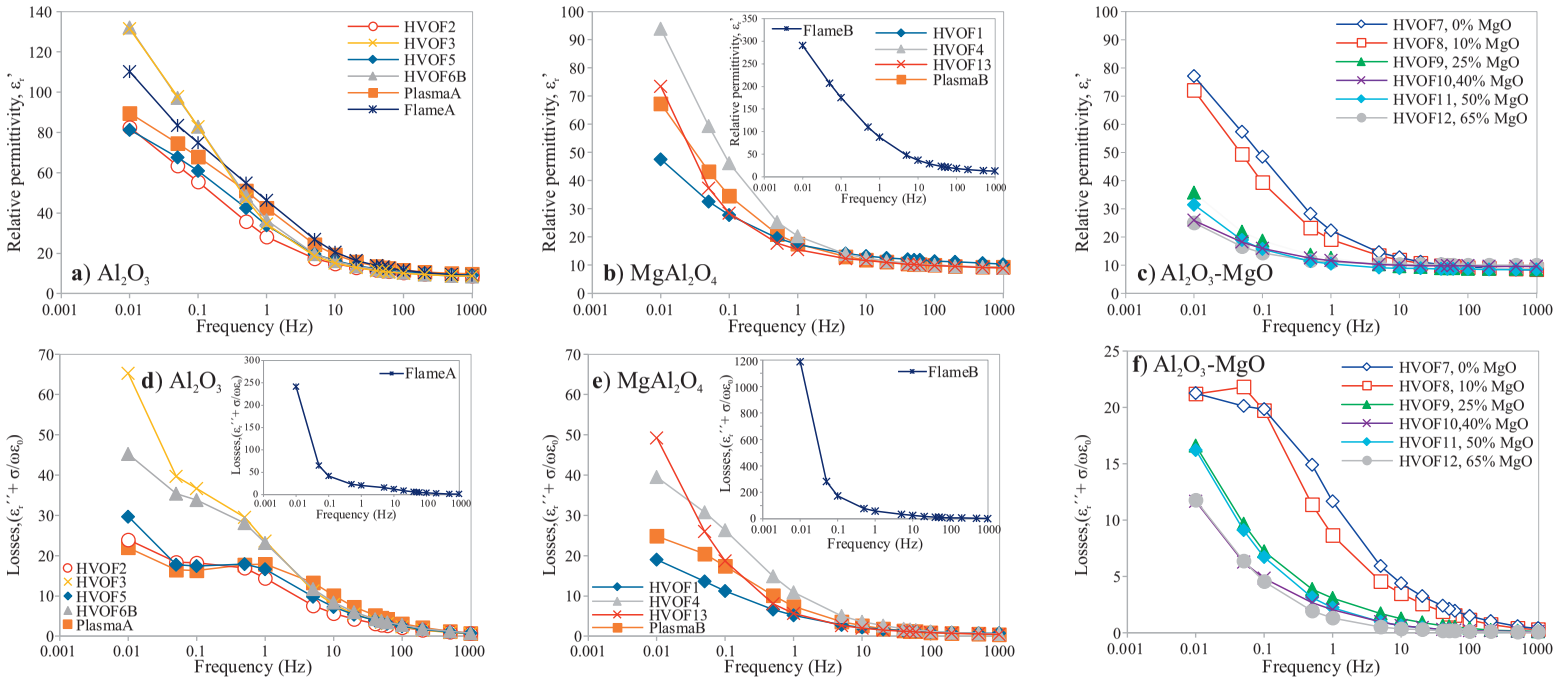

Figure 6.1: The real part of relative permittivity (indicated as $\mathrm{Re}\{\varepsilon_r*\}$), as a function of frequency at 20 °C/RH 20%: a) Al_2O_3 coatings [P4, P5, P8], b) $MgAl_2O_4$ coatings [P2, P5] and c) Al_2O_3–MgO coatings [P6]. The flame sprayed $MgAl_2O_4$ coating (FlameB) is placed in inset in order to distinguish the differences between the HVOF and the APS $MgAl_2O_4$ coatings better. The dielectric loss (indicated as $\mathrm{Im}\{\varepsilon_r*\}$) as a function of frequency at 20 °C/RH 20%: d) Al_2O_3 coatings [P4, P5, P8], e) $MgAl_2O_4$ coatings [P2, P5] and f) Al_2O_3–MgO coatings [P6]. The flame sprayed Al_2O_3 and $MgAl_2O_4$ coatings (FlameA and FlameB) are placed in inset in order to distinguish the differences between the HVOF and APS coatings better. Dielectric losses at 1 kHz and 1 Hz are also given in Table A.1. The measuring voltage was 200 V_{peak} which corresponds the electric field of 0.5–1V_{peak}/µm. However, the measuring electric field was 0.3V_{peak}/µm for the alumina coatings HVOF6B, PlasmaA and FlameA [P8].

lower frequencies, the loss increase rapidly which can indicate either DC conductivity or low-frequency dispersion (LFD) which is also called quasi-DC conduction [144–148]. According to literature [144–146, 149, 150], a pure DC conduction behavior requires that the real the part of the relative permittivity is constant during the whole frequency range while at the lowest frequencies the losses are increasing steeply in a double-logarithmic scale. Since the real part of relative permittivity of the coatings increases/disperses at the low frequencies, the observed behavior is related to LFD phenomenon. However, in a log-log plot the slopes of the real and imaginary parts of the relative permittivity differs to some extent, and thus the observed behavior is not purely following LFD theory either.

In general, the dielectric loss of HVOF and APS sprayed $MgAl_2O_4$ coatings are lower than the those of Al_2O_3 coatings in the frequency range of 0.5–1000 Hz. At the lowest frequencies (below 1 Hz), some minor material differences can be noticed between different coating materials since the loss contributions of the alumina coatings are not systematically always higher than the loss behavior of spinel coatings. The loss results of Al_2O_3 and $MgAl_2O_4$ coatings are in coherence with the DC resistivity results because the same coatings have high losses and low resistivities.

Although the relative permittivity of flame sprayed alumina coating, FlameA, is very similar to the APS and HVOF alumina coatings, the total loss contribution of FlameA differs to some extent from the other alumina coatings in the whole measuring frequency range but at the lowest frequencies the difference is significant. However, the total loss contribution of flame sprayed spinel coating, FlameB, differ even more from the loss of HVOF and APS sprayed spinel coatings, see Figure 6.1e. In addition, the loss of the spinel coating, FlameB, is significantly higher than the loss of the flame sprayed alumina coating, FlameA.

The lowest relative permittivities and loss levels are observed for the Al_2O_3–MgO coatings (HVOF7–12) which exhibited also the highest DC resistivities. As it can be seen from the Figure 6.1c, the relative permittivities of all Al_2O_3–MgO coatings are at similar level from 20 Hz to 1 kHz. Below 10 Hz, the permittivities of HVOF7 (0% MgO) and HVOF8 (10% MgO) are significantly higher than the permittivities of HVOF9–12 (25%–65% MgO) which are more or less at the same level. In addition, the total loss contribution of HVOF7 and HVOF8 are higher in comparison to the dielectric loss of HVOF9–12 but the difference can be seen already at the highest frequencies, see Figure 6.1f. The dielectric loss of the alumina coating HVOF7 are the lowest among the alumina coatings. Adding MgO to Al_2O_3 decreases the relative permittivity and dielectric loss in particular at the lowest frequencies. The amount of 40% or 65% MgO gives the lowest permittivities and loss in the whole frequency range although these coatings have long vertical cracks.

6.1.1 Effect of microstructure and phase change

As it has already been discussed in the previous chapters, the microstructure of the coatings has an obvious effect on the dielectric properties which can also be seen in the

relative permittivity and dielectric loss results. The bulk alumina typically exhibits very low dielectric loss [100, 107] but the alumina coatings have high loss in particular at the lowest frequencies where the DC conductivity is very dominant. In addition, the real part of relative permittivity of alumina coating can be slightly higher or at a similar level in comparison to bulk alumina at the highest frequencies. However, the values are typically reported only at one frequency in literature [9, 28, 47, 64, 73, 85, 90]. As the results here show, it is important to know the permittivity and loss behavior as a function of frequency since the properties of ceramic coatings are strongly frequency dependent. The lamellar microstructure with interfaces and regions of different dielectric performance enhance the permittivity of the coatings which can at least partly explain the differences between bulk alumina and alumina coatings. Although the ambient humidity was kept at a low level in the measurements (Figure 6.1), the remaining ambient humidity probably also had at least a slight increasing effect on the results.

High porosity or high gas permeability does not exhibit decreasing effect on the dielectric loss of the coatings since the lowest loss from all the coatings are obtained for the Al_2O_3–MgO coatings HVOF10 (40% MgO) and HVOF12 (65% MgO) which have high gas permeabilities. In addition, the gas permeabilities of the alumina coatings HVOF3 and HVOF6B differ significantly but the losses are very similar, except at the lowest frequency (0.01 Hz). Thus, other material properties than high porosity or gas permeability (e.g. hygroscopicity, the amount of crystalline and amorphous regions, the thickness of lamellae etc.) can explain the differences between the coatings. For example, the smaller powder particle size of alumina coating HVOF2 can explain the lower relative permittivity and dielectric loss in comparison to the loss of the higher particle size HVOF3 since the thickness of lamellae are thinner when smaller powders are utilized. However, this is opposite to the results obtained by Brown *et al.* [85]. They reported that smaller particle size coating exhibits the highest relative permittivity and dielectric loss [85]. This was linked to the fact that the smaller particle size coatings exhibit lower amount of α-Al_2O_3 than the higher particle size coatings, but the thickness of lamellae was not evaluated in the analysis [85].

According to literature [4, 12, 23, 28, 43, 53, 63, 70, 74, 75, 80, 84–91], the alumina coatings consist of metastable γ-Al_2O_3 as the main phase and stable α-Al_2O_3 as the minor phase due to the rapid solidification during the spray process. According to literature [65, 83, 84], the amount of α-Al_2O_3 can originate from unmelted particles or from particles which are melted only a little on the outer surface of the particle but the major part of α-Al_2O_3 is proposed nucleating directly from the melt. The high amount of γ-Al_2O_3 can be problematic for dielectric properties since the physical properties of γ-Al_2O_3 are generally inferior to those of α-Al_2O_3, e.g. γ-Al_2O_3 is more hygroscopic [28, 65, 85]. The spray process, e.g. the spray velocity, the particle distribution, and spray distance affects the γ–α ratio [58, 65, 66, 86, 87, 90, 151]. Gao *et al.* [90] noticed that in a plasma sprayed alumina coating the amount of α-Al_2O_3 was higher (higher amount of unmelted particles) when the plasma arc current was lower. Furthermore, the relative permittivity was lower

with lower plasma arc current [90], see Table 2.1. Brown *et al.* [85] noticed also that the amount of α-phase increases with the particle size, and this can be explained by the lower relative permittivity and dielectric loss in the higher particle size coatings. Brown *et al.* [85] and Pawlowski [28] proposed that the occurrence of metastable phases have major influence on the relative permittivity of alumina coatings than the high porosity. According to literature [24, 28, 85], the high amount of γ-Al_2O_3 increases significantly relative permittivities and dielectric loss of the coatings with increasing humidity. The effect of temperature and humidity on relative permittivity and dielectric loss will be discussed in detail in the next Sub-chapter 6.1.2.

The rod flame sprayed alumina coatings consist of higher amount of unmelted particles which can be seen from the cross-sectional micrographs, see Figure 5.2. According to literature [65, 84], the amount of α-Al_2O_3 can originate from the unmelted particles, and thus the high amount α-phase should have decreasing effect on the relative permittivity and dielectric loss of flame sprayed alumina coatings in comparison to HVOF and plasma sprayed coatings. According to the results of this thesis, the relative permittivity and dielectric loss of FlameA are higher than those of HVOF and plasma sprayed alumina coatings, and thus this is not in coherence with the aforementioned hypothesis based on the literature. However, the findings in this thesis are understandable since the coating properties are process-dependent and several factors affect the relative permittivity and dielectric loss, not only one feature, e.g. a phase structure.

6.1.2 Effect of temperature and humidity

Effect of temperature and humidity was studied for HVOF, APS and rod flame sprayed alumina coatings in [P8]. Figure 6.2 shows the relative permittivities and the total loss contributions of the HVOF, APS and flame sprayed Al_2O_3 coatings (HVOF6B, PlasmaA & FlameA) as a function of frequency at 20–60 °C [P8]. As it can be seen from the figures, at the low frequencies (below 1 Hz) the permittivities and the losses increase 3–5 orders of magnitude, indicating low-frequency dispersion mechanism rather than DC conduction since the real part of permittivity is not constant [144–146]. The slopes of real and imaginary parts of relative permittivity differ to some extent, and thus the observed behavior does not fully follow LFD theory although the real parts increase quite steeply. However, at the highest humidity conditions the slopes are quite similar indicating that the results could follow LFD theory. This is understandable since according to literature [144] increasing humidity enhance the LFD phenomenon. At higher frequencies, the increase of relative permittivity with humidity is much lower. However, it needs to be emphasized that the given permittivity values are the real parts of the complex permittivity (see Eq. 2.9) and do not thus include the loss related component, only the real polarizability related component. Main part of the increased permittivity is most probably originating from absorbed water (for pure H_2O: $\varepsilon_r \approx 80$ at 20 °C), mainly by the Maxwell-Wagner polarization mechanism.

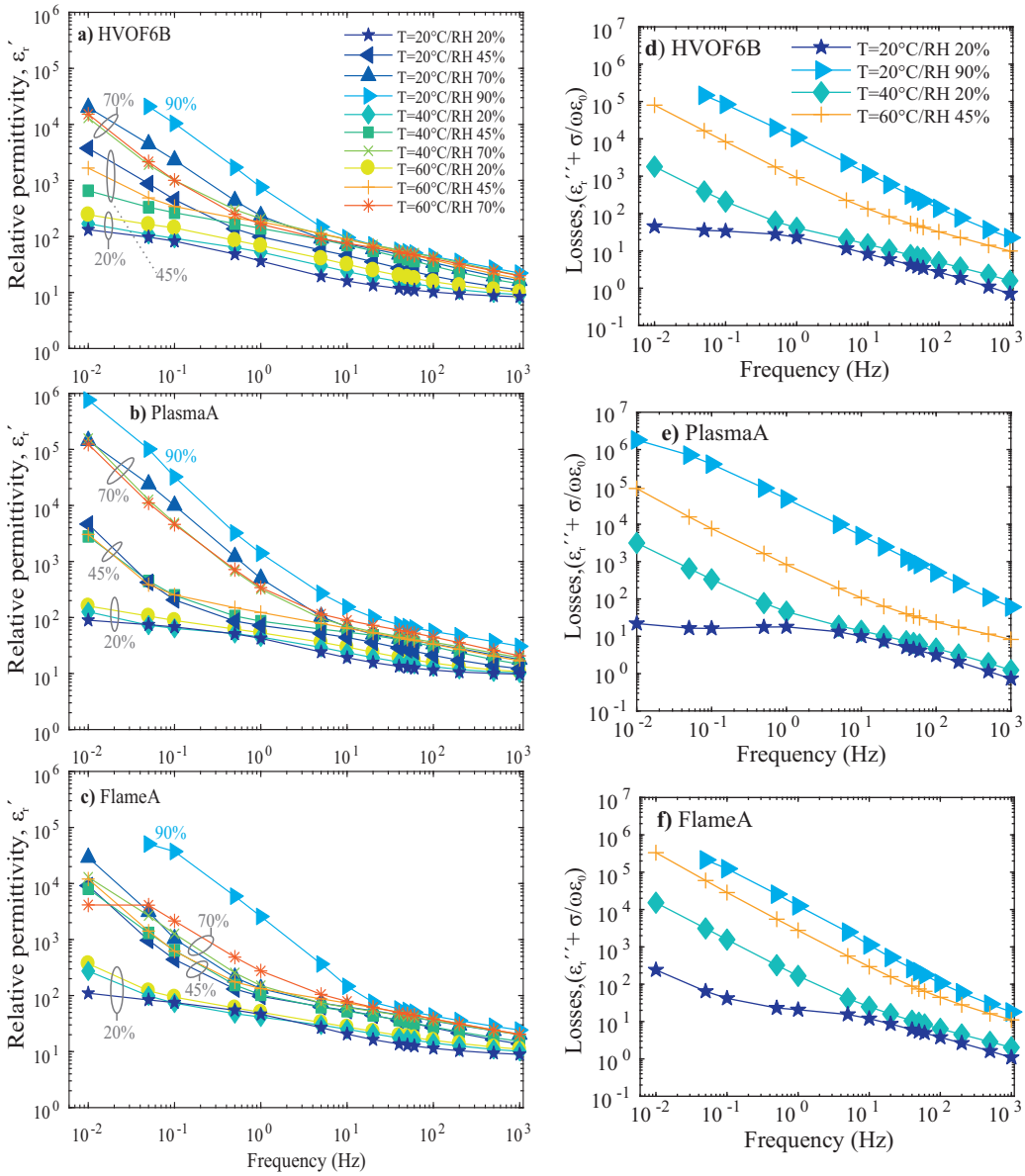

Figure 6.2: a)–c) Relative permittivity (indicated as Re{ε^*}) and d)–f) loss (indicated Im{ε^*}) of HVOF, APS and flame sprayed Al_2O_3 coatings as a function of frequency when the measuring electric field was 0.3 $V_{peak}/\mu m$). In RH 90% measurements, the high loss caused problems and due to this the permittivity data at the lowest frequencies are missing. [P8]

Figure 6.3 presents the real parts of the relative permittivities and the total loss contributions for HVOF, plasma and flame sprayed $MgAl_2O_4$ coatings (HVOF13, PlasmaB & FlameB) with increasing temperature (20 °C to 60 °C) when relative humidity was either 20% or 45% [P2]. The relative permittivities and the total losses of the spinel coatings increase with temperature and humidity like those properties of the alumina coatings. However, the permittivities of the spinel coatings HVOF13 and PlasmaB increases approximately one order of magnitude at the lowest frequencies when the temperature and humidity increased from 20 °C/RH 20% to 60 °C/RH 45% while the relative permittivity of HVOF and plasma sprayed alumina coatings increased approximately two orders of magnitude. For flame sprayed alumina and spinel coatings, the increase in relative permittivity is in a similar range.

The increase in the real part of relative permittivity with increasing humidity is well in line with the literature since Brown *et al.*[85] noticed that the real part of the relative permittivity of plasma sprayed alumina coating increased from 8.3 to 9.8 at 100 kHz when the relative humidity increased from 0% to 95%. In here, the relative permittivity of plasma sprayed alumina coating increased from 9.8 to 30.6 at 1 kHz when the humidity increased from 20% to 90% at 20 °C.

At 20 °C/RH 20%, the real parts of the relative permittivities of alumina coatings HVOF6B, PlasmaA and FlameA are 8.4, 9.8 and 8.9 at the frequency of 1 kHz, respectively. In [9], the relative permittivity of HVOF alumina coatings varied from 5.9 to 8.2 at 10 kHz which is quite well in line with the results obtained in here. Brown *et al.* [85] noticed that the relative permittivity of plasma alumina coating was 11–23 at 1 kHz when the highest value was obtained for the coating which exhibited the lowest powder particle size. Correspondingly, the lowest relative permittivity was obtained for the highest particle size coating [85]. These values are quite well in line with the real part of the relative permittivity of PlasmaA at 20 °C/RH 45% and 20 °C/RH 70% where the permittivity was 12.2 and 17.8, respectively. Pawlowski [28] reported that real part of the relative permittivity of plasma sprayed alumina coatings was 6–8 at 1 kHz, which is slightly lower than reported in here. The differences in the relative permittivities can be partly explained by the different sample preparation procedure since in [85] the coating samples were conditioned for 13 hours at 135 °C and in [28] for 1–3 days at 120 °C while in here the samples were heat-treated in 120 °C for two hours. Longer heat-treatment time removes more completely moisture from a porous coating which can be seen as a lower relative permittivity.

It should be also noted that the measuring voltage was 1 V_{rms} in [28] while in here the measuring voltage depends on the coating thickness varying from 57 V_{rms} to 69 V_{rms} corresponding to the electric field of 0.3 V_{peak}/µm. Although the measuring field might affect the relative permittivity, we noticed in [P5] that at the frequency of 100 Hz the real part of the relative permittivities of HVOF sprayed alumina and spinel coatings (HVOF1–4) are not dependent on the measuring electric field (in the range of 0.1–5 V/µm). However, at the low frequencies (0.1 Hz) small increase in the real part of

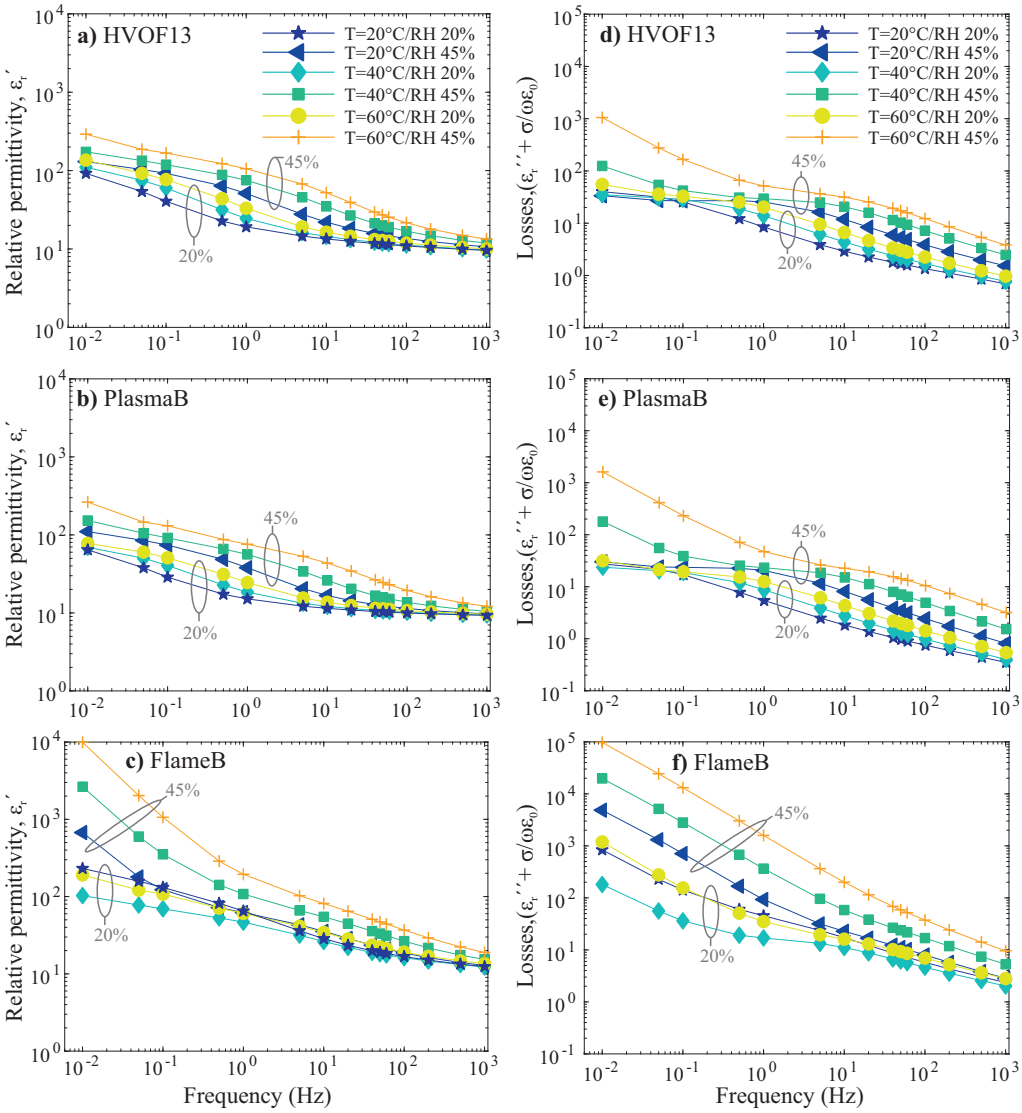

Figure 6.3: a)–c) Relative permittivity (indicated as Re{ε*}) and d)–f) loss (indicated Im{ε*}) of HVOF, APS and flame sprayed $MgAl_2O_4$ coatings as a function of frequency when the measuring electric field was 0.3 $V_{peak}/\mu m$) [P2].

relative permittivity can be seen for some of the coating materials when the electric field is above 0.5 V/µm which is the same transition electric field noticed in the non-linear DC conductivity behavior [P5].

As it can be seen from Figures 6.2d)–f) and 6.3d)–f), the losses of Al_2O_3 and $MgAl_2O_4$ coatings increase with increasing humidity. At the lowest frequencies, the dielectric loss of spinel coatings increase only 1–2 orders of magnitude while the loss of alumina coatings increase 3–4 orders of magnitude. The effect of increasing humidity on the loss of the alumina coatings at the various temperatures can be seen in detail in Figure 6.4 where the losses are presented at the frequencies of 50 Hz and 0.1 Hz. It needs to be emphasized that the presented values indicate total measured losses including the contributions of both DC conductivity and polarization (see Eq. 2.10). At the highest loss level (above ∼100), a slope of approximately −1 can be seen indicating low-frequency dispersion instead of DC conductivity since the real part of relative permittivity increases almost similar slope with the imaginary part. A notable increase in the loss can be seen for the alumina coatings at 60 °C/RH 45%. However, the losses of the spinel coatings are increasing more slowly and the increasing component is not so dominant, in particular, for HVOF13 and PlasmaB.

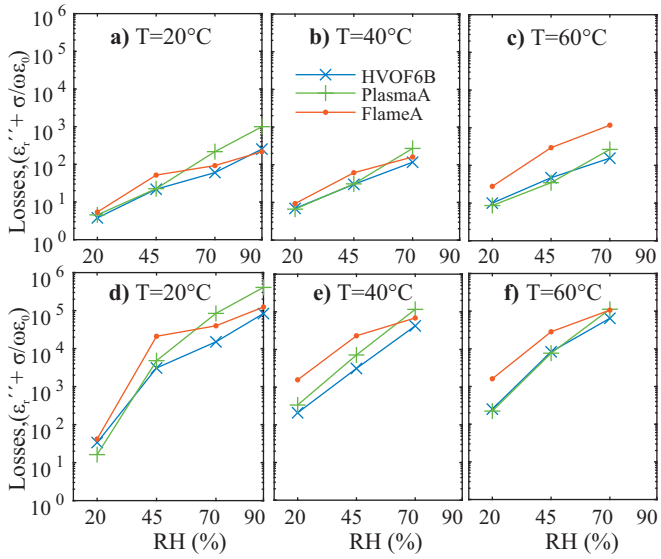

Figure 6.4: The dielectric loss of alumina coatings at the frequencies of 50 Hz (a–c) and 0.1 Hz (d–f). [P8]

The HVOF sprayed coatings (HVOF6B & HVOF13) have the lowest losses while the flame sprayed coatings (FlameA & FlameB) exhibit the highest values for each type of material, respectively, see Figures 6.2 & 6.3. This similar trend was also noticed in the DC resistivity results. In addition, the spinel coatings have lower losses than the alumina coatings which is well in line with the DC resistivity results since the spinel coatings exhibited higher DC resistivities [P2] than the alumina coatings [P8].

The results indicate that the dielectric properties of thermally sprayed alumina and spinel coatings differ from that of bulk alumina, and thus lamellar microstructure together with the phase composition differences most probably affect the dielectric properties. In addition, the properties of alumina change during thermal spraying process since the coating consist mainly of metastable γ-Al_2O_3 and α-Al_2O_3 is only as a minor phase [4, 12, 23, 28, 43, 63, 70, 74, 75, 84, 88–91]. Brown *et al.* [85] and Pawlowski [28] proposed that high relative permittivity of plasma sprayed alumina coating is related to high γ-Al_2O_3 content. Toma *et al.* [23] noticed that HVOF sprayed alumina coating had higher α-phase content than plasma alumina coating. Correspondingly at high humidities (>RH 75%) the HVOF alumina coating had higher resistivity than plasma alumina coatings but at low humidities (<RH 45%) the HVOF and plasma alumina coatings exhibited similar resistivities [23].

It can be criticized that the high γ-Al_2O_3 content of thermally sprayed alumina coatings cannot completely explain their sensitivity to the humidity since Favre *et al.* [152] noticed that the DC resistivity of α-Al_2O_3 powder decreased approximately five orders of magnitude when the relative humidity increased from 20% to 80% which is approximately similar decrease obtained for the coatings in this study and in literature [23, 29]. In addition, thermally sprayed $MgAl_2O_4$ coatings exhibit also moisture sensitive nature despite the stable thermodynamic phase structure in a coating since the DC resistivity of the $MgAl_2O_4$ coatings decreased with increasing humidity while the relative permittivity and dielectric losses increased [23, 85]. It can be concluded that the $MgAl_2O_4$ coatings are less sensitive to humidity increases than Al_2O_3 coatings. All in all, the nature of all thermally sprayed ceramic coatings is moisture sensitive.

If the operation temperatures of a thermally sprayed coatings are low enough, a coating can be impregnated with an organic or inorganic sealant in order to make it more insensitive against the moisture penetration [11, 30, 77, 90]. At the same time, the utilization of the sealants also improves the material and dielectric properties of the impregnated coating [4]. According to our preliminary experiments of the utilization of sealants, the breakdown strength can be even 70–90% higher, DC resistivity is two order of magnitude higher and non-linear conductivity is not noticed, the real part of relative permittivity increase only slightly at the lowest frequencies, and dielectric loss is much lower in comparison to the properties of as-sprayed coatings.

6.2 Relative permittivity and dielectric loss at higher electric fields

The effect of electric field on relative permittivity and dielectric loss was studied for HVOF sprayed alumina (HVOF2 & HVOF3) and spinel (HVOF1 & HVOF4) coatings at 20 °C, RH 20% [P5]. Figure 6.5 presents the real part of relative permittivity and the total loss contribution of the studied coatings. At the frequency of 100 Hz, the relative permittivity of all studied coatings are approximately 10 at all the electric field strengths. At the lower

frequency (0.1 Hz), lowest relative permittivity is obtained for the MgO-Al_2O_3 coating (HVOF1). In addition, the permittivity of HVOF1 does not increase with increasing electric field which is opposite to the permittivity of the other $MgAl_2O_4$ coating (HVOF4). The alumina coating deposited from smaller particle size powder (HVOF2) has lower relative permittivity at 0.1 Hz than the other alumina sample (HVOF3) made from larger particle size powder. The relative permittivity of both alumina coatings increase slightly with an increasing electric field but the increase is quite small.

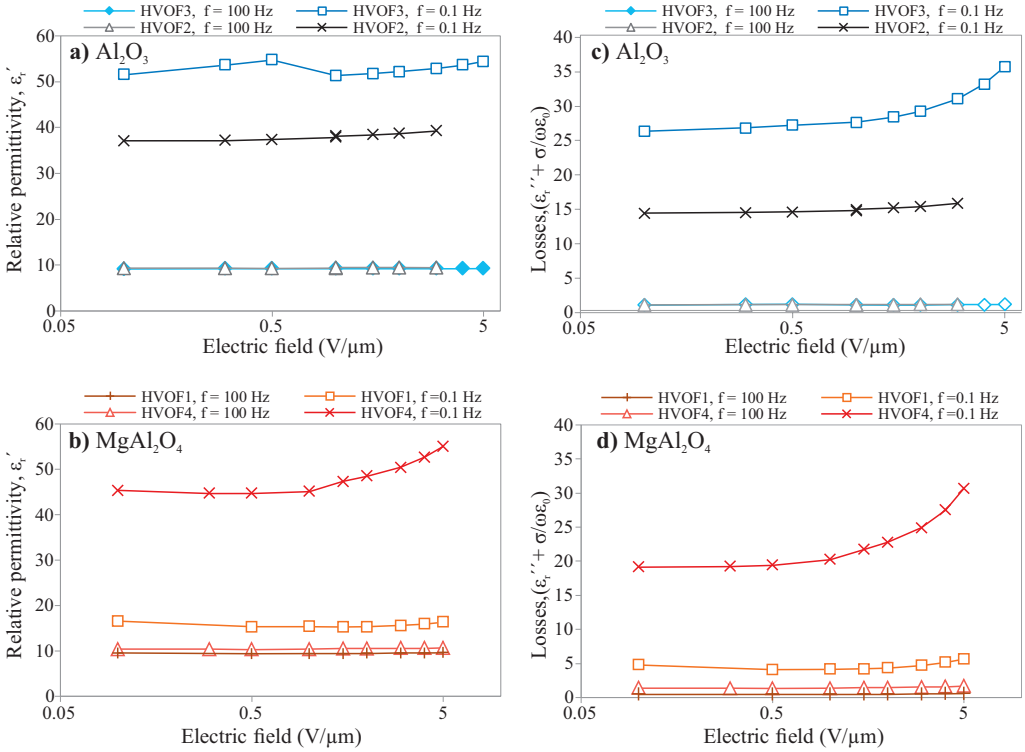

Figure 6.5: The real part of relative permittivity (indicated as Re$\{\varepsilon_r*\}$ of the HVOF sprayed Al_2O_3 (a) and the HVOF sprayed $MgAl_2O_4$ (b) coatings as a function of electric field together with the corresponding dielectric loss (indicated Im$\{\varepsilon^*\}$) for Al_2O_3 (c) and $MgAl_2O_4$ (d). The measurements were performed at 20 °C/RH 20%. [P5]

The total loss contribution of the coatings (HVOF1–4) at the frequency of 100 Hz is at an approximately similar level which can be seen from Figure 6.5c)–d). However, at the frequency of 0.1 Hz the losses of alumina and spinel coatings differ significantly. The alumina coating HVOF2 and the spinel coating HVOF1 are only slightly dependent on the electric field at the low frequency (0.1 Hz). In addition, the alumina coating (HVOF2) has higher loss level than the spinel coating (HVOF1) which is in coherence with the DC resistivity results reported in Sub-chapter 5.1 and in literature [23]. The dielectric loss contribution of the alumina coating HVOF3 and the spinel coating HVOF4 are dependent on the electric field in particular above 0.5 V/µm. As it can be noticed from Figure 5.2,

the spinel coating HVOF1 and the alumina coating HVOF2 exhibit quite similar lamellar microstructure which may explain their similar type of behavior in DC resistivity as well as in dielectric loss at low frequencies. These two coatings have smaller lamellar size. In addition, the amount of amorphous regions is higher than in the HVOF3 and HVOF4 which exhibits quite similar behavior in the dielectric loss at low frequencies although the actual values differ.

Because some permanent changes occurred for the alumina and spinel coatings during the DC resistivity measurements in [P1, P2, P7], the relative permittivity and dielectric loss measurements were repeated for the studied coatings (HVOF1–4) in order to verify the possible permanent changes. After the first measurements, the coatings were placed at controlled conditions (20 °C, RH 20%) and the measurements were remade on the next day. This procedure was repeated for the studied coating materials (HVOF1–4) two times. The changes in the dielectric loss were notable in particular for the alumina coating HVOF3 which was actually measured four times in order to verify further the permanent changes.

Figure 6.6 presents the dielectric loss of HVOF3 at the frequency of 0.1 Hz as a function of electric field from the first to the fourth measurement. At the low electric fields (below 1 V/µm), the dielectric loss is at a similar level in all the different measurements, but at higher field strengths the loss increased notably after the second measurement. Thus, some permanent changes occurred in the material. It can be speculated that some of the vertical cracks inside the coating broke into more conducting state short circuiting part of the lamellae, which further changed the capacitance of the coating and increased the conductivity. Since the short-circuiting occurs after a certain electric field, the loss behavior at lower fields is repeatable. The dielectric loss of the other alumina coating (HVOF2) increased quite similarly as the loss behavior of HVOF3 indicating similar permanent material changes presented in Figure 6.6. However, for the spinel coatings

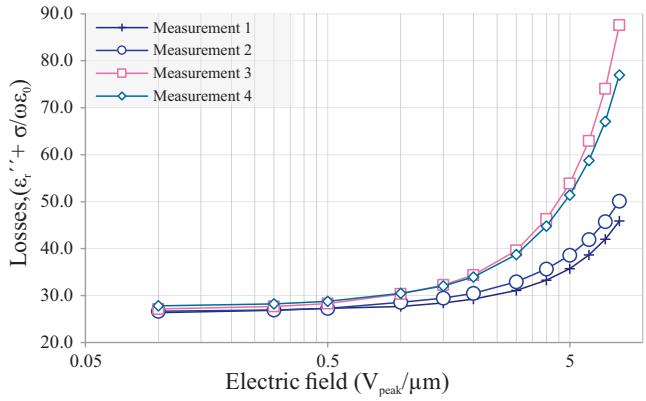

Figure 6.6: The dielectric loss of the alumina coating, HVOF3, at a frequency of 0.1 Hz as a function of electric field when the loss measurements were repeated four times [P5].

(HVOF1 & HVOF4) similar increase in the relative permittivity and dielectric loss cannot be observed which can be linked to the differences in the microstructures, e.g. fewer amount of micro-cracks in the spinel coatings.

As a conclusion, it can be said that the electric field dependency of the relative permittivity and dielectric loss of the ceramic coatings is not as obvious as it was in DC resistivity. Depending on the material, increasing the electric field either increased the permittivity and the loss or kept those as constant in the low frequency range. At the highest frequency, the permittivity and loss of the coatings were independent of the electric field.

6.3 Considerations and implications

At the high frequencies, the real parts of the relative permittivities for the studied thermally sprayed alumina and spinel coatings are in coherence with the relative permittivities of bulk alumina reported in literature. In the low frequency range, the relative permittivities of the studied coatings increases notably which is most probably due to interfacial polarization in the layered crystalline-amorphous microstructure of coatings which have varying conductivities. In the low frequency range, HVOF and plasma sprayed spinel coatings exhibit slightly lower relative permittivities than the alumina coatings while the flame sprayed alumina and spinel coatings have significantly higher relative permittivities.

At the highest frequencies, the total dielectric loss contribution between different coating materials are very similar but in the low frequency range the HVOF sprayed spinel coatings have the lowest losses in general while the flame sprayed spinel coating has the highest loss level. At the lowest frequencies, the total loss contribution of the coatings increases remarkably which indicates a low-frequency dispersion/quasi-DC conduction contribution due to the increasing real part of relative permittivity. Thus, the dielectric losses of the coatings are significantly higher than that of bulk alumina. The layered microstructure of the coatings might explain the higher total loss contribution of alumina and spinel coatings in comparison to that of bulk alumina.

Increasing temperature and humidity increases the relative permittivity and dielectric loss of alumina and spinel coatings particularly at the lowest frequencies. These major increases are attributable to the highly hygroscopic nature of the coatings. For the alumina coatings, high amount of γ-Al_2O_3 can partly explain the hygroscopic nature. However, this cannot alone explain the hygroscopicity in the studied ceramic coatings because the relative permittivity and dielectric losses of the spinel coatings increased as well, particularly, at the high humidity conditions. It can be concluded that the nature of thermally sprayed ceramic coatings is moisture sensitive, which highly affects the relative permittivity and dielectric loss.

Chapter 7

Conclusions

In this chapter, the final concluding discussion of the electrical performance of the studied thermally sprayed ceramic coatings are given. In addition, a brief discussion of possible future research work related to the topic of this thesis is given.

7.1 Main conclusions and scientific contributions

Thermal spraying is an effective and rather low cost method to produce a protective layer on a component surface. In addition, the method enables tight deposition on different substrate materials which can have challenging geometries. Thermally sprayed ceramic, e.g. alumina and spinel, coatings are usually utilized as heat or wear resistant coatings. They can also be utilized as an electrical insulating layer, particularly, at high temperatures or in harsh environments. Although several applications exist, the use of alumina and spinel coatings in insulation systems is still today lower than the use in other applications. It has been estimated that the utilization of the coatings in insulation systems will increase in the future. Thermally sprayed ceramic coating is deposited layer-by-layer, and thus the microstructure includes crystalline and amorphous regions as well as some amount of porosity. Due to this, the microstructure of the coating differs from the bulk ceramic which exhibits mainly crystalline structure. Consequently, the electrical performance differs as well. Due to the aforementioned aspects, one of the main objectives of this thesis was to study and develop suitable measurement methods for comprehensive dielectric characterization of ceramic coatings. In this thesis, the dielectric characterizations included the following tests, from which a comprehensive evaluation of the electrical performance can be made: i) linearly ramped breakdown voltage tests, ii) step-wisely increased breakdown voltage tests, iii) voltage endurance tests, iv) DC resistivity tests at low and high electric fields, and v) relative permittivity and dielectric loss tests at low and high electric fields.

Several different alumina and spinel raw materials were studied to form wide perspective of the electrical performance of the coatings. For all the studied coatings, a comprehensive study of dielectric properties included DC breakdown performance, DC resistivity, relative

permittivity and dielectric losses at controlled conditions (20 °C/RH 20%). According to these results, the high-velocity oxygen fuel (HVOF) sprayed spinel coatings have the highest breakdown strength, DC resistivity and the lowest dielectric losses while the rod flame sprayed alumina and spinel coatings exhibit lower breakdown strength and DC resistivity as well as higher dielectric losses. The dielectric properties of atmospheric plasma sprayed (APS) alumina and spinel coatings are very close to those of HVOF coatings, except the breakdown strengths which are notably lower for APS coatings. The differences between the coatings deposited by utilizing different spray methods are understandable since the highest particle velocity of HVOF spray method enhance the coating properties (e.g. density, porosity, amount of unmelted regions etc.) while the low particle velocity of rod flame spray diminish the material properties and furthermore the dielectric performance.

As mentioned earlier, the microstructure of a thermally sprayed ceramic coatings is formed layer-by-layer from several molten powder particles called splats. During the spray process, the attaching surface of the splat cools down more rapidly than the other parts, causing the rapidly cooling part to form amorphous phase and other sections more crystalline. In addition, the coating consists of unmelted particles, pores, voids and some amount of vertical cracks. The effects of the special micro- and phase-structures on the dielectric properties was one of the main objectives of this thesis, and the effects are seen in several ways in this thesis.

The porosities are rather similar in between the different coating materials. Due to this, no clear correlation between porosity and short-term DC breakdown performance or any other dielectric property can be observed. In some test series, high gas permeability (volumetric porosity) can correlate with the lower breakdown strength but this correlation cannot be seen for all the studied coatings. The observations emphasize that the coating structure is complex and it is difficult to find clear correlations between one specific material property and the electrical performance.

The role of microstructure can also be seen in the relative permittivity and dielectric losses of the ceramic coatings. At the highest frequencies, the relative permittivities of the coatings are more or less constant being at similar level with bulk alumina. However, at the lower frequencies the relative permittivity increases rapidly which most probably indicate interfacial polarization occurring at the crystalline-amorphous interfaces in the coating. Also, the role of microstructure can be seen in the dielectric losses since the losses of the coatings are notably higher than those of bulk ceramic. Related to this, notable low-frequency dispersion contribution can be seen in the dielectric losses in the low frequency region which can be linked to the layered microstructure.

Conduction mechanisms were studied and analyzed comprehensively which was one of the main objectives of this thesis. Unlike for bulk alumina, the DC resistivity of the coatings is field dependent and the conduction mechanism is not fully following the space charge limited conduction (SCLC) theory. Only at the lowest electric fields (typically below 0.5 V/µm), the DC resistivities of the studied coatings are at similar level with

that of bulk alumina while at higher electric fields the coatings exhibit strong non-linear resistivity. Based on the high field DC conductivity data analysis, it is proposed that the coatings follow only partly the SCLC theory. This behavior is suggested to be based on the layered structure with crystalline and amorphous regions. These regions exhibit different conductivities resulting in uneven DC electric field distribution.

Another main objective was to study the effect of ambient conditions on the dielectric properties. It is verified that the dielectric properties of the ceramic coatings are very sensitive to external effects, i.e. i) the utilization of insulation oil preventing flashovers on the coating surface in breakdown voltage tests, ii) increasing the air temperature, or iii) increasing relative humidity. During the breakdown voltage tests, the insulation oil penetrates very easily inside a ceramic coating causing the breakdown strength of oil impregnated coating to be roughly two times higher than the breakdown strength of ceramic coating. Air temperature has only a minor effect on the breakdown strength in the temperature range of 20–180 °C but in the range of 300–800 °C the breakdown strength of alumina coatings decreases gradually being at 800 °C only 14% of the value obtained at 20 °C/RH 20%. Increasing the relative humidity has no clear effect on breakdown performance of ceramic coatings. However, increasing humidity decreases the DC resistivity several orders of magnitude and increases the relative permittivity and dielectric losses significantly as well. Increasing humidity has more notable influence on the dielectric properties of alumina coatings than those of spinel coatings. This difference most probably occurs due to the high amount of highly hygroscopic metastable γ-Al_2O_3, which exhibits always in thermally sprayed alumina coating due to rapid solidification during the spray process, while no phase alterations occur in the spinel coatings. However, the phase changes does not explicitly explain the moisture sensitive of thermally sprayed coatings, and it is proposed that the nature of thermally sprayed ceramic coating is moisture sensitive due to the layered microstructure with voids and pores. If the ceramic coatings are utilized at low temperatures, the coatings can be sealed with an organic or an inorganic sealant to be more insensitive to the humidity effects. However, it needs to be emphasized that the sealing affects the electrical performance of the ceramic coatings.

In order to utilize thermally sprayed ceramic coatings in real applications, their long-term performance need to be known in addition to their short-term properties. The step-wisely increased breakdown voltage tests showed roughly the levels of breakdown strengths under longer stresses. In practice approximately 10–40% decrease from the short-term results were observed. However, the step tests did not provide enough information of the long-term breakdown performance. Thus, long DC voltage endurance tests were performed to analyze the material degradation and to enable estimation of possible service electric fields, which was one of the main objectives of this thesis as well. According to the results, no clear material degradation was observed for the studied HVOF sprayed alumina or spinel coatings. Short-term dielectric properties indicated that HVOF spinel coatings exhibit better dielectric performance than HVOF alumina coatings but this kind of evident difference was not observed in the long-term test. According to the long-term

test results, at normal ambient conditions a suitable maximum service stress level for the both coatings could be in the range of 10 V/µm which is approximately 25–30% of the short-term breakdown strength.

7.2 Future research topics

This thesis presents suitable methods to analyze the electrical performance of thermally sprayed ceramic coatings. Comprehensive analysis of the effects of microstructure and ambient conditions were made for several different coating materials. The following further research topics could enhance the understanding of the dielectric performance:

- As the humidity was verified to affect significantly the performance of the coatings, future studies should be done for highly dried samples. This may better reveal differences between the different coatings. In practice, the moisture could be removed better when the samples are heat-treated in a vacuum oven. In addition, some measurements, in particular DC resistivity and dielectric losses, could be performed in the vacuum oven.

- One of the most interesting findings of this thesis is the strong non-linear DC resistivity which starts at quite low electric fields. Some proposal about the possible reasons are made but there are still quite many open questions about the root causes of this phenomenon. For example, the physical microstructure with amorphous/crystalline regions, pores, etc. could be tried to be modeled in a suitable multiphysics software together with the dielectric properties in order to find more detailed answers to the observed phenomena.

- The effects of ambient conditions were studied comprehensively in this thesis. However, the high temperature effect on DC resistivity and dielectric losses would be interesting research question, especially if the operating temperatures in real applications are high. In addition, it would be interesting to increase the stress durations and electric fields in the DC resistivity measurements in order to reach the real long-term performance of the materials.

- This thesis focused mainly on the short-term dielectric properties of the ceramic coatings although the long-term breakdown performance was studied for two coating materials. In the future, a broader long-term test series with coating samples of all different spray methods would be an interesting addition. This should also include the aspects to study the partial discharge endurance under various stresses which was left outside of the scope of this thesis.

- The results presented in this thesis give an overview of the dielectric properties of the ceramic coatings and possible operation regions where coating materials could be utilized. However, in order to use the coatings in real applications more

characterization is needed focusing also on application specific tests which could include e.g. the aforementioned PD tests, pulsed voltage or other specific excitations, and tests where coating is deposited on an application specific geometries.

References

[1] P. Fauchais, A. Vardelle, and B. Dussoubs, "Quo vadis thermal spraying?," *Journal of Thermal Spray Technology*, vol. 10, no. 1, pp. 44–66, 2001.

[2] L. Pawlowski, *The Science and Engineering of Thermal Spray Coatings*. Chichester, West Sussex, England: John Wiley & Sons Ltd, 2nd ed., 2008.

[3] P. Fauchais and A. Vardelle, "Thermal Sprayed Coatings Used Againts Corrosion and Corrosive Wear," in *Advanced Plasma Spray Applications* (H. S. Jazi, ed.), ch. Chapter1, p. 237, InTech, 2012.

[4] P. L. Fauchais, J. V. Heberlein, and M. I. Boulos, *Thermal Spray Fundamentals*. Boston, MA: Springer US, 2014.

[5] C. U. Hardwicke and Y.-C. Lau, "Advances in Thermal Spray Coatings for Gas Turbines and Energy Generation: A Review," *Journal of Thermal Spray Technology*, vol. 22, no. 5, pp. 564–576, 2013.

[6] A. Vardelle, C. Moreau, J. Akedo, and et al., "The 2016 Thermal Spray Roadmap," *Journal of Thermal Spray Technology*, vol. 25, no. 8, pp. 1376–1440, 2016.

[7] "Thermal Spray Market - Growth, Trends, COVID-19 Impact, and Forecasts (2022 - 2027)," tech. rep., Mordor Intelligence, 2022.

[8] P. Fauchais, "Understanding plasma spraying," *Journal of Physics D: Applied Physics*, vol. 37, no. 9, pp. R86–R108, 2004.

[9] E. Turunen, T. Varis, S.-P. Hannula, A. Vaidya, A. Kulkarni, J. Gutleber, S. Sampath, and H. Herman, "On the role of particle state and deposition procedure on mechanical, tribological and dielectric response of high velocity oxy-fuel sprayed alumina coatings," *Materials Science and Engineering: A*, vol. 415, no. 1-2, pp. 1–11, 2006.

[10] A. Sharma, "Thermal Spray Coatings for Electrical and Electronic Applications," in *ASM Handbook, Volume 05A - Thermal Spray Technology* (R. C. J. Tucker, ed.), pp. 262–269, ASM International, 2013.

[11] J. Luth, M. Cichosz, M. Lehmann, S. Hartmann, and F. Trenkle, "High Velocity Oxygen Fuel Sprayed Insulation Coatings for Applications in High Power Electronics," in *ITSC 2015- Proceedings of the International Thermal Spray Conference*, pp. 1026–1030, ASM International, 2015.

[12] J. Kotlan, R. C. Seshadri, S. Sampath, P. Ctibor, Z. Pala, and R. Musalek, "On the dielectric strengths of atmospheric plasma sprayed Al2O3, Y2O3, ZrO2–7% Y2O3 and (Ba,Sr)TiO3 coatings," *Ceramics International*, vol. 41, no. 9, pp. 11169–11176, 2015.

[13] G. Berard, P. Brun, J. Lacombe, G. Montavon, A. Denoirjean, and G. Antou, "Influence of a Sealing Treatment on the Behavior of Plasma-Sprayed Alumina Coatings Operating in Extreme Environments," *Journal of Thermal Spray Technology*, vol. 17, no. 3, pp. 410–419, 2008.

[14] M. R. Dorfman, "Thermal Spray Coatings," in *Handbook of Environmental Degradation of Materials* (Myer Kutz, ed.), ch. 19, pp. 569–596, Elsevier, second ed., 2012.

[15] J.-P. Delplanque, S. Johson, Y. Zhou, and L. Shaw, "Spray Deposition and Coating Processes," in *Materials Processing Handbook*, ch. 11, pp. 1–31, Taylor & Francis Group, LLC, 2007.

[16] A. Vaidya, V. Srinivasan, T. Streibl, M. Friis, W. Chi, and S. Sampath, "Process maps for plasma spraying of yttria-stabilized zirconia: An integrated approach to design, optimization and reliability," *Materials Science and Engineering A*, vol. 497, no. 1-2, pp. 239–253, 2008.

[17] E. Bakan and R. Vaßen, "Ceramic Top Coats of Plasma-Sprayed Thermal Barrier Coatings: Materials, Processes, and Properties," *Journal of Thermal Spray Technology*, vol. 26, no. 6, pp. 992–1010, 2017.

[18] B. Basu and K. Balani, *Advanced Structural Ceramics*. Wiley-American Ceramic Society Inc, 2011.

[19] E. Klyatskina, E. Rayón, G. Darut, M. Salvador, E. Sánchez, and G. Montavon, "A study of the influence of TiO2 addition in Al2O3 coatings sprayed by suspension plasma spray," *Surface and Coatings Technology*, vol. 278, pp. 25–29, 2015.

[20] V. Matikainen, K. Niemi, H. Koivuluoto, and P. Vuoristo, "Abrasion, Erosion and Cavitation Erosion Wear Properties of Thermally Sprayed Alumina Based Coatings," *Coatings*, vol. 4, no. 1, pp. 18–36, 2014.

[21] N. H. Menzler, F. Tietz, S. Uhlenbruck, H. P. Buchkremer, and D. Stöver, "Materials and manufacturing technologies for solid oxide fuel cells," *Journal of Materials Science*, vol. 45, no. 12, pp. 3109–3135, 2010.

[22] M. Rautanen, *Improving sealing, electrical contacts, and corrosion resistance in solid oxide fuel cell stacks*. Doctoral thesis, Aalto University, 2015.

[23] F.-L. Toma, S. Scheitz, L.-M. Berger, V. Sauchuk, M. Kusnezoff, and S. Thiele, "Comparative study of the electrical properties and characteristics of thermally sprayed alumina and spinel coatings," *Journal of Thermal Spray Technology*, vol. 20, no. 1-2, pp. 195–204, 2011.

[24] S. Sampath, "Thermal Spray Applications in Electronics and Sensors: Past, Present,

and Future," *Journal of Thermal Spray Technology*, vol. 19, no. 5, pp. 921–949, 2010.

[25] G. Mauer, R. Vaßen, and D. Stöver, "Thin and Dense Ceramic Coatings by Plasma Spraying at Very Low Pressure," *Journal of Thermal Spray Technology*, vol. 19, no. 1-2, pp. 495–501, 2010.

[26] S.-L. Zhang, C.-X. C.-J. Li, S. Liu, C.-X. C.-J. Li, G.-J. Yang, P.-J. He, L.-L. Yun, B. Song, and Y.-X. Xie, "Thermally Sprayed Large Tubular Solid Oxide Fuel Cells and Its Stack: Geometry Optimization, Preparation, and Performance," *Journal of Thermal Spray Technology*, vol. 26, no. 3, pp. 441–455, 2017.

[27] K. Ahn, B. W. Wessels, and S. Sampath, "Spinel humidity sensors prepared by thermal spray direct writing," *Sensors and Actuators B: Chemical*, vol. 107, no. 1, pp. 342–346, 2005.

[28] L. Pawlowski, "The relationship between structure and dielectric properties in plasma-sprayed alumina coatings," *Surface and Coatings Technology*, vol. 35, no. 3-4, pp. 285–298, 1988.

[29] F.-L. Toma, L.-M. Berger, S. Scheitz, S. Langner, C. Rödel, A. Potthoff, V. Sauchuk, and M. Kusnezoff, "Comparison of the Microstructural Characteristics and Electrical Properties of Thermally Sprayed Al2O3 Coatings from Aqueous Suspensions and Feedstock Powders," *Journal of Thermal Spray Technology*, vol. 21, no. 3-4, pp. 480–488, 2012.

[30] H.-J. Kim, S. Odoul, C.-H. Lee, and Y.-G. Kweon, "The electrical insulation behavior and sealing effects of plasma-sprayed alumina–titania coatings," *Surface and Coatings Technology*, vol. 140, no. 3, pp. 293–301, 2001.

[31] E. E. J. Young, E. Mateeva, J. J. J. Moore, B. Mishra, and M. Loch, "Low pressure plasma spray coatings," in *International Conference on Metallurgic Coatings and Thin Films*, vol. 377–378, pp. 788–792, 2000.

[32] H. L. Filmer, J. Hochstrasser, A. R. Nicoll, and S. Rangaswamy, "Plasma spray deposition of alumina-based ceramic coatings," *American Ceramic Society Bulletin*, vol. 69, no. 12, pp. 1955–1958, 1990.

[33] I. O. Owate and R. Freer, "Ac breakdown characteristics of ceramic materials," *Journal of Applied Physics*, vol. 72, no. 6, pp. 2418–2422, 1992.

[34] E. Dutarde, S. Dinculescu, and T. Lebey, "On some electrical characteristics of AlN and Al2O3," in *Electrical Insulation, 2000. Conference Record of the 2000 IEEE International Symposium on*, pp. 172–175, 2000.

[35] J. Liebault, J. Vallayer, D. Goeuriot, D. Treheux, and F. Thevenot, "How the trapping of charges can explain the dielectric breakdown performance of alumina ceramics," *Journal of the European Ceramic Society*, vol. 21, no. 3, pp. 389–397, 2001.

[36] D. Malec, V. Bley, T. Lebey, F. Talbi, and F. Lalam, "Investigations on dielectric

breakdown of ceramic materials," in *CEIDP '05. 2005 Annual Report Conference on Electrical Insulation and Dielectric Phenomena, 2005.*, pp. 63–66, IEEE, 2005.

[37] M. Touzin, D. Goeuriot, H.-J. J. Fitting, C. Guerret-Piécourt, D. Juvé, and D. Tréheux, "Relationships between dielectric breakdown resistance and charge transport in alumina materials—Effects of the microstructure," *Journal of the European Ceramic Society*, vol. 27, no. 2-3, pp. 1193–1197, 2007.

[38] D. Malec, V. Bley, F. Talbi, and F. Lalam, "Contribution to the understanding of the relationship between mechanical and dielectric strengths of Alumina," *Journal of the European Ceramic Society*, vol. 30, no. 15, pp. 3117–3123, 2010.

[39] F. Talbi, F. Lalam, and D. Malec, "Dielectric breakdown characteristics of alumina," in *Proceedings of 2010 International Conference on Solid Dielectrics (ICSD)*, pp. 1–4, 2010.

[40] C. Neusel, H. Jelitto, D. Schmidt, R. Janssen, F. Felten, and G. A. Schneider, "Dielectric breakdown of alumina single crystals," *Journal of the European Ceramic Society*, vol. 32, no. 5, pp. 1053–1057, 2012.

[41] C. Neusel and G. A. Schneider, "Dependence of the breakdown strength on thickness and permittivity," in *2013 IEEE International Conference on Solid Dielectrics (ICSD)*, pp. 31–35, IEEE, 2013.

[42] B. Block, Y. Kim, and D. K. Shetty, "Dielectric Breakdown of Polycrystalline Alumina: A Weakest-Link Failure Analysis," *Journal of the American Ceramic Society*, vol. 96, no. 11, pp. 3430–3439, 2013.

[43] A. Kulkarni, J. Gutleber, S. Sampath, A. Goland, W. B. Lindquist, H. Herman, A. J. Allen, and B. Dowd, "Studies of the microstructure and properties of dense ceramic coatings produced by high-velocity oxygen-fuel combustion spraying," *Materials Science and Engineering A*, vol. 369, no. 1-2, pp. 124–137, 2004.

[44] M. Oksa, E. Turunen, T. Suhonen, T. Varis, and S.-P. Hannula, "Optimization and Characterization of High Velocity Oxy-fuel Sprayed Coatings: Techniques, Materials, and Applications," *Coatings*, vol. 1, no. 1, pp. 17–52, 2011.

[45] S. Amada and T. Hirose, "Influence of grit blasting pre-treatment on the adhesion strength of plasma sprayed coatings: fractal analysis of roughness," *Surface and Coatings Technology*, vol. 102, no. 1, pp. 132–137, 1998.

[46] D. E. Crawmer, "Plasma Spray Coatings," in *Encyclopedia of Materials: Science and Technology* (K. H. J. Buschow, R. W. Cahn, M. C. Flemings, B. Ilschner, E. J. Kramer, Subhash Mahajan, and P. Veyssière, eds.), pp. 7035–7040, Elsevier, 2001.

[47] S. Sampath, J. Longtin, R. Gambino, H. Herman, R. Greenlaw, and E. Tormey, "Direct-Write Thermal Spraying of Multilayer Electronics and Sensor Structures," in *Direct-Write Technologies for Rapid Prototyping Applications* (A. Pique and D. Chrisey, eds.), ch. 9, pp. 261–302, Elsevier, 2002.

[48] J. R. Davis, *Handbook of Thermal Spray Technology.* United States of America:

ASM International, 2004.

[49] P. Fauchais, M. Fukumoto, A. Vardelle, and M. Vardelle, "Knowledge Concerning Splat Formation: An Invited Review," *Journal of Thermal Spray Technology*, vol. 13, no. 3, pp. 337–360, 2004.

[50] V. Sobolev, J. Guilemany, and J. Nutting, *High Velocity Oxy-fuel Spraying Theory, Structure-Property Relationships and Applications*. The Institute of Materials, Minerals and Mining by Maney Publishing House, 2004.

[51] S. Kuroda, J. Kawakita, M. Watanabe, and H. Katanoda, "Warm spraying—a novel coating process based on high-velocity impact of solid particles," *Science and Technology of Advanced Materials*, vol. 9, no. 3, p. 033002, 2008.

[52] M. Schwartz, "Coatings (Thermal Spray Processes)," in *Innovations in Materials, Manufacturing, Fabrication, and Enviromental Safety,* (M. Schwartz, ed.), pp. 385–444, CRC Press Taylor & Francis Group, 2011.

[53] S. Safai and H. Herman, "Plasma-sprayed materials," in *Ultrarapid quenching of liquid alloys*, pp. 183–214, Academic Press, 1981.

[54] P. Fauchais, M. Vardelle, and S. Goutier, "Latest Researches Advances of Plasma Spraying: From Splat to Coating Formation," *Journal of Thermal Spray Technology*, vol. 25, no. 8, pp. 1534–1553, 2016.

[55] P. Fauchais, M. Vardelle, and S. Goutier, "Atmospheric Plasma Spraying Evolution Since the Sixties Through Modeling, Measurements and Sensors," *Plasma Chemistry and Plasma Processing*, vol. 37, no. 3, pp. 601–626, 2017.

[56] P. Ctibor, R. Lechnerová, and V. Beneš, "Quantitative analysis of pores of two types in a plasma-sprayed coating," *Materials Characterization*, vol. 56, no. 4-5 SPEC. ISS., pp. 297–304, 2006.

[57] S. Costil, C. Verdy, R. Bolot, and C. Coddet, "On the Role of Spraying Process on Microstructural, Mechanical, and Thermal Response of Alumina Coatings," *Journal of Thermal Spray Technology*, vol. 16, no. 5-6, pp. 839–843, 2007.

[58] E. Turunen, T. Varis, T. E. Gustafsson, J. Keskinen, T. Fält, and S.-P. P. Hannula, "Parameter optimization of HVOF sprayed nanostructured alumina and alumina–nickel composite coatings," *Surface and Coatings Technology*, vol. 200, no. 16-17, pp. 4987–4994, 2006.

[59] Y. Liu, T. E. Fischer, and A. Dent, "Comparison of HVOF and plasma-sprayed alumina/titania coatings—Microstructure, mechanical properties and abrasion behavior," *Surface and Coatings Technology*, vol. 167, no. 1, pp. 68–76, 2003.

[60] C. J. Li and A. Ohmori, "Relationships between the microstructure and properties of thermally sprayed deposits," *Journal of Thermal Spray Technology*, vol. 11, no. 3, pp. 365–374, 2002.

[61] I. Shakhova, E. Mironov, F. Azarmi, and A. Safonov, "Thermo-electrical properties of the alumina coatings deposited by different thermal spraying technologies,"

Ceramics International, vol. 43, no. 17, pp. 15392–15401, 2017.

[62] P. Fauchais, G. Montavon, and G. Bertrand, "From Powders to Thermally Sprayed Coatings," *Journal of Thermal Spray Technology*, vol. 19, no. 1, pp. 56–80, 2010.

[63] R. McPherson, "A review of microstructure and properties of plasma sprayed ceramic coatings," *Surface and Coatings Technology*, vol. 39-40, pp. 173–181, 1989.

[64] S. Beauvais, V. Guipont, M. Jeandin, D. Jeulin, A. Robisson, and R. Saenger, "Study of the Porosity in Plasma-Sprayed Alumina through an Innovative Three-Dimensional Simulation of the Coating Buildup," *Metallurgical and Materials Transactions A*, vol. 39, no. 11, pp. 2711–2724, 2008.

[65] R. McPherson, "On the formation of thermally sprayed alumina coatings," *Journal of Materials Science*, vol. 15, no. 12, pp. 3141–3149, 1980.

[66] H. C. Chen, E. Pfender, B. Dzur, and G. Nutsch, "Microstructural characterization of radio frequency and direct current plasma-sprayed Al2O3 coatings," *Journal of Thermal Spray Technology*, vol. 9, no. 2, pp. 264–273, 2000.

[67] R. McPherson and B. Shafer, "Interlamellar contact within plasma-sprayed coatings," *Thin Solid Films*, vol. 97, no. 3, pp. 201–204, 1982.

[68] G. Antou, G. Montavon, F. Hlawka, A. Cornet, and C. Coddet, "Characterizations of the pore-crack network architecture of thermal-sprayed coatings," *Materials Characterization*, vol. 53, no. 5, pp. 361–372, 2004.

[69] S. Deshpande, A. Kulkarni, S. Sampath, and H. Herman, "Application of image analysis for characterization of porosity in thermal spray coatings and correlation with small angle neutron scattering," *Surface and Coatings Technology*, vol. 187, no. 1, pp. 6–16, 2004.

[70] S. Beauvais, V. Guipont, M. Jeandin, D. Juve, D. Treheux, A. Robisson, and R. Saenger, "Influence of Defect Orientation on Electrical Insulating Properties of Plasma-Sprayed Alumina Coatings," *Journal of Electroceramics*, vol. 15, no. 1, pp. 65–74, 2005.

[71] O. Amsellem, F. Borit, D. Jeulin, V. Guipont, M. Jeandin, E. Boller, and F. Pauchet, "Three-dimensional simulation of porosity in plasma-sprayed alumina using microtomography and electrochemical impedance spectrometry for finite element modeling of properties," *Journal of Thermal Spray Technology*, vol. 21, no. 2, pp. 193–201, 2012.

[72] U. Klement, J. Ekberg, and S. T. Kelly, "3D Analysis of Porosity in a Ceramic Coating Using X-ray Microscopy," *Journal of Thermal Spray Technology*, vol. 26, no. 3, pp. 456–463, 2017.

[73] A. Kulkarni, S. Sampath, A. Goland, H. Herman, and B. Dowd, "Computed microtomography studies to characterize microstructure-property correlations in thermal sprayed alumina deposits," *Scripta Materialia*, vol. 43, no. 5, pp. 471–476, 2000.

[74] Y. Gao, M. Jie, and Y. Liu, "Mechanical properties of Al2O3 ceramic coatings prepared by plasma spraying on magnesium alloy," *Surface and Coatings Technology*, vol. 315, pp. 214–219, 2017.

[75] S. Dong, B. Song, H. Liao, and C. Coddet, "Dielectric properties of Al2O3 coatings deposited via atmospheric plasma spraying and dry-ice blasting correlated with microstructural characteristics," *Applied Physics A: Materials Science and Processing*, vol. 118, no. 1, pp. 283–290, 2015.

[76] J. Kitamura, H. Ibe, F. Yuasa, and H. Mizuno, "Plasma sprayed coatings of high-purity ceramics for semiconductor and flat-panel-display production equipment," *Journal of Thermal Spray Technology*, vol. 17, no. 5-6, pp. 878–886, 2008.

[77] J. Knuuttila, P. Sorsa, and T. Mäntylä, "Sealing of thermal spray coatings by impregnation," *Journal of Thermal Spray Technology*, vol. 8, no. 2, pp. 249–257, 1999.

[78] Y. Gao, X. Xu, Z. Yan, and G. Xin, "High hardness alumina coatings prepared by low power plasma spraying," *Surface and Coatings Technology*, vol. 154, pp. 189–193, 2002.

[79] F.-L. Toma, L.-M. Berger, C. C. Stahr, T. Naumann, and S. Langner, "Microstructures and Functional Properties of Suspension-Sprayed Al2O3 and TiO2 Coatings: An Overview," *Journal of Thermal Spray Technology*, vol. 19, no. 1-2, pp. 262–274, 2010.

[80] C. C. Stahr, S. Saaro, L.-M. Berger, J. Dubský, K. Neufuss, and M. Herrmann, "Dependence of the Stabilization of α-Alumina on the Spray Process," *Journal of Thermal Spray Technology*, vol. 16, no. 5-6, pp. 822–830, 2007.

[81] J. Ilavsky, C. C. Berndt, H. Herman, P. Chraska, and J. Dubsky, "Alumina-base plasma-sprayed materials—Part II: Phase transformations in aluminas," *Journal of Thermal Spray Technology*, vol. 6, no. 4, pp. 439–444, 1997.

[82] P. Chráska, J. Dubsky, K. Neufuss, and J. Písacka, "Alumina-base plasma-sprayed materials part I: Phase stability of alumina and alumina-chromia," *Journal of Thermal Spray Technology*, vol. 6, no. 3, pp. 320–326, 1997.

[83] R. J. Damani and P. Makroczy, "Heat treatment induced phase and microstructural development in bulk plasma sprayed alumina," *Journal of the European Ceramic Society*, vol. 20, no. 7, pp. 867–888, 2000.

[84] R. McPherson, "Formation of metastable phases in flame- and plasma-prepared alumina," *Journal of Materials Science*, vol. 8, no. 6, pp. 851–858, 1973.

[85] L. Brown, H. Herman, and R. MacCrone, "Plasma-sprayed insulated metal substrates," in *Proceedings of the Elevent International Thermal Spray Conference*, pp. 507–512, 1986.

[86] G. Heintze and S. Uematsu, "Preparation and structures of plasma-sprayed γ- and α-Al2O3 coatings," *Surface and Coatings Technology*, vol. 50, no. 3, pp. 213–222,

1992.

[87] R. Venkataraman, P. Singh, and R. Krishnamurthy, "Enhanced α phase stability during plasma spraying of alumina-13 mol% titania," *Journal of the American Ceramic Society*, vol. 89, no. 2, pp. 734–736, 2006.

[88] G. Di Girolamo, A. Brentari, C. Blasi, and E. Serra, "Microstructure and mechanical properties of plasma sprayed alumina-based coatings," *Ceramics International*, vol. 40, no. 8, pp. 12861–12867, 2014.

[89] P. Zamani and Z. Valefi, "Microstructure, phase composition and mechanical properties of plasma sprayed Al2O3 , Cr2O3 and Cr2O3 -Al2O3 composite coatings," *Surface and Coatings Technology*, vol. 316, pp. 138–145, 2017.

[90] J. Gao, X. Xiong, and Y. Gao, "The effect of the α/γ phase on the dielectric properties of plasma sprayed Al2O3 coatings," *Journal of Materials Science: Materials in Electronics*, vol. 28, no. 16, pp. 12015–12020, 2017.

[91] Y. An, S. Li, G. Hou, X. Zhao, H. Zhou, and J. Chen, "Mechanical and tribological properties of nano/micro composite alumina coatings fabricated by atmospheric plasma spraying," *Ceramics International*, vol. 43, no. 6, pp. 5319–5328, 2017.

[92] J. Rong, K. Yang, Y. Zhuang, J. Ni, H. Zhao, S. Tao, X. Zhong, and C. Ding, "Phase and Microstructure Evolution and Toughening Mechanism of a Hierarchical Architectured Al2O3–Y2O3 Coating under High Temperature," *Journal of Thermal Spray Technology*, vol. 27, no. 3, pp. 358–370, 2018.

[93] T. Owoseni, J. Murray, Z. Pala, E. Lester, D. Grant, and T. Hussain, "Suspension high velocity oxy-fuel (SHVOF) spray of delta-theta alumina suspension: Phase transformation and tribology," *Surface and Coatings Technology*, vol. 371, pp. 97–106, 2019.

[94] L. A. Dissado and J. Fothergill, *Electrical Degradation and Breakdown in Polymers*. The Institution of Electrical Engineering and Technology, London, United Kingdom, first ed., 1992.

[95] R. Bartnikas and R. Eichhorn, eds., *Engineering Dielectrics Volume IIA, Electrical Properties of Solid Insulating Materials: Molecular Structure and Electrical Behavior*. Philadelphia, USA: American Society for Testing and Materials, 1983.

[96] K. C. Kao, *Dielectric Phenomena in Solids*. Elsevier, 2004.

[97] J. O'Dwyer, "Breakdown in Solid Dielectrics," *IEEE Transactions on Electrical Insulation*, vol. EI-17, no. 6, pp. 484–487, 1982.

[98] J. J. O'Dwyer, *The Theory of Electrical Conduction and Breakdown in Solid Dielectrics*. Oxford: Clarendon Press, 1973.

[99] E. Kuffel, W. Zaengl, and J. Kuffel, *High Voltage Engineering: Fundamentals*. Oxford, United Kingdom: Elsevier Ltd, second ed., 2000.

[100] A. Moulson and J. M. Herbert, *Electroceramics*. John Wiley & Sons Ltd, second ed., 2003.

[101] M. Ieda, "Dielectric Breakdown Process of Polymers," *IEEE Transactions on Electrical Insulation*, vol. EI-15, no. 3, pp. 206–224, 1980.

[102] M. Yoshimura and H. K. Bowen, "Electrical Breakdown Strength of Alumina at High Temperatures," *Journal of the American Ceramic Society*, vol. 64, no. 7, pp. 404–410, 1981.

[103] I. O. Owate and R. Freer, "Dielectric breakdown of ceramics and glass ceramics," in *Sixth International Conference on Dielectric Materials, Measurements and Applications*, pp. 443–446, 1992.

[104] S. Carabajar, C. Olagnon, G. Fantozzi, and C. Le Gressus, "Relations between electrical breakdown field and mechanical properties of ceramics," in *Proceedings of 1995 Conference on Electrical Insulation and Dielectric Phenomena*, pp. 278–291, 1995.

[105] C. Neusel and G. A. Schneider, "Size-dependence of the dielectric breakdown strength from nano- to millimeter scale," *Journal of the Mechanics and Physics of Solids*, vol. 63, no. February, pp. 201–213, 2014.

[106] C. Neusel, H. Jelitto, D. Schmidt, R. Janssen, F. Felten, and G. A. Schneider, "Thickness-dependence of the breakdown strength: Analysis of the dielectric and mechanical failure," *Journal of the European Ceramic Society*, vol. 35, no. 1, pp. 113–123, 2015.

[107] F. Talbi, F. Lalam, and D. Malec, "DC conduction of Al2O3 under high electric field," *Journal of Physics D: Applied Physics*, vol. 40, no. 12, pp. 3803–3806, 2007.

[108] L. Haddour, N. Mesrati, D. Goeuriot, and D. Tréheux, "Relationships between microstructure, mechanical and dielectric properties of different alumina materials," *Journal of the European Ceramic Society*, vol. 29, no. 13, pp. 2747–2756, 2009.

[109] Z. Jouini, D. Malec, and Z. Valdez-Nava, "Effect of mechanical prestress on the dielectric strength of alumina," in *Proceedings of the 2016 IEEE International Conference on Dielectrics, ICD 2016*, vol. 2, pp. 1089–1092, IEEE, 2016.

[110] A. Si Ahmed, J. Kansy, K. Zarbout, G. Moya, J. Liebault, and D. Gœuriot, "Microstructural origin of the dielectric breakdown strength in alumina: A study by positron lifetime spectroscopy," *Journal of the European Ceramic Society*, vol. 25, no. 12, pp. 2813–2816, 2005.

[111] C. Neusel, H. Jelitto, and G. A. Schneider, "Electrical conduction mechanism in bulk ceramic insulators at high voltages until dielectric breakdown," *Journal of Applied Physics*, vol. 117, no. 15, p. 154902, 2015.

[112] H. Wintle, "Conduction Processes in Polymers," in *Engineering Dielectrics Volume IIA, Electrical Properties of Solid Insulating Materials: Molecular Structure and Electrical Behavior* (R. Bartnikas and R. Eichhorn, eds.), ch. Chapter 3, Baltimore: ASTM International, 1983.

[113] P. K. Karahaliou, M. Theodoropoulou, C. A. Krontiras, N. Xanthopoulos, S. N.

Georga, M. N. Pisanias, M. Kokonou, A. G. Nassiopoulou, and A. Travlos, "Transient and alternating current conductivity of nanocrystalline porous alumina thin films on silicon, with embedded silicon nanocrystals," *Journal of Applied Physics*, vol. 95, no. 5, pp. 2776–2780, 2004.

[114] R. Bartnikas, "Dielectric Loss in Solids," in *Engineering Dielectrics Volume IIA, Electrical Properties of Solid Insulating Materials: Molecular Structure and Electrical Behavior* (R. Bartnikas and R. M. Eichhorn, eds.), ch. Chapter 1, Baltimore: ASTM International, 1983.

[115] R. D. Shannon and G. R. Rossman, "Dielectric constant of MgAl2O4 spinel and the oxide additivity rule," *Journal of Physics and Chemistry of Solids*, vol. 52, no. 9, pp. 1055–1059, 1991.

[116] J. P. Borja, T.-m. Lu, and J. Plawsky, *Dielectric Breakdown in Gigascale Electronics*. Springer Briefs in Materials, Springer International Publishing, 2016.

[117] J. J. Steppan, J. A. Roth, L. C. Hall, D. A. Jeannotte, and S. P. Carbone, "A Review of Corrosion Failure Mechanisms during Accelerated Tests: Electrolytic Metal Migration," *Journal of The Electrochemical Society*, vol. 134, no. 1, pp. 175–190, 1987.

[118] R. Manepalli, F. Stepniak, S. Bidstrup-Allen, and P. Kohl, "Silver metallization for advanced interconnects," *IEEE Transactions on Advanced Packaging*, vol. 22, no. 1, pp. 4–8, 1999.

[119] S. Yang, J. Wu, and A. Christou, "Initial stage of silver electrochemical migration degradation," *Microelectronics Reliability*, vol. 46, no. 9-11, pp. 1915–1921, 2006.

[120] H. M. Naguib and B. K. Mac Laurin, "Silver Migration and the Reliability of Pd/Ag Conductors in Thick-Film Dielectric Crossover Structures," *IEEE Transactions on Components, Hybrids, and Manufacturing Technology*, vol. 2, no. 2, pp. 196–207, 1979.

[121] G. T. Kohman, H. W. Hermance, and G. H. Downes, "Silver Migration in Electrical Insulation," *Bell System Technical Journal*, vol. 34, no. 6, pp. 1115–1147, 1955.

[122] G. Harsanyi, "Electrochemical Processes Resulting in Migrated Short Failures in Microcircuits," *IEEE Transactions on Components Packaging and Manufacturing Technology Part A*, vol. 18, no. 3, pp. 602–610, 1995.

[123] Y. Mei, D. Ibitayo, X. Chen, S. Luo, and G.-Q. Lu, "Migration of sintered nanosilver die-attach material on alumina substrate at high temperatures," in *2011 12th International Conference on Electronic Packaging Technology and High Density Packaging*, vol. 1, pp. 1–6, IEEE, 2011.

[124] Y. Mei, G.-Q. Lu, X. Chen, S. Luo, and D. Ibitayo, "Migration of Sintered Nanosilver Die-Attach Material on Alumina Substrate Between 250 °C and 400 °C in Dry Air," *IEEE Transactions on Device and Materials Reliability*, vol. 11, no. 2, pp. 316–322, 2011.

[125] G.-Q. Lu, W. Yang, Y. Mei, X. Li, G. Chen, and X. Chen, "Effects of DC bias and spacing on migration of sintered nanosilver at high temperatures for power electronic packaging," in *2013 14th International Conference on Electronic Packaging Technology*, pp. 925–930, IEEE, 2013.

[126] G.-Q. Lu, W. Yang, Y.-H. Mei, X. Li, G. Chen, and X. Chen, "Mechanism of Migration of Sintered Nanosilver at High Temperatures in Dry Air for Electronic Packaging," *IEEE Transactions on Device and Materials Reliability*, vol. 14, no. 1, pp. 311–317, 2014.

[127] G. T. Kohman, J. M. A. de Bruyne, G. T. Kohraan, and J. M. A. de Bruyne, "The migration of silver through and on the surface of insulating materials," in *1954 Conference On Electrical Insulation*, pp. 55–56, IEEE, 1954.

[128] H. Ling and A. Jackson, "Correlation of silver migration with temperature-humidity-bias (THB) failures in multilayer ceramic capacitors," *IEEE Transactions on Components, Hybrids, and Manufacturing Technology*, vol. 12, no. 1, pp. 130–137, 1989.

[129] W. Hauschild and W. Mosch, *Statistical Techniques for High-Voltage Engineering*. Milton Keynes: Lightning Source UK LTd, 1992.

[130] "IEC 62539 Guide for the statistical analysis of electrical insulation breakdown data," 2007.

[131] "IEC standard 60093 Methods of test for volume resistivity and surface resistivity of solid electrical insulating materials," 1980.

[132] "ASTM Standard D257 - 07 Standard Test Methods for DC Resistance and Conductance of Insulating Materials," 2007.

[133] "IEC standard 60250 Recommended methods for the determination of the permittivity and dielectric dissipation factor of electrical insulating materials at power, audio and radio frequencies including metre wavelengths," 1969.

[134] R. Bartnikas, "Dielectrics and Insulators," in *The Electrical Engineering Handbook, Second Edition*, Electrical Engineering Handbook, CRC Press, 1997.

[135] "ASTM Standard D-149-09(2013) Standard Test Method for Dielectric Breakdown Voltage and Dielectric Strength of Solid Electrical Insulating Materials at Commercial Power Frequencies," 2013.

[136] P. H. F. Morshuis and J. J. Smit, "Partial discharges at DC voltage: their mechanism, detection and analysis," *Dielectrics and Electrical Insulation, IEEE Transactions on*, vol. 12, no. 2, pp. 328–340, 2005.

[137] E. P. Song, J. Ahn, S. Lee, and N. J. Kim, "Effects of critical plasma spray parameter and spray distance on wear resistance of Al2O3–8 wt.%TiO2 coatings plasma-sprayed with nanopowders," *Surface and Coatings Technology*, vol. 202, no. 15, pp. 3625–3632, 2008.

[138] M. Touzin, D. Goeuriot, C. Guerret-Piécourt, D. Juvé, and H.-J. Fitting, "Alumina based ceramics for high-voltage insulation," *Journal of the European Ceramic*

Society, vol. 30, no. 4, pp. 805–817, 2010.

[139] H. Khare and D. Burris, "A quantitative method for measuring nanocomposite dispersion," *Polymer*, vol. 51, no. 3, pp. 719–729, 2010.

[140] J. Ye, H. Khare, and D. Burris, "Quantitative characterization of solid lubricant transfer film quality," *Wear*, vol. 316, no. 1-2, pp. 133–143, 2014.

[141] G. Chen and J. Zhao, "Space charge and thickness dependent dc electrical breakdown of solid dielectrics," in *2012 International Conference on High Voltage Engineering and Application*, pp. 12–15, IEEE, 2012.

[142] G. Chen, J. Zhao, S. Li, and L. Zhong, "Origin of thickness dependent dc electrical breakdown in dielectrics," *Applied Physics Letters*, vol. 100, no. 22, p. 222904, 2012.

[143] M. Lenzlinger, "Fowler-Nordheim Tunneling into Thermally Grown SiO2," *Journal of Applied Physics*, vol. 40, no. 1, p. 278, 1969.

[144] A. Jonscher, *Dielectric relaxation in solids*. London: Chelsea Dielectrics Press, 1983.

[145] L. A. Dissado and R. M. Hill, "Anomalous low-frequency dispersion. Near direct current conductivity in disordered low-dimensional materials," *Journal of the Chemical Society, Faraday Transactions 2*, vol. 80, no. 3, p. 291, 1984.

[146] A. K. Jonscher, "Dielectric relaxation in solids," *Journal of Physics D: Applied Physics*, vol. 32, no. 14, pp. R57–R70, 1999.

[147] A. A. Abdelmalik, S. J. Dodd, L. A. Dissado, N. M. Chalashkanov, and J. C. Fothergill, "Charge transport in thermally aged paper impregnated with natural ester oil," *IEEE Transactions on Dielectrics and Electrical Insulation*, vol. 21, no. 5, pp. 2318–2328, 2014.

[148] N. Chalashkanov and L. Dissado, "Dielectric Measurements in the Frequency Domain—Dos and Don'ts," *IEEE Electrical Insulation Magazine*, vol. 38, no. 5, pp. 28–38, 2022.

[149] A. Jonscher and L. Levesque, "Volume low-frequency dispersion in a semi-insulating system," *IEEE Transactions on Electrical Insulation*, vol. 23, no. 2, pp. 209–213, 1988.

[150] A. Jonscher and A. Husain, "Dynamic transport on humid silica surface I," *Physica B: Condensed Matter*, vol. 217, no. 1-2, pp. 29–34, 1996.

[151] C. Li, A. Ohmori, and R. Mcpherson, "The relationship between microstructure and Young's modulus of thermally sprayed ceramic coatings," *Journal of Materials Science*, vol. 32, no. 4, pp. 997–1004, 1997.

[152] F. Favre, F. Villieras, Y. Duval, E. Mcrae, and C. Rapin, "Influence of relative humidity on electrical properties of α-Al 2O3 powders: Resistivity and electrochemical impedance spectroscopy," *Journal of Colloid and Interface Science*, vol. 286, no. 2, pp. 615–620, 2005.

Appendix A

Short-term electrical performance of the studied coatings

Table A.1: The electrical performance of the studied coatings at at 20 °C, RH20% [P1]–[P8]. The breakdown fields of the studied coatings at the breakdown probabilities of 10%, 63.2% and 90% and Weibull β. The statistical analysis of the breakdown data was performed using Weibull++ software. DC resistivity of the coatings are presented at two different electric fields. The dielectric losses are presented at two frequencies when the measuring voltage was 200 V_{peak} which corresponds the electric field of 0.5–1V_{peak}/µm. However, the measuring electric field was 0.3V_{peak}/µm for the alumina coatings HVOF6B, PlasmaA and FlameA [P8].

Sample		BDS ($V\,\mu m^{-1}$)				DC resistivity ($\Omega\,m$)		Dielectric loss		Publication
		$E_{10\%}$	α, $E_{63.2\%}$	$E_{90\%}$	β	$E = 0.5\,V\,\mu m^{-1}$	$E = 2\,V\,\mu m^{-1}$	at 1 Hz	at 1 kHz	
HVOF1	exp. Al_2O_3–MgO	22.6	32.3	36.8	6.3	5.6×10^{12}	1.6×10^{12}	0.67	5.12	[P5]
HVOF2	com. Al_2O_3	15.3	23.3	27.3	5.3	4.4×10^{12}	1.8×10^{12}	0.67	14.4	[P5]
HVOF3	com. Al_2O_3	21.6	26.2	28.2	11.6	5.2×10^{11}	6.5×10^{10}	0.62	23.7	[P5]
HVOF4	com. $MgAl_2O_4$	15.0	20.6	23.2	7.1	4.5×10^{12}	6.5×10^{11}	0.49	10.8	[P5]
HVOF5	com. Al_2O_3	25.7	31.8	34.5	10.5	3.5×10^{12}	8.0×10^{11}	0.65	16.6	[P4, P7]
HVOF6A	com. Al_2O_3	23.9	34.0	38.8	6.4	-	-	-	-	[P3]
HVOF6B	com. Al_2O_3	22.9	35.1	41.2	5.3	1.1×10^{12}	1.9×10^{11}	0.71	23.2	[P7, P8]
HVOF7	exp. 100% Al_2O_3	31.7	39.2	42.3	10.7	4.8×10^{12}	2.6×10^{12}	0.37	11.6	[P6, P7]
HVOF8	90% Al_2O_3–10% MgO	40.8	48.1	51.2	13.6	7.7×10^{12}	5.1×10^{12}	0.28	8.6	[P6, P7]
HVOF9	75% Al_2O_3–25% MgO	41.5	49.6	52.9	12.7	2.3×10^{13}	1.7×10^{13}	0.12	3.0	[P6, P7]
HVOF10	60% Al_2O_3–40% MgO	16.6	24.1	27.7	6.0	2.1×10^{13}	1.6×10^{13}	0.09	2.0	[P6]
HVOF11	50% Al_2O_3–50% MgO	33.9	40.3	43.0	13.1	3.1×10^{13}	2.2×10^{13}	0.08	2.2	[P6, P7]
HVOF12	35% Al_2O_3–65% MgO	14.0	22.0	26.0	5.0	1.7×10^{13}	1.6×10^{13}	0.06	1.3	[P6]
HVOF13	exp. $MgAl_2O_4$	9.8	14.6	17.0	5.6	3×10^{12}	2.2×10^{11}	0.41	5.6	[P1, P2]
PlasmaA	com.Al_2O_3	8.6	19.4	26.2	2.8	2.0×10^{12}	4.3×10^{11}	0.73	17.9	[P7, P8]
PlasmaB	exp. $MgAl_2O_4$	12.6	18.2	20.8	6.2	4.6×10^{12}	5.4×10^{11}	0.37	7.5	[P2]
FlameA	com. Al_2O_3	12.5	14.1	14.7	19.8	3.2×10^{11}	9.6×10^{9}	1.09	20.7	[P8]
FlameB	com. $MgAl_2O_4$	13.2	18.4	20.7	6.8	1.5×10^{11}	8.1×10^{8}	2.85	58.8	[P2]

Publications

Publication I

Dielectric properties of HVOF sprayed ceramic coatings

M. Niittymäki, T. Suhonen, U. Kanerva, J. Metsäjoki and K. Lahti

Proceedings of IEEE International Conference on Solid Dielectrics, ICSD, pp. 389–392, 2013

DOI:10.1109/ICSD.2013.6619769

Dielectric Properties of HVOF Sprayed Ceramic Coatings

Minna Niittymäki and Kari Lahti
Department of Electrical Engineering
Tampere University of Technology
Tampere, Finland
minna.niittymaki@tut.fi

Tomi Suhonen, Ulla Kanerva and Jarkko Metsäjoki
Advanced Materials
VTT Technical Research Centre of Finland
Espoo, Finland

Abstract— **Thermally sprayed ceramic coatings can be used as electrical insulators for example in high temperature applications (e.g. fuel cells) or in other demanding conditions. In electrical insulation applications the mostly used coating materials are aluminum oxide, magnesium oxide and magnesium aluminate. In general, only few reports of dielectric properties of thermally sprayed ceramic coatings can be found in literature and further analysis is thus needed. In addition, the measurement methods and conditions in previous research are often not fully documented, complicating the evaluation and comparison of the properties of different coatings. The aim of this paper was to characterize dielectric properties of thermally sprayed ceramic spinel coating sprayed with high-velocity oxygen fuel (HVOF) technique. The studied dielectric properties are DC resistivity, DC dielectric breakdown strength, as well as permittivity and dielectric losses at different frequencies. All measurements were made at temperature of 20 °C and at relative humidity of 20 %. Dielectric properties and the composition of coating material are presented and analyzed.**

Keywords— thermal spraying; HVOF; spinel; coating; resistivity; dielectric spectroscopy; dielectric breakdown strength

I. INTRODUCTION

Thermally sprayed insulating ceramic coatings can be used in demanding conditions where normal insulating materials such as for example polymers cannot be used. As an electrically insulating coating material the most commonly used materials are aluminum oxide (Al_2O_3) and magnesium aluminate ($MgAl_2O_4$). In general, only little research of dielectric properties of thermally sprayed ceramic coatings can be found in literature. In addition, the measurement methods and conditions in previous research are often not fully documented, complicating the evaluation and comparison of the properties of different coatings.

Earlier studies of electrical properties of thermally sprayed coatings are focused on the HVOF (high velocity oxygen fuel) and plasma sprayed alumina coatings [1, 2, 3, 4]. One paper presented DC resistance and DC dielectric breakdown strength of HVOF and plasma sprayed spinel coatings at room temperature conditions and at high humidity levels [3]. Formerly, dielectric spectroscopy studies have been made only for plasma sprayed alumina [1]. The results of the papers [3, 4] indicate that electrical properties of HVOF sprayed alumina and spinel coatings require to be examined more detailed and it has been already seen that especially the microstructure of a coating affects significantly to the electrical properties.

This paper presents the dielectric properties of thermally sprayed magnesium aluminate (spinel) concentrating on the DC resistivity, relative permittivity and dielectric losses as a function of frequency, and DC dielectric strength. All measurements are performed at temperature of 20 °C and relative humidity of 20 %.

II. EXPERIMENTAL

A. Studied Thermally Sprayed Ceramic Coating

The raw materials of the used spinel powder were AlO(OH) (particle size 40 nm and purity 99.99 %) and $Mg(OH)_2$ (particle size 300 – 1800 nm and purity 99.8 %). The proportions of raw materials correspond to a stoichiometric magnesium aluminum spinel ($MgAl_2O_4$). During the sintering process, aluminum hydroxide and magnesium hydroxide formed to $MgAl_2O_4$ –powder. The used spinel powder was experimentally agglomerated by spray drying (Niro p6.3 pilot) and sintered at temperature of 1300 °C. After sintering, the powder particles had very dense microstructure and particle size of the powder was from 6 µm to 21 µm which is very suitable size for HVOF-process.

The $MgAl_2O_4$–powder was deposited on stainless steel substrate (size of 100 mm x 100 mm) by HVOF –process. Number of studied samples was four (A, B, C and D). Table I illustrates the porosity values of the coatings which were measured by optical micrographs and scanning electron microscope (SEM) with two measuring methods: secondary electrons (SE) and back-scattering electrons (BSE). The coating thicknesses of the samples were defined both from cross section figures of two samples deposited at the same time with samples A, B, C and D, and by magnetic measuring device (Elcometer 456C). In the latter case, the thickness result of a sample is an average value of 10 measurements made along the electrode area. The measurement results are presented in Table II. In Fig. 1 the cross-section figures of the studied spinel coating are shown.

Some deviation is noticed in the thickness values because the substrate is not smooth due to the the sandblasting of the substrate before depositing the ceramic coating. In addtion to that, the coating itself has lamellar microstructure causing a sligthly non-smooth surface.

B. Sample Preparation

Dielectric spectroscopy and DC breakdown measurements were made at temperature of 20 °C and relative humidity of

TABLE I. POROSITY OF THE STUDIED THERMALLY SPRAYED COATING.

Porosity [%]		
SEM/SE	***SEM/BSE***	***Optical micrographs***
0.6	1.74	0.25

TABLE II. COATING THICKNESS OF THE STUDIED SAMPLES.

Coating thickness (µm)			Standard deviation (µm)	
Average from cross-section figure	***Average from magnetic measurement for sample A***	***Average from magnetic measurement for sample D***	***Sample A***	***Sample D***
342	362	359	10.0	9.6

20 %, but the DC resistivity measurements were made at temperature of 20 °C and relative humidity of 25 %.These conditions were maintained at the climate room of TUT High voltage laboratory. The samples were preconditioned at 120 °C for two hours and then stabilized at 20 °C and RH 20 % for 12 hours before measurements. Before DC resistivity and relative permittivity –measurements, a round silver electrode was painted on the middle of a coating. The diameter of the electrode was 50 mm. In addition, a shield electrode was painted around the measuring electrode to neglect possible surface currents. From cross section figures it was studied that the used high purity silver paint did not penetrate inside the studied thermally sprayed coating.

C. DC Resistivity

Resistivity measurements were made using Keithley 6517B electrometer and Keihtley Resistivity test fixture 8009. The test voltage was maintained until a stabilized current level (i.e. pure resistive current) was reached. In practice, the tests were performed at test voltages from 10 V to 1000 V and the stabilized DC current was measured 1000 s after voltage application. At higher test voltages (corresponding to field strengths above ohmic region), the DC current did not fully stabilize during the measurement period. In these cases, the resistivity values were also defined according the currents measured 1000 s after voltage application. The volume resistivity of a material was thus defined according to IEC standard 60093 (or ASTM D257-07). [5,6]

D. Dielectric Spectroscopy

Relative permittivity and dielectric losses of the materials were studied with an insulating diagnosis (IDA 200) analyzer

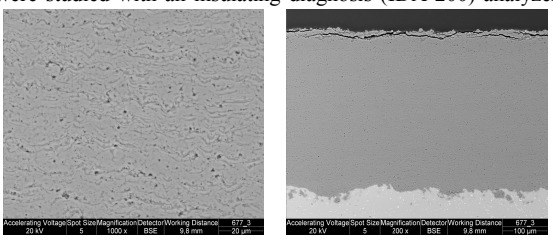

Fig. 1. Cross-section figures of the studied coating.

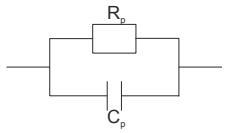

Fig. 2. Equivalent RC parallel electrical circuit in dielectric spectroscopy measurements

device. During the measurements, a sinusoidal voltage with varying frequency was applied over the sample. The true RMS value of the measuring voltage was 140 V. The complex impedance of a sample was calculated from the measured test voltage and the current through a sample which is expressed as the equivalent parallel RC circuit model (Fig. 2). The relative permittivity (ε_r) and dissipation factor (tan δ) were calculated from the measured parallel resistance and capacitance with Eq. (1) - (2):

$$\varepsilon_r \approx \varepsilon_r' = \frac{C_p}{C_0} - \frac{C_e}{C_0}, \tag{1}$$

$$\tan\delta = \frac{1}{R_p C_0 \omega}, \tag{2}$$

where C_p is measured parallel capacitance and R_p parallel resistance of the equivalent circuit model of a dielectric (Fig. 2). C_0 is the so called geometric capacitance of test sample (vacuum in place of the insulation) and ω is angular frequency. The edge field correction (C_e) was not used because the shield electrode was utilized in the measurements. All the test sample arrangements were according to IEC standard 60250 [7].

Loss index (ε_r'') includes all losses of a sample: both conductive and dielectric ones. It can be defined from relative permittivity and dissipation factor, tan δ, with Eq. (3).

$$\varepsilon_r'' = \varepsilon_r \tan\delta \tag{3}$$

E. DC Dielectric Breakdown Strength

Breakdown voltage measurements were made with linearly ramped DC voltage. The measurements were made without immersing the samples into transformer oil because it has been found that the oil immerses into the porous coating and thus increases the dielectric strength of a coating. The used electrode was a flat ended stainless steel rod with a diameter of 10 mm and edge rounding radius of 1 mm. No painted, sputtered or by other means embedded electrodes on the specimen surface were used. The ramp rate of the test voltage was 100 V/s throughout the test until breakdown occurred.

After the breakdown voltage was measured, the thickness of a coating was measured from the breakdown point to define exactly the dielectric breakdown field strength for the coating. The thicknesses were measured with a magnetic measurement device (Elcometer 6517B). Dielectric breakdown field strength of a coating was calculated dividing the breakdown voltage by the corresponding thickness of the breakdown point. The average value of dielectric strength of a sample was calculated from five parallel test results.

III. RESULTS AND DISCUSSION

A. DC Resistivity

Normally the DC resistance of an insulating material is an approximately fixed value (ohmic behavior) at normal service field strengths. During DC resistivity measurements of these samples it was noticed that the conduction of the samples was not ohmic at different voltages. Due to this a more detailed measurement series was performed to find out the region of ohmic conduction and the corresponding change to non-ohmic conduction. Table III presents the resistivity values for samples A and D at different electric fields. Fig. 3 presents the defined resistivity values as a function of electric field. It can be observed that the resistivity of the coating is approximately $3*10^{12}$ Ωm at field strengths below ~0.5 V/µm indicating ohmic conduction behavior but above that a clearly non-ohmic behavior can be noticed. In [8], at high temperatures (800 °C – 1400 °C) it was observed that bulk alumina had ohmic behavior at voltages below 100 V which corresponds approximately field strength of 0.8 V/µm and above 150 V (~1.3 V/µm) it had non ohmic behavior but this was not studied at room temperature conditions [8].

Since the resistivities changed remarkably at higher measuring voltages, some kind of a pre-breakdown behavior may have taken place during the measurements. Due this the measurements were repeated on next day to find out if some permanent changes had taken place during the first measurements. Fig. 4 illustrates the resistivity values of sample A as a function of electric field on the 1st measurement day, when the measurement voltages were from 25 V to 1000 V, and on the 2nd measurement day when the voltages were from 50 V to 1000 V. It can be noticed that material had some permanent degradation during the first measurements because the resistivity values are lower on the 2nd day than on the 1st day. Some pre-breakdown mechanism probably occurs when the electric field is above approximately 0.5 V/µm.

TABLE III. MEASUREMENT VOLTAGE, ELECTRIC FIELD AND RESISTIVITY FOR SAMPLE A AND D .

Measurement voltage (V)	Electric field (V/µm)	Resistivity (Ωm) for sample A	Resistivity (Ωm) for sample D
10	0.03		2.54E+12
20	0.06		2.97E+12
25	0.07	2.87E+12	
30	0.08		3.31E+12
40	0.11		3.51E+12
50	0.14	3.05E+12	3.68E+12
60	0.17		3.80E+12
70	0.19		3.87E+12
75	0.21	3.15E+12	
100	0.28	3.18E+12	
125	0.35	3.16E+12	
150	0.41	3.10E+12	
175	0.48	2.92E+12	
200	0.55	2.80E+12	
300	0.83	1.86E+12	
400	1.11	1.29E+12	
500	1.38	8.06E+11	
600	1.66	4.37E+11	
700	1.94	2.22E+11	
800	2.21	1.19E+11	
900	2.49	7.03E+10	
1000	2.77	4.59E+09	

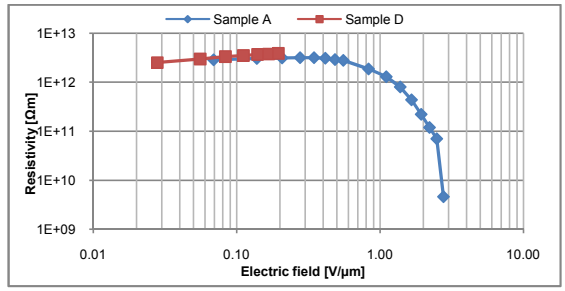

Fig. 3. DC resistivity as a function of electric field for samples A.

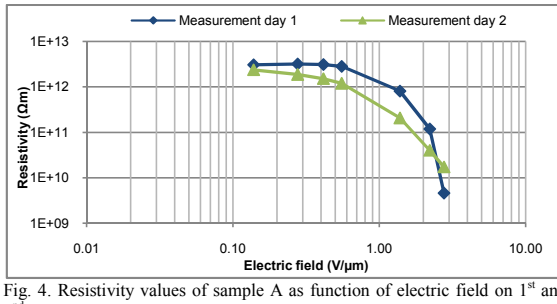

Fig. 4. Resistivity values of sample A as function of electric field on 1st and 2nd measurement day.

The observed non-ohmic behavior at relatively low field strengths may be related to the lamellar microstructure of the coating (Fig. 1). The coating consists of areas of bulk spinel material ('splats' formed in the spraying process), very rapidly cooled interfacial layers in between them and air voids which all probably have different dielectric properties. Electric field may thus be inhomogeneous due to this and more highly stressed layers may break down in the pre-breakdown region. The conduction behavior of the coatings will be studied in more detail in the future and for example the role of interfacial areas will be investigated.

B. Dielectric Spectroscopy

Fig. 5 presents the relative permittivity as a function of frequency for the sample A. The relative permittivity is 10.3 at frequency of 50 Hz. In [9], the relative permittivity of bulk

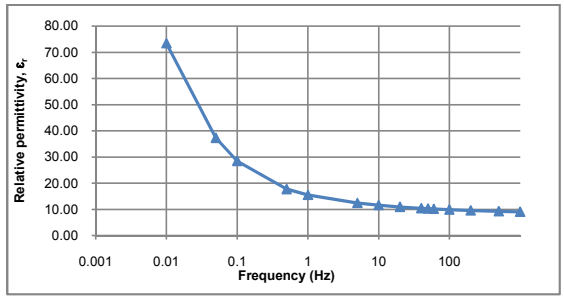

Fig. 5. Relative permittivity of sample A as a function of frequency.

spinel was approximately 8 – 8.5 at 1 MHz [9]. Fig. 6 illustrates the loss index of sample A as a function of frequency. The loss index is 1.1 at 50 Hz. In general, both the permittivity and the loss index are high compared to bulk insulating materials especially at low frequencies. This is probably related to the microstructure of thermally sprayed coatings described in section II. Quite high interfacial polarization may be expected due to the lamellar coating structure increasing both permittivity and losses at lower frequencies. The measuring voltage falls in the ohmic conduction range observed in the DC measurements.

C. DC Dielectric Breakdown Strength

Table IV shows the DC dielectric breakdown strength for samples B and C. Five breakdown results were measured for both samples and average values are defined from these values. The dielectric strengths vary greatly between different measurement points. In [3], the dielectric strength of one type of HVOF spinel ($MgAl_2O_4$) coatings with thickness of 200 µm was ~ 31 V/µm and for a spinel sample of thickness of ~95 µm it was 39 V/µm at room conditions. In [3], it was only indicated that the measurements were made at room conditions and thus the results cannot be directly compared because the humidity affects greatly to the electrical properties of ceramic coatings. The breakdown measurements were performed for as-sprayed coatings without baking samples before measurement and silver painted electrode was used on the top of samples in the breakdown measurements [3]. Because the microstructure, measurement arrangements and measurement conditions are different in this study than in the earlier research [3], the measurement results cannot, anyhow, be directly compared.

IV. CONCLUSIONS

In the DC resistivity measurements, the studied thermally sprayed HVOF spinel coating indicated non-ohmic behavior already at quite low field strengths of approx. 0.5V/µm and above. During DC measurements performed at < 3V/µm field strengths at least some permanent changes were observed. The average DC breakdown field strength of the spinel coating was measured to be 14 and 17 V/µm for the samples, respectively, but the deviation of the results were really high. Relative permittivity and loss index of the material were rather high especially at lower frequencies.

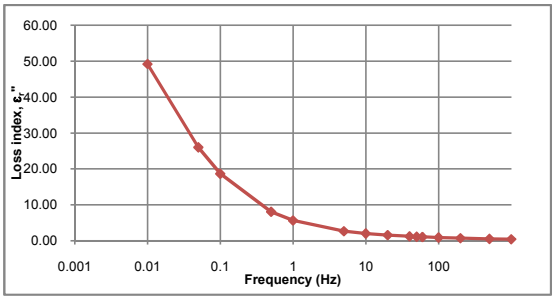

Fig. 6. Loss index of sample A as a function of frequency.

TABLE IV. DC DIELECTRIC BREAKDOWN STRENGTH

Sample	Measurement number	Breakdown voltage (V)	Thickness of the sample (µm) at the measurement point	Breakdown strength (V/µm)	Average breakdown strength (V/µm)	Standard deviation (V/µm)
B	1	3945	342	11.5	13.5	2.1
	2	5680	342	16.6		
	3	4720	347	13.6		
	4	5110	363	14.1		
	5	4065	350	11.6		
C	1	7225	333	21.7	16.9	4.8
	2	4875	348	14.0		
	3	7590	335	22.7		
	4	4190	322	13.0		
	5	4480	338	13.3		

All the results are supposed to be related to the lamellar microstructure (with also some porosity) of thermally sprayed coatings. The probably different dielectric properties of interfacial areas and the bulk may enhance the interfacial polarization and losses especially at lower frequencies. Interfacial layers probably contribute also on the non-ohmic conductivity observed.

REFERENCES

[1] L. Pawłowski, "The relationship between structure and dielectric properties in plasma-sprayed alumina coatings," *Surface and Coatings Technology,* vol. 35, pp. 285-298, 1988.

[2] M. Prudenziati, "Development and the implementation of high-temperature reliable heaters in plasma spray technology," *Journal of Thermal Spray Technology,* vol. 17, pp. 234-243, 2008.

[3] F.L. Toma, S. Scheitz, L.M. Berger, V. Sauchuk, M. Kusnezoff and S. Thiele, "Comparative study of the electrical properties and characteristics of thermally sprayed alumina and spinel coatings," *Journal of Thermal Spray Technology,* vol. 20, pp. 195-204, 2011.

[4] F.L. Toma, L.M . Berger, S. Scheitz, S. Langner, C. Rödel, A. Potthoff, V. Sauchuk and M. Kusnezoff, "Comparison of the Microstructural Characteristics and Electrical Properties of Thermally Sprayed Al_2O_3 Coatings from Aqueous Suspensions and Feedstock Powders," *Journal of Thermal Spray Technology.,* vol. 21, pp. 480-488, 2012.

[5] "Standard Test Methods for DC Resistance and Conductance of Insulating Materials," *ASTM Standard D257 - 07*, 2007.

[6] "Methods of test for volume resistivity and surface resistivity of solid electrical insulating materials," *IEC Standard 60093*, 1980.

[7] "Recommended methods for the determination of the permittivity and dielectric dissipation factor of electrical insulating materials at power, audio and radio frequencies including metre wavelengths," *IEC Standard 60250,* 1969.

[8] M. Yoshimura and H. K. Bowen, "Electrical Breakdown Strength of Alumina at High Temperatures," *Journal of American Ceramic Society*, vol. 64, pp. 404-410, 1981.

[9] R.D. Shannon and G.R. Rossman, "Dielectric Constant of $MgAl_2O_4$ Spinel and the Oxide Additivity Rule," *Journal of Physics and Chemistry Solids*, vol. 52, pp. 1055-1059, 1991,

Publication II

Influence of humidity and temperature on the dielectric properties of thermally sprayed ceramic $MgAl_2O_4$ coatings

M. Niittymäki, T. Suhonen, U. Kanerva, J. Metsäjoki and K. Lahti

2014 IEEE Conference on Electrical Insulation and Dielectric Phenomena (CEIDP), pp. 94-97, 2014

DOI: 10.1109/CEIDP.2014.6995894

Influence of Humidity and Temperature on the Dielectric Properties of Thermally Sprayed Ceramic $MgAl_2O_4$ Coatings

Minna Niittymäki and Kari Lahti
Department of Electrical Engineering
Tampere University of Technology
Tampere, Finland
minna.niittymaki@tut.fi

Tomi Suhonen, Ulla Kanerva and Jarkko Metsäjoki
Materials and Manufacturing
VTT Technical Research Centre of Finland
Espoo, Finland

***Abstract* — Thermally sprayed ceramic coatings can be used as electrically insulating materials for example in high temperature applications (e.g. fuel cells) or in other demanding conditions where ceramic-based solutions are needed instead of e.g. polymers. The dielectric properties of thermally sprayed ceramic coatings are strongly affected by external conditions. The aim of this paper is to characterize the dielectric properties of thermally sprayed ceramic $MgAl_2O_4$ coatings; especially the effects of ambient conditions on certain dielectric properties of thermally sprayed coatings are studied. DC resistivity at various electric field strengths as well as permittivity and losses at different frequencies is reported in the paper for $MgAl_2O_4$ samples made by three different thermal spray techniques. These measurements were performed at three temperatures as well as at two different relative humidities. The DC breakdown strength was studied at one condition. Due to the slightly open porous microstructure of the studied coatings, increasing humidity particularly increases the dc conductivity and relative permittivity.**

Keywords— thermal spraying; HVOF; plasma; flexicord; spinel; coating; resistivity; dielectric spectroscopy; dielectric breakdown strength

I. INTRODUCTION

In high temperature applications (e.g. fuel cells) or in other demanding conditions, ceramic-based insulation solutions are needed instead of polymers. Ceramic material can be thermally sprayed to e.g. demanding geometries. The mostly used insulating coating materials are alumina (Al_2O_3), magnesium oxide (MgO) and magnesium aluminate ($MgAl_2O_4$). Although there are clearly needs and applications for thermally sprayed insulating coatings, in general, only a few studies on the dielectric properties of thermally sprayed ceramic coatings can be found in literature and further analysis is required.

The dielectric properties of thermally sprayed ceramic coatings are strongly affected by ambient conditions [1], [2]. Most of the earlier studies of electrical properties of thermally sprayed coatings are focused on the HVOF (high velocity oxygen fuel) and plasma sprayed alumina coatings [1]–[4]. For $MgAl_2O_4$ (spinel) coatings mainly DC resistivity and DC breakdown strength measurements are performed earlier at room temperature conditions, but in [1] the resistivity was also studied in high humidity [5]. Formerly, dielectric spectroscopy studies have been made for HVOF sprayed alumina at various ambient conditions, but dielectric spectroscopy studies of plasma sprayed alumina as well as HVOF sprayed spinel have been reported only at room temperature conditions [2], [4], [5]. Due to the lamellar and slightly porous microstructure of thermally sprayed ceramic coatings, the influence of temperature and humidity on the dielectric properties is required to be examined in more detail. The aim of this paper is to study the dielectric properties of three differently sprayed spinel coatings at various ambient conditions.

II. EXPERIMENTAL

A. Studied Thermally Sprayed Ceramic Coatings

Three thermally sprayed ceramic coatings of different coating techniques were deposited on stainless steel substrates (size of 100 mm x 100 mm). Experimental $MgAl_2O_4$–powder was deposited by HVOF-process, more detailed information of this HVOF coating is presented in [5]. Commercial $MgAl_2O_4$–powder was deposited by atmospheric plasma spraying and commercial $MgAl_2O_4$ flexicord by flame spraying.

The coating thicknesses of the samples were defined by magnetic measuring device (Elcometer 456B). The mean value of the thickness was calculated from 10 parallel measurements covering the electrode area. The mean thicknesses, standard deviations and gas permeability values of the coatings are presented in Table I. The higher the gas permeability, the more porous the material is. According to the results, the HVOF coating is the least porous and the flame sprayed flexicord is the most porous of the studied materials. Because the coating base is not smooth due to the grit blasting, some deviation is noticed in the thickness values. In addtion to that, the coatings themselves exhibit lamellar microstructure causing a sligthly non-smooth surface. The coatings were tested as-sprayed.

B. Sample Preparation and Test Procedures

DC resistivity and dielectric spectroscopy measurements

TABLE I. THICKNESSES, STANDARD DEVIATIONS AND GAS PERMEABILITIES OF THE STUDIED COATINGS.

Material	Thickness (µm)	SD (µm)	Gas permeability (nm^2)
HVOF	362	10.0	5.85
Plasma	333	10.8	13.1
Flexicord	360	8.1	19.89

were performed at various ambient conditions (+20°C, +40°C, +60°C; RH 20 %, 45 %). The coatings were stabilized at each ambient condition for 3 hours before the measurements. Prior to the stabilizing period at each ambient condition, the samples were dried at 120 °C for one hour and then placed at dry conditions because the same sample was used at all these measurement conditions. At first, the dc resistivity at various electric fields was measured and then the dielectric spectroscopy measurements were performed. In addition, the DC dielectric breakdown strength (DBS) measurements were performed at 20°C, RH 20 %.

For the DC resistivity and relative permittivity measurements, a round silver electrode (∅= 50 mm) was painted on the middle of a coating sample. In addition, a shield electrode was painted around the measuring electrode to neglect possible surface currents. For breakdown measurements, a silver electrode (∅= 11 mm) was painted on the sample surface to improve the contact between the voltage electrode and the coating. Silver paint penetration was studied from cross-sectional optical micrographs. It was observed that the used paint (SPI Conductive Silver Paint) did not penetrate into the coating.

A. DC Resistivity

Resistivity measurements were made using Keithley 6517B electrometer. The test voltage was maintained until a stabilized current level (i.e. pure resistive current) was reached. In practice, the tests were performed at test voltages ranging from 10 V to 1000 V at 20°C, RH 20 % in order to study the resistivity as a function of electric field in detail. At the other ambient conditions, the resistivities were measured at the electric fields of 0.1 V/µm, 0.3 V/µm, 0.5 V/µm, 1.5 V/µm and 2.5 V/µm. The stabilized DC current was measured 300 s after the voltage application. Anyhow, at higher test voltages (corresponding to field strengths above ohmic region), the DC current did not fully stabilize during the measurement period. Despite of this the resistivity values were determined similarly in these cases. All the measuring arrangements were in accordance with the standards IEC 60093 or ASTM D257-07. [5]–[7]

B. Dielectric Spectroscopy

Relative permittivity and dielectric losses of the materials were studied with an insulating diagnosis analyzer device (IDA 200). During the measurements, a sinusoidal voltage with varying frequency was applied over the sample. The measuring electric field was 0.3 V_{peak}/µm unlike in [2], [5] where the measuring voltage was 200 V_{peak} corresponding to the electric fields 0.71 V_{peak}/µm in [2] and 0.55 V_{peak}/µm in [5].

The complex impedance of a sample is calculated from the measured test voltage and the current through a sample which is expressed by IDA device as the equivalent parallel RC circuit model. The relative permittivity (ε_r) and dissipation factor (tan δ) were calculated from the measured parallel resistance and capacitance with Eq.(1)-(2), where C_p is measured parallel capacitance and R_p parallel resistance of the equivalent circuit model of a dielectric. C_0 is the so-called geometric capacitance of test sample (vacuum in place of the insulation) and ω is the angular frequency. The edge field correction (C_e) was not used because the shield electrode was utilized in the measurements. All the test arrangements were performed in accordance with the IEC standard 60250. [8]

$$\varepsilon_r \approx \varepsilon_r' = \frac{C_p}{C_0} - \frac{C_e}{C_0}, \tag{1}$$

$$\tan\delta = \frac{1}{R_p C_0 \omega}, \tag{2}$$

Loss index (ε_r'') includes all the losses of a sample: both conductive and dielectric ones. It can be defined from relative permittivity and dissipation factor, tan δ, with Eq. (3).

$$\varepsilon_r'' = \varepsilon_r \tan\delta \tag{3}$$

C. DC Dielectric Breakdown Strength

Breakdown (bd) voltage measurements were made with a linearly ramped DC voltage. The measurements were made without oil immersion because the oil penetrates into the porous coating and thus increases the dielectric strength of a coating. During the breakdown tests, the samples were clamped between two stainless steel electrodes: a rod (∅= 11 mm) and a flat plate (∅=50 mm). The used rod electrode was flat-ended and edge-rounded with a radius of 1 mm. A software controlled linear ramp rate of 100 V/s was used throughout the test until breakdown occurred. [9]

Before painting the silver electrodes on the sample surfaces, the thickness of a coating was measured from the electrode area to define exactly the dielectric breakdown field strength. Dielectric breakdown field strength of a coating was calculated dividing the breakdown voltage by the corresponding thickness of the breakdown point.

D. Statistical Analysis of Breakdown Strength Results

Breakdown process of any dielectric material is inherently of stochastic nature causing statistical distribution of breakdown results. Typically dielectric breakdown strength of solid materials is Weibull distributed due to which also these results were fitted to that distribution. The cumulative density function of a two-parameter Weibull distribution is given in Eq. (4):

$$F(t,\alpha,\beta) = 1 - \exp\left\{\left(\frac{t}{\alpha}\right)^{\beta}\right\} \tag{4}$$

where $F(t)$ is the breakdown probability, t is the measured breakdown strength (V/µm), α is the scale parameter (V/µm) and β is the shape parameter (V/µm). The scale parameter represents the breakdown strength at the 63.2 % failure probability and the shape parameter indicates the slope of the theoretical distribution. The statistical analysis was performed using Weibull++ software and the Maximum Likelihood method was used in the parameter estimation.

III. Results and Discussion

A. DC resistivity

Figure 1 illustrates the resistivities of the coatings as a function of electric field at all studied ambient conditions. The resistivities of all the coatings are at quite a similar level at lowest electric fields at 20°C. When temperature is increased to 40 °C, a permanent change can be seen for the Flexicord coating (which can be seen also in permittivity, Fig. 2). For HVOF and Plasma increasing temperature has not as high influence although DC resistivity of all the coatings decreases when the temperature increases. In general, relative humidity has larger influence on the resistivity in comparison to temperature. The changes, in general, may be linked to the porosity and hydrophilicity of thermally sprayed ceramic coatings.

Flexicord has the highest porosity and its resistivity decreases more with increasing humidity. However, despite the rather high porosity of Plasma coating its behavior does not differ much from HVOF sample. Other properties (e.g. phase composition, interface properties, etc.) are thus also of importance.

B. Dielectric Spectroscopy

The relative permittivities of all the coatings increase especially with relative humidity, as it can be observed from Fig. 2 where the relative permittivity of the coatings is presented as a function of frequency at all the studied ambient conditions. Major permanent changes in the coatings did not occur during the measurements at high temperatures and humidities, except for Flexicord. This is confirmed by the permittivity measurements made after the aforementioned measurements which indicate that the permittivities of the HVOF and plasma samples are only slightly changed in comparison to the initial values at 20°C, RH20%. However, when temperature was increased from 20°C to 40°C, some permanent changes occurred in Flexicord sample which may be

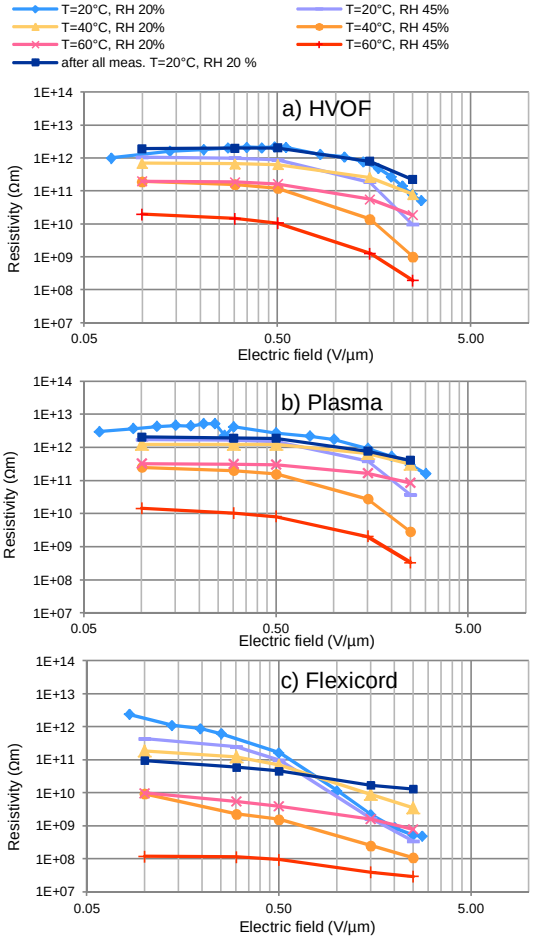

Fig. 1. DC resistivity of the studied coatings in all studied ambient conditions and after these measurements: a) HVOF sprayed, b) plasma sprayed and c) flame sprayed flexicord.

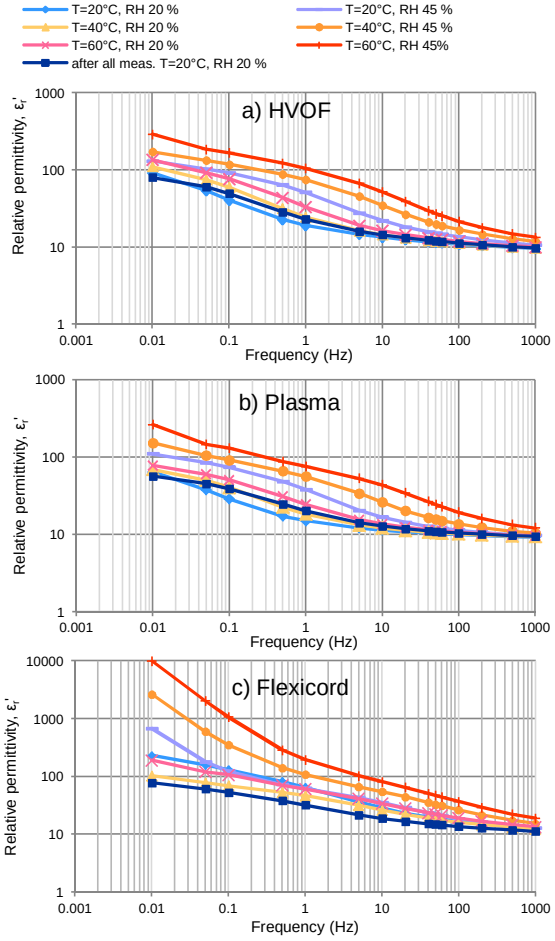

Fig. 2. Relative permittivity as a funtion a frequency for all studied coatings in all studied ambient conditions and after these measurements: a) HVOF sprayed, b) plasma sprayed and c) flame sprayed flexicord.

e.g. due to breakdowns in the interfaces inside the coating.

Loss index was also defined for all the materials. The behavior of the coatings was similar as the relative permittivity; the dielectric losses increased when the temperature increased and also the influence of relative humidity was similar. Flexicord had the highest dielectric losses whereas the HVOF had the lowest throughout the studied frequency range.

C. DC dielectric breakdown strength

Figure 3 presents the DC dielectric breakdown strength distribution of the studied spinel coatings along with the corresponding Weibull parameters. Typically, HVOF sprayed coatings have higher breakdown strength values than the coatings sprayed with other techniques due to the more dense structure of HVOF sprayed coatings. For this HVOF coating the mean was, anyhow, only 13.6 V/µm (SD=2.5 V/µm) while e.g. in [1] the mean dielectric strength of HVOF spinel coating was ~31 V/µm (thickness 200 µm). The reason of this is supposed to be the experimental powder used for HVOF coating.

In the case of the plasma and HVOF samples the similar Weibull β values indicate similar material homogeneities despite the differences in the raw materials and spraying techniques. However, the Flexicord sample shows even higher Weibull beta in comparison to the HVOF and plasma samples indicating even higher distribution homogeneity. If the weakest spot of Flexicord (8.4 V/µm) is excluded from the Weibull parameter calculation, the resulting α and β parameters are 18.5 V/µm and 15.9, respectively.

D. Discussion

DC resistivities of all the coatings are quite similar at low electric fields. Due to the special microstructure, hydrophilicity and slightly porous structure of thermally sprayed ceramic coatings, humidity can be absorbed in the coating. This can be seen in both the resistivity and dielectric spectroscopy results which show higher dependency on relative humidity than on temperature.

Like the humidity also the temperature has a clear influence on the dielectric properties, as increasing temperature decreases

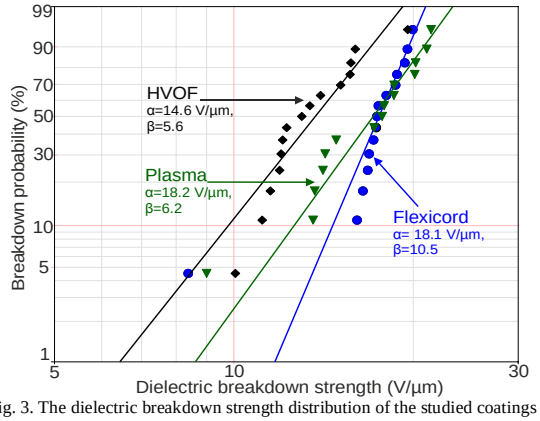

Fig. 3. The dielectric breakdown strength distribution of the studied coatings and the Weibull parameters α and β.

the DC resistivity and increases the relative permittivity and the dielectric losses. However, it is difficult to distinguish exactly the individual effects of temperature and humidity although quite good indications can be made based on the RH 20 % results. In any case it is obvious that the dielectric measurements of thermally sprayed ceramic coatings should be made at controlled conditions and good documentation of the measurements conditions is of significant importance.

Flexicord had the highest porosity and dielectric strength but the lowest dc resistivity. HVOF and Plasma samples have lower porosities and breakdown strengths but higher dc resistivities in comparison to Flexicord. It may be speculated that the slightly higher conductance of Flexicord may form a more preferable charge distribution in the dielectric for DC strength and this way improve the fast rate-of-rise DC breakdown strength.

IV. Conclusions

In DC resistivity and dielectric spectroscopy measurements, the relative humidity has higher influence on the results than temperature. This can be linked to the coatings capability to absorb moisture. Thus, the dielectric measurements should be performed at carefully controlled conditions in order to be able to compare results to other studies. The highest DC breakdown strength was measured for flame sprayed Flexicord which had the lowest resistivity although more dense HVOF coatings typically has the highest dielectric strength. The main reason for this result is probably in the properties of the experimental powder used for HVOF coating.

References

[1] F.-L. Toma, L. M. Berger, S. Scheitz, S. Langner, C. Rödel, A. Potthoff, V. Sauchuk, and M. Kusnezoff, “Comparison of the Microstructural Characteristics and Electrical Properties of Thermally Sprayed Al 2O 3 Coatings from Aqueous Suspensions and Feedstock Powders,” *J. Therm. Spray Technol.*, vol. 21, no. 3–4, pp. 480–488, 2012.

[2] M. Niittymäki, B. Rotthier, T. Suhonen, J. Metsäjoki, and K. Lahti, “Effects of ambient conditions on the dielectric properties of thermally sprayed ceramic coatings,” in *Proceedings of the 23th Nordic Insulation Symposium Nord-IS 2013*, 2013, Trondheim, Norway, pp. 131–135.

[3] F. L. Toma, S. Scheitz, L. M. Berger, V. Sauchuk, M. Kusnezoff, and S. Thiele, “Comparative study of the electrical properties and characteristics of thermally sprayed alumina and spinel coatings,” *J. Therm. Spray Technol.*, vol. 20, no. 1–2, pp. 195–204, 2011.

[4] L. Pawłowski, “The relationship between structure and dielectric properties in plasma-sprayed alumina coatings,” *Surf. Coatings Technol.*, vol. 35, no. 3–4, pp. 285–298, 1988.

[5] M. Niittymäki, K. Lahti, T. Suhonen, U. Kanerva, and J. Metsäjoki, “Dielectric properties of HVOF sprayed ceramic coatings,” in *Proceedings of the IEEE International Conference on Solid Dielectrics*, 2013, Bologna, Italy, pp. 389–392.

[6] “IEC standard 60093 Methods of test for volume resistivity and surface resistivity of solid electrical insulating materials,” no. IEC Standard 60093. IEC, 1980.

[7] “ASTM Standard D257 - 07 Standard Test Methods for DC Resistance and Conductance of Insulating Materials,” no. ASTM Standard D257–07. ASTM International, West Conshohocken, PA, 2007.

[8] “IEC standard 60250 Recommended methods for the determination of the permittivity and dielectric dissipation factor of electrical insulating materials at power, audio and radio frequencies including metre wavelengths,” no. IEC Standard 60250. IEC, 1969.

[9] M. Niittymäki, J. Metsäjoki, T. Suhonen, and K. Lahti, "Breakdown strength of thermally sprayed ceramic coatings - effects of different test procedures," *J. Therm. Spray Technol.* (unpublished, under review)

Publication III

Dielectric breakdown strength of thermally sprayed ceramic coatings: effects of different test arrangements

M. Niittymäki, T. Suhonen, J. Metsäjoki and K. Lahti

Journal of Thermal Spray Technology, vol. 24, no. 3, pp. 542–551, 2015.

DOI: 10.1007/s11666-014-0211-1

JTTEE5
DOI: 10.1007/s11666-014-0211-1
1059-9630/$19.00 © ASM International

Dielectric Breakdown Strength of Thermally Sprayed Ceramic Coatings: Effects of Different Test Arrangements

Minna Niittymäki, Kari Lahti, Tomi Suhonen, and Jarkko Metsäjoki

(Submitted July 4, 2014; in revised form November 12, 2014)

Dielectric properties (e.g., DC resistivity and dielectric breakdown strength) of insulating thermally sprayed ceramic coatings differ depending on the form of electrical stress, ambient conditions, and aging of the coating, however, the test arrangements may also have a remarkable effect on the properties. In this paper, the breakdown strength of high velocity oxygen fuel-sprayed alumina coating was studied using six different test arrangements at room conditions in order to study the effects of different test and electrode arrangements on the breakdown behavior. In general, it was shown that test arrangements have a considerable influence on the results. Based on the results, the recommended testing method is to use embedded electrodes between the voltage electrode and the coating at least in DC tests to ensure a good contact with the surface. With and without embedded electrodes, the DBS was 31.7 and 41.8 V/μm, respectively. Under AC excitation, a rather good contact with the sample surface is, anyhow, in most cases acquired by a rather high partial discharge activity and no embedded electrodes are necessarily needed (DBS 29.2 V/μm). However, immersion of the sample in oil should strongly be avoided because the oil penetrates quickly into the coating affecting the DBS (81.2 V/μm).

Keywords Al_2O_3, breakdown strength, coating, dielectric, HVOF, thermal spraying

1. Introduction

Thermally sprayed ceramic coatings, such as alumina and magnesium aluminate, can be utilized as an electrical insulation in demanding conditions (e.g., in harsh environments or in high-temperature applications) where normal insulating materials, such as polymers, cannot be used. However, relatively few studies on the dielectric properties of thermally sprayed ceramic coatings can be found in literature which makes this area of research interesting and necessary. In order to be able to design electrical insulation systems based on thermally sprayed ceramics, the electrical performance of these materials must be known. The performance is defined by dielectric parameters (e.g., permittivity, tan δ, resistivity, and breakdown strength) which are, anyhow, not constant values but differ depending on the form of electrical stress (e.g., DC, AC, frequency of AC, transients) and ambient conditions (such as temperature, humidity) and also the aging of a material (long-term properties). Arrangements during tests and measurements may affect the results remarkably. Due to the above reasons, the measurements of dielectric parameters are typically made according to standards, like IEC 60243-1 or ASTM D 149-09(2013) for dielectric breakdown strength. Although a certain standard is used, there are often several details which may vary between separate tests. In the case of breakdown measurements, for example, different voltage application methods and electrode configurations may be used as well as different insulating mediums may be used around the test sample to prevent surface arcing and flashovers over the sample. Since details of test arrangements may have an effect on the test results, tests shall always be documented in detail and comparisons between the results of different tests shall be made with careful consideration (Ref 1, 2).

Because of the spraying process, the microstructure of thermally sprayed coating consists of splats, voids, cracks, and different kinds of defects due to which thermally sprayed coatings have some degree of porosity. Increased porosity decreases the dielectric breakdown strength of thermally sprayed ceramic coating (Ref 3, 4). Typically, insulating solid ceramics is less porous than the thermally sprayed coatings. Due to this, solid ceramics may usually be tested as immersed in insulating oil to prevent flashovers over the sample surface, because the oil will not easily penetrate inside the material structure and thus affect the test results. Most of the previous studies on insulating ceramics are focused on the electrical properties of solid alumina which has different microstructural properties than thermally sprayed coatings, and due to this direct comparison between the dielectric properties of solid and thermally sprayed materials is not reasonable. Quite many of the breakdown strength measurements of

Minna Niittymäki and **Kari Lahti**, Tampere University of Technology, Tampere, Finland; and **Tomi Suhonen** and **Jarkko Metsäjoki**, VTT Technical Research Centre of Finland, Espoo, Finland. Contact e-mail: minna.niittymaki@tut.fi.

Published online: 01 January 2015

the solid ceramics are made using AC voltage (50 or 60 Hz), but the dielectric breakdown strength measurements of ceramic coatings are typically performed using DC voltage in air without oil immersion (Ref 3-16).

As it was mentioned earlier, the used electrode configuration may have influence on the dielectric breakdown results. In Ref 3, 17-19 the breakdown measurements of thermally sprayed ceramic coatings were performed without silver-painted or other way embedded electrodes on sample surface, but in Ref 4, 5 silver-painted electrodes were used to improve the contact between the steel electrode and the coating. The effect of steel electrode shape was studied for solid alumina in Ref 11, and a ball-shaped electrode was recommended. The ball-shaped electrode arrangement is also introduced in the IEC standard 60672-2, but since it requires a ball-shaped hole to be machined in the sample to be tested and as a consequence of this a rather thick sample is required, this method is not in practice applicable to thermally sprayed coatings (Ref 20). However, when a ball-shaped electrode is used, the electric field distribution over the tested area is more homogenous, and thus it is a more preferable electrode arrangement for breakdown testing. On the other hand, the tested area is really small since the maximal field strength is present only at the vicinity of the head of the ball electrode. Due to this, a rather high deviation of results can be expected in Ref 20 with this arrangement and as a consequence, a large number of parallel tests are needed in order to get a realistic view of the breakdown distribution over the large areas of a material. Actually, the IEC Standard 60672-2 recommends using a test method where a ball-shaped hole is not machined in the sample.

The breakdown test results of thermally sprayed ceramics are usually presented as an average value from five to ten parallel measurements (Ref 3-5, 17, 18). Typically, breakdown data of solid ceramics are also presented as Normal distribution values (mean and standard deviation), but in Ref 11 the weakest link failure analysis was used in a case of solid alumina, and the results were analyzed statistically with two distributions: Weibull and Laplace. The latter was reported to agree better than Weibull. In typical solid electrical insulations (e.g., polymers), Weibull analysis is normally performed for breakdown data if the parallel measurements of more than 10 are made (Ref 11, 21, 22).

In this paper, the breakdown strength of one type of high velocity oxygen fuel (HVOF)-sprayed aluminum oxide coating is studied with several different test arrangements at room temperature conditions. The breakdown measurements are performed with silver-painted electrodes and without any embedded electrodes in air and in oil mainly with DC voltage. Statistical analysis, such as Normal and Weibull distributions, are performed for the breakdown data. The measurement methods are documented in detail, and the effect of electrode arrangements as well as the effect of insulation oil immersion is analyzed. The dependence between the coating microstructure and the breakdown strength is also discussed.

Table 1 Main spray parameters

Parameter	
Spray distance, mm	170
Gas parameters, L/min	
H_2	700
O_2	350
N_2	20
Sweeps, pcs	15
Scanning step size, mm	4
Relative torch scan velocity, m/s	1

2. Experimental

2.1 Studied Material

Commercial fused high purity Al_2O_3-powder (99.9 wt. %, Praxair) was deposited on carbon steel substrate by high velocity oxygen fuel (HVOF) spraying method. The particle size of the powder was from 5 to 22 μm which is a very suitable size for HVOF process. The used HVOF gun was HV2000 (Praxair), and the main spray parameters are listed in Table 1. The coating was tested as sprayed without any polishing, grinding, or sealing because a sealer can fill the voids of the coating, thus affecting the results (Ref 3).

The porosity values of the studied coating were defined by image analysis from optical micrographs (OM) with image magnification of 320 and using scanning electron microscope (SEM) micrographs taken with two detectors: secondary electron detector (SE) and backscattered electron detector (BSE) both with image magnification of 1000. The porosity values were defined by three OM images and by two SEM images. Five parallel surface roughness measurements were made with 2D-profilometer along the coating surface.

2.2 Sample Preparation

DC resistivity, relative permittivity, and breakdown strength measurements were made at the temperature of 20 °C and at the relative humidity of 45%. These conditions were maintained in the big climate room of TUT High voltage laboratory where all the measurement actions were made at the above-mentioned ambient conditions. At first, the samples were preconditioned at 120 °C for 2 h and then stabilized at 20 °C and RH 45% for 12 h before the measurements. For DC resistivity and relative permittivity measurements, a round silver electrode (∅ = 50 mm) was painted on the middle of a coating sample before preconditioning. In addition, a shield electrode was painted around the measuring electrode to neglect possible surface currents. For some of the breakdown measurements, silver electrodes (∅ = 11 mm) were painted on the samples before preconditioning. Silver paint penetration was studied from cross-sectional optical micrographs. It was observed that the used paint (SPI Conductive Silver Paint) did not penetrate into the coating.

2.3 DC Resistivity and Relative Permittivity of the Studied Material

DC resistivity was studied at three different electric field strengths because some thermally sprayed ceramic coatings have shown non-ohmic behavior already at quite low electric fields (Ref 18). DC resistivity measurements were made using Keithley 6517B electrometer. The test voltage was maintained until a stabilized current level (i.e., pure resistive current) was reached. In practice, the tests were performed at test voltages ranging from 10 to 30 V, and the stabilized DC current was measured approximately 1000 s after the voltage application. The DC resistivity was calculated using the mean value of the stabilized current at 998-1000 s, the test voltage, and the sample thickness. All the measurement arrangements were in accordance with the standards IEC 60093 or ASTM D257-07 (Ref 23, 24).

Relative permittivity and dielectric losses of the material were studied with an insulating diagnosis analyzer device (IDA 200). During the measurements, a sinusoidal voltage with varying frequency was applied across the sample. The measuring voltage was 200 V_{peak} corresponding to the electric field of 1.5 $V_{peak}/\mu m$.

The complex impedance of a sample was expressed by IDA device as an equivalent parallel RC circuit model and calculated from the measured test voltage and the current through a sample. The relative permittivity (ε_r) and dissipation factor (tan δ) were calculated from the measured parallel resistance and capacitance using Eq 1, 2, where C_p is the measured parallel capacitance and R_p the parallel resistance of the equivalent circuit model of the dielectric. C_0 is the so-called geometric capacitance of the test sample (vacuum in place of the insulation) and ω is the angular frequency. The edge field correction (C_e) was not used in these measurements because a shield electrode was utilized in the measurements. All the test arrangements were performed in accordance with the IEC standard 60250 (Ref 25).

$$\varepsilon_r \approx \varepsilon_r' = \frac{C_p}{C_0} - \frac{C_e}{C_0} \quad \text{(Eq 1)}$$

$$\tan\delta = \frac{1}{R_p C_0 \omega}. \quad \text{(Eq 2)}$$

Loss index (ε_r'') includes all the losses of a sample: both conductive and dielectric ones (as well as the dissipation factor). It can be defined from relative permittivity and dissipation factor, tan δ, using Eq 3.

$$\varepsilon_r'' = \varepsilon_r \tan\delta. \quad \text{(Eq 3)}$$

2.4 Breakdown Measurements

During the breakdown tests, the samples were clamped between two stainless steel electrodes: a rod (∅ = 11 mm) and a flat plate (∅ = 50 mm). The used rod electrode was flat-ended and edge-rounded with a radius of 1 mm. Schematic figure of this measurement bench is illustrated in Fig. 1(b). Some of the measurements were made with a graphite felt disk electrode (∅ = 11 mm, the thickness of 0.76 mm) placed in between the stainless steel rod electrode and the coating, and some of the measurements were made in oil immersion with "Shell Diala oil DX Dried" insulation oil.

Breakdown measurements were made using six different measuring arrangements:

(1) at DC voltage in air without oil immersion or painted electrodes on coating surface
(2) at DC voltage in oil immersion without painted electrodes
(3) at DC voltage with silver-painted electrodes (∅ = 11 mm) in air
(4) at DC voltage with graphite disk electrodes (∅ = 11 mm) in air
(5) at DC voltage with silver-painted electrodes (∅ = 11 mm) in oil
(6) at AC voltage (50 Hz) in air without oil immersion or painted electrodes.

All the breakdown voltage measurements were made with linearly ramped DC or AC voltage. Software-controlled linear ramp rate of 100 V/s was used in all tests. In oil measurements, the ramp rate of the voltage was started 30 s after the sample was immersed in the oil. The schematic figure of the measurement circuit is presented in Fig. 1(a). The used DC voltage source was Spellman

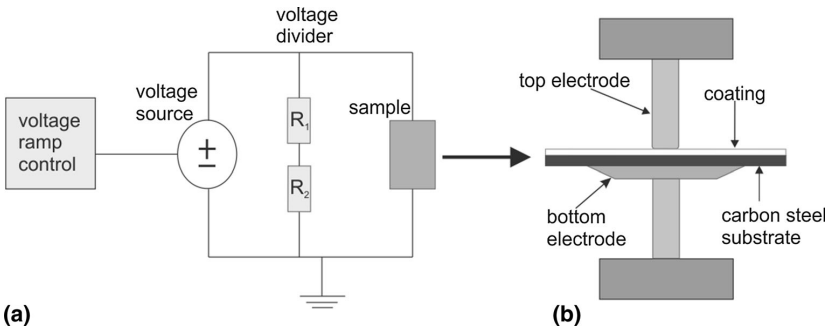

Fig. 1 (a) Measurement circuit of the breakdown measurements and (b) schematic figure of the measurement bench where the sample is clamped between the rod electrode and the larger flat electrode

SL1200 ($U_{max} = 130$ kV). In the DC measurements, the voltage divider was Spellman HVD 100-1 resistive voltage divider ($U_n = 100$ kV and scale factor 10000:1). The used AC voltage source was Hipotronics test transformer ($U_{max,rms} = 50$ kV), and the measured voltage was recorded directly from the high voltage side of the transformer. After each test, a confirmation was made to check that a breakdown had occurred, not a flashover along the surface of the coating.

After the measurements, the thicknesses of samples without silver-painted electrodes were measured at the point right next to the breakdown points to define exactly the dielectric breakdown field strength of each breakdown point. For the samples with silver-painted electrodes, the thickness of each coating was measured before painting the silver electrodes. The thicknesses were measured with a magnetic measuring device (Elcometer 456B).

In DC tests, the dielectric breakdown strength of a coating, E_b, was calculated by dividing the measured breakdown voltage, V, by the corresponding thickness of the breakdown point, d, (Eq 4). In AC tests, the dielectric breakdown strength was calculated by dividing the measured peak value of the measured AC voltage by the thickness of the measurement point since the peak value of the ac-based breakdown strength is comparable to the DC dielectric breakdown strength.

$$E_b = \frac{V}{d}. \quad \text{(Eq 4)}$$

2.5 Statistical Analysis of Breakdown Data

The mean value and experimental standard deviation of Normal distribution can be easily calculated from dielectric breakdown strength data. However, typically the electrical breakdown data of solid insulations are Weibull, Gumbel, or log-normal distributed. These distributions can be used reliably only if at least 10 parallel tests are made because less test results are not statistically relevant enough. Typically, Weibull distribution is used to analyze the breakdown voltage data of solid insulations. This distribution is a one of the extreme value distributions which means that the system fails when the weakest link of the system fails. The cumulative density function of a two-parameter Weibull distribution is given in Eq 5:

$$F(t, \alpha, \beta) = 1 - \exp\left\{\left(\frac{t}{\alpha}\right)^{\beta}\right\}, \quad \text{(Eq 5)}$$

where $F(t)$ is the breakdown probability, t is the measured breakdown strength (V/μm), α is the scale parameter (V/μm), and β is the shape parameter (V/μm). Both α and β are positive values. The scale parameter represents the breakdown strength at the 63.2% failure probability and it is analogous to the mean of Normal distribution. The shape parameter is a measure of the range of failure voltages. Larger β means that the range of breakdown voltages is smaller. β is analogous to the inverse of standard deviation of the Normal distribution (Ref 21, 22).

Weibull parameters can be estimated in different ways such as using Maximum Likelihood estimation (MLE) and rank-regression methods. The statistical analysis was performed using Weibull++ software, and the Maximum Likelihood method was used in the parameter estimation.

3. Results

3.1 Properties of the Studied Coating

The mean porosity values of the studied HVOF coating are listed in Table 2. They were defined by image analysis from optical micrographs and by scanning electron microscope (SEM) micrographs taken with two detectors: secondary electron (SE) and backscattering electron (BSE). A cross-section surface image of the studied HVOF-sprayed Al_2O_3 coating is shown in Fig. 2 where the darker spots are pores and voids. The typical lamellar microstructure of thermally sprayed ceramic coating can be seen in Fig. 2. The substrate of the coating was grit blasted before spraying to enhance the attachment of the coating which, anyhow, has an effect on the thickness deviation of the coating (Fig. 3a). A cross-section image taken by optical microscope is shown in Fig. 3(b) where the rough substrate surface can obviously be seen. The thickness variation of the coating (minimum = 89 μm, average = 115 μm) is also illustrated in Fig. 3(b). The mean value of the surface roughness, R_a, is 2.7 μm with a standard deviation of 0.15 μm which is a typical value for HVOF-sprayed coatings.

Table 2 Porosity of the studied coating

Measurement method	Magnification	Average porosity, %	SD, %
optical micrographs	×320	1.4	0.1
SEM/SE	×1000	1.1	0.5
SEM/BSE	×1000	2.2	0.2

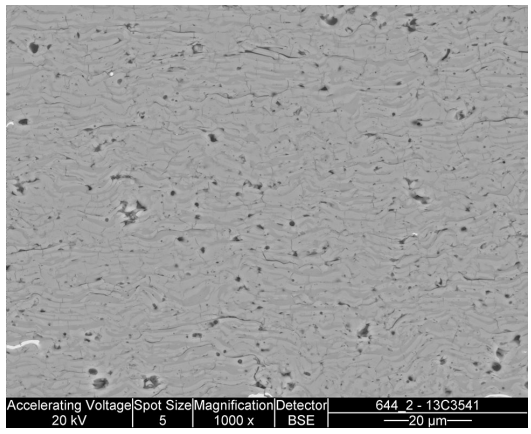

Fig. 2 Cross-section figure of the studied coating taken by SEM/BSE

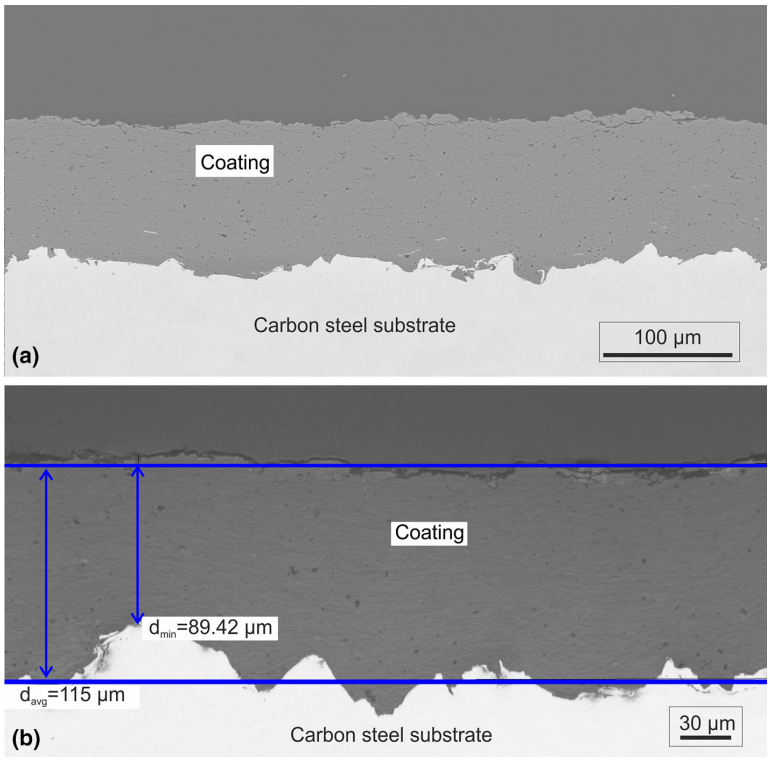

Fig. 3 (a) Cross-section figure of the studied coating taken by SEM/BSE. (b) Cross-section figure of the studied HVOF coating taken by optical microscope. Thickness variation is marked in the figure; 89.42 µm is the lowest value and 115 µm is the average value

Table 3 DC resistivity of the studied material at low electric field strengths (T = 20 °C, RH 45%)

Thickness, µm	Voltage, V	Electric field, V/µm	Resistivity, Ωm
92	10	0.11	4.66E+12
	20	0.22	3.80E+12
	30	0.33	1.12E+12

3.2 DC Resistivity and Relative Permittivity

Low field DC resistivities of the studied alumina coatings are given in Table 3. In author's previous studies, the resistivity of HVOF alumina was 9×10^{12} Ωm at the electric field of 0.5 V/µm (thickness 279 µm), and the resistivity of HVOF spinel was 2.9×10^{12} Ωm at the electric field of 0.5 V/µm (Ref 17, 18). Thus, the resistivity values obtained in this paper are at a similar level compared to the previous studies. The relative permittivity and the loss index of the studied material at various frequencies are given in Table 4; measured values are lower than in author's previous studies (HVOF alumina, 279 µm), presumably due to the different raw materials and the different sample thickness (Ref 17).

Table 4 Relative permittivity of the studied material at various frequencies, the RMS value of the measuring voltage was 140 V which corresponds to the electric field of 1.5 V_{rms}/µm (T = 20 °C, RH 45%)

Frequency, Hz	Relative permittivity, ε_r	Loss index, ε_r''
1	10.4	1.94
10	8.5	0.93
50	7.9	0.50
100	7.7	0.37
1000	7.4	0.16

3.3 Dielectric Breakdown Strength

Fifteen parallel breakdown measurements for the HVOF-sprayed alumina coating were made with each of the six different test arrangements mentioned in Chapter 2. The mean values of the dielectric breakdown strengths and the corresponding experimental standard deviations were calculated and are presented in Table 5 and Fig. 4. The deviation of dielectric breakdown strength between parallel measurements was quite large with all the arrangements. The thickness variation of the samples is also listed in Table 5, where the mean and standard

Table 5 Average dielectric breakdown strength of 15 parallel measurements and experimental standard deviations in different test arrangements as well as Weibull parameters and the breakdown probabilities at 10 and 90% failure probability ($T = 20$ °C, RH 45%)

Voltage form	Test arrangement	Mean thickness, µm	SD, µm	Average DBS, V/µm	SD, V/µm	Weibull, parameters			
						α, V/µm	β	DBS, V/µm at probability 10%	DBS, V/µm at probability 90%
DC	Dry	114	3.0	41.8	8.1	44.9	6.6	32.0	51.0
DC	Dry + silverpaint	116	3.2	31.7	5.8	34.0	6.4	23.9	38.8
DC	Dry + graphite	115	3.9	37.1	4.5	39.1	8.6	30.1	43.1
DC	Oil	111	5.0	81.2	20.2	89.0	4.3	52.7	108.1
DC	Oil + silverpaint	114	4.1	45.5	7.2	48.3	8.5	37.0	53.3
AC	Dry	114	4.4	29.2	6.0	31.5	6.1	21.8	36.2

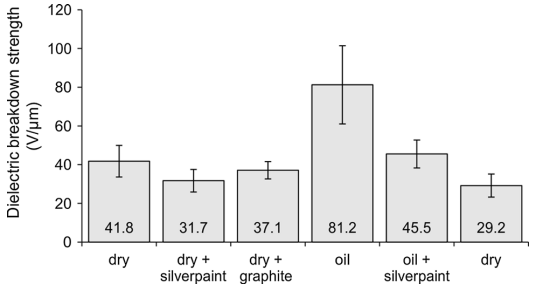

Fig. 4 Average dielectric breakdown strength with different test arrangements. The error bars show the experimental standard deviations

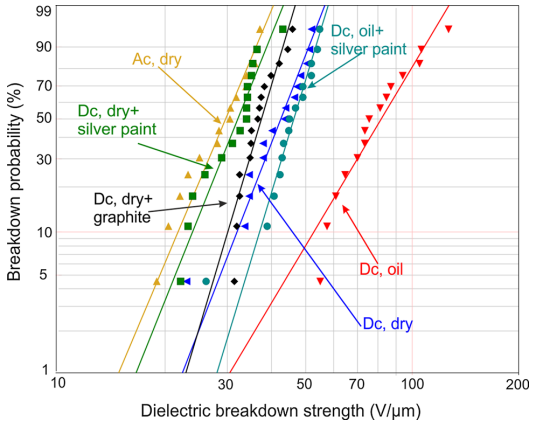

Fig. 5 Weibull distributions with different test arrangements: AC dry, DC dry, DC dry with silver-painted electrodes, DC dry with graphite electrodes, DC oil, and DC oil with silver-painted electrodes

deviation of 15 measured breakdown point thicknesses are shown. Weibull parameters α (the breakdown field at the failure probability of 63.2%) and β (shape parameter) of the breakdown measurements are also presented in

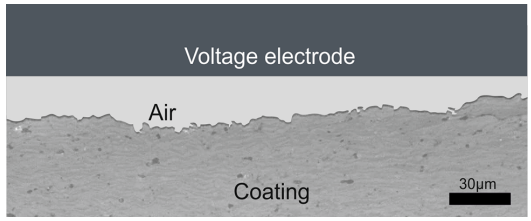

Fig. 6 Formed air gap between the voltage electrode and the tested coating during the breakdown measurements

Table 5 along with the breakdown field values at the breakdown probabilities of 10 and 90%. Better comparison between different test arrangements can be made using Weibull distributions illustrated in Fig. 5, where all the breakdown events are shown. Probability of breakdown is shown in *y*-axis, and the dielectric breakdown strength is in *x*-axis.

As it can be seen from the results, large variation of breakdown strength results was depending on the test arrangement used. Anyhow, the differences in the results are well understandable. In DC tests, the lowest result (31.7 V/µm) was obtained with the air-insulated arrangement with embedded silver paint electrodes. In this way, the whole electrode area (∅ = 11 mm) is truly tested in each individual breakdown test. In other words, the weakest point of the breakdown strength distribution over the tested area is measured in this case. Due to the same reason, it is also understandable that the deviation of the results is one of the smallest in this case. The deviation of thickness measured along the electrode area has an effect on the breakdown strength results but this will be discussed in detail in Chapter 4.

However, a 44% higher result (45.5 V/µm) was obtained with otherwise exactly similar test arrangements except that the whole test setup was placed in the oil. The reason for the remarkable increase is most probably that the oil had enough time to penetrate into the coating and fill the voids and pores of the coating even though the breakdowns occurred approximately 1 min 30 s after the sample was immersed in the oil. Breakdown strength of transformer oil is clearly higher (~100 V/µm) than that of

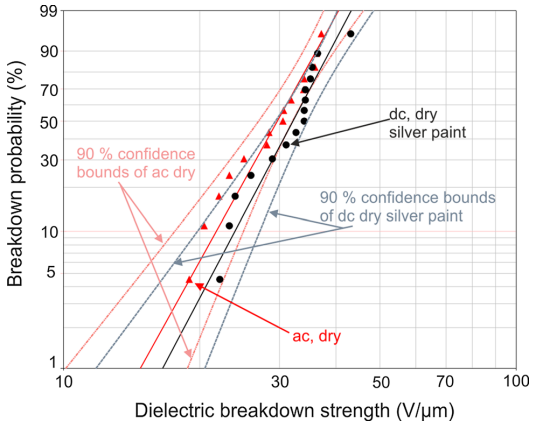

Fig. 7 Comparison between the results of AC breakdown test in air and the DC test with silver-painted electrodes in air

air or Al_2O_3 coatings (Ref 26, 27). It may be assumed that the breakdown path develops in dry conditions through the air-filled pores and voids in the coating. When the voids are filled with highly insulating oil, the breakdown strength of the oil-impregnated coating will increase.

When the breakdown test was made without any embedded electrode on the coating surface, the steel electrode will contact only some of the highest points of the coating, as illustrated in Fig. 6. Evidently, those contact points will be tested in parallel with test arrangements of this kind, and the weakest point will cause the breakdown. In this case, there is air between the steel electrode and the coating surface, and partial discharges will take place in this volume above a certain field strength defined by Paschen's law (Ref 26). The plasma channel of an electrical arc is well conductive, and in this way the point of coating where partial discharge takes place will be tested as well. Since partial discharges will ''bombard'' the surface of the coating rather intensively (this way testing most of the area of the coating under the electrode) especially in the case of AC voltage stress, it is understandable that the result obtained with this arrangement at AC test voltage (29.2 $V_{AC,peak}/\mu m$) was close to the result obtained with DC voltage with the silver-painted electrodes (see Fig. 7). In the case of DC excitation, the partial discharge repetition rate is typically much lower (Ref 26, 28), which is probably at least one of the reasons for the higher result in that case (41.8 V/μm). In the case of lower partial discharge activity, the smaller area will be ''bombarded'' and tested. Also, in this case, the test voltage has time to increase to a higher level before discharge arc takes place at a point weak enough to cause breakdown.

However, in the case where a piece of graphite felt disk ($\varnothing = 11$ mm) was placed between the steel rod electrode and the coating, the breakdown strength (37.1 V/μm) was between the case of silver-painted electrodes and the case of steel electrode in air. The graphite felt is a slightly soft allowing better contact with the highest points of the coating than the stainless steel electrode itself. Due to this, the tested area is larger than in the case without any embedded electrode but the area is still smaller than in the case with silver-painted electrodes.

When the air gap between stainless steel electrode and the coating is filled with a well insulating medium like transformer oil, no partial discharges will take place and only the contact points of electrode and the coating will be tested. Understandably, a significantly higher breakdown strength (81.2 V/μm) and deviation of the results were measured with this test arrangement.

4. Discussion

When measuring the breakdown voltage of an insulating material, several parameters such as the rate of raise and frequency of the test voltage, specimen thickness, electrode material, configuration, and attachment as well as temperature affect the dielectric breakdown strength. Humidity and aging of the material typically also affect the results (Ref 21).

In Ref 4, 5, silver-painted electrodes were used, and the dielectric breakdown strength of HVOF-sprayed alumina was reported to be 34 V/μm for 120 μm coating and 22 V/μm for 200-210 μm coating at room temperature ambient, while 31.7 V/μm was now measured with the same electrode arrangements for 116 μm thick samples at a temperature of 20 °C and relative humidity of 45%. In author's previous studies (Ref 17), a test procedure with air-insulated steel electrode without embedded contacts was used, and an average dielectric breakdown strength of 31.3 V/μm (SD = 2.1 V/μm) was measured for HVOF-sprayed alumina (thickness of 270 μm) at a temperature of 20 °C and relative humidity of 20%. In this study, the mean value with similar arrangements was 41.8 V/μm ($T = 20$ °C/RH = 45%, 116-μm sample). The thicker sample partly explains the difference although the ambient humidity was now higher, and the raw material as well as the spraying parameters was different than in the previous study. Anyhow, it can be concluded that the results obtained in this study are in line with the above-mentioned earlier studies.

4.1 Effect of Thickness

In Ref 3, 4, it was discussed that the increased amount of voids, cracks, and other defects in the ceramic coating probably decreases the dielectric breakdown strength. The unideal features of the coating are normally the weakest points, and thus increased amount of those decreases the materials' capability to withstand high voltages. Because the microstructure of thermally sprayed coating consists of voids, splats, and pores forming lamellar structure (Fig. 2), the breakdown channel probably forms along the voids. Thus, the breakdown channel might be longer than the measured thickness. In Ref 6, 16, the effect of direction and actual length of breakdown channel through an alumina ceramic material on the breakdown strength has

been discussed. The formation of the breakdown channel in the coating microstructure is an interesting detail, but from the definition of a breakdown strength, it is clear that the breakdown strength of a material must be calculated using the perpendicular thickness of a coating.

In general, the thickness of an insulating material has an effect on the breakdown field strength of material, and thinner samples have typically higher breakdown strengths than thicker ones. There are several reasons for this, partly dependent on breakdown mechanism. In the case of electro thermal breakdown mechanism, the thinner insulation will withdraw heat easier resulting in higher breakdown field strength. From a more general statistical point of view, according to the so-called enlargement law, there is a higher probability to have weak points in larger volume of insulating material due to which the breakdown will take place with higher probability in a case of thicker or larger insulation. This enlargement law is generally expressed mathematically as a power-law relationship (Eq 6) where the exponent, n, has to be determined for each material composition separately (E is electric strength and d is the thickness of the sample) (Ref 22, 26, 29).

$$E_2 = E_1 \left({}^{d_2}/_{d_1} \right)^{-n}. \quad \text{(Eq 6)}$$

In Ref 8, the influence of thickness on the AC breakdown strength of solid alumina ceramics was studied, and an empirical equation was defined based on the measured data for breakdown strength calculation for ceramics with the thickness of 0.7-3.5 mm (Eq 7) (V_b is the breakdown voltage, t is the thickness of the sample). The idea of evolution law is that the results with different thicknesses are comparable when all the results are calculated for 3-mm-thick insulation using Eq 7. This empirical equation is also used in other studies of breakdown strength of solid alumina, but in the previous studies of thermally spayed coatings, the calculations of breakdown strength are made according to Eq 4 without any thickness corrections. In any case, these empirically defined equations shall be used with careful consideration.

$$E_b = \frac{V_b}{t}\sqrt{\frac{t}{3}}. \quad \text{(Eq 7)}$$

The thickness of a coating can be defined either from cross-section figures or with magnetic measuring device. Cross-section figures are usually taken only from a certain small section of a sample. When several breakdown measurements are made from several samples (although all sprayed at the same time, the same method and the same powder), it might be that the thickness of the coating at the breakdown point is not the same what was defined from cross-section figure. Also, from the cross section of the studied material (Fig. 3b), it can be seen that the actual coating thickness varied more than 25 μm in the small area depending on where the value was defined. Because of this variation of thickness, in this paper, the measurements were made with magnetic measuring device at each breakdown point. Due to the measuring principle, the thickness measured with magnetic measuring device is always an average value over a rather small area. This kind of local but averaged thickness measurement is one practical and good way (together with the cross section) to define the thickness. Anyhow, it is clear that the rather high local deviation of thickness will cause remarkable deviation and error in the individual breakdown field results. This fact underlines the need to make large number of parallel measurements to average the individual errors.

Because the silver paint penetrates even into the deepest notches of the surface, the actual breakdown path (thickness) most probably starts from one of these notches. The ball-shaped head of the magnetic thickness measurement device does not fit into these small notches. This might result in a situation where the device gives the thicknesses mainly comparable to the peaks or the average of the surface roughness deviation of a sample. The measured values were, in practice, the only usable thickness values for breakdown strength calculations. Due to the above-mentioned facts, the defined breakdown strength results for this setup are, on average, most probably to some extent too small.

4.2 Effect of Oil

Oil immersion is often used in breakdown measurements to avoid flashovers on the sample surface, and it has been used in several solid alumina measurements (Ref 6-9, 11, 14-16). In Ref 11, two different insulation oils were compared in the breakdown measurements of solid alumina ceramic, which porosity and gas permeability was zero, unlike in thermally sprayed ceramics. Thus, in these cases, the use of oil is reasonable because the tested materials have not had open porosity so that the oil could penetrate into the ceramics. Anyhow, care shall be taken to avoid oil layers between the electrodes and the ceramic.

Typical thermally sprayed coating consists of voids, splats, and unmelted particles, i.e., there is some porosity in the coating (Fig. 2). Because of the porosity of the ceramic coatings, the oil penetrates very quickly into the coating and fills the voids when the sample is placed in the oil bath. The breakdown strength of the insulation system of oil and alumina coating is significantly higher than alumina coating. Thus, it can be concluded that the oil immersion is not a recommended measurement method for the breakdown testing of thermally sprayed ceramics.

However, if the flashovers cause problems while making the breakdown testing and oil immersion is not an option; the sample can be placed only partly in the oil. The idea is that the testing area is dry so that it is isolated from the oil by an insulating cylinder. The cylinder is pressed tightly against a ceramic sample with the help of a rubber O-ring sealing toward the specimen surface. The high voltage rod electrode is placed in the middle of the cylinder and pressed against the ceramic sample. Small amounts of insulation oil can be poured outside this plastic cylinder.

4.3 Effect of Electrode Arrangements

In Ref 11, the comparison between stainless steel ball and the cylindrical plate electrodes was made in the

breakdown measurements of alumina at AC voltage and the breakdown strength was higher with ball electrodes. It is well known that when using a ball electrode as a voltage electrode and a spherical hole is machined onto the sample for it, the slight local field enhancement is not formed in the tested area. Due to this, maximum electric field strength is achieved with this test setup (this measurement arrangement is also mentioned in IEC standard 60672-2). However, preparing a spherical hole on coating samples is really laborious which makes it impractical to use this test arrangement with thermally sprayed ceramic coatings. Actually, ASTM Standard D149-09(2013) also recommends using fixed cylindrical electrodes with flat ends which is the commonly used method in the breakdown testing of solid insulating materials.

According to the breakdown testing standard ASTM D149-09(2013), painted electrodes can be used but the painting may affect the results (Ref 1). In this paper, when the silver-painted electrodes were used, the breakdown strength of the alumina coating decreased both in air and oil arrangements, since the whole electrode area was tested and truly the weakest point of the coating over that area was found. In addition, in all the air-insulated arrangements, partial discharge activity has an effect on the tested area, which is discussed in the following. However, the difference between the test results with and without embedded electrodes depends on the variation of the breakdown strength over the electrode area. In the case of a more homogeneous material also the breakdown distribution is, in practice, more homogeneous, and consequently the difference between the results of the test arrangements is smaller.

However, if a graphite disk was used between the voltage electrode and the coating, the breakdown strength was lower than without any embedded electrodes and the deviation was the lowest, indicating that the slightly soft graphite felt improves the contact with the coating. Due to this, larger electrode area will be tested than in the case of steel rod electrode.

4.4 Effect of Partial Discharges

As it was discussed earlier, partial discharges occur in dry measurements without any embedded electrodes between the voltage electrode and the coating because an air gap is formed there as shown in Fig. 6. The highest value for air gap is approximately 15 μm in the figure. The breakdown strength of air is presented by Paschen curve as a function of thickness multiplied by air pressure. According to Paschen curve for air at a temperature of 20 °C and in normal air pressure, the breakdown voltage for 15-μm-thick air gap is 450 V (Ref 26).

Partial discharges (pd) obviously affect the breakdown results as shown in this paper by improving the electrical contact with the coating. The pd activity was measured for one of the HVOF samples, and in the case of AC excitation the discharges started at the peak voltage of 1060 V (total electrode voltage) with a repetition rate of approximately 800 discharges per minute. In the DC case, the inception voltage was 1700-2000 V_{peak}, and the repetition rate was obviously lower than in the AC case. Due to this difference, the coating withstood higher voltage levels in DC breakdown test (41.8 V/μm) than in AC case (29.2 V/μm) when embedded electrodes were not used. When silver-painted electrodes were used, the whole painted area was continuously tested. Due to this, the breakdown occurred at a lower voltage level (31.7 V/μm) which was actually close to the AC result (29.2 V/μm). Supposing the evidently high pd activity at AC voltage can provide a proper contact over the electrode area, this result also indicates that the polarity of test voltage has no major influence on the results.

5. Conclusions

The dielectric breakdown strength of thermally sprayed alumina coating was studied with six various test arrangements. Because thermally sprayed coating is a porous material, the used insulation oil penetrates into pores of the coating as well as between the electrode and coating surface if no coating surface-embedded electrode is used. In practice, this occurs very fast after the sample is placed in the oil bath. Thus, the dielectric breakdown strength of the oil impregnated alumina coating is measured to be 94% higher than without oil immersion. Due to this, oil immersion is not a recommended measurement method for the breakdown testing of thermally sprayed ceramics.

Silver-painted electrodes on the coating surface improve the contact between the stainless steel rod electrode and the coating surface. The tested area is also larger than without any embedded electrodes. In this case, the deepest points on the coating surface are tested so that the weakest point of the painted area is truly found. Due to this, the DC breakdown strength test result is 24% lower than in the case without embedded electrodes.

If embedded electrodes are not used, partial discharges take place between the voltage electrode and the coating improving the contact (test area) between them. Under AC excitation, the partial discharge activity is more extensive than in the DC case resulting in very similar dielectric breakdown strength results than with the coating surface-embedded electrodes. In the DC case, the rather low discharge activity leads to smaller test area and higher breakdown test results. Anyhow, this method can be used to compare different materials but it shall be kept in mind that the obtained breakdown results are probably slightly higher than the results obtained with an arrangement with surface-embedded electrodes.

In the case of silver-painted electrodes on the surface, the typically averaged coating thickness measurement may lead to use of slightly too high thickness and correspondingly too low breakdown strength. In general, the marked variation of the coating thickness is a source of uncertainty and variation of the results. To minimize the uncertainty, a high enough number of parallel measurements is needed, typically at least 10 is preferred.

All the measurement arrangements include imperfections mainly arising from the unsmoothed surfaces of the substrate and the coating. Those could be avoided if coatings were sprayed on a smooth surface, and the coatings were grinded and polished before testing. In practice, thermally spayed coatings cannot be sprayed on completely smooth substrate; however, it might be possible to coat smooth-grinded substrates for breakdown tests if higher accuracy is required. In any case, the use of oil shall be avoided.

In general, among other details the test arrangements of the breakdown tests have a considerable effect on the results gathered. Due to this, care should be taken when evaluating the results obtained in different studies. The full documentation of the test conditions is a necessity.

References

1. ''ASTM Standard D-149-09(2013) Standard Test Method for Dielectric Breakdown Voltage and Dielectric Strength of Solid Electrical Insulating Materials at Commercial Power Frequencies,'' ASTM International, West Conshohocken, PA, 2013
2. ''IEC Standard 60243-1 Electric Strength of Insulating Materials—Test Methods—Part 1: Tests at Power Frequencies,'' IEC, 2013
3. L. Pawłowski, The Relationship Between Structure and Dielectric Properties in Plasma-sprayed Alumina Coatings, *Surf. Coatings Technol.*, 1988, **35**(3–4), p 285-298
4. F.L. Toma, L.M. Berger, S. Scheitz, S. Langner, C. Rödel, A. Potthoff, V. Sauchuk, and M. Kusnezoff, Comparison of the Microstructural Characteristics and Electrical Properties of Thermally Sprayed Al_2O_3 Coatings from Aqueous Suspensions and Feedstock Powders, *J. Therm. Spray Technol.*, 2012, **21**(3–4), p 480-488
5. F.L. Toma, S. Scheitz, L.M. Berger, V. Sauchuk, M. Kusnezoff, and S. Thiele, Comparative Study of the Electrical Properties and Characteristics of Thermally Sprayed Alumina and Spinel Coatings, *J. Therm. Spray Technol.*, 2011, **20**(1–2), p 195-204
6. C. Neusel, H. Jelitto, D. Schmidt, R. Janssen, F. Felten, and G.A.A, Schneider, Dielectric Breakdown of Alumina Single Crystals, *J. Eur. Ceram. Soc.*, 2012, **32**(5), p 1053-1057
7. C. Neusel and G.A. Schneider, Journal of the Mechanics and Physics of Solids Size-Dependence of the Dielectric Breakdown Strength from Nano- to Millimeter Scale, *J. Mech. Phys. Solids*, 2014, **63**(February), p 201-213
8. J. Liebault, J. Vallayer, D. Goeuriot, D. Treheux, and F. Thevenot, How the Trapping of Charges can Explain the Dielectric Breakdown Performance of Alumina Ceramics, *J. Eur. Ceram. Soc.*, 2001, **21**(3), p 389-397
9. M. Touzin, D. Goeuriot, C. Guerret-Piécourt, D. Juvé, and H.-J. Fitting, Alumina Based Ceramics for High-Voltage Insulation, *J. Eur. Ceram. Soc.*, 2010, **30**(4), p 805-817
10. M. Touzin, D. Goeuriot, H.J. Fitting, C. Guerret-Piécourt, D. Juvé, and D. Tréheux, Relationships Between Dielectric Breakdown Resistance and Charge Transport in Alumina Materials-Effects of the Microstructure, *J. Eur. Ceram. Soc.*, 2007, **27**(2–3), p 1193-1197
11. B. Block, Y. Kim, and D.K. Shetty, Dielectric Breakdown of Polycrystalline Alumina: A Weakest-Link Failure Analysis, *J. Am. Ceram. Soc.*, 2013, **96**(11), p 3430-3439
12. J.J. O'Dwyer, Breakdown in Solid Dielectrics, *Electr. Insul. IEEE Trans.*, 1982, **IE-17**(6), p 484-487
13. L. Haddour, N. Mesrati, D. Goeuriot, and D. Tréheux, Relationships Between Microstructure, Mechanical and Dielectric Properties of Different Alumina Materials, *J. Eur. Ceram. Soc.*, 2009, **29**(13), p 2747-2756
14. I.O. Owate and R. Freer, AC Breakdown Characteristics of Ceramic Materials, *J. Appl. Phys.*, 1992, **72**(6), p 2418-2422
15. M. Touzin, D. Goeuriot, H. Fitting, D. Juv, and D. Tr, Relationships Between Dielectric Breakdown Resistance and Charge Transport in Alumina Materials—Effects of the Microstructure, *J. Eur. Ceram. Soc.*, 2007, **27**, p 1193-1197
16. F. Talbi, F. Lalam, and D. Malec, Dielectric Breakdown Characteristics of Alumina, *Proceedings of 2010 International Conference on Solid Dielectrics (ICSD)*, Potsdam, Germany, 2010, p 1–4
17. M. Niittymäki, B. Rotthier, T. Suhonen, J. Metsäjoki, and K. Lahti, Effects of Ambient Conditions on the Dielectric Properties of Thermally Sprayed Ceramic Coatings, *Proceedings of the 23th Nordic Insulation Symposium Nord-IS 2013*, Trondheim, Norway, 2013, p 131–135
18. M. Niittymäki, K. Lahti, T. Suhonen, U. Kanerva, and J. Metsäjoki, Dielectric Properties of HVOF Sprayed Ceramic Coatings, *Proceedings of the IEEE International Conference on Solid Dielectrics*, Bologna, Italy, 2013, p 389–392
19. E. Turunen, T. Varis, S.-P. Hannula, A. Vaidya, A. Kulkarni, J. Gutleber, S. Sampath, and H. Herman, On the Role of Particle State and Deposition Procedure on Mechanical, Tribological and Dielectric Response of High Velocity Oxy-fuel Sprayed Alumina Coatings, *Mater. Sci. Eng. A*, 2006, **415**(1–2), p 1-11
20. IEC standard 60672-2, *Ceramic and Glass Insulating Materials—Part2: Methods of Test*. IEC, 1999
21. IEC 62539, *Guide for the Statistical Analysis of Electrical Insulation Breakdown Data*, IEC, 2007
22. W. Hauschild and W. Mosch, *Statistical Techniques for High-Voltage Engineering*, Lightning Source UK LTd, Milton Keynes, 1992, p 310
23. ''ASTM Standard D257 - 07 Standard Test Methods for DC Resistance and Conductance of Insulating Materials'', ASTM Standard No. D257–07, ASTM International, West Conshohocken, PA, 2007
24. ''IEC Standard 60093 Methods of Test for Volume Resistivity and Surface Resistivity of Solid Electrical Insulating Materials,'' IEC Standard No. 60093, IEC, 1980
25. ''IEC standard 60250 Recommended Methods for the Determination of the Permittivity and Dielectric Dissipation Factor of Electrical Insulating Materials at Power, Audio and Radio Frequencies Including Metre Wavelengths, IEC Standard No. 60250, IEC, 1969
26. E. Kuffel, W.S. Zaengl, and J. Kuffel, *High Voltage Engineering: Fundamentals, Second edi*, Elsevier Ltd, Oxford, 2000, p 539
27. R. Bartnikas, Dielectrics and Insulators, *The Electrical Engineering Handbook, Second Edition*, CRC Press, Boca Raton, 1997
28. P.H.F. Morshuis and J.J. Smit, Partial Discharges at DC Voltage: their Mechanism, Detection and Analysis, *Dielectr. Electr. Insul. IEEE Trans.*, 2005, **12**(2), p 328-340
29. B. Tareev, *Physics of Dielectric Materials*, Mir Publishers, Moscow, USSR, 1979, p 270

Publication IV

DC dielectric breakdown behavior of thermally sprayed ceramic coatings

M. Niittymäki, T. Suhonen, J. Metsäjoki and K. Lahti

24th Nordic Insulation Symposium (NORD-IS 15), pp. 499–510, 2015

DOI: 10.5324/nordis.v0i24.2289

DC Dielectric Breakdown Behavior of Thermally Sprayed Ceramic Coatings

Minna Niittymäki[1], Tomi Suhonen[2], Jarkko Metsäjoki[2] & Kari Lahti[1]

[1]*Tampere University of Technology, Department of Electrical Engineering, Tampere, Finland*
[2]*Technical Research Centre of Finland, Espoo, Finland*

Abstract

Previous studies of dielectric properties of thermally sprayed insulating ceramic coatings are focused on linearly ramped dielectric breakdown strength as well as DC resistivity, relative permittivity and dielectric loss characterizations. However, reports of the effects of ramp rate or of any kind of long term stressing on the breakdown strength cannot be found in literature. The aim of this paper was to study the DC breakdown behavior of one type of HVOF sprayed alumina coating under different stresses. It can be concluded that the ramp rate of DC breakdown measurement has no remarkably influence on the breakdown strength. The breakdown behavior was also studied using step-by-step tests with two constant step voltages and step durations. The DC resistivity of the alumina coating showed strong dependence on the applied electric field. The resistivity behaved ohmicly below the field strength of ~0.5 V/µm and above ~8…12 V/µm, however, the resistivity decreased approximately three decades in the non-ohmic region (0.5 V/µm →). At electric field strengths above ~25 V/µm, the degradation started in the material leading to breakdown. However, when the step duration was longer (60 min), the degradation process started already slightly below the applied field of 25 V/µm.

1 Introduction

Thermally sprayed ceramic coatings can be used as an electrical insulation in demanding conditions such as in high temperature applications e.g. fuel cells. Thermal spraying as a method enables to manufacture insulating layer on a challenging geometry in quite inexpensive way. Despite of the clear needs for such insulating coatings, previous studies of the dielectric properties of thermally sprayed insulating ceramic coatings are focused on linearly ramped dielectric breakdown strength as well as DC resistivity, relative permittivity and dielectric loss characterizations [1]–[8]. Anyhow, reports of the effects of ramp rate or of any kind of longer term stressing on the breakdown strength cannot be found in literature. In some cases, the ramp rate is found to have an effect on the breakdown strength of certain insulation materials, with higher ramp rate giving higher breakdown strength for the material due to the space charge phenomena [9], [10].

The aim of this paper was to study the DC breakdown behavior of one type of thermally sprayed Al_2O_3 ceramic coating under different stresses as well as the permittivity, dielectric losses and DC resistivity of the coating. The breakdown behavior was studied with two different linear ramp rates and with stepwise breakdown tests varying the step size and duration enabling evaluations of the possible changes in the breakdown mechanisms.

The DC resistivity of thermally sprayed coatings has been reported to be non-ohmic when the electric field is increased above certain electric field (typically the level was only ~0.5 V/µm) [5], [6], [8]. However, DC resistivity has been measured previously only at electric field strengths varying from 0.1 V/µm to 5 V/µm due to the limitations of the measuring device used. In order to study the DC resistivity at higher electric fields, new measurement setup needed to be developed. In practice, a sensitive current measuring system was included in the stepwise breakdown measurements enabling the resistivity determination at each voltage level until the breakdown occurred.

In [8], the relative permittivity and loss index was studied as a function of electric field in order to investigate the effect of electric field on these properties. As a conclusion, especially the loss index is dependent on the electric field at low frequencies which is well in line with the previous studies focused on the non-ohmic behavior of DC resistivity [5], [6]. However, in this paper the focus is not on these properties and thus relative permittivity and loss index were measured only at one electric field strength.

2 Experimental

2.1 Studied Material

Commercial Al_2O_3 powder was sprayed using high-velocity-oxygen-fuel (HVOF) technique on stainless steel substrate. The powder particle size varied from 7 µm to 29 µm which is a typical range for ceramic powders used in HVOF spraying. In the spraying process the powder particles are heated and accelerated towards the substrate, the melted particles form droplets which hit the substrate or coating surface forming a coating consisting of splats with interfaces in between. The surfaces of the splats cool down faster than the internal parts and due to this the surfaces are normally more amorphous areas, while the internal parts are typically crystalline. These splats form the lamellar structure of a coating while the coating exhibits also defects e.g. voids as well as some cracks. During the cooling at least some vertical cracks are rather easily formed in the coating, and these are problematic for electrical insulation materials. However, thermally sprayed coatings exhibit quite typically at least some vertical cracks and the length and amount of the cracks

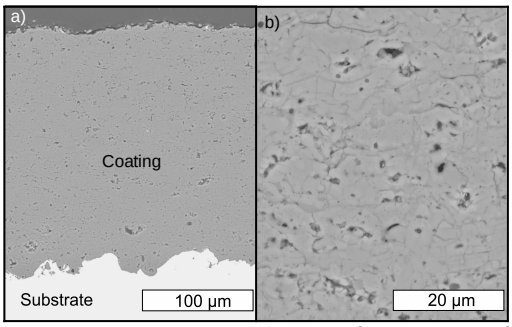

Figure 1 – SEM/BSE micrograph images of a cross-section of the studied alumina coating, with magnifications of 200 (**a**) and 1000 (**b**).

play an important role. The lamellar microstructure of the studied coating can be seen in the Figure 1.

The coating thicknesses of the samples were defined by magnetic measuring device (Elcometer 456B) as well as from cross-section surface images taken by optical micrographs [7]. In the magnetic measurements the mean values and the experimental standard deviations of the thicknesses were calculated from 10 parallel measurements covering the electrode area used in the DC resistivity and dielectric spectroscopy measurements (Table 1).

Porosity of the coatings were defined by image analysis from optical micrographs (OM) and from scanning electron microscope (SEM) images using secondary electron (SE) and backscattering electron (BSE) detectors [7] (Table 1). While making the image analysis from the SEM figures, some problems occurred and due to this the obtained porosity values are most probably too small, however, the values are given as a reference in Table 1. In addition to above, the gas (nitrogen) permeability of the coating is also presented in Table 1. Typically, high gas permeability value of a material indicates high porosity. The OM porosity of the studied alumina coating is notably higher (6 %) than the porosities of the HVOF alumina coatings in [8] where the porosity values were below 2 %. The gas permeabilities of the coatings in [8] were 5.7 nm^2 and 19.2 nm^2 while in this paper the gas permeability is 11.1 nm^2. Thus, the gas permeability values probably give more realistic view of the actual porosity of the material.

Table 1 – Porosity and thickness of the studied coating defined by using various methods as well as the gas (nitrogen) permeability of the material.

Thickness (µm)	From magnetic. meas	228
	SD	6.2
	From cross-section image	215
Porosity (%)	OM	6.0
	SEM/SE	1.7
	SEM/BSE	3.7
Gas permeability (nm^2)		11.1

2.2 Sample Preparation and Test Procedures

For the DC resistivity and relative permittivity measurements, a round silver electrode (∅=50 mm) was painted on the middle of a coating sample after the thickness measurements. In addition, a shield electrode was painted around the measuring electrode to neglect possible surface currents. For breakdown measurements silver electrodes (∅=11 mm) were painted on the sample surface to improve the contact between the voltage electrode and the coating. The used silver paint (SPI Conductive Silver Paint) was studied not to penetrate into the coating [7]. After painting the electrodes the samples were at first dried at 120 °C for two hours followed by conditioning at climate room at 20 °C, RH 20 % for at least 12 h before the measurements. All measurements for the samples were also performed in climate room at the above mentioned conditions.

2.3 Relative Permittivity and Dielectric Losses

Relative permittivity and dielectric losses of the material were studied with an insulation diagnosis analyzer device (IDA 200, U_{max}=200 V_{peak}). During the measurements, a sinusoidal voltage with varying frequency was applied over the sample. The measuring electric field strength was 0.88 V_{peak}/µm equaling the voltage of 200 V_{peak}.

The complex impedance of a sample was calculated from the measured test voltage and the current through a sample which was expressed by IDA device as the equivalent parallel RC circuit model. The relative permittivity (ε_r) and dissipation factor (*tan* δ) were calculated from the measured parallel resistance and capacitance using Eq. (1)-(2), where C_p is measured parallel capacitance and R_p parallel resistance of the equivalent circuit. C_0 is the so-called geometric capacitance of the test sample (vacuum in place of the insulation) and ω is the angular frequency. The edge field correction (C_e) was not used because the shield electrode was utilized in the measurements. Loss index (ε_r'') includes all the losses of a sample: both conductive and dielectric ones. It can be defined from relative permittivity and dissipation factor, *tan* δ, with Eq. (3). All the test arrangements were performed in accordance with the IEC standard 60250 [11].

$$\varepsilon_r \approx \varepsilon_r' = \frac{C_p}{C_0} - \frac{C_e}{C_0} \quad (1)$$

$$\tan\delta = \frac{1}{R_p C_0 \omega} \quad (2)$$

$$\varepsilon_r'' = \varepsilon_r \tan\delta \quad (3)$$

2.4 DC Resistivity

Resistivity measurements were made using Keithley 6517B electrometer. The test voltage was maintained until a stabilized current level (i.e. pure resistive current) was reached. In practice, the tests were performed at test voltages ranging from 10 V to 1000 V

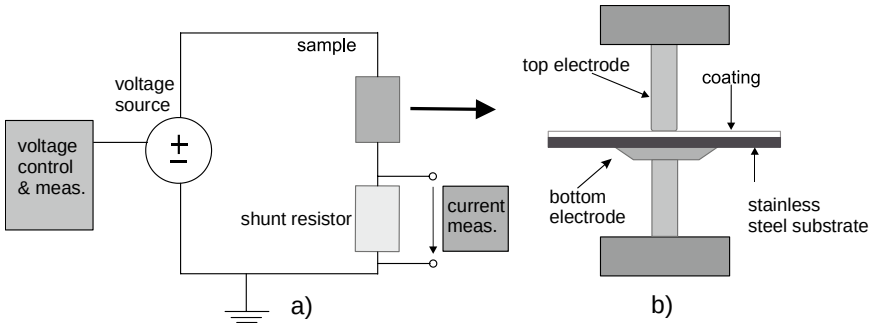

Figure 2 – The schematic figure of the measurement circuit used in the stepwise breakdown tests.

in order to study the resistivity as a function of electric field. The stabilized DC current was measured 1000 s after the voltage application. The resistivity was defined from the test voltage, the stabilized current, electrode geometry and sample thickness. All the measuring arrangements were in accordance with the standards IEC 60093/ASTM D257-07 [12], [13]. In addition to the electrometer measurements, resistivities of the coatings at higher field strengths were determined based on the current measurements made during the stepwise breakdown measurements (details in Section 2.5).

2.5 DC Breakdown Strength

DC breakdown measurements were performed either with linearly or stepwise increased DC voltage. Oil immersion was not used in the measurements because the coatings are porous allowing oil to penetrate into the coating which significantly affects the breakdown strength [7]. During the breakdown (BD) tests, the samples were clamped between two stainless steel electrodes: a flat-ended rod (∅= 11 mm) and a flat plate (∅=20 mm).

A software controlled linear ramp rate of 100 V/s or 1000 V/s was used throughout the ramp tests until breakdown occurred [7]. Dielectric breakdown strength (DBS) of a coating was calculated dividing the breakdown voltage by the corresponding coating thickness at the painted electrode (∅=11 mm) location.

The stepwise measurements were made with two different step durations, 6 min and 60 min. The 6 min step tests were started at the voltage level of 250 V which was the step size as well. The 60 min step measurements were started at the voltage of 4000 V (~18.6 V/µm) while the step size was 500 V. The schematic figure of the measurement circuit is presented in Figure 2. The current was measured throughout the test with the help of shunt resistor which was either 1 MΩ or 10 kΩ depending on the signal level and the signal was measured with Keithley 2001 DMM. The voltage source was Keihtley 2290-10 power supply (U_{max}=10 kV).

3 Results and Discussion

3.1 Relative Permittivity and Dielectric Losses

Figure 3 presents the relative permittivity and the loss index of the studied coating as a function of frequency at the electric field of 0.88 V_{peak}/µm. The relative permittivity is 11.7 at the frequency of 50 Hz and the loss index at the same frequency is 3.4. These values are quite typical for HVOF sprayed alumina coatings at dry ambient conditions [4], [8].

3.2 DC Resistivity

DC resistivity was defined as a function of electric field which was varied from 0.04 V/µm to 4.4 V/µm. The resistivity as a function of electric field can be seen in Figure 4a. It can be observed that the resistivity is practically ohmic when the applied field is below 0.5 V/µm and above that the resistivity decreases non-ohmicly as reported in [5]–[7], [8].

Because the maximum voltage of Keithley electrometer is 1 kV and the coatings are typically approximately 200 µm thick, it was not possible to measure the DC conductivity above the electric field strengths of approximately 5 V/µm with this device. Thus, a new measurement setup was developed in order to study the DC resistivity behavior of thermally sprayed coatings up to the breakdown field strengths. In practice, the current and the voltage was measured and recorded during the stepwise breakdown tests allowing

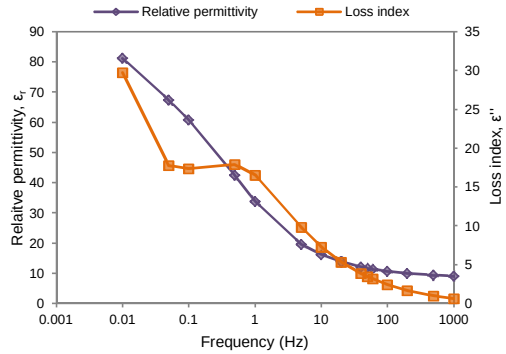

Figure 3 – The relative permittivity and the loss index of the studied material as a function of frequency.

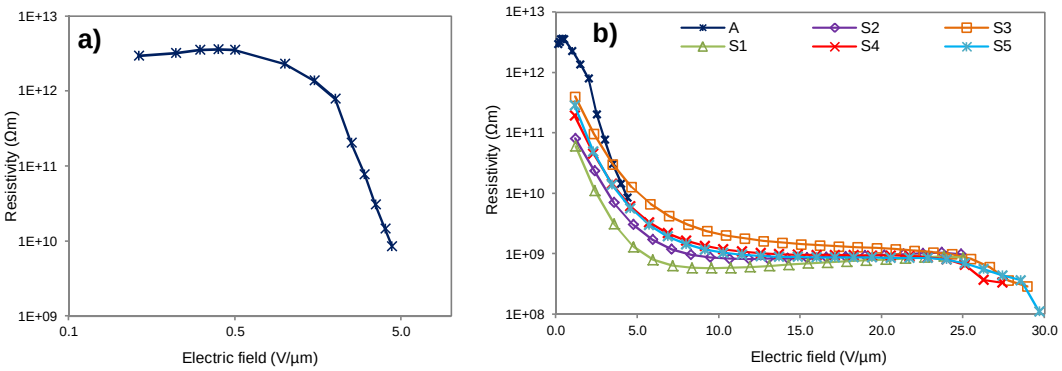

Figure 4 – **a)** DC resistivity of the studied coating (sample A) as a function of electric field (log-log-axis). **b)** DC resistivities of all the samples as a function of electric field (y-axis is logarithmic).

an estimation of DC resistivity to be made at higher field strengths. It is considered as estimation because typically the DC current did not fully stabilize during the 6 min measurement periods. Anyhow, the estimations are rather good (i.e. currents were close to the stabilized levels). Naturally, the resistivies were defined at the end of each step. This DC resistivity as a function of electric field is presented in Figure 4b.

It can be noticed from Figure 4b that the resistivity of the studied coating can be divided to certain operating areas. The resistivity was ~10^{12} Ωm and in ohmic region when the applied electric field was below 0.5 V/µm (Figure 4b). When the applied field was from 0.5 V/µm to 8…12 V/µm, the resistivity was in the non-ohmic region and decreased approximately three decades (Figure 4b). At the field strengths from 8…12 V/µm to 25 V/µm the resistivity was settled to ~10^{9} Ωm, (except in case of sample S3). When the applied field was close to the breakdown strength, the resistivity started to slightly decrease which can be seen in Figure 4b indicating an initiation of degradation/pre-breakdown process approximately from 25 V/µm.

Typically DC resistivity of insulating materials is defined at quite low voltage level (below 1 kV) but due to the shown behavior this can lead in erroneous indication of the material property since the behavior at higher service field strengths can be evidently different. Thus, better estimation of the DC resistivity of thermally sprayed ceramic coating can be defined when the applied electric field is above 10 V/µm or at service stress level of the material.

3.3 DC Breakdown Strength

3.3.1 Ramp tests

When the ramp rate was 100 V/s, the mean breakdown strength of 10 parallel measurements was 29.7 V/µm while the corresponding experimental standard deviation was 1.5 V/µm. At 10 times higher ramp rate (1000 V/s), the mean breakdown strength was 31 V/µm (SD=2.4 V/µm). It can be concluded that the ramp rate has no significant effect on the breakdown strength of these thermally sprayed ceramics because the breakdown strengths of different ramping rates are almost in the range of the standard deviations and thus the effects due to e.g. space charge accumulation cannot be noticed. The breakdown strength of the studied coating (ramp rate 100 V/s) is at similar level to the strengths obtained in previous studies [4], [7], [8] for HVOF sprayed alumina coatings.

3.3.2 Step tests

The step-by-step tests were carried out with 6 min and 60 min step durations. Table 2 presents the breakdown strength and total duration of each these tests. In addition, the mean and experimental standard deviations from five parallel DBS tests are given. The step voltage was two times higher in the 60 min tests than in 6 min tests, decreasing the 'resolution' of the 60 min tests. In the 60 minute tests the total stress duration of the samples varied from 100 min to 236 min. In the 6 min tests this variation was from 121 min to 159 min. Thus, the total duration was at quite similar level in both test types.

During the stepwise breakdown measurements certain problems took place in the one hour tests and thus all the recorded current data were not valid. Due to this, Figure 5a presents only the currents measured for the samples L2, L3 and L5 as a function of time.

As it was discussed earlier in Section 3.2, a kind of

Table 2 – Breakdown strength of the studied alumina coating in step-by-step tests. The step duration was 6 min for S-samples and 60 min for the L-samples.

Sample	DBS (V/µm)	Time to breakdown	Mean (V/µm)	SD (V/µm)
S1	25.0	121 min	27.2	2.0
S2	24.9	121 min		
S3	28.9	152 min		
S4	27.4	145 min		
S5	29.7	159 min		
L1	27.36	182 min	23.9	2.3
L2	22.83	144 min		
L3	20.27	100 min		
L4	24.77	236 min		
L5	24.12	187 min		

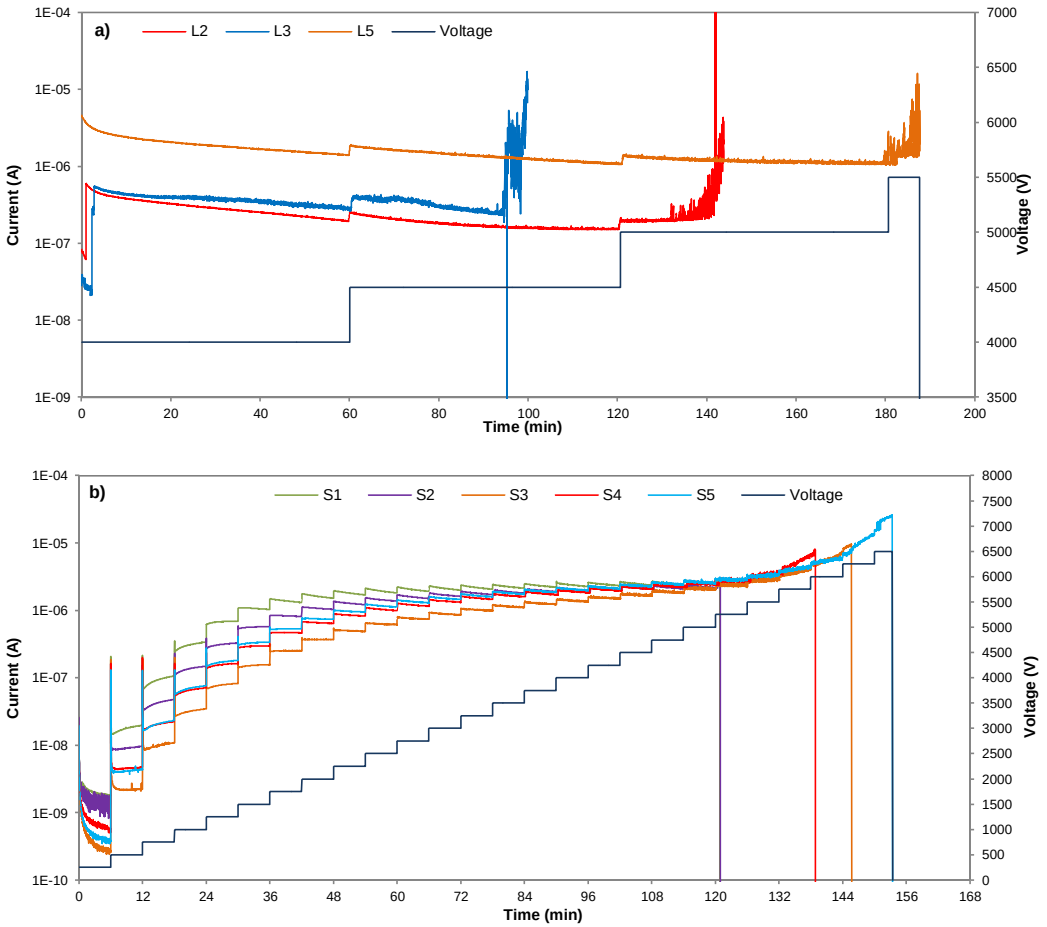

Figure 5 – **a)** Measured DC current of the studied material samples as well as the step-by-step voltage, when the step duration was 60 min, step voltage 500 V and the test was started at the voltage level of 4 kV. **b)** Measured DC currents as a function time during the 6 min/250 V step test with a start level of 250 V.

degradation/failure process started typically before the studied thermally sprayed alumina coating broke down which can be seen as a decrease in DC resistivity (Figure 4b). This same behavior can also be noticed in the 60 min step tests when the current started to increase approximately two minutes before the samples broke down (Figure 5a). It can also be noticed from the Figure 5a that the samples L2 and L5 have quite similar behavior throughout the test although their current levels and the breakdown strength differed. The currents of these two samples seemed to stabilize during the last full steps, 4.5 and 5.0 kV, respectively. On the third step (5 kV), the current of L2 was stable until the degradation started two minutes before the breakdown. A quite similar process took place for the sample L5 after increasing the test voltage to 5.5 kV. During this failure process, the resistivity of samples L2 and L5 decreased approximately one decade before the final breakdown. Similar decrease was also seen, especially, in the resistivity of sample S5 tested in 6 min step test (Figure 4b). Although sample L3 had almost similar degradation process just before the breakdown, the current started to slightly increase already in the middle of the first voltage step (4 kV). Thus, some kind of failure process started already at this point and continued on the second step (4.5 kV) The final current increase started 2 min before the breakdown.

3.4 Further Discussion of the Field Dependent Behavior of the Coating

Figure 4b presented the DC resistivity as a function of electric field and Figure 5b shows the corresponding DC currents of 6 min step tests. As it was discussed earlier, the DC resistivity behavior of the studied coating can be divided into different areas:

- electric field below 0.5 V/µm: the resistivity behaves ohmicly, ~ 10^{12} Ωm

- electric field from 1 V/µm to 8…12 V/µm: the resistivity behaves non-ohmicly
- electric field from 8…12 V/µm to 25 V/µm: the resistivity behaves ohmicly at a new region, ~10^9 Ωm
- electric field above ~25 V/µm: degradation/pre-breakdown region

From Figure 5b it can be noticed that the currents of all S-samples stabilized at the first step (~ 1 V/µm) in the end of the measurement period although the values are different. At the second step (~ 2 V/µm) the currents of samples S3 and S4 stabilized while the currents of the other samples started to gradually increase. At the higher voltage levels, all the currents were not stabilized during the measurement periods indicating that the material was in the non-ohmic region. The currents settled at quite similar level when the applied field was 8…12 V/µm. The currents of samples S3-S5 started to gradually increase when the field reached to 25 V/µm. This similar behavior can be noticed in DC resistivity as a decrease (Figure 4b). Breakdown strength of samples S1 and S2 was 25 V/µm and the degradation process was not seen for these samples. Also, these two samples had higher current levels than the other samples during the whole test duration.

It seems that above the electric field strength of 25 V/µm the current started to gradually increase in case of all samples before the breakdowns occurred in the 6 min step tests. If the breakdown strength of the sample was 25 V/µm, no degradation before the breakdown can be seen. Based on this small set of results, the 25 V/µm may be seen as a kind of coating microstructure specific limit for the final degradation of this coating. However, when the step duration was longer (60 min), the degradation process started already below the 25 V/µm. Thus, the maximum possible service stress level for the studied thermally sprayed coating might be from ~10 V/µm to ~20 V/µm at most (taking not into account safety margins). Naturally, further long-term ageing tests are needed for more confident result.

4 Conclusions

The ramp rate in DC breakdown measurement has no significant effect on the breakdown strength of HVOF sprayed alumina coating. The breakdown behavior was also studied with increasing the voltage step-by-step with two constant step voltages and step durations. The DC resistivity was also defined from the shorter step duration tests. The DC resistivity of the alumina coating showed strong dependence on the applied electric field. The resistivity behaved ohmicly below ~0.5 V/µm and above ~8…12 V/µm, however, the resistivity decreased approximately three decades in the non-ohmic region (~0.5V/µm – ~8...12 V/µm). At electric field strengths above 25 V/µm, the degradation started in the material leading to breakdown. However, when the step duration was longer (60 min), the degradation process started already slightly below the applied field of 25 V/µm.

References

[1] L. Pawłowski, "The relationship between structure and dielectric properties in plasma-sprayed alumina coatings," *Surf. Coatings Technol.*, vol. 35, no. 3–4, pp. 285–298, 1988.

[2] F.L. Toma, S. Scheitz, L. M. Berger, V. Sauchuk, M. Kusnezoff, and S. Thiele, "Comparative study of the electrical properties and characteristics of thermally sprayed alumina and spinel coatings," *J. Therm. Spray Technol.*, vol. 20, no. 1–2, pp. 195–204, 2011.

[3] F.L. Toma, L. M. Berger, S. Scheitz, S. Langner, C. Rödel, A. Potthoff, V. Sauchuk, and M. Kusnezoff, "Comparison of the Microstructural Characteristics and Electrical Properties of Thermally Sprayed Al 2O 3 Coatings from Aqueous Suspensions and Feedstock Powders," *J. Therm. Spray Technol.*, vol. 21, no. 3–4, pp. 480–488, 2012.

[4] M. Niittymäki, B. Rotthier, T. Suhonen, J. Metsäjoki, and K. Lahti, "Effects of ambient conditions on the dielectric properties of thermally sprayed ceramic coatings," in *Proceedings of the 23th Nordic Insulation Symposium Nord-IS 2013*, 2013, pp. 131–135.

[5] M. Niittymäki, K. Lahti, T. Suhonen, U. Kanerva, and J. Metsäjoki, "Dielectric properties of HVOF sprayed ceramic coatings," in *Proceedings of the IEEE International Conference on Solid Dielectrics*, 2013, pp. 389–392.

[6] M. Niittymäki, T. Suhonen, J. Metsäjoki, and K. Lahti, "Influence of Humidity and Temperature on the Dielectric Properties of Thermally Sprayed Ceramic MgAl2O4 Coatings," in *2014 Annual Report Conference on Electrical Insulation and Dielectric Phenomena*, 2014, pp. 94–97.

[7] M. Niittymäki, K. Lahti, T. Suhonen, and J. Metsäjoki, "Dielectric Breakdown Strength of Thermally Sprayed Ceramic Coatings: Effects of Different Test Arrangements," *J. Therm. Spray Technol.*, vol. 24, no. 3, pp. 542–551, Jan. 2015.

[8] M. Niittymäki, T. Suhonen, J. Metsäjoki, and K. Lahti, "Electric Field Dependency of Dielectric Behavior of Thermally Sprayed Ceramic Coatings," in *2015 IEEE 11th International Conference on the Properties and Applications of Dielectric Materials (ICPADM)*, 2015, (submitted).

[9] G. Chen and J. Zhao, "Space charge and thickness dependent dc electrical breakdown of solid dielectrics," in *2012 International Conference on High Voltage Engineering and Application*, 2012, pp. 12–15.

[10] G. Chen, J. Zhao, S. Li, and L. Zhong, "Origin of thickness dependent dc electrical breakdown in dielectrics," *Appl. Phys. Lett.*, vol. 100, no. 22, p. 222904, 2012.

[11] "IEC standard 60250 Recommended methods for the determination of the permittivity and dielectric dissipation factor of electrical insulating materials at power, audio and radio frequencies including metre wavelengths," no. IEC Standard 60250. IEC, 1969.

[12] "IEC standard 60093 Methods of test for volume resistivity and surface resistivity of solid electrical insulating materials," no. IEC Standard 60093. IEC, 1980.

[13] "ASTM Standard D257 - 07 Standard Test Methods for DC Resistance and Conductance of Insulating Materials," no. ASTM Standard D257–07. ASTM International, West Conshohocken, PA, 2007.

Publication V

Electric field dependency of dielectric behavior of thermally sprayed ceramic coatings

M. Niittymäki, T. Suhonen, J. Metsäjoki and K. Lahti

IEEE International Conference on the Properties and Applications of Dielectric Materials (ICPADM), pp. 500–503, 2015

DOI: 10.1109/ICPADM.2015.7295318

Electric Field Dependency of Dielectric Behavior of Thermally Sprayed Ceramic Coatings

Minna Niittymäki and Kari Lahti
Department of Electrical Engineering
Tampere University of Technology
Tampere, Finland
minna.niittymaki@tut.fi

Tomi Suhonen and Jarkko Metsäjoki
Advanced Materials
VTT Technical Research Centre of Finland
Espoo, Finland

***Abstract*— High temperature applications e.g. fuel cells require ceramic based insulation solutions instead of polymers. The aim of this paper was to characterize the dielectric properties of thermally sprayed ceramic coatings; especially the electric field dependency of AC and DC behavior of thermally sprayed ceramic coatings. One of the spinel samples and one of the alumina samples have quite similar lamellar microstructure which may partly explain their similar type of behavior in DC resistivity as well as in AC loss indexes at low frequencies. These two samples had smaller lamellar size than the other alumina and spinel samples which also had quite similar behavior of AC losses at low frequencies, respectively. In addition to the lamellar size and structure, also micro cracks in the coating microstructure are proposed to have an effect on the dielectric behavior and its electric field dependency.**

Keywords*— *thermal spraying; HVOF; ceramic; coating; alumina; spinel; dielectric spectroscopy; dc conductivity; loss index; resistivity; breakdown

I. INTRODUCTION

High temperature applications such as fuel cells require ceramic based insulation solutions instead of polymers. Thermal spraying is a fast and relatively inexpensive method for producing electrical insulation for demanding application conditions and geometries. While various materials can be thermally sprayed, in electrical insulation applications the commonly used materials are alumina (Al_2O_3) and magnesium aluminate ($MgAl_2O_4$). Although there are clear needs and applications for electrically insulating coating materials, the previous studies of the dielectric properties of thermally sprayed ceramic coatings are focused on dielectric breakdown properties and only a few studies on dc conductivity, relative permittivity and dielectric losses can be found in the literature [1]–[7]. However, previous studies on the DC conductivity of thermally sprayed coatings typically indicate that the conductivity quite typically increases non-linearly already at quite low electric fields [5]. Thus the aim of this paper is to study the DC resistivity and especially the relative permittivity and dielectric losses of thermally sprayed alumina and magnesium aluminate coatings as a function of electric field. All such studies have to be carried out at controlled conditions because ambient conditions have major influence on the dielectric properties of thermally sprayed ceramic coatings [1], [4], [6]. Because the coatings have special microstructure which most probably has a remarkable effect on the dielectric properties [1], the influence of the microstructure of the studied coatings on the DC and AC behavior is analyzed.

978-1-4799-8903-4/15/$31.00 ©2015 IEEE

II. EXPERIMENTAL

A. Studied Materials

The coatings were manufactured from two commercial alumina (Al_2O_3) powders and two different experimental spinel ($MgAl_2O_4$) powders which were sprayed by high-velocity-oxygen-fuel (HVOF) technique on stainless steel substrates. The difference in Al_2O_3 powders was different particle size, HVOF2 powder has smaller particle size (2-10 μm) than HVOF3 (5-25 μm). $MgAl_2O_4$ coating HVOF1 was sprayed from Al_2O_3-MgO composite powder which formed into a spinel coating during the spraying process. However, the other $MgAl_2O_4$ coating (HVOF4) was sprayed from a spinel form $MgAl_2O_4$ powder.

When the powder particles are heated and accelerated towards the substrate in the spraying process, melted particles form droplets which splat on the substrate/coating surface forming a coating consisting of splats with interfaces in between. The surfaces of the splats cool down faster than the internal parts, and due to this the surfaces are normally more amorphous areas while the internal parts are typically more crystalline. These splats form the lamellae of a coating but the coating exhibits also defects e.g. voids as well as some cracks. During the cooling at least some vertical cracks are rather easily formed in the coating, which are typically problematic for electrical insulation materials. However, thermally sprayed coatings exhibit quite typically at least some vertical cracks but the length and amount of the cracks play an important role. It can be noticed from Fig. 1 that the spinel sample HVOF1 and the alumina sample HVOF2 exhibit quite similar lamellar microstructure where clear crystalline (lighter) and amorphous (darker) areas can be seen. However, alumina sample HVOF3 has only small amount of amorphous areas and spinel sample HVOF4 has significantly smaller amount of amorphous areas than the other spinel HVOF1. In addition, HVOF1 and HVOF2 samples have smaller lamellar size than the alumina sample HVOF3 and the spinel sample HVOF 4.

The coating thicknesses of the samples were defined by magnetic measuring device (Elcometer 456B) and from cross-section surface images taken by optical micrographs [7]. In the magnetic measurements the mean values and the experimental standard deviations of the thicknesses were calculated from 10

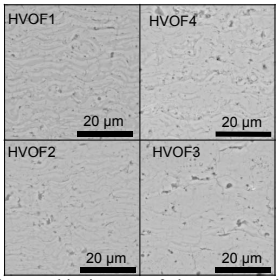

Fig.1.SEM/BSE micrographic images of the cross-sections of the studied coatings.

parallel measurements covering the electrode area used in the DC resistivity and dielectric spectroscopy measurements. The coating thickness values have quite large deviation partly due to the grit blasting made for the steel substrates, which makes the surface of the rather unsmooth.

Porosity values of the coatings were defined by image analysis from optical micrographs (OM) and from scanning electron microscope (SEM) by two detectors secondary electron (SE) and backscattering electron (BSE) [7] which are presented in Table I. In addition, the thickness values and gas (nitrogen) permeability of the coatings are presented in Table I. Typically, higher gas permeability indicates more porous material, but as it can be seen from Table I alumina sample HVOF3 has very high gas permeability in comparison to the other samples although the porosity values are at quite similar level with the others. This difference is most probably due to the vertical cracks seen in the microstructure image of the coating HVOF3 (Fig.1).

B. Sample Preparation and Test Procedures

For the DC resistivity and relative permittivity measurements, a round silver electrode (∅=50 mm) was painted on the middle of a coating sample. In addition, a shield electrode was painted around the measuring electrode to neglect possible surface currents. For breakdown measurements silver electrodes (∅=11 mm) were painted on the sample surface to improve the contact between the voltage electrode and the coating. The used silver paint (SPI Conductive Silver Paint) did not penetrate into the coating [7]. After painting the electrodes the samples were at first dried at 120 °C for two hours followed by conditioning at climate room at 20 °C, RH 20 % for at least 12 h before the measurements. All the measurements for the samples were also performed in the climate room at above the mentioned conditions.

TABLE I. THICKNESS, POROSITY AND GAS PERMEABILITY VALUES FOR THE STUDIED COATINGS USING DIFFERENT MEASUREMENT METHODS.

	Sample	**HVOF 2**	**HVOF 3**	**HVOF 1**	**HVOF 4**
	Composition	Al_2O_3	Al_2O_3	MgO-Al_2O_3	$MgAl_2O_4$
Thickness	From magnetic meas. mean (µm)	208	281	130	196
	From magnetic meas. SD (µm)	3.9	9.1	3.1	3.4
	From cross-section image (µm)	209	288	125	195
Porosity	OM (%)	1.9	1.7	0.9	1.3
	SEM/SE (%)	1.0	1.0	0.6	1.3
	SEM/BSE (%)	1.9	3.0	1.4	2.4
	Gas permeability (nm^2)	5.7	19.2	3.0	3.2

C. DC Resistivity Measurements

Resistivity measurements were made using Keithley 6517B electrometer. The test voltage was maintained until a stabilized current level (i.e. pure resistive current) was reached. In practice, the tests were performed at test voltages ranging from 10 V to 1000 V in order to study the resistivity as a function of electric field. The stabilized DC current was measured 1000 s after the voltage application. All the measuring arrangements were in accordance with the standards IEC 60093/ASTM D257-07.

D. Dielectric Spectroscopy

Relative permittivity and dielectric losses of the materials were studied with an insulation diagnosis analyzer device (IDA 200, U_{max}=200 V_{peak}) and its high voltage unit (IDA HV unit, U_{max}=30 kV_{peak}). During the measurements, a sinusoidal voltage with varying frequency was applied over the sample. The measuring electric field varied from 0.1 V/µm to 5 V/µm. The measuring electric field was limited to quite low levels (corresponding possible service stress levels) to ensure that samples will not break down during the measurements.

The complex impedance of a sample was calculated from the measured test voltage and the current through a sample which was expressed by IDA device as the equivalent parallel RC circuit model. The relative permittivity (ε_r) and dissipation factor (*tan* δ) were calculated from the measured parallel resistance and capacitance using Eq. 1-2, where C_p is measured parallel capacitance and R_p parallel resistance of the equivalent circuit model of a dielectric. C_0 is the so-called geometric capacitance of the test sample (vacuum in place of the insulation) and ω is the angular frequency. The edge field correction (C_e) was not used because the shield electrode was utilized in the measurements. Loss index (ε_r'') includes all the losses of a sample: both conductive and dielectric ones. It can be defined from relative permittivity and dissipation factor, *tan* δ, with Eq.3. All the test arrangements were performed in accordance with the IEC standard 60250.

$$\varepsilon_r \approx \varepsilon_r' = \frac{C_p}{C_0} - \frac{C_e}{C_0}, \quad (1)$$

$$\tan\delta = \frac{1}{R_p C_0 \omega}, \quad (2)$$

$$\varepsilon_r'' = \varepsilon_r \tan\delta \quad (3)$$

E. DC Breakdown Strength Measurements

DC breakdown (bd) voltage measurements were made with a linearly ramped DC voltage. Oil immersion was not used in the measurements because the coatings are porous allowing oil to penetrate into the coating which significantly affects the breakdown strength [7]. During the breakdown tests, the samples were clamped between two stainless steel electrodes: a flat-ended rod (∅= 11 mm) and a flat plate (∅=50 mm). A software controlled linear ramp rate of 100 V/s was used throughout the test until breakdown occurred. Dielectric breakdown field strength of a coating was calculated dividing

the breakdown voltage by the corresponding coating thickness at the painted electrode (∅=11 mm) location.

III. Results and Discussion

A. DC Resistivity

Figure 2 presents the DC resistivity of the studied alumina and spinel coatings as a function of electric field. It can be noticed that all the samples have non-ohmic behavior already at quite low electric field values (approximately ≥ 0.5 V/µm) as it was also reported in [5], [6].

It can be observed that the resistivity of alumina HVOF3 is almost one decade lower than the resistivity of the other studied coatings. This is most probably due to the notable vertical cracks of the sample which probably is also one reason, together with the voids, for the high gas permeability value of this sample. The larger powder particle size of HVOF3 coating may also partly explain the difference in resistivity of the alumina samples, since it may lead to the thicker coating lamellae observable in Fig.1. The DC resistivity of MgO-Al_2O_3 sample (HVOF1) is at very similar level with the Al_2O_3 sample HVOF2, but the spinel HVOF4 sample has lower resistivity above the electric field of 0.5 V/µm. This difference in HVOF4 may be partly due to the larger size of lamellae than in HVOF1 (Fig.1).

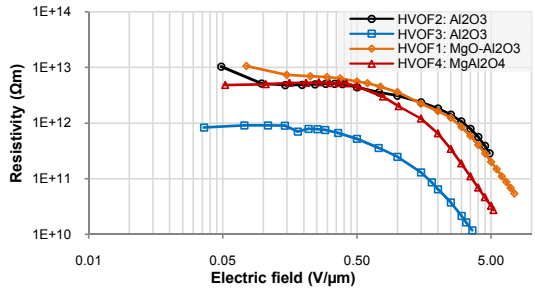

Fig. 2. DC resistivity of the studied materials as a function of electric field.

B. Dielectric Spectroscopy

Figure 3a-b presents the relative permittivity of the studied alumina and spinel coatings. At the frequency of 100 Hz the relative permittivity of all samples are ~10 at all the electric field strengths. At the lower frequency (0.1 Hz), lowest relative permittivity was measured for MgO-Al_2O_3 sample (HVOF1) and the permittivity does not increase with increasing electric field unlike in the case of $MgAl_2O_4$ sample (HVOF4). Alumina sample made from smaller particle size powder (HVOF2) has lower relative permittivity at 0.1 Hz than the other alumina sample (HVOF3) made from larger particle size powder. The permittivity of both alumina samples increase slightly with increasing electric field but the effect is quite small.

The loss indexes of all the coatings at the frequency of 100 Hz are approximately at similar level (Fig. 3c-d). However, at the frequency of 0.1 Hz the loss indexes of alumina and spinel samples differ significantly. Alumina sample HVOF2 and spinel sample HVOF1 are only slightly dependent on the electric field at 0.1 Hz. In addition, the alumina sample (HVOF2) has higher loss index than the spinel sample (HVOF1). The loss index of alumina sample HVOF3 and spinel sample HVOF4 are dependent on the electric field especially above 0.5 V/µm. As it can be noticed from Fig. 1, the spinel sample HVOF1 and the alumina sample HVOF2 exhibit quite similar lamellar microstructure which may explain their similar type of behavior in DC resistivity as well as in AC loss indexes at low frequencies. These two samples

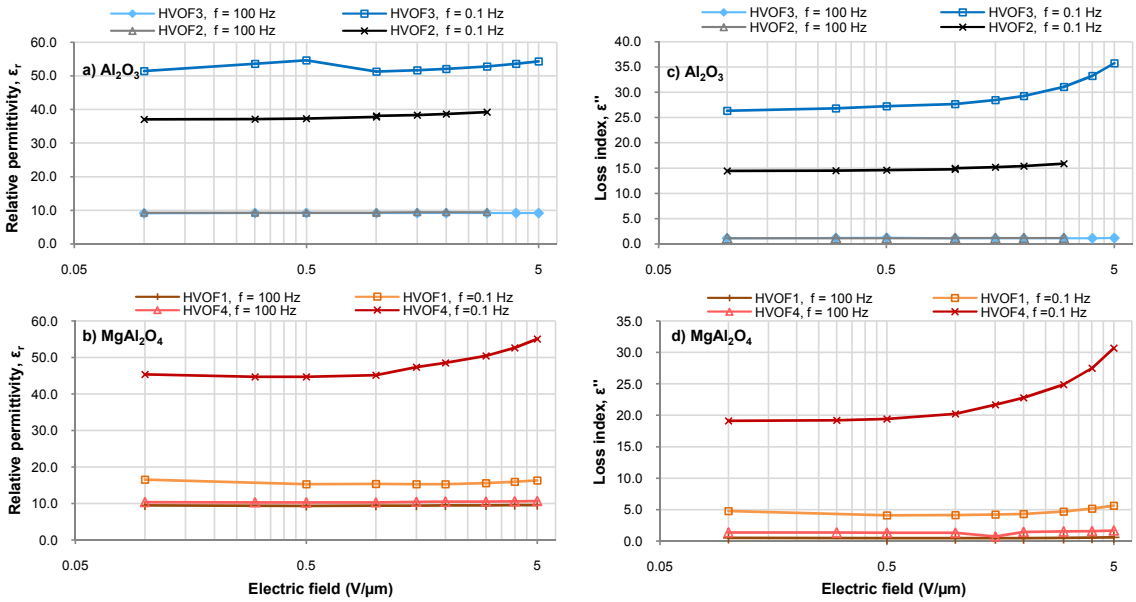

Fig.3. Relative permittivity of a) alumina and b) spinel coatings as a function of electric field. Loss index of c) alumina samples and d) spinel samples with two frequencies as a function of electric field.

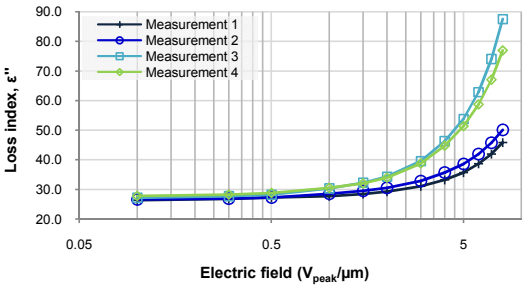

Fig. 4. Loss index of sample HVOF3 at frequency of 0.1 Hz as a function electric field after different measurements.

have smaller lamellar size and the amount of amorphous areas is higher than in the HVOF3 and HVOF 4 which in turn have quite similar behavior in AC losses at low frequencies although the actual values differ.

Because DC resistivity measurements caused some permanent changes to the thermally sprayed ceramics in [6], dielectric spectroscopy measurements were remade for the studied samples in order to verify the possible permanent changes. The samples were placed again in controlled conditions (20°C, RH 20%) and the measurements were remade on the next day. This procedure was repeated for all the studied samples two times and the changes in the AC losses were significant especially in the case of sample HVOF3 which was measured four times due to this. Figure 4 shows the loss index of HVOF3 at a frequency of 0.1 Hz as a function of electric field from the first measurement to the fourth.

It can be observed that at low electric fields (below 1 V/µm), the loss indexes are at similar level in the different measurements, but at higher field strengths the loss indexes increased notably after the second measurement. Thus some permanent changes occurred in the material, probably some of the vertical cracks inside the coating broke into more conducting state short circuiting part of the lamellae, which further changed the capacitance of the coating and increased the conductivity. Since certain field strength is required for the short circuiting, the behavior at lower field strengths is repeatable. The loss index of the other alumina coating (HVOF2) increased in a quite similar way indicating similar permanent material changes. However, the loss index and relative permittivity of the spinel samples (HVOF1 and HVOF4) did not increase like the properties of alumina most probably due to the fewer amount of micro cracks.

C. DC Breakdown Strength

Table II shows the mean dielectric breakdown strength from five parallel measurements for all the studied coatings as well as the corresponding experimental standard deviations. The MgO-Al_2O_3 coating (HVOF1) has the highest breakdown strength but on the other hand the deviation is also the highest. However, the other spinel sample (HVOF4) has notably lower DBS probably because of the different lamellar size (Fig. 1). Despite the highest DC conductivity and measured material degradation during the characterizations, the alumina sample

TABLE II. MEAN BREAKDOWN STRENGTH AND EXPERIMENTAL STANDARD DEVIATIONS FOR THE STUDIED COATINGS.

Sample	Mean DBS (V/µm)	SD (V/µm)
HVOF1: MgO-Al_2O_3	30.2	5.3
HVOF4: $MgAl_2O_4$	19.3	3.7
HVOF2: Al_2O_3	21.6	4.4
HVOF3: Al_2O_3	25.1	2.7

HVOF3 has higher DBS in comparison to the other alumina (HVOF2).

IV. CONCLUSIONS

Microstructural properties of thermally sprayed ceramic coatings have been discussed as well as the role of these properties on their electrical behavior. Particularly, vertical micro cracks are suggested to be one reason for the noticed non-linearity along the applied field strength. In addition, size of lamellae and the amount of amorphous areas may also have significant effect on the dielectric properties, especially in AC loss indexes at low frequencies and in DC resistivity. In general, the spinel samples had lower AC loss indexes than alumina samples. In addition, the DC resistivity was typically higher than that of alumina coating which is in line with the AC behavior.

The studied coatings were tested as-sprayed without any electrical pre-stressing. In the dielectric spectroscopy measurements of alumina coatings certain permanent changes occurred already at rather low field strengths representing realistic service stresses. Thus, in order to reflect better real application behavior, it is recommended to make some electrical pre-stressing prior to the characterizations.

REFERENCES

[1] F. L. Toma, S. Scheitz, L. M. Berger, V. Sauchuk, M. Kusnezoff, and S. Thiele, "Comparative study of the electrical properties and characteristics of thermally sprayed alumina and spinel coatings," *J. Therm. Spray Technol.*, vol. 20, no. 1–2, pp. 195–204, 2011.

[2] F.-L. Toma, L. M. Berger, S. Scheitz, S. Langner, C. Rödel, A. Potthoff, V. Sauchuk, and M. Kusnezoff, "Comparison of the Microstructural Characteristics and Electrical Properties of Thermally Sprayed Al 2O 3 Coatings from Aqueous Suspensions and Feedstock Powders," *J. Therm. Spray Technol.*, vol. 21, no. 3–4, pp. 480–488, 2012.

[3] L. Pawłowski, "The relationship between structure and dielectric properties in plasma-sprayed alumina coatings," *Surf. Coatings Technol.*, vol. 35, no. 3–4, pp. 285–298, 1988.

[4] M. Niittymäki, B. Rotthier, T. Suhonen, J. Metsäjoki, and K. Lahti, "Effects of ambient conditions on the dielectric properties of thermally sprayed ceramic coatings," in *Proceedings of the 23th Nordic Insulation Symposium Nord-IS 2013*, 2013, pp. 131–135.

[5] M. Niittymäki, K. Lahti, T. Suhonen, U. Kanerva, and J. Metsäjoki, "Dielectric properties of HVOF sprayed ceramic coatings," in *Proceedings of the IEEE International Conference on Solid Dielectrics*, 2013, pp. 389–392.

[6] M. Niittymäki, T. Suhonen, J. Metsäjoki, and K. Lahti, "Influence of Humidity and Temperature on the Dielectric Properties of Thermally Sprayed Ceramic MgAl2O4 Coatings," in *2014 Annual Report Conference on Electrical Insulation and Dielectric Phenomena*, 2014, pp. 94–97.

[7] M. Niittymäki, K. Lahti, T. Suhonen, and J. Metsäjoki, "Dielectric Breakdown Strength of Thermally Sprayed Ceramic Coatings: Effects of Different Test Arrangements," *J. Therm. Spray Technol.*, vol. 24, no. 3, pp. 542–551, Jan. 2015.

Publication VI

Role of microstructure in dielectric properties of thermally sprayed ceramic coatings

M. Niittymäki, I. Rytöluoto, T. Suhonen, J. Metsäjoki and K. Lahti

2016 IEEE International Conference on Dielectrics (ICD), pp. 500–503, 2016

DOI: 10.1109/ICD.2016.7547811

Role of Microstructure in Dielectric Properties of Thermally Sprayed Ceramic Coatings

Minna Niittymäki, Ilkka Rytöluoto and Kari Lahti
Department of Electrical Engineering
Tampere University of Technology
Tampere, Finland
minna.niittymaki@tut.fi

Jarkko Metsäjoki and Tomi Suhonen
Thermal Spray, Advanced Materials
VTT Technical Research Centre of Finland
Espoo, Finland

***Abstract*— Thermally sprayed insulating ceramic coatings can be utilized in conditions where polymers are inapplicable. The coatings exhibit a special lamellar microstructure with interfaces and some defects (e.g. voids, cracks) in between. The aim of this study was to analyze the relationship between the microstructural features and the dielectric properties of various thermally sprayed ceramics. The structural characterization of the ceramic coatings was made based on following properties: porosity, volumetric gas permeability and the characteristic size of crystalline lamella. High gas permeability of the coatings decreased the breakdown strength but similar effect cannot be seen in the DC resistivity and the permittivity results. Decrease of DC resistivity at high humidity did not correlate to microstructural properties; rather it is speculated to indicate the hydrophilic nature of the coatings. The characteristic crystalline domain sizes showed no clear correlation with the dielectric properties.**

Keywords—thermal; spray; ceramic; coating; alumina; spinel; resistivity; permittivity; breakdown; microstructure; porosity

I. INTRODUCTION

Thermally sprayed insulating ceramic coatings can be utilized in conditions where polymers are inapplicable. In order to use the coatings in real applications, the role of microstructural features in the dielectric properties has to be known. The coatings are deposited in layers forming a lamellar structure consisting of interfaces and some defects (e.g. voids and cracks) [1]–[3]. Especially, the cracks enable easier charge carrier movement [4] which is problematic for insulating coatings.

Typically, porosity is used to characterize the microstructure of thermally sprayed ceramic coatings. The determination of the porosity can be made by using several methods [5]. Typical method is image analysis which is made by using cross-sectional micrographs taken by optical or scanning electron microscopes [3]–[7]. Although the image analysis gives a good estimation about the porosity [5], the defined value does not represent the volumetric porosity of a coating which would take into consideration the unique shape of the voids which have influence on the mechanical properties of the coatings [3]. However, the shape and orientation of the pores can be defined by using 3-dimensional images instead of the 2D images [8], [9] but the analyzing methods are not as widely used as the methods based on the 2D images. Anyhow, the porosity cannot be the only structural parameter to determine the microstructure of the coatings, and quantitative methods are also required [3].

The influence of the microstructural features on the dielectric properties have been discussed previously in [1], [6] in which the high porosity has been suggested to decrease the breakdown strength. However, it has been also reported that porosity does not clearly affect the breakdown strength of thermally sprayed coatings [7], [10], [11]. In addition, the size of the lamella and the amount of amorphous areas has been discussed to affect the dielectric losses at low frequencies and DC conductivity but the analysis was made only visually [11]. The aim of this paper is to link several microstructural features (porosity, gas permeability, the size of lamella) to the dielectric properties of various thermally sprayed ceramic coatings.

II. EXPERIMENTAL

A. Material characterization

Six different experimental $MgO–Al_2O_3$ powders were sprayed by high-velocity oxygen fuel (HVOF)–thermal spray method on stainless steel substrates. The amount of MgO in the powder varied from 0 mol% to 65 mol%. Detailed information of the studied coatings is given in Table1. The coating thickness was determined either by using magnetic measuring device (Elcometer 456B) or from cross-sectional images taken by optical microscopy (Table 1). The high standard deviation in thickness is partly due to the grit-blasting made for the steel substrates in order to ensure good adhesion between the ceramic and the steel.

The porosities of the coatings were determined by analyzing cross-sectional micrographs taken by optical microscopy (OM, 320× magnification) and by scanning electron microscope (SEM, 1000× magnification) using both secondary electron detector (SE) and backscattered electron detector (BSE), see Table 1. The porosities were determined as the ratio of total area of voids to the total image area. In addition to image analysis, the gas (nitrogen) permeability (GP) was measured for the coatings, providing an indirect measure of the porosity with a higher gas permeability indicating a higher porosity.

In order to analyze the lamellar morphologies, the SEM/BSE images were converted into binary pixel matrices

TABLE I. POWDER COMPOSITIONS OF THE STUDIED HVOF COATINGS, THE DEFINED POROSITIES, THICKNESSES AND CRYSTALLINE LAMELLA THICKNESS (L_F).

Sample	Powder composition	L_f (µm)	Porosity				Thickness (µm)		
			OM (%)	*SEM/SE (%)*	*SEM/BSE (%)*	*GP (nm^2)*	*From cross-section image*	*From magnetic measurement*	*SD*
HVOF7	100 mol% Al_2O_3	2.184	2.9	1.0	2.6	7.71	255	237	10.2
HVOF8	90 mol% Al_2O_3 – 10 mol% MgO	2.157	3.0	1.2	3.1	4.76	195	193	8.0
HVOF9	75 mol% Al_2O_3 – 25 mol% MgO	1.507	2.5	1.2	3.1	3.86	190	184	7.9
HVOF10	60 mol% Al_2O_3 – 40 mol% MgO	2.463	3.1	1.1	3.0	13.3	235	241	13.8
HVOF11	50 mol% Al_2O_3 – 50 mol% MgO	1.697	2.4	1.1	3.8	6.27	257	215	2.4
HVOF12	35 mol% Al_2O_3 – 65 mol% MgO	1.460	2.3	1.6	3.8	15.5	191	234	10.0

corresponding to the crystalline and amorphous areas and analyzed quantitatively in MATLAB. In accordance with the free-space length developed by Khare & Burris [12], quantitative determination of the characteristic size of a morphological domain of interest provides means to relate structural features and material properties. In this paper, the free-space length, L_f, was utilized to characterize the size of the crystalline domains of the coatings. Free-space length can be defined as the size of the largest randomly placed box for which the most probable number of intersecting pixels corresponding to amorphous regions is zero. The MATLAB code, retrieved and used according to the literature [12], [13], iterates to box size by Monte Carlo approach—a more thorough description of the method is presented in [12], [13].

B. Dielectric characterization

For DC resistivity and permittivity measurements, a round electrode (Ø=50 mm) was painted on the sample surface using a silver paint (SPI High Purity Silver Paint). In addition, a shield electrode was painted around the measuring electrode to neglect possible surface currents. For breakdown measurements, smaller silver painted electrodes (Ø=11 mm) were prepared. After painting the electrodes, the samples were at first dried at 120 °C for two hours followed by conditioning at a climate room at 20 °C/RH 20 % for at least 12 h before the measurements. All the measurements were also performed at the formerly mentioned conditions in the climate room.

DC breakdown voltage measurements were performed with linearly increased DC voltage (100 V/s) using methods depicted in [14]. Oil immersion was not used in the measurements because the coatings are porous allowing oil to penetrate into the coating which significantly affects the breakdown strength [14]. During the breakdown (BD) tests, a stainless steel rod electrode (Ø=11mm) was placed on the top of the painted electrode while the stainless steel substrate acted as the other electrode. Dielectric breakdown strength (DBS) was calculated by dividing the breakdown voltage by the coating thickness at the painted electrode location.

Typically dielectric breakdown strength of solid materials is Weibull distributed and due to this the results were fitted to this distribution. The cumulative density function of a two-parameter Weibull distribution is given as

$$F(x,\alpha,\beta) = 1 - \exp\left\{\left(\frac{x}{\alpha}\right)^{\beta}\right\} \quad (1)$$

where $F(x)$ is the breakdown probability, x is the measured breakdown strength (V/µm), α is the scale parameter (V/µm) and β is the shape parameter. The scale parameter represents the breakdown strength at the 63.2 % failure probability and the shape parameter indicates the slope of the theoretical distribution. The statistical analysis was performed using Weibull++ software and the Maximum Likelihood method was used in the parameter estimation.

Resistivity measurements were made using Keithley 6517B electrometer. In order to study the resistivity as a function of applied electric field, the test electric field varied from ~0.1 V/µm to ~5 V/µm. The test voltage was maintained for a time period of 1000 s at each voltage step. The resistivity was defined from the stabilized current value in the end of the measurement period. All the measuring arrangements were in accordance with the IEC standard 60093.

Relative permittivity and dielectric losses of the material were studied with an insulation diagnostic analyzer device (IDA 200, U_{max}=200 V_{peak}). During the measurements, a sinusoidal voltage (200 V_{peak}) with varying frequency (1 kHz–0.1 Hz) was applied over the sample. The permittivity of a coating was calculated using the equivalent parallel RC-circuit. All the test arrangements were performed in accordance with the IEC standard 60250.

III. RESULTS AND DISCUSSION

A. Structural analysis

Exemplifying SEM/BSE cross-sectional morphologies are presented in Fig. 1, showing the porous nature and the lamellar crystal structure of the coatings. While the porosities determined from the cross-sectional micrographs were found to be relatively similar for all the coatings, the gas permeability measurements indicated significant differences between the coatings, see Table1. This is most likely due to the fact that gas permeability provides a more accurate estimate of the volumetric porosity than a single cross-sectional micrograph. It is noted that the varying amount of small vertical cracks visible in the cross-sectional images likely contribute to porosity and gas permeability, with this being most prominent for HVOF10 which exhibited particularly long vertical cracks (see Fig. 1 and Table1). Fig. 1 also presents the corresponding binary images utilized for quantitative determination of the characteristic crystalline domain size and the calculated free-space lengths. While HVOF9 and HVOF12 were found to exhibit slightly more compact amorphous–crystalline regions, the overall differences remained small and showed no clear correlation with the MgO-content.

B. DC breakdown strength

Breakdown voltage measurements were performed for 15 parallel samples of each coating. The breakdown strength of the coatings is presented in Fig. 2. The highest breakdown strengths were obtained for HVOF9 (25 % MgO) and HVOF8 (10 % MgO) while the lowest breakdown strengths were

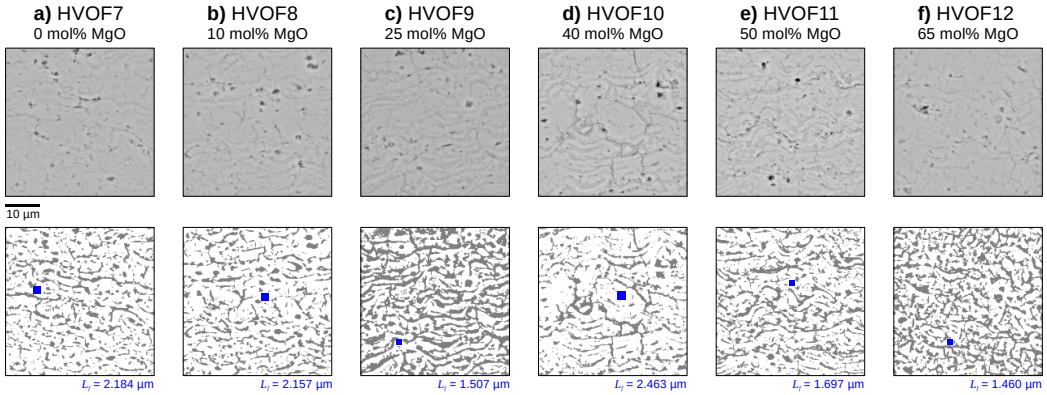

Fig. 1. Zoomed-in portions of the SEM/BSE cross-sectional images of the studied coatings at 1000× magnification. The total studied image areas were 121×98 µm^2. The top row presents the original SEM images, with light gray, dark gray and black image regions corresponding to the crystalline, amorphous and void (porosity) regions. The bottom row presents the corresponding binary images utilized for the quantitative structural analysis. The free-space length, L_f, characterizing the size of the crystalline domain is presented in each figure. Free-space length determination was performed iteratively in MATLAB (in manual mode) by gradually increasing the amount of random tests up to 100,000 in order to obtain high statistical accuracy.

measured for HVOF12 (65 % MgO) and HVOF10 (40 % MgO). Interestingly, the breakdown strength of the alumina (HVOF7, 0 % MgO) and spinel (HVOF11, 50 % MgO) is very similar although typically the HVOF spinel coatings exhibit higher breakdown strength than the HVOF alumina coatings [6], [11].

The significant difference between the lowest and the highest DBS can be explained by the differences in gas permeabilities. The relationship between the GP and breakdown strength is presented in Fig. 2 in which the Weibull parameters (α & β) are shown as a function of gas permeability. It was noted that a coating with a high GP value also showed lower breakdown strength. On the other hand, the characteristic crystalline domain sizes showed no clear correlation with the breakdown strength, which suggests that the porosity and the vertical cracks (structural defects) play a more determining role in the DBS of the coating than the crystalline–amorphous morphology, in coherence with [1], [6]. It is also remarked that the observed long vertical cracks, particularly in HVOF10, likely affect the DBS. However, a more detailed analysis of the amount and size of the cracks is not presented in this paper.

Obviously, the amount of MgO has also some effect on the breakdown strength. However, this effect is difficult to obtain comparing the breakdown strengths because HVOF10 (40 % MgO) exhibit long vertical cracks and high GP in comparison to the HVOF9 (25 % MgO) and HVOF11 (50 % MgO). Even though, it can be noticed that 10 % or 25 % MgO content in a coating produced the highest breakdown strength. When the MgO amount is 0 % or 50%, the breakdown strength is lower. However, the breakdown strengths of HVOF7 and HVOF11 (39.2 V/µm and 40.3 V/µm, respectively) is well in line with our previous studies [11], [14].

C. DC resistivity

DC resistivity as a function of electric field is presented in Fig. 3a). The lowest resistivity was measured for HVOF7 (100 % Al_2O_3). When 10 % MgO was mixed with Al_2O_3, the resistivity increased slightly (HVOF8). The DC resistivities of the coatings (HVOF9–HVOF12) were practically at similar level. In addition, the non-ohmic behavior cannot be seen for these coatings at the studied field strengths, however the HVOF7 and HVOF8 exhibit the typical non-ohmic behavior of thermally sprayed ceramic coatings [11], [15].

In order to study the effect of high humidity on the DC resistivity of the coatings, DC resistivity (2–4 V/µm) was measured for the coatings HVOF8–HVOF12 at 20 °C/RH 90 % conditions. The resistivity decreased ~5 decades. The difference could not be seen to correlate with any of the

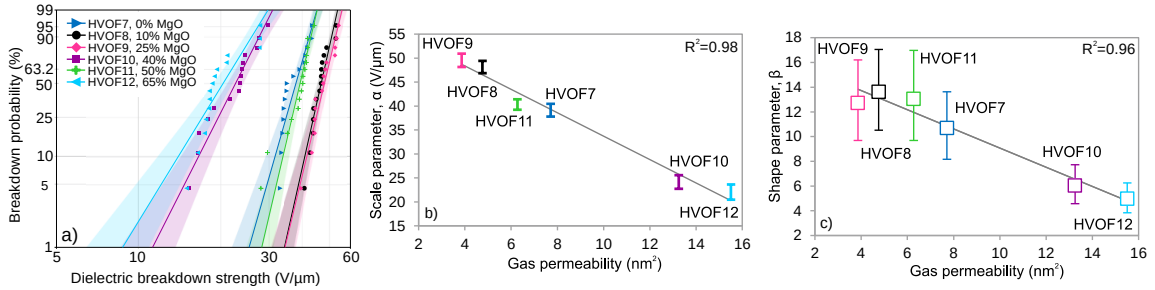

Fig. 2. a) DC breakdown strength of the coatings in Weibull probability plot where the shaded areas present 90 % confidence bounds. b)–c) Weibull parameters α and β as a function of gas permeability where the error bars present the 90 % confidence bounds for the parameters.

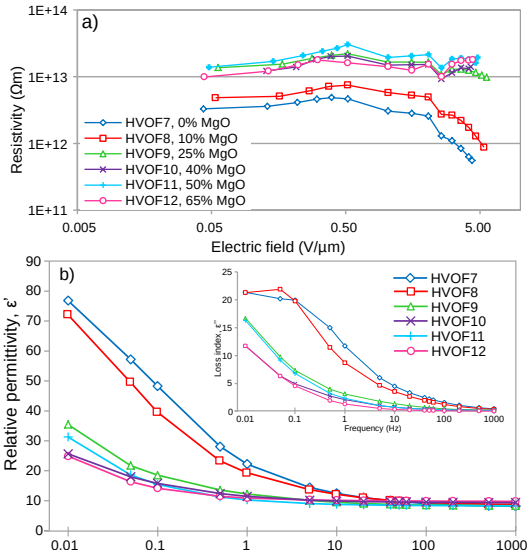

Fig. 3. a) DC resistivity as a function of electric field b) relative permittivity as a function of frequency for the studied coatings and the loss index ε_r'' as a function frequency (inset).

defined microstructural parameters, like gas permeabilities. Similar decrease in resistivity was also reported in [6] in which the DC resistivity was measured for HVOF alumina and spinel coatings which were kept in RT/RH ~95 % conditions for 48 h before the resistivity measurements. In [6], it was discussed that the coatings are sensitivity to humidity due to the nature of the material, the microstructure and the phase composition. Thus, it can be speculated that the hydrophilic nature of the coatings has more significant effect on the DC resistivity than long vertical cracks or high gas permeability.

D. Relative permittivity and dielectric losses

The relative permittivity (ε') and the loss index (ε'') of the studied coatings as a function of frequency is shown in Fig. 3b). At frequencies from 20 Hz to 1 kHz, the relative permittivity is at similar level for all the coatings. Below 10 Hz differences exist, the HVOF7 and HVOF8 having the highest permittivities. The permittivities of the coatings HVOF9–HVOF12 are more or less at same level. The loss indices of HVOF7 and HVOF8 are significantly higher than those of the other coatings. The losses of HVOF9–HVOF12 are also at a similar level. Thus, the loss index results are well in line with the DC resistivity results. However, no coherence with any of the defined microstructural features (e.g. gas permeability) can be seen in permittivity or in loss index.

IV. Conclusions

The structural characterization of thermally sprayed ceramic coatings was made based on following properties: porosity, volumetric gas permeability and the size of characteristic crystalline lamella. High gas permeability of the coatings decreased the breakdown strength but similar effect cannot be seen in the DC resistivity and the permittivity results. It was also remarked that the observed long vertical cracks likely affected the breakdown strength. Decrease of DC resistivity at high humidity did not correlate to microstructural properties; rather it is speculated to indicate the hydrophilic nature of the coatings. The characteristic crystalline domain sizes showed no clear correlation with the dielectric properties.

References

[1] L. Pawłowski, "The relationship between structure and dielectric properties in plasma-sprayed alumina coatings," *Surf. Coatings Technol.*, vol. 35, no. 3–4, pp. 285–298, 1988.

[2] L. Pawlowski, *The Science and Engineering of Thermal Spray Coatings.* Chichester, West Sussex, England: John Wiley & Sons Ltd, 2008.

[3] C.-J. Li and A. Ohmori, "Relationships between the microstructure and properties of thermally sprayed deposits," *J. Therm. Spray Technol.*, vol. 11, no. 3, pp. 365–374, 2002.

[4] S. Beauvais, V. Guipont, F. Borit, M. Jeandin, M. Español, K. A. Khor, A. Robisson, and R. Saenger, "Process-microstructure-property relationships in controlled atmosphere plasma spraying of ceramics," *Surf. Coatings Technol.*, vol. 183, no. 2–3, pp. 204–211, May 2004.

[5] S. Deshpande, A. Kulkarni, S. Sampath, and H. Herman, "Application of image analysis for characterization of porosity in thermal spray coatings and correlation with small angle neutron scattering," *Surf. Coatings Technol.*, vol. 187, no. 1, pp. 6–16, Oct. 2004.

[6] F. L. Toma, S. Scheitz, L. M. Berger, V. Sauchuk, M. Kusnezoff, and S. Thiele, "Comparative study of the electrical properties and characteristics of thermally sprayed alumina and spinel coatings," *J. Therm. Spray Technol.*, vol. 20, no. 1–2, pp. 195–204, 2011.

[7] J. Kotlan, R. C. Seshadri, S. Sampath, P. Ctibor, Z. Pala, and R. Musalek, "On the dielectric strengths of atmospheric plasma sprayed Al2O3, Y2O3, ZrO2–7% Y2O3 and (Ba,Sr)TiO3 coatings," *Ceram. Int.*, vol. 41, no. 9, pp. 11169–11176, Nov. 2015.

[8] S. Beauvais, V. Guipont, M. Jeandin, D. Jeulin, A. Robisson, and R. Saenger, "Study of the Porosity in Plasma-Sprayed Alumina through an Innovative Three-Dimensional Simulation of the Coating Buildup," *Metall. Mater. Trans. A*, vol. 39, no. 11, pp. 2711–2724, Jul. 2008.

[9] O. Amsellem, F. Borit, D. Jeulin, V. Guipont, M. Jeandin, E. Boller, and F. Pauchet, "Three-dimensional simulation of porosity in plasma-sprayed alumina using microtomography and electrochemical impedance spectrometry for finite element modeling of properties," *J. Therm. Spray Technol.*, vol. 21, no. 2, pp. 193–201, Sep. 2012.

[10] E. E. J. Young, E. Mateeva, J. J. Moore, B. Mishra, and M. Loch, "Low pressure plasma spray coatings," *Int. Conf. Metall. Coatings Thin Film.*, vol. 377–378, no. 0, pp. 788–792, Jan. 2000.

[11] M. Niittymäki, T. Suhonen, J. Metsäjoki, and K. Lahti, "Electric Field Dependency of Dielectric Behavior of Thermally Sprayed Ceramic Coatings," in *2015 IEEE 11th International Conference on the Properties and Applications of Dielectric Materials (ICPADM)*, 2015, pp. 500–503.

[12] H. S. Khare and D. L. Burris, "A quantitative method for measuring nanocomposite dispersion," *Polymer (Guildf).*, vol. 51, no. 3, pp. 719–729, Feb. 2010.

[13] J. Ye, H. S. Khare, and D. L. Burris, "Quantitative characterization of solid lubricant transfer film quality," *Wear*, vol. 316, no. 1–2, pp. 133–143, Aug. 2014.

[14] M. Niittymäki, K. Lahti, T. Suhonen, and J. Metsäjoki, "Dielectric Breakdown Strength of Thermally Sprayed Ceramic Coatings: Effects of Different Test Arrangements," *J. Therm. Spray Technol.*, vol. 24, no. 3, pp. 542–551, Jan. 2015.

[15] M. Niittymäki, T. Suhonen, J. Metsäjoki, and K. Lahti, "Influence of Humidity and Temperature on the Dielectric Properties of Thermally Sprayed Ceramic MgAl2O4 Coatings," in *2014 Annual Report Conference on Electrical Insulation and Dielectric Phenomena*, 2014, pp. 94–97.

Publication VII

DC conduction and breakdown behavior of thermally sprayed ceramic coatings

M. Niittymäki, T. Suhonen, J. Metsäjoki and K. Lahti

IEEE Transactions on Dielectrics and Electrical Insulation, vol. 24, no. 1, pp. 499–510, 2017

DOI: 10.1109/TDEI.2016.006156

DC Conduction and Breakdown Behavior of Thermally Sprayed Ceramic Coatings

Minna Niittymäki, Kari Lahti
Tampere University of Technology
Department of Electrical Engineering
P.O. Box 692
FI-33101 Tampere, Finland

Tomi Suhonen and **Jarkko Metsäjoki**
VTT Technical Research Centre of Finland
P.O. Box 1000
FI-02044 VTT, Finland

ABSTRACT

In this study, the DC conductivity from low electric fields up to breakdown fields is studied for several different thermally sprayed ceramic coatings. Although the DC conductivity of bulk alumina ceramic has been observed to follow the space charge limited current conduction mechanism, the studied ceramic coatings do not follow or follow only partly this mechanism. Possible reason for this is their different microstructure since bulk alumina exhibits fully crystalline microstructure while the ceramic coating consists of crystalline and amorphous regions as well as voids, defects and numerous interfaces. A possible conduction mechanism of the ceramic coatings based on the different conductivities of the amorphous and crystalline regions of the coatings is proposed. The microstructural features (e.g. volumetric porosity) are found to affect the breakdown strength for some of the studied coatings. The step-test breakdown strengths of the coatings were lower than the ramp-test ones due to the longer stress durations in step tests giving an indication of effects of electrical stress duration and possible short-term degradation of the coatings.

Index Terms — **Dielectric breakdown, conductivity, thermally sprayed ceramic coating, alumina, spinel.**

1 INTRODUCTION

THERMALLY sprayed electrically insulating coatings can be utilized in special operation conditions like in harsh environments or in high temperature applications such as in solid oxide fuel cells where the typical operating temperatures can vary from 500 to 800 °C [1]. Typically, the materials used for manufacturing of insulating coatings are alumina (Al_2O_3) or spinel ($MgAl_2O_4$) which can be either in powder or cord form. In the spraying process, thermal energy is generated either by chemical (combustion) or electrical (plasma or arc) methods in order to melt and accelerate the powder particles towards the substrate [2, 3]. The molten particles form droplets which hit the substrate or coating surface forming a coating consisting of thin layers of lamellae (called splats) with interfaces in between [2, 3]. The surfaces of the splats cool down faster than the internal parts and due to this the surfaces are normally more amorphous, while the internal parts are typically crystalline [3, 4]. These splats form the lamellar main structure of a coating while the coating exhibits also defects e.g. voids and often also some cracks [2, 3]. During the cooling at least some vertical cracks are rather easily formed in the thermally sprayed ceramic coating, which is especially problematic in electrical insulation materials. The length and the amount of cracks play an important role in the dielectric properties of the ceramic coatings. Especially, the DC breakdown strength has been found to decrease when long vertical cracks exhibit in a ceramic coating [5].

In this paper, the studied coatings are deposited either by high-velocity oxygen fuel (HVOF) process, which is a flame spray method in which a fuel gas (e.g. ethylene) and oxygen are used to create a high temperature combustion jet, or by plasma arc process. The main difference between the above processes is that the temperature of the flame in HVOF spraying is much lower (~3100 °C) than that of the plasma arc (~5500 °C) in plasma spraying [2, 3]. On the other hand, the particle velocity is much higher in the HVOF process (610–1060 m/s) than in the plasma process (240 m/s) [2], [6]. Accordingly, HVOF process typically results in a very dense and well-bonded coating suitable for many applications [2, 3].

Manuscript received on 13 July 2016, in final form 19 October 2016, accepted 3 November 2016. Corresponding author: M. Niittymäki.

Previous studies on the dielectric properties of HVOF and plasma sprayed Al_2O_3 and $MgAl_2O_4$ coatings have been focused on the short-term progressive breakdown strength, DC resistivity at low electric fields, and relative permittivity and dielectric losses [7–14]. Our previous studies have shown that thermally sprayed ceramic coatings exhibit strong non-ohmic conductivity starting from very low electric field strengths (~1 V/µm) originating from the special microstructure of the ceramic coatings [10, 11, 13]. However, our previous measurements on the conductivity were limited to low electric fields of ~5 V/µm or less due to the limitations of the measurement setup [10, 11, 13]. In order to study the DC conductivity of the ceramic coatings up to breakdown fields, a new measurement system has recently been developed and applied in the DC conductivity analysis of a HVOF sprayed alumina coating [15].

Typically, the DC conduction behavior of solid insulation materials can be explained by theoretical conduction mechanisms such as Schottky injection, Poole-Frenkel or space charge limited current (SCLC) mechanisms [16, 17]. Neusel et al. [18] and Talbi et al. [19] have observed that the DC conductivity of bulk alumina follows the SCLC mechanism. However, similar conductivity studies have not been conducted for thermally sprayed ceramic coatings. Typically, bulk alumina ceramic exhibits fully crystalline microstructure while ceramic coatings have amorphous and crystalline regions as well as voids and numerous interfaces. Due these differences, the DC conductivity of the coatings differs significantly from the bulk ceramic at low [10, 11, 13] and high [15, 18, 19] electric fields.

The aim of this paper is to study the DC conductivity over the full range from low electric fields up to breakdown fields for several different thermally sprayed ceramic coatings. In addition, the DC conduction mechanism is analyzed in detail. Moreover, the breakdown behavior of the coatings is studied utilizing linearly increased (short-term) test voltage and step-wisely increased voltage in order to get an indication of the possible short-term degradation of the coatings.

2 EXPERIMENTAL

2.1 MATERIAL CHARACTERZATION

Six different (Al_2O_3 or Al_2O_3/MgO) powders were thermally sprayed by the HVOF technique at VTT. In addition, one Al_2O_3 powder was deposited using atmospheric plasma spraying technique. Detailed information of all the studied coatings is listed in Table 1. The commercial alumina powders utilized in the coatings HVOF5, HVOF6 and Plasma differed slightly from each other. However, the same experimental alumina powder was used in coatings HVOF7–11 while the amount of MgO was varied from 0 to 50%. All the coatings were sprayed on 2.5 mm thick stainless steel substrates which were grit-blasted before coating deposition.

Figure 1 presents the cross-section images of the studied coatings taken by scanning electron microscope (SEM) with backscattered electron detector. The porous nature of the coatings as well as the lamellar structure can be seen from the images. The porosities of the coatings were defined by image analysis using the cross-sectional micrographic images of either optical microscope (OM) or SEM with two detectors: secondary electron detector (SE) or backscattered electron detector (BSE). In image analysis, the image magnification was 320 in OM images and 1000 in SEM images. The defined porosity values are listed in Table 1**.** In addition, the gas (nitrogen) permeability (GP) was measured for the coatings in accordance with ISO 4022 standard. Typically, high gas permeability indicates high porosity. Especially, this relationship can be noticed when comparing the OM and SEM/BSE porosities to the gas permeabilities. The porosities of plasma alumina defined from SEM images are at a higher level than the values of HVOF aluminas which is understandable due to the higher particle velocity in the HVOF process [2, 3].

Sample thicknesses were measured with Elcometer 456B device from the electrode areas (Ø=11 mm or Ø=50 mm depending on the test). The average thicknesses and standard deviations of the coatings are listed in Table 1 (10 parallel measurements from the 50 mm electrode area). In addition, the coating thicknesses were also determined from the cross-section images taken by optical micrographs and the obtained values are given in Table 1. The standard deviations of the thicknesses are quite large which may partly be due to the grit blasting of the coating substrate and consequently uneven lower surfaces of the coatings [11]. In addition, the spraying process itself does not produce fully smooth coating surface which also partly explains the thickness deviation. Anyhow, the thicknesses obtained by the two methods were at similar level although separate samples were utilized for the measurements.

2.2 DIELECTRIC CHARACTERIZATION

2.2.1 SAMPLE PREPARATION

For DC conductivity measurements below 1 kV voltages, a round electrode (Ø=50 mm) was painted on the sample surface using a special silver paint (SPI High Purity Silver Paint). In addition, a shield electrode was painted around the measuring electrode to prevent possible surface

Table 1. Studied materials and their properties.

Sample	Powder composition	Porosity				Thickness (µm)		
		OM (%)	SEM/SE (%)	SEM/BSE (%)	GP (nm^2)	From cross-section image	From magnetic measurement	SD
HVOF5	commercial Al_2O_3 (agglomerated & sintered)	6.0	1.7	3.7	11.1	215	228	6.2
HVOF6	commercial Al_2O_3 (fused)	1.4	1.4	1.4	3.2	333	307	6.1
HVOF7	experimental Al_2O_3 (agglomerated & sintered)	2.9	1.0	2.6	7.7	255	237	10.2
Plasma	commercial Al_2O_3 (fused)	2.3	2.4	3.6	–	245	271	11.4
HVOF8	90 % Al_2O_3 – 10 % MgO (agglomerated & sintered)	3.0	1.2	3.1	4.8	195	193	8.0
HVOF9	75 % Al_2O_3 – 25 % MgO (agglomerated & sintered)	2.5	1.2	3.1	3.9	190	184	7.9
HVOF11	50 % Al_2O_3 – 50 % MgO (agglomerated & sintered)	2.4	1.1	3.8	6.3	257	215	2.4

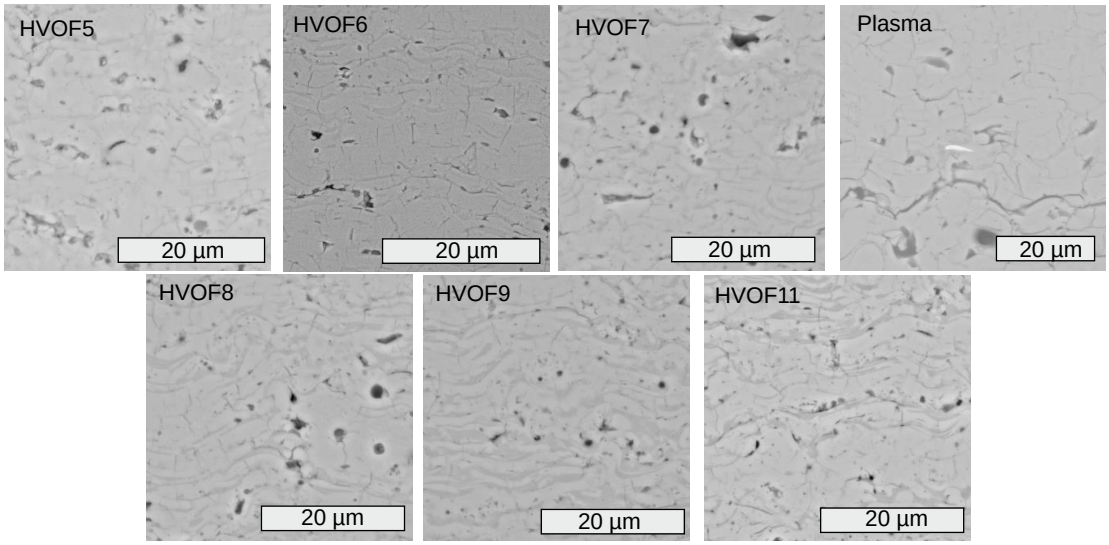

Figure 1. SEM/BSE cross-sectional images of the studied coatings at 1000× magnification. The ligth gray image areas correspond to the crystalline regions while the dark gray areas correspond to the amorphous regions. The black image areas are voids indicating the porosity of a coating.

currents, see Figure 3. For the DC conductivity and breakdown measurements above 1 kV, smaller silver painted electrodes (Ø=11 mm) were prepared, see Figure 3. In this setup, no guard ring was used. According to preliminary experiments, the surface currents were evaluated to be rather small compared to the current through the sample and the variation between the parallel samples. Our previous study indicated that the silver paint does not penetrate into the coating [12]. After painting the electrodes, the samples were at first dried at 120 °C for two hours followed by conditioning in a climate room at 20 °C, RH 20% for at least 12 h before the measurements. All the measurements were also performed at these controlled conditions in the climate room.

2.2.2 DC CONDUCTION MEASUREMENTS

DC conductivity was measured using two different measurement setups due to the wide measurement range and sensitivity required for the leakage current measurements. Below 1 kV voltages, the DC conduction current measurements were performed using Keithley 6517B electrometer. The measuring electric field was varied from 0.1 V/µm to ~4 V/µm and the measurement period for each voltage level was 1000 s. During each measurement period, the pure constant DC conduction current was normally reached. During the measurements, a stainless steel electrode (Ø=50 mm) was placed on the top of the silver painted area on the coating sample while the stainless steel substrate of the sample acted as the other electrode. The current density was determined from the average of the stabilized DC current measured over 990–1000 s after the voltage application. All the measuring arrangements were in accordance with the standard IEC 60093 [20].

Above 1 kV voltages, the DC conductivity was studied by increasing the voltage step-wisely in 250 V/10 min steps starting from 250 V until breakdown occurred. During the measurements, a stainless steel rod electrode (Ø=11 mm, edge rounding 1 mm) was placed on the top of the silver painted area on the coating sample while the stainless steel substrate of the sample acted as the other electrode. In order to avoid surface flashovers at the highest test voltages (in practice for all HVOF coatings), a plastic cylinder with an O-ring sealing towards the coating surface was clamped around the measuring electrode (Ø=11 mm) to extend the surface distance over the solid insulation. The typical oil immersion –method cannot be used due to the porous nature of the coatings [12]. The schematic figure of the measurement circuit as well as the test bench is presented in Figure 2. The sample current was measured throughout the tests by a shunt resistor (1 MΩ or 10 kΩ depending on the signal level) and a Keithley 2001 digital multimeter. The voltage source control and data recording was performed using LabVIEW-based software. The voltage source was Keithley 2290-10 power supply (U_{max}=10 kV).

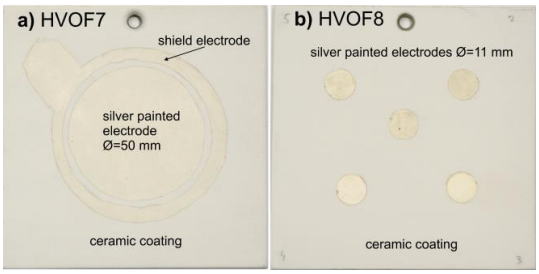

Figure 3. Photographs of the electrode arrangements utilized in the conductivity measurements below 1 kV (**a**) and above 1 kV (**b**) voltage levels. The photographs were taken after the measurements.

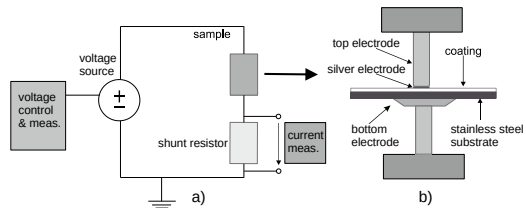

Figure 2. Schematic figure of the measurement circuit and test bench used in DC conductivity measurements above 1 kV.

2.2.3 BREAKDOWN VOLTAGE MEASUREMENTS

Breakdown strengths of the materials were measured by using the above described step-wise tests as well as by utilizing linear ramp tests (ramp rate of 100 V/s throughout the test). The measurement arrangements were otherwise similar to the step-tests but the voltage source was Spellman SL1200 (U_{max}=20 kV) and the voltage was measured using a resistive voltage divider (Spellman HVD-100-1, division ratio 10000:1) [12]. Dielectric breakdown strength (DBS) of a coating was calculated by dividing the breakdown voltage by the corresponding coating thickness at the painted electrode (∅=11 mm) location. Despite obvious edge field enhancement at the edges of the painted electrodes, the breakdown locations were noticed to be distributed reasonably well along the electrode area. This is supposed to be caused by the rather high deviations in the breakdown strength.

2.2.4 STATISTICAL ANALYSIS OF THE BREAKDOWN DATA

Typically, the dielectric breakdown strength of solid materials is Weibull distributed and due to this the results were fitted to this distribution. The cumulative density function of a two-parameter Weibull distribution is given as

$$F(x) = 1 - \exp\left\{-\left(\frac{x}{\alpha}\right)^{\beta}\right\}, x \geq 0, \quad (1)$$

where $F(x)$ is the breakdown probability, x is the measured breakdown strength (V/µm), α is the scale parameter (V/µm) and β is the shape parameter. The scale parameter represents the breakdown strength at the 63.2% failure probability and the shape parameter indicates the slope of the theoretical distribution. The statistical analysis was performed using Weibull++® software and the Maximum Likelihood method was used in the parameter estimation.

3 RESULTS AND DISCUSSION

3.1 GENERAL BEHAVIOR OF DC CONDUCTION CURRENTS

Figure 4a-4g presents the measured currents for each studied coating sample as a function of time when the voltage was increased step-wisely until breakdown. The breakdown strengths defined from these measurements are presented in Figure 4h. It can be noticed that the coatings exhibit strong non-linear voltage-current relationship and quite large deviation in breakdown results as well as in the conduction currents between the parallel samples. It can be observed from Figure 4 that the coatings exhibit a 'transition-field' region where highly non-ohmic conductivity is increasing to a new current level until breakdown occurs.

The focus of this study is to compare the DC conductivities of the different coating materials in a more general sense rather than to determine the DC conductivity of only one type of coating material in detail using very large number of parallel samples. The conduction current behavior of the HVOF coatings sprayed using commercial alumina powders (HVOF5 and HVOF6) is quite similar although the absolute current values differed. In addition, it can be noted that one of the samples of HVOF5 coating differs significantly from the other four samples. The conductivity of plasma sprayed alumina generally is at a similar level with HVOF6 coating. However, the current of plasma coating changes more rapidly in the 'transition-field' region with non-ohmic conduction than in the HVOF coatings. The conduction current behavior of HVOF7 and HVOF8 is very similar which is understandable due to the similar amounts of MgO (HVOF7 0%, HVOF8 10%) added in the same Al_2O_3 powder. The conductivity of HVOF9 (25% MgO) is very similar with alumina HVOF5 although the actual current level of HVOF9 is lower than the current of HVOF5. Three of five parallel samples of HVOF11 (50% MgO) did not break down until the maximum voltage of the power supply was reached. In addition, the current levels of those three samples were clearly lower than the currents of the samples which broke down. Although there are clear general differences between the materials, the typical current levels just prior the breakdown events were roughly at a level of ~10^{-6} A for all the coatings.

3.2 ANALYSIS OF THE CONDUCTION CURRENTS VERSUS ELECTRIC FIELD

In order to evaluate the conduction processes of the coatings in more detail, current densities of the studied coatings were determined as a function of applied electric field. Although the steady-state current level was not reached at each applied voltage level (this can be especially seen in the 'transition field' region, see Figure 4), the current densities of the materials were defined from the mean values of the current at the end of each voltage step (550–580 s). It should be underlined that in 'the transition fields' the defined current densities do not thus represent DC conductivity implicitly. Figure 5 presents the defined current densities of five parallel samples of each coating as a function of applied electric field. In addition, the average current densities of the five parallel samples are presented. Anyhow, for HVOF5 the average current density was defined only from four samples because one of the five samples exhibited totally different conduction behavior.

As it can be noticed from Figure 5, the current densities measured using the low (L1) and high (H1–H5) field measurement setups differed to some extent. This is most probably because the sensitivity of the high field measurement setup was insufficient at the lowest test fields (see the high noise in the lowest test voltages in Figure 4). Separate samples were utilized at low and high field measurements. Quite large deviation between the parallel samples (H1–H5) can be seen and it can further explain the difference. As it was mentioned previously, the materials are also in a 'transition-field' region with non-ohmic conduction when the high and low field setups are comparable. In this region, the currents did not fully reach the steady-state level during the test period of 10 min and thus the defined values did not represent the true DC conductivity.

In order to further study, the differences between the materials, the experimental data were plotted as log (J) versus log (E) where approximately straight lines with different slopes at different regions of field strengths may be obtained. Least-square technique was utilized to define the best fits for the conduction currents, and thus to define the slopes for each region. Table 2 presents the defined slopes

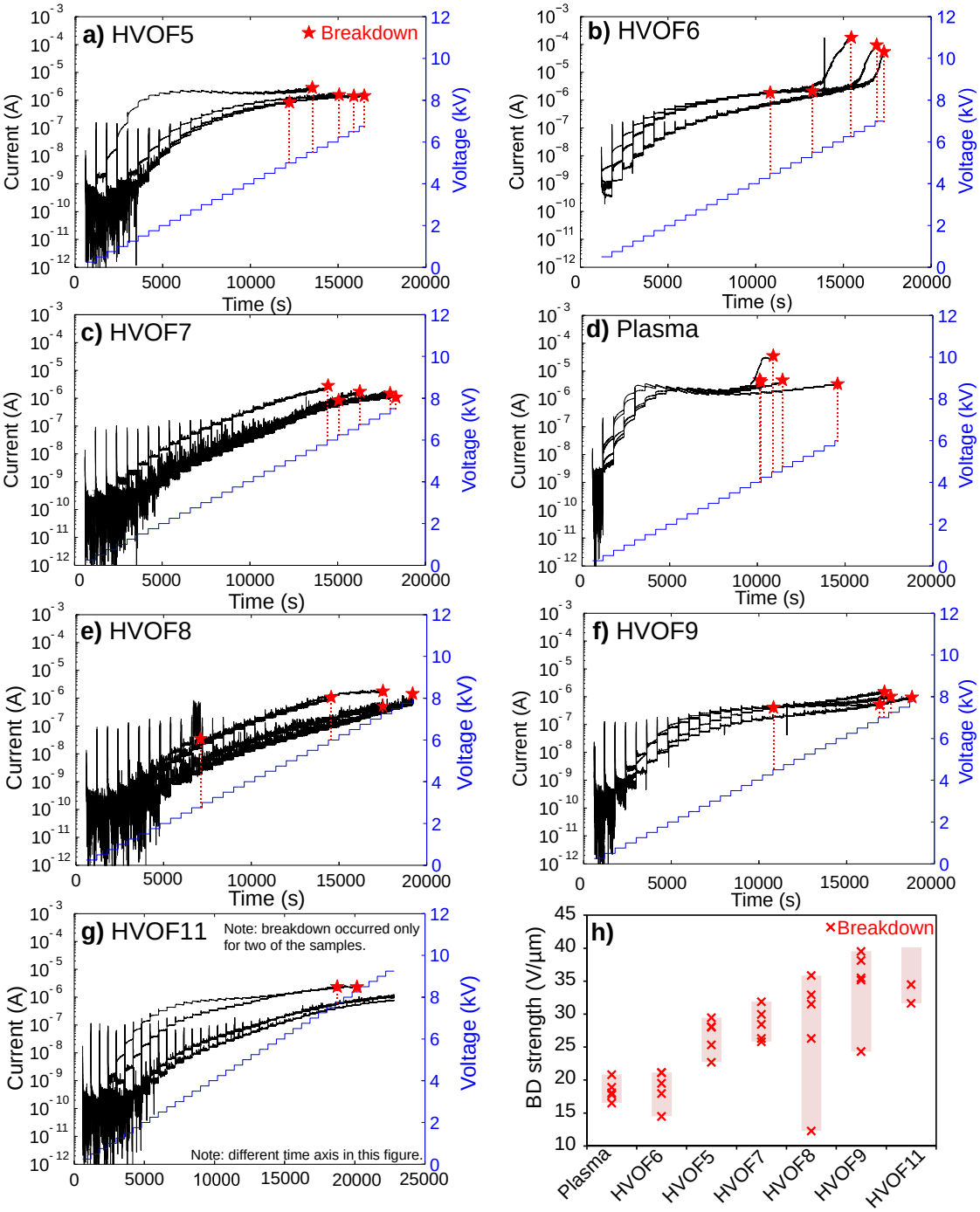

Figure 4. a–g Measured DC currents of the studied materials as a function of time. The start voltage was 250 V which corresponds the electric field of ~1 V/µm. The red stars and the dashed lines indicate the occurrence of breakdown (current and voltage, respectively). It should be underlined that breakdown occurred only for two out of five samples for HVOF11 since the maximum voltage level of the power supply was reached. **h)** The breakdown strengths of the studied coatings in which the cross presents individual breakdown measurement and the bar indicates the deviation between the minimum and maximum strengths. For HVOF11 the upper limit of the bar presents the maximum electric field reached for the samples which did not break down during the tests.

of the mean current densities in different areas as well as the estimated transition electric fields between the different regions.

At low field levels (Area 1), all the studied coatings are obviously ohmic because the defined slopes are close to unity indicating that electric field/voltage is directly proportional to the current. The estimated transition field to non-ohmic region varies between the materials. The lowest field (~0.5 V/µm) is noticed for alumina coatings HVOF6 and Plasma. Slightly higher transition field (~1 V/µm) can be observed for the other commercial HVOF sprayed alumina (HVOF5) but the highest transition field (~2 V/µm) of the alumina coatings is obtained for experimental alumina HVOF7. The transition field of HVOF8 is the same as it is

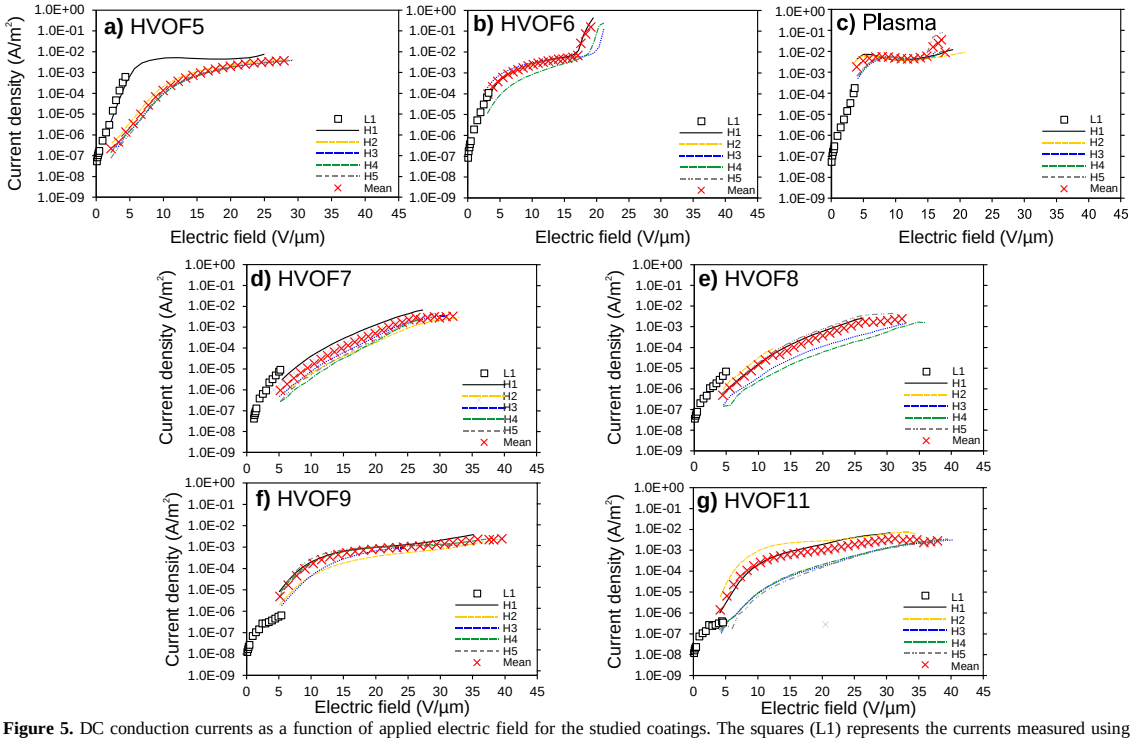

Figure 5. DC conduction currents as a function of applied electric field for the studied coatings. The squares (L1) represents the currents measured using Keithley electrometer and the lines (H1–H5) presents the conduction currents recorded using the above 1 kV measurement setup. The crosses represent the average current densities defined from the five parallel conductivity measurements performed until breakdown, except for HVOF5 the average current density is defined from four parallel measurements.

for HVOF7 probably due to the almost similar powder composition (10% MgO versus 0% MgO). The highest transition field (~4 V/µm) is noted for the coatings with higher amount of MgO: HVOF9 (25% MgO) and HVOF11 (50 % MgO).

In the next region (Area 2), the conductivities of the coatings are highly non-ohmic since the defined slopes vary from 2.8 to 6.2. As it was already mentioned earlier in this 'transition field' region the currents did not fully stabilize during the DC step-stress periods (10 min), instead they were still increasing at the end of the periods. Thus, the real levels of stabilized DC current would have been slightly higher than the reported values, and the above mentioned slopes would have been correspondingly higher as well. All in all, it can be concluded that a considerable transition from ohmic conduction state to another state occurs in this region. Typically, the transition field of HVOF coatings from Area 2 to Area 3 is ~10 V/µm. However, the transition field of HVOF5 is higher (17 V/µm) but in [15] the transition field of HVOF5 has been reported to be 10.5 V/µm although the DC stress period was only 6 min. This indicates that the conductivities of the parallel samples of a coating material deviate notably. The lowest transition field is noted for plasma sprayed alumina coating (5.9 V/µm). The differences in conductivities and breakdown strength between HVOF and plasma coatings may be linked to their different microstructure (Figure 1) caused by the different spraying temperatures and powder particle velocities in the spraying processes.

In Area 3, the defined slopes are roughly two indicating that the current density is proportional to the square of the electric field. However, HVOF7 and HVOF8 exhibit similar but clearly higher slopes (~5) than the other HVOF coatings, and thus these two coatings exhibit similar behavior as the other coatings in the previous area. In addition, the conductivity of plasma alumina differs from the HVOF

Table 2. Estimated transition electric fields and corresponding slopes of the mean current densities (log–log scale) for the studied materials as well as the relative permittivity measured at the voltage of 200 V_{peak}. The detailed measurement procedure of the permittivity measurements is presented in [11–13], [15].

	Area 1		Area 2		Area 3		Area 4		Permittivity
Sample	*E* (V/µm)	Slope	*E* (V/µm)	Slope	*E* (V/µm)	Slope	*E* (V/µm)	Slope	ε_r (at 1 kHz)
HVOF5	0 – 1.0	1.1	1 –16.6	5.7	16.6 – 28	2.2	–	–	9.1
HVOF6	0 – 0.5	1.1	0.5 – 8.6	3.4	8.6 – 17.1	1.8	17.1–	21.7	8.5
HVOF7	0 – 2.0	1.2	2 – 10.5	2.8	10.5 – 24.1	5.3	24.1–	1.3	8.3
Plasma	0 – 0.5	1.0	0.5 – 5.9	4.3	5.9 – 13.9	−0.3	13.9–	12.2	9.8
HVOF8	0 – 2.0	1.1	2 – 7.8	2.8	7.8 – 26.6	4.9	26.6–	2.6	8.5
HVOF9	0 – 3.9	1.2	3.9 – 10.3	4.5	10.3 – 37.6	1.6	–	–	8.5
HVOF11	0 – 4.1	1.1	4.1 – 9.4	6.2	9.4 – 26.1	2.1	26.1–	1.1	8.4

coatings because the plasma reached ohmic level in this area but this may be noticed only by visual evaluation because the obtained slope has negative value due to differences between the parallel samples current density values.

Breakdowns occurred for the alumina coating HVOF5 and spinel HVOF9 in Area 3 but for the rest of the materials the breakdowns occur in Area 4. Although a rapid current increase before breakdown has previously been observed for alumina HVOF5 in [15], no such increase in conduction current is observed for HVOF5 in this study. However, similar rapid current increase is seen for some of the samples of alumina (HVOF6 and Plasma) because the obtained slopes in Area 4 are very high (see Figure 4 and Figure 5).

Throughout the tests, the conduction behavior of the coating HVOF8 (10% MgO) is very similar to the alumina HVOF7 (0% MgO) but in Area 4 the conductivity of HVOF7 is ohmic (slope ~1) while the conductivity of HVOF8 is equal to the square of electric field (slope ~2). Thus, it may be concluded that adding 10% MgO to the Al_2O_3 has only effect when the applied electric field is above 25 V/µm. The conduction behavior of the other two spinel coatings (HVOF9, 25% MgO and HVOF11, 50% MgO) is very similar throughout Areas 1–3. However, the breakdown occurred for HVOF9 in Area 3 while the breakdowns of HVOF11 occurred in Area 4 in which HVOF11 exhibits ohmic conduction behavior (slope ~1). Thus, it seems that the amount of MgO (25 or 50%) has influence on the conduction behavior only when the field is above ~26 V/µm.

3.3 MATERIAL DEGRADATION

Our previous studies [10] have shown that the DC resistivity of a HVOF sprayed experimental spinel coating decreased remarkably when the resistivity as a function of electric field (~0.1–3 V/µm) was repeated. Due to these permanent changes, the conductivity measurements below 1 kV were repeated for some of the samples in this study (two aluminas: HVOF5 and HVOF7, and one spinel: HVOF11) in order to identify possible permanent changes at low electric fields. The selected coatings represent the conduction behavior of the coatings in general manner.

Figure 6 presents the original DC conduction currents of the above coatings as a function of electric field together with the results of repeated measurements made later on.

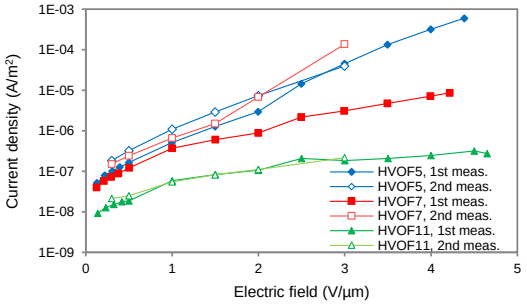

Figure 6. DC conduction currents as a function of electric field for two alumina coatings (HVOF5 and HVOF7) as well as one spinel coating (HVOF11). The data of 1st measurement is same as it has been shown in Figure 4.

The time between the measurements was several months and during that time the samples were kept in a desiccator at room temperature/low relative humidity to avoid ageing. It can be noticed that some permanent changes occurred for the experimental alumina coating (HVOF7) at already low electric fields since the conductivity increases remarkably during the second measurement period. The conductivity of the commercial alumina (HVOF5) also increased slightly during the second measurement time but the difference is not so significant. No permanent changes occurred for the spinel coating (HVOF11).

Because these permanent changes occur already at very low electric fields, it is evident that it is not meaningful to perform conduction mechanism analysis for all the studied materials. In order to carry out the conduction mechanism study for HVOF5 and HVOF11, the conductivity measurements were also repeated at high fields to ensure that no permanent changes/degradation occur in the materials. Three more samples of alumina HVOF5 were prepared and conductivity measurements were made for these samples with steps of 500 V/10 min until the voltage level of 3500 V was reached. The voltage corresponds to the electric field of ~15 V/µm which is approximately half of the breakdown strength of the HVOF5. The measurements showed that no permanent changes occur for the samples of HVOF5 when the measurements were repeated on the next day.

The procedure of conductivity measurements for HVOF11 was similar but the measurements were performed until the voltage level of 5500 V was reached. This level corresponds to the field of ~22 V/µm which is roughly half of the breakdown strength of HVOF11. The measurements were performed for the samples that did not break down in the step tests with 250 V/10 min steps. These measurements indicate that the current densities are at similar levels when the measurements were repeated two or three times (500 V/10 min).

During the first applications of higher electric fields, permanent changes in the conductivity may occur for some of the coatings. The permanent changes might be due to the changes occurred in the interfaces of amorphous-crystalline regions of the coatings.

3.4 CONDUCTION MECHANISMS ANALYSIS

In order to evaluate the dominant conduction mechanism of thermally sprayed ceramic coatings, the measured conductivity data are analyzed in accordance with several theoretical conduction mechanisms despite the fact that the steady-state current level was not reached at each voltage level, especially in the 'transition-field' region. Because the possible dominating conduction mechanism of thermally sprayed ceramics is not so evident, all theoretical conduction mechanisms are discussed even though some of the mechanisms occur only at very high electric fields for other materials such as polymers [16], and are thus not relevant for thermally sprayed ceramic coatings. The conduction mechanism study is only carried out for alumina HVOF5 and spinel HVOF11 for which no material degradation was noticed and the measured conduction behavior can thus be considered to be stable.

Charge injection from electrodes can be described either by Schottky or Fowler-Nordheim injection mechanisms which both occur at very high fields for polymers, e.g. the latter takes places ~10^9 V/m and the former one occurs slightly lower fields [16, 17]. Although thermally sprayed ceramic coatings exhibit significantly lower breakdown strengths than polymers, the Fowler-Nordheim plots (log (J/E^2) versus $1/E$) were made for HVOF5 and HVOF11 [21, 22]. The obtained plots indicate that Fowler-Nordheim tunneling can be excluded as the dominating conduction mechanism for the studied thermally sprayed ceramic coatings because the slopes differed clearly from those reported in [21, 22] where the Fowler-Nordheim tunneling occurred for the studied materials.

In the Schottky analysis, the measured data is plotted as ln (J) versus $E^{1/2}$ (Schottky plot) which results a straight line where theoretical value of relative permittivity can be evaluated. Thus, the comparison between the theoretical and measured high frequency permittivities can be made. For both coatings (HVOF5, HVOF11) the relative permittivities defined from the Schottky plot are ~70% smaller than the measured ones (Table 2), and thus the pure Schottky injection can also be excluded as the dominating conduction mechanism of the thermally sprayed coatings.

At high electric fields, one of the bulk-limited conduction mechanisms is Poole-Frenkel where the theoretical relative permittivity can be defined from the slope of the Schottky plot (ln (J) versus $E^{1/2}$). The physical base of Poole-Frenkel model is very simplified and the analysis must be made as an-order-of-magnitude calculation [16]. Although this consideration is made, the defined theoretical values are ~95% smaller than the measured ones. Thus, it can be concluded that the Poole-Frenkel conduction mechanism is not the dominating one for the ceramic coatings.

Space charge limited current (SCLC) mechanism is one of the bulk limited conduction mechanisms and it describes how the conduction current behavior changes with increasing applied electric field [16, 17]. In order to validate this mechanism, experimental J–E data can be plotted in double logarithmic scale (see Figure 7) [16, 17]. According to this mechanism, at low field strengths (field below the transition field, E_{TR}) the voltage-current relation is ohmic due to the thermally generated carriers [16, 17]. The current density is thus directly proportional to the voltage. Correspondingly, the slope is unity in a plot of log J – log E [16, 17].

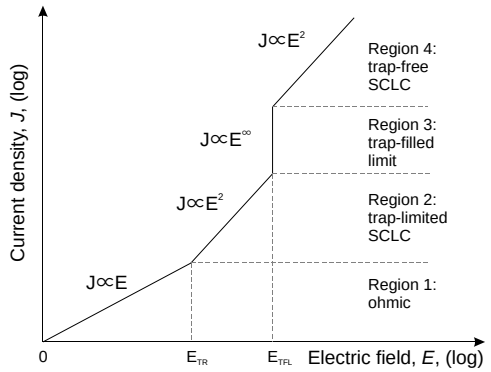

Figure 7. Relationship between electric field and current in accordance with the space charge limited current –theory. The figure is revised from [16].

At higher fields (Region 2), the conduction is no longer ohmic because charge can inject from electrode into the bulk and it has difficulties to move further through the material [16, 17]. Thus, a space charge is formed in vicinity of the electrodes and throughout the bulk and this charge will limit the further movement of charges which is known as SCLC [16, 17]. When the applied field has reached the level of E_{TR} (see Figure 7), the space charge limited current dominates over the ohmic component [16, 17]. The current is thus proportional to the square of electric field and the slope is two in a plot of log J – log E (Figure 7). When the applied field has reached the trap-filled limit field, E_{TFL}, all the traps in the dielectric are filled and the slope increases from two (see Region 3 in Figure 7) to infinity. At the fields above E_{TFL}, the trap-free space charge conduction might take place and the slope is two (Region 4 in Figure 7) if the breakdown did not occur before this region was reached [16].

It has been reported in [18, 19] that a bulk alumina ceramic follows the SCLC mechanism. However, the conductivities of alumina HVOF5 and spinel HVOF11 coatings do not fully follow the SCLC theory since after the initial ohmic region (Area 1 in Table 2) the conductivity is not proportional to the square of the electric field as indicated by the calculated slope of ~6 (Table 2). After this region, the slope should be higher than two in accordance with the SCLC theory (Region 3 in Figure 7) but the slopes of the coatings are ~2. According to the SCLC theory, the slope should be two again in the last area (Region 4 in Figure 7) but the slope of HVOF11 is ~1 in Area 4 indicating ohmic behavior. It can be concluded that the studied thermally sprayed ceramic coatings either do not follow or follow only partly the SCLC theory unlike the sintered alumina [17, 18]. The difference in the conduction behaviors of the bulk and the thermally sprayed alumina is most probably due to their different microstructures. Bulk alumina exhibits fully crystalline structure while the thermally sprayed coatings have lamellar structure consisting of both amorphous and crystalline areas as well as voids and defects (Figure 1). Due to above facts, the coatings most probably exhibit a variety of trap levels which partly explains the deviation of the performance from the ideal SCLC theory.

A thermally sprayed coating should be considered as an insulation system consisting of different regions which exhibit different dielectric properties. Thus, it can be speculated that the amorphous regions probably have higher conductivity than the crystalline regions. The differences in conductivity and the resulting uneven field distribution might be the reason why the coatings followed only partly the SCLC theory. Although there are many uncertainties, it can be speculated that thermally sprayed coatings could follow the SCLC theory as follows:

- At low electric fields (Area 1), the conductivity is clearly ohmic. Since the amorphous regions most probably exhibit higher conductivity than the crystalline regions, the electric field concentrates on the crystalline regions. Thus, the conduction behavior

of a coating is dominated by the conductivity of the crystalline regions.

- At higher electric fields, charges start to collect into the interfacial areas and traps forming space charge. When a certain transition electric field, E_{TR}, is reached, the space charge limited current dominates over the ohmic component in the crystalline-amorphous interfaces of a coating. Theoretically, the current density is proportional to the square of electric field when there is only one trap depth in the material. In the coatings, the microstructure varies along the material and due to this the E_{TR} and the current density changes are not as ideal, instead the changes take place 'smoothly'.
- When the conductivity increases in the crystalline regions, this also changes/equalizes the electric field distribution between the crystalline and amorphous regions at the same time. Due to this, at first the current is limited and is increasing with a slope lower than two but after a while the electric field is more concentrated on the amorphous regions, and thus the current is increasing strongly with a slope higher than two. This can occur since the transition field (E_{TR}) of amorphous regions is expected to be lower than the transition field of the crystalline regions due to their different conductivities.
- After this transition field range where a new electric field distribution is formed for a coating by the SCLC currents of amorphous and crystalline regions, the current of a coating system is increasing with a slope of ~2.

At higher test voltages prior to breakdowns, partial breakdowns of certain regions are suggested to occur. Just before breakdowns, rapid current increase was measured for certain coatings (HVOF6, Plasma). This is most probably caused by partial breakdowns e.g. in the amorphous regions and/or at the interfaces between the splats which may take place because the trap filled limit (E_{TFL}) of that region is reached. According to the SCLC theory, a sudden fast current increase occurs, when the E_{TFL} is reached. However, this current increase should lead to breakdown very rapidly [16]. As the current increase of the coatings did not occur as rapidly, it is suggested that the breakdown for some of the coatings proceeded partially, and this way the breakdown process was delayed.

3.5 DC BREAKDOWN STRENGTH

Figure 8 presents the DC breakdown strengths of the coatings when the voltage was increased with 100 V/s linear ramp rate. Two-parameter Weibull distributions were fitted to the breakdown data. The Weibull parameters α and β are listed in Table 3 along with the breakdown strengths at the breakdown probabilities of 10% and 90%.

The lowest breakdown strength (Weibull α) is obtained for the plasma sprayed alumina. In addition, the deviation between the parallel samples is large (the difference between the breakdown probability of 10% and 90%). The Weibull β of Plasma also is clearly lower than the Weibull β of HVOF coatings which show very similar values (see the inset in Figure 8b). The lowest breakdown strength (Weibull

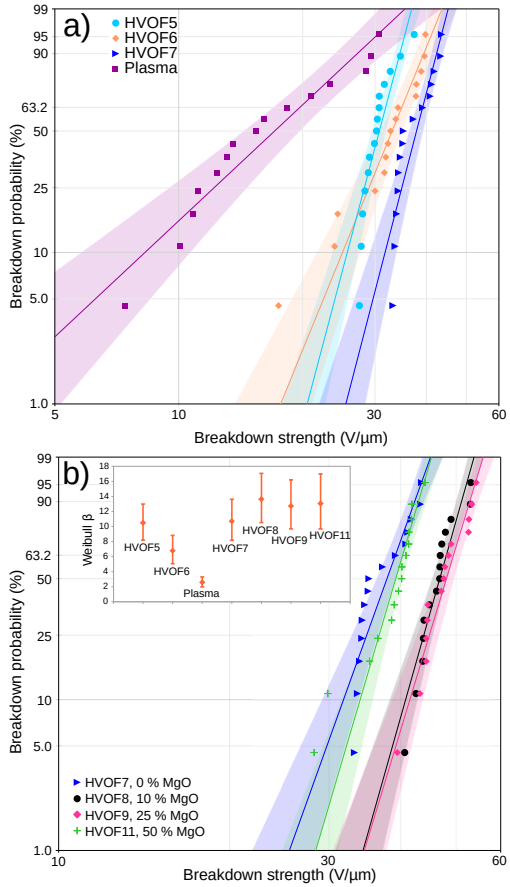

Figure 8. DC breakdown strength of the coatings when the voltage was increased linearly at the ramp rate of 100 V/s to breakdown. The shaded areas represent 90% confidence bounds. The inset shows the Weibull β and its 90% confidence limits.

Table 3. Weibull parameters α and β as well as the breakdown strenghts at the breakdown probabilities of 10% and 90%.

	Plasma	HVOF5	HVOF6	HVOF7	HVOF11	HVOF8	HVOF9
10%	8.3	25.7	25.0	31.7	33.9	40.8	41.5
α	19.7	31.8	34.8	39.2	40.3	48.1	49.6
90%	27.2	34.5	39.4	42.3	43.0	51.2	52.9
β	2.6	10.5	6.8	10.7	13.1	13.6	12.7

α) for the HVOF coatings is obtained for HVOF5 and only slightly higher value for HVOF6 which both were manufactured from different commercial alumina powders. The experimental alumina coating (HVOF7) exhibits the highest breakdown strength of the alumina coatings and the breakdown strength is at a similar level with HVOF11 (50% MgO). Typically, the breakdown strength of HVOF alumina coatings are significantly lower than the breakdown strength of HVOF spinels [8, 13]. The highest breakdown strengths are obtained for HVOF8 (10% MgO) and HVOF9 (25% MgO) which practically exhibit equal breakdown strengths (Weibull α).

Due to the rather high deviation of parallel breakdown results, it is difficult to distinguish the exact effect of MgO content on the breakdown strengths. However, it seems that adding MgO in Al_2O_3 improves the breakdown strength, and

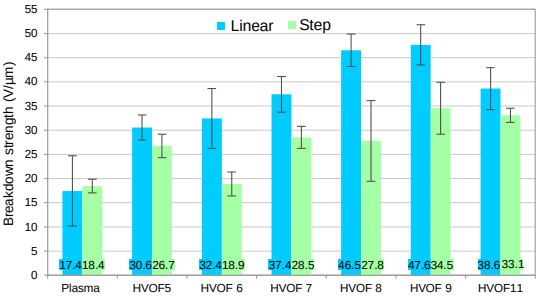

Figure 9. DC breakdown strength of the coatings from linear ramp rate and from step measurements. The results from step tests are the same as what has been presented in Figure 4h). The error bar represents the experimental standard deviations of parallel measurements (15 test in linear ramp tests and two or five tests in step tests).

the amount of 25% gives the highest breakdown strength in step and linear tests (see Table 3, Figure 8 and Figure 9).

Other microstructural features, e.g. gas permeability which is related to the volumetric porosity of a coating, seem to affect the breakdown strength of the HVOF coatings deposited from experimental powders (HVOF7–HVOF11) more obviously than the amount of MgO [5]. The higher gas permeability results in lower breakdown strength since the highest breakdown strength was obtained for HVOF9 (GP 3.9 nm^2) and the lowest for HVOF7 (GP 7.7 nm^2) [5]. Because HVOF11 (50% MgO) has quite similar breakdown strength and gas permeability with HVOF7 (0% MgO), it can be speculated that the gas permeability has a more profound effect on the breakdown strength than the MgO content [5]. However, the effect of gas permeability on the breakdown strength is not as evident when the comparison is made for all studied HVOF coatings since the gas permeability of the alumina coating HVOF6 (3.2 nm^2) is the lowest one of the HVOF coatings but the breakdown strength is not the highest one even though the comparison is only made between the alumina coatings. Anyhow, the HVOF5 coating (the other commercial alumina powder) exhibits higher gas permeability (11.1 nm^2) and slightly lower breakdown strength than the other commercial HVOF alumina coating (HVOF6). Although the difference between the breakdown strengths is not significant, it might be speculated that the difference is partly due to their different volumetric porosities.

Figure 9 presents the average breakdown strengths of the coatings when the voltage was increased either linearly or step-wisely. For plasma sprayed alumina the breakdown strength in step-test is practically same as the breakdown strength in ramp-test because the deviation between the parallel samples in linear tests is significant (see Figure 8a). For HVOF coatings, the step-test breakdown strengths are lower than the ramp-test breakdown strengths. The difference is from 3.9 V/µm (HVOF5) to 18.7 V/µm (HVOF8). It is understandable that the step-test breakdown strength is lower than the ramped one due to the clearly longer stress durations. The differences thus give an indication of the effects of electric stress duration and possible time dependent degradation of the coatings. An interesting continuation of this work would be long-term ageing testing for evaluating suitable service field strengths of the coatings.

4 CONCLUSIONS

In this study, the DC conductivities of several different thermally sprayed ceramic coatings were studied in order to determine the conduction behavior of the coatings in general manner. Although great differences in the conductivities of the different coatings were observed, it was seen that in all coating types the conduction currents reached similar level prior to the breakdown.

Thermally sprayed ceramic coatings exhibit a special lamellar microstructure consisting of crystalline and amorphous regions as well as voids and defects, while bulk ceramics exhibit fully crystalline structure. Due to this difference, their DC conductivities differ; thermally sprayed ceramic coatings exhibit strong non-linear conduction behavior already at low field strengths unlike bulk ceramics. In addition, as opposed to bulk alumina, the ceramic coatings do not follow or follow only partly the space charge limited current conduction mechanism while the bulk alumina has been reported to follow this mechanism. A possible conduction mechanism for the ceramic coatings was proposed based on the differences in the conductivities of the amorphous and crystalline regions of the coating which further causes an uneven electric field distribution in a coating.

Due to the large variations in the DC breakdown strength, it was difficult distinguish the exact effects of MgO content or porosity. However, it seems that the volumetric porosity has a more profound effect on the breakdown strength for the experimental coatings, higher porosity indicating lower breakdown strength. The step-test breakdown strengths of the coatings were lower than the ramp-test ones due to the clearly longer stress durations in step-tests which gives an indication of the effects of electric stress durations and possible short-term degradation of the coatings. An interesting continuation of this work would be long-term ageing testing for evaluating of suitable service field strengths of the coatings.

ACKNOWLEDGMENT

Nida Riaz and Juuso Kukkaro are greatly acknowledged for performing most of the DC conductivity measurements.

REFERENCES

[1] N. H. Menzler, F. Tietz, S. Uhlenbruck, H. P. Buchkremer, and D. Stöver, “Materials and manufacturing technologies for solid oxide fuel cells,” J. Mater. Sci., Vol. 45, No. 12, pp. 3109–3135, Feb. 2010.

[2] J. R. Davis, *Handbook of Thermal Spray Technology*, Vol. 3, USA, ASM International, 2004.

[3] L. Pawlowski, *The Science and Engineering of Thermal Spray Coatings*. Chichester, West Sussex, England: John Wiley & Sons Ltd, 2008.

[4] E. E. J. Young, E. Mateeva, J. J. Moore, B. Mishra, and M. Loch, “Low pressure plasma spray coatings,” Int. Conf. Metall. Coatings Thin Film., Vol. 377–378, pp. 788–792, 2000.

[5] M. Niittymäki, I. Rytöluoto, J. Metsäjoki, T. Suhonen, and K. Lahti, “Role of Microstructure in Dielectric Properties of Thermally Sprayed Ceramic Coatings,” IEEE 1st Int’l. Conf. Dielectr., 2016.

[6] V. V. Sobolec, J. M. Guilemany, and J. Nutting, *High Velocity Oxy-fuel Spraying Theory, Structure-Property Relationships and Applications*. The Institute of Materials, Minerals and Mining, Maney Publishing House, 2004.

[7] L. Pawłowski, “The relationship between structure and dielectric properties in plasma-sprayed alumina coatings,” Surf. Coatings

Technol., Vol. 35, No. 3–4, pp. 285–298, 1988.
[8] F. L. Toma, S. Scheitz, L. M. Berger, V. Sauchuk, M. Kusnezoff, and S. Thiele, "Comparative study of the electrical properties and characteristics of thermally sprayed alumina and spinel coatings," J. Therm. Spray Technol., Vol. 20, No. 1–2, pp. 195–204, 2011.
[9] F. L. Toma, L. M. Berger, S. Scheitz, S. Langner, C. Rödel, A. Potthoff, V. Sauchuk, and M. Kusnezoff, "Comparison of the Microstructural Characteristics and Electrical Properties of Thermally Sprayed Al_2O_3 Coatings from Aqueous Suspensions and Feedstock Powders," J. Therm. Spray Technol., Vol. 21, No. 3–4, pp. 480–488, 2012.
[10] M. Niittymäki, K. Lahti, T. Suhonen, U. Kanerva, and J. Metsäjoki, "Dielectric properties of HVOF sprayed ceramic coatings," IEEE Int'l. Conf. Solid Dielectr., pp. 389–392, 2013.
[11] M. Niittymäki, T. Suhonen, J. Metsäjoki, and K. Lahti, "Influence of Humidity and Temperature on the Dielectric Properties of Thermally Sprayed Ceramic $MgAl_2O_4$ Coatings," IEEE Conf. Electr. Insul. Dielectr. Phenomena, pp. 94–97, 2014.
[12] M. Niittymäki, K. Lahti, T. Suhonen, and J. Metsäjoki, "Dielectric Breakdown Strength of Thermally Sprayed Ceramic Coatings: Effects of Different Test Arrangements," J. Therm. Spray Technol., Vol. 24, No. 3, pp. 542–551, 2015.
[13] M. Niittymäki, T. Suhonen, J. Metsäjoki, and K. Lahti, "Electric Field Dependency of Dielectric Behavior of Thermally Sprayed Ceramic Coatings," IEEE 11th Int'l. Conf.e Properties and Applications of Dielectr. Materials (ICPADM), pp. 500–503, 2015.
[14] J. Kotlan, R. C. Seshadri, S. Sampath, P. Ctibor, Z. Pala, and R. Musalek, "On the dielectric strengths of atmospheric plasma sprayed Al_2O_3, Y_2O_3, ZrO_2–7% Y_2O_3 and (Ba,Sr)TiO_3 coatings," Ceram. Int., Vol. 41, No. 9, pp. 11169–11176, 2015.
[15] M. Niittymäki, T. Suhonen, J. Metsäjoki, and K. Lahti, "DC Dielectric Breakdown Behavior of Thermally Sprayed Ceramic Coatings," 24th Nordic Insul. Sympos. Materials, Components and Diagnostics, pp. 80–85, 2015.
[16] L. A. Dissado and J. C. Fothergill, *Electrical Degradation and Breakdown in Polymers*, First edit., The Institution of Electrical Engineering and Technology, London, UK, 1992.
[17] R. Bartinikas and R. M. Eichhorn, Eds., *Engineering Dielectrics* Vol. IIA, *Electrical Properties of Solid Insulating Materials: Molecular Structure and Electrical Behavior*. Philadelphia, USA: American Society for Testing and Materials, 1983.
[18] C. Neusel, H. Jelitto, and G. A. Schneider, "Electrical conduction mechanism in bulk ceramic insulators at high voltages until dielectric breakdown," J. Appl. Phys., Vol. 117, No. 15, p. 154902, 2015.
[19] F. Talbi, F. Lalam, and D. Malec, "DC conduction of Al_2O_3 under high electric field," J. Phys. D. Appl. Phys., Vol. 40, No. 12, pp. 3803–3806, 2007.
[20] "IEC standard 60093 Methods of test for volume resistivity and surface resistivity of solid electrical insulating materials," no. IEC Standard 60093. IEC, 1980.
[21] M. Lenzlinger, "Fowler-Nordheim Tunneling into Thermally Grown SiO_2," J. Appl. Phys., Vol. 40, No. 1, p. 278, 1969.
[22] J. J. O'Dwyer, *The Theory of Electrical Conduction and Breakdown in Solid Dielectrics*. Oxford: Clarendon Press, 1973.

Minna Niittymäki (S'13) was born in Sahalahti, Finland, on 29 March 1984. She received the M.Sc. degree in electrical engineering from Tampere University of Technology in 2012. Since then she has been working as Researcher in the high voltage research group of the Department of Electrical Engineering at TUT, with the aim towards Ph.D. degree. Her current research interests are in the area of insulation materials focusing on the dielectric characterization of thermally sprayed insulating ceramic coatings.

Kari Lahti (M'01) was born in Hämeenlinna, Finland in 1968. He received the M.Sc. and Doctoral degrees in electrical engineering from Tampere University of Technology in 1994 and 2003, respectively. Since then he has worked at the Department of Electrical Engineering at TUT, currently as a Research Manager and Adjunct Professor. He is the head of TUT's research group on high voltage insulation systems. He has also been responsible for the high voltage laboratory services at TUT since 2002. His research interests are in the area of high voltage engineering including surge arresters, nanocomposite insulation systems, environmental testing of high voltage materials and apparatus, high voltage testing methods and dielectric characterization of insulating materials.

Tomi Suhonen was born in Helsinki, Finland, on 24 December 1978. He is a Senior Scientist and Manager of multiscale materials modelling activities at VTT Technical Research Centre of Finland. He has 13 years' experience in scientific research related to advanced materials and has published more than 70 scientific papers and holds several international patents.

Jarkko Metsäjoki was born in Rauma, Finland, on 18 March 1982. He received M.Sc. degree in materials science from Tampere University of Technology (TUT) in 2008. He has worked at TUT, Braunschweig University of Technology, and since 2012 he has been working at VTT Technical Research Centre of Finland Ltd as Research Scientist. He is currently also a PhD student at Aalto University. His research interests include material characterization of thermally sprayed ceramic coatings.

Publication VIII

Effect of temperature and humidity on dielectric properties of thermally sprayed alumina coatings

M. Niittymäki, T. Suhonen, J. Metsäjoki and K. Lahti

IEEE Transactions on Dielectrics and Electrical Insulation, vol. 25, no. 3, pp.908–918, 2018

DOI: 10.1109/TDEI.2018.006892

Effect of Temperature and Humidity on Dielectric Properties of Thermally Sprayed Alumina Coatings

Minna Niittymäki and **Kari Lahti**
Tampere University of Technology
Electrical Energy Engineering
P.O. Box 692
FI-33101 Tampere, Finland

Tomi Suhonen and **Jarkko Metsäjoki**
VTT Technical Research Centre of Finland
P.O. Box 1000
FI-02044 Espoo, Finland

ABSTRACT

Breakdown strength, DC resistivity, permittivity and loss of thermally sprayed alumina coatings were studied at various temperatures and relative humidities. The studied coatings were sprayed by utilizing three different spray techniques: flame, high-velocity oxygen fuel (HVOF) and plasma spraying. Breakdown behavior of HVOF sprayed alumina were studied up to very high temperatures (800 °C). At 20–180°C, no significant trend could be seen in the breakdown strength of HVOF and plasma sprayed alumina coatings. The breakdown strength of alumina coatings decreased gradually from 300 to 800 °C reaching a value which was only 14% of the breakdown strength measured at 20 °C/RH 20%. Increasing humidity (from 20 to 90%) decreased the DC resistivity of the alumina coatings five orders of magnitude. Correspondingly, permittivity and losses increased with the humidity; in most cases with a notable contribution due to DC conduction. The material behavior may be linked to the microstructure of coatings consisting of amorphous and crystalline regions with interfaces in between. Moreover, the alumina coatings exhibited notable amount of highly hygroscopic γ-phase which also affected the moisture sensitivity of the coatings.

Index Terms — **Alumina, aluminum oxide, thermally sprayed ceramic coating, flame spray, HVOF, plasma spray, dielectric breakdown, resistivity, conductivity, permittivity, dielectric losses**

1 INTRODUCTION

ALUMINA (Al_2O_3) is a widely used electrical insulation material in high temperature applications since it exhibits high hardness and refractory nature [1]. Thermal spraying is an effective and rather low cost method to produce a protective/insulating layer for demanding conditions such as thermal barrier coating in gas turbine components, protective insulation layer in aero-engine parts or in fuel cells [2, 3]. In the thermal spraying process, the raw alumina is typically in powder form but it can also be used in rod form [2–4]. During spraying, thermal energy is generated either by chemical (combustion) or electrical (plasma or arc) methods in order to melt and accelerate the ceramic powder particles towards the substrate [2, 3]. The molten particles form droplets which hit on the substrate (e.g. steel plate) or on the coating surface forming a coating consisting of thin layers of lamellae (called splats) [2, 3]. In particular, the lower surfaces of the splats cool down faster than the internal parts.

Manuscript received on 3 July 2017, in final form 1 February 2018, accepted 28 February 2018. Corresponding author: M. Niittymäki.

Due to this, the surfaces are normally more amorphous, while the internal parts are typically crystalline [3, 5]. In addition to the splats, the coating exhibits some unmelted powder particles, voids and often also some cracks which can be formed during cooling [1–3]. If long perpendicular cracks are formed, the breakdown strength of a thermally sprayed ceramic coating can decrease significantly as noticed in our previous study on $MgAl_2O_4$ coating [6].

Previous studies of the dielectric properties of thermally sprayed alumina coatings are mostly focused on the breakdown strength at room temperature. However, the effect of high temperature on the breakdown strength of alumina coatings is not studied although one relevant application for alumina coatings is solid oxide fuel cells which have very high operating temperatures (500–800 °C) [7]. Thus, one aim of this paper is to study the breakdown strength of alumina coatings at 120–800 °C. In addition, the breakdown strength is studied at the temperatures of 20–60 °C at various humidities in order to distinguish the possible effect on humidity.

The alumina coatings have a special lamellar microstructure, which differs significantly from sintered bulk alumina, and due to this direct comparison between the dielectric properties of these two is not worthwhile. Furthermore, the sintered alumina and alumina powder utilized in thermal spraying consist of thermodynamically stable α-Al_2O_3 as the main crystalline phase but due to the rapid solidification during the spraying [8] the alumina coatings exhibit metastable γ-phases as a main phase [9-13]. This γ-Al_2O_3 is highly hygroscopic [3, 14] which can be one reason for the significant increase of dielectric constants and losses of the coatings at high humidity [11, 15, 16]. However, the high amount of γ-phase in alumina coating cannot only explain the moisture sensitivity since the DC resistivity of $MgAl_2O_4$ coatings, which have stable crystalline phases, decreased several orders of magnitude with increasing humidity in [6, 12]. Thus, it should be emphasized that the special microstructure together with the hygroscopic nature can explain the moisture sensitive nature of the alumina coatings. However, the effect of humidity and temperature on the DC resistivity, permittivity and loss of thermally sprayed alumina coatings is not comprehensively studied. Due to this, together with the breakdown study the other aim of this paper is study the effect of temperature (20–60 °C) and humidity (20–90%) on the DC resistivity, permittivity and losses of thermally sprayed alumina coatings.

1.1 BACKGROUND

In this paper, the studied alumina coatings are deposited by utilizing three different spraying processes which are flame spraying, high-velocity oxygen fuel (HVOF) spraying, and atmospheric air plasma spraying (APS). The main differences between these techniques are flame temperature and powder particle velocity. In flame and HVOF spraying, the flame temperature is ~3000 °C [1, 3] while in the plasma spraying the temperature is >15000 °C [1, 2]. The powder particle velocities in flame, HVOF and plasma spraying are 30–120 m/s [1, 3], ~700–800 m/s [1, 17] and 100–300 m/s [1, 13], respectively. In particular, the high powder particle velocity improves the coating properties which can be seen in HVOF sprayed coatings as well-adhered and dense structures [1, 3]. However, numerous and complex processing parameters affect the coating properties and microstructure [4]. According to Kotlan *et al.* [13], increasing the spray distance in plasma spraying decreased the dielectric breakdown strength of alumina coating. However, increasing the spray distance had decreasing effect on the particle velocity and temperature [13], and thus it is difficult to distinguish exactly the effect of processing parameters on the dielectric properties.

The studies on the dielectric properties of thermally sprayed Al_2O_3 coatings are mainly focused on the dielectric breakdown strength. The DC breakdown strength of plasma sprayed alumina coatings has been reported to be 10–20 V/µm [11], 17–36 V/µm [18] and 22–23 V/µm [12] at room temperature conditions. Slightly higher DC breakdown strength is typically obtained for HVOF sprayed alumina: 22–34 V/µm [12], 20–32 V/µm [14] and 32 V/µm [19]. The AC breakdown strength of HVOF alumina coating was 29 V_{peak}/µm in our previous study [19]. The AC breakdown strength of plasma sprayed alumina coatings have been reported to be 13.5–16.6 V/µm [13], 6–17 V/µm [18] and 20–115 V/µm [5]. However, in [5] the breakdown measurements were performed in insulating oil. In our previous studies [19], the breakdown strength of HVOF sprayed alumina coating increased significantly in oil immersion in comparison to the breakdown strength obtained without oil since the thermally sprayed ceramic coatings are typically quite porous and sensitive to the moisture and liquids.

In comparison to the alumina coatings, sintered alumina exhibits typically dense and fully crystalline structure. Thus, utilization of insulation oil in breakdown voltage measurements has not been observed to affect the breakdown strength of sintered alumina [20–27]. However, the DC breakdown strength of sintered alumina can be at similar or higher level with the alumina coatings, being 90–150 V/µm [20], 30–130 V/µm [28], and 26–96 V/µm [25]. AC breakdown strength of sintered alumina is at a very similar level with the ceramic coatings since it was 31.6 V/µm [21], 15–34 V/µm [27], 22 V/µm [22], 13–15 V/µm [23], 19–25 V/µm [24], and 10–42 V/µm [26]. It should be noted that the thicknesses of the sintered alumina are typically higher than those of the coatings.

Typically, sintered alumina has higher DC resistivity (>10^{12} Ωm) [27] but the DC resistivity of thermally sprayed alumina coating can vary from 10^6 to 10^{11} Ωm [11, 12, 29]. Our previous studies [30–34] have shown that DC resistivity of thermally sprayed Al_2O_3 and $MgAl_2O_4$ coatings can be at the level of ~10^{12} Ωm at the electric fields below 1 V/µm but at higher electric fields the resistivity decreases several decades indicating a strong non-ohmic conductivity. In addition, the DC resistivity of the Al_2O_3 and $MgAl_2O_4$ coatings have been found to decrease several decades when the relative humidity increased [6, 12] which can be linked to moisture sensitive nature of the coatings.

Interestingly, notable differences in dielectric constant has not been reported. The dielectric constant of sintered alumina was 9 at 1 MHz [22, 27] and 7 at 1 kHz [25], while for plasma sprayed alumina it was 6–8 [11] and 11–23 [15] at 1 kHz, and for HVOF alumina 6–8 [35] at 10 kHz. However, the measuring frequencies are quite high and the microstructural differences between bulk and coating cannot be seen as clearly as they may be noticed in the DC conductivity and in the slow charging phenomena at lower frequencies. However, the dielectric constant of plasma sprayed alumina increased with humidity which was explained by the hygroscopic nature of the alumina coatings due to the high amount of metastable γ-phase instead the stable α-phase [15, 16].

1.2 THEORETICAL CONSIDERATIONS

Compared to typical insulating materials, the dielectric behavior of thermally sprayed ceramic coatings is remarkably different. Due to the manufacturing process, the coatings exhibit layered structure which consists of splats with clear interfaces in between (see Figure 1). As it was shown in [5], [33], amorphous and crystalline regions exist in the splats. These regions most probably have different conductivities as it was discussed in our previous studies in [33] where it was shown that the conduction mechanism of the coatings differ from the SCLC mechanism known for Al_2O_3 [22, 36]. A suggested conduction mechanism for the coatings in [33]

satisfies the measured non-linear conduction behavior and is based on the microstructural and phase differences of the coatings. Different conductivities in the different regions will lead the non-uniform field distribution and further, when the highly stressed regions turn into dominating SCLC conduction, the other regions still have ohmic conduction, resulting in the measured behavior.

Based on above, it may be hypothesized that the microstructure full of interfaces and splat volumes with presumably varying conductivities tend to enhance the interfacial type of polarization mechanisms at low frequencies, at least in cases with highest resistivity. On the other hand, at the same time the conductivity of the coatings may be remarkably high, which tend to limit and prevent the charging phenomena. When the DC conductivity is high, the conductivity σ will notably contribute to the imaginary part of the complex permittivity (ε_r*) [37]. It can be defined as:

$$\varepsilon_r^* = \varepsilon_r' - j\left(\varepsilon_r'' + \frac{\sigma}{\omega\varepsilon_0}\right) \quad (1)$$

where ε_r' is the is real part of the permittivity, ε_r'' is the loss term due to polarization, σ is DC conductivity, ω is the angular frequency, and ε_0 is vacuum permittivity [37]. Any dielectric measurement result always includes both loss components, caused by both polarization and conduction.

2 EXPERIMENTAL

2.1 MATERIAL CHARACTERIZATION

Three different Al_2O_3 materials were sprayed by HVOF, plasma or flame spray methods. In HVOF process, the coatings were deposited from fused high purity Al_2O_3 powder (99.9 wt %, Praxair). In plasma spraying process, another fused high purity Al_2O_3 powder (99.25 wt%, Saint-Gobain) was utilized. In the flame spray process, the Al_2O_3 was in a cord form (99.7 wt%, Saint-Gobain). All the coatings were sprayed on stainless steel substrates (100 × 100 × 2.5 mm). Before the spraying, the substrates were grit-blasted to ensure better adhesion between the substrate and the ceramic coating.

Breakdown voltage measurements for HVOF coatings were also made at high temperatures (200–800 °C). Since alumina and steel have different thermal expansion coefficients, which can cause problems at high temperatures, 80 µm thick bond coatings (NiCrAlY, H.C. Starck) were HVOF sprayed on the substrates before HVOF spraying the alumina powder (99.9 wt%, Praxair). The bond coat was found to have no significant effect on the breakdown strength of alumina coatings.

Figure 1 presents the cross-section images of the studied coatings. As it can be seen from the figure, all the coatings exhibit porous nature and lamellar structure. The porosities of the coatings were determined by analyzing cross-sectional micrographs taken by several different microscopy techniques, see Table 1. The porosities of Plasma coating defined from SEM images are at a higher level than those of HVOF coating which is attributable to the higher particle velocity in the HVOF process [2, 3]. The spraying process of Flexicord samples differs from the HVOF and plasma processes which can explain the higher porosities of Flexicord.

Sample thicknesses were measured with magnetic measuring device (Elcometer 456B) from the electrode areas (Ø=11 mm or Ø=50 mm depending on the test). The average thicknesses and standard deviations are listed in Table 1 (10 parallel measurements from the 50 mm electrode area). In addition, the coating thicknesses were also determined from cross-section images taken by optical microscope (Table 1). The standard deviations of the thicknesses are quite high which is partly due to the grit blasting of the coating substrate and consequently uneven lower surfaces of the coatings. In addition, the spraying process itself does not produce fully smooth coatings, which also partly explain the thickness deviation.

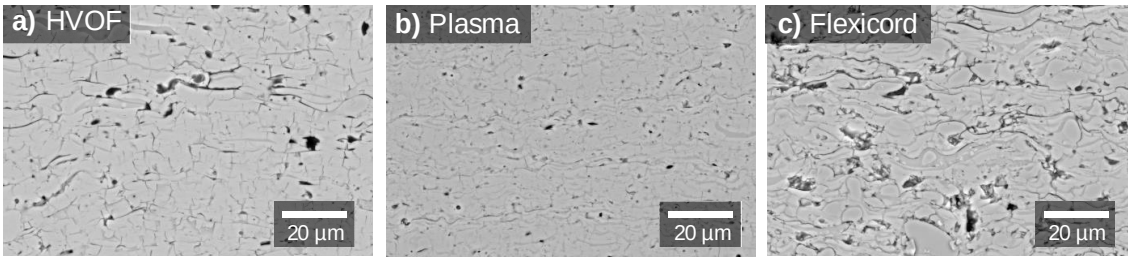

Figure 1. SEM/BSE cross-sectional images of the studied coatings at 1000× magnification (a–c). Black image regions correspond to void type imperfections, while in general, the light grey regions indicate crystalline material and the slightly darker color correspond to amorphous regions. Mainly in Flexicord image also unmelted particle regions can be seen.

Table 1. Raw material info of the studied coatings. The porosities of the coatings were defined from cross-sectional images taken by either optical microscope (OM, 320× magnification) and scanning electron microscope (SEM, 1000× magnification) using secondary electron detector (SE) and backscattered electron detector (BSE). Thicknesses of the coatings were determined by using cross-section images and utilizing magnetic measuring device.

Sample	Powder composition	Porosity (%)			Thickness (µm)		
		OM	SEM/SE	SEM/BSE	From cross-section image	From magnetic measurement	SD
HVOF	commercial Al_2O_3 (fused powder)	1.4	1.4	1.4	333	307	6.1
Plasma	commercial Al_2O_3 (fused powder)	2.3	2.4	3.6	245	271	11.4
Flexicord	commercial Al_2O_3 (cord)	2.7	3.8	4.8	235	225	4.4

2.2 DIELECTRIC CHARACTERIZATION

2.2.1 Sample preparation and measurement conditions

For DC resistivity and permittivity measurements, a round electrode (Ø=50 mm) was painted on the sample surface using a special silver paint (SPI High Purity Silver paint). In addition, a shield electrode was painted around the measuring electrode to prevent possible surface currents. For DC breakdown voltage measurements performed at the temperatures of 20–180 °C, smaller silver painted electrodes (Ø=11 mm) were prepared. Our previous study indicated that the silver paint does not penetrate into the coating [19]. After painting the electrodes, the samples were first dried at 120 °C for two hours followed by conditioning in a climate room at 20 °C/RH 20% for at least 12 h before the measurements. At 200–800 °C, the breakdown voltage measurements of HVOF coating were made without any embedded electrodes on the sample surface.

At 20–60 °C, the measurements were performed in a climate room where the temperature and relative humidity were controlled. The detailed measurement conditions are given in Table 2. The breakdown measurements for all coating types were made at 120 and 180 °C in a custom made oven. In addition, the breakdown behavior of HVOF sprayed alumina coating was also studied at the temperatures of 200, 300, 350, 400, 600 and 800 °C in a high temperature oven.

The coating samples were stabilized for three hours at the measurement conditions in the climate room before the resistivity, permittivity or breakdown measurements. In all the high temperature measurements, the coatings were placed into the oven at room temperature and the temperature was slowly increased to the set value. For the breakdown measurements at 120 and 180 °C, the heating times required for the samples to stabilize to set temperature were carefully determined prior to actual breakdown measurements. At 120 °C the stabilization period was one hour and at 180 °C it was two hours. At the high temperatures (200–800 °C), the temperature was increased with a ramp of 25 °C/min to the set point. When the steel substrate reached the set temperature, an hour was waited until the first breakdown measurement was started. After the measurements, the oven was switched off and the samples were left in the oven to slowly cool down to ~20 °C.

2.2.2 DC breakdown strength

DC breakdown voltage measurements were performed by utilizing linearly increased DC voltage (ramp rate of 100 V/s throughout the test). The voltage source control and data recording was performed using LabVIEW-based software. The voltage source was Spellman SL1200 (U_{max}=20 kV) and the voltage was measured using a resistive voltage divider (Spellman HVD-100-1, divider ratio 10000:1) [19].

Table 2. Measurement temperatures and relative humidities and the corresponding absolute humidities for resistivity and permittivity measurements. The breakdown measurement conditions are bolded.

Temperature (°C)	RH (%)	Absolute humidity (g/m^3)
20	**20**	**3.5**
20	**45**	**7.8**
20	70	12.2
20	90	15.6
40	**20**	**10.3**
40	**45**	**23.1**
40	70	35.9
60	20	26.1
60	**45**	**58.7**
60	70	91.3

At 20–180 °C, a stainless steel rod electrode (Ø=11mm, edge rounding 1 mm) was placed on top of the silver painted area on the coating sample while the stainless steel substrate of the sample acted as the other electrode. In order to avoid surface flashovers at the highest test voltages at 20–60 °C, a plastic cylinder with an O-ring seal was clamped on the coating surface around the measuring electrode (Ø=11 mm) to extend the surface distance over the solid insulation. For high temperature measurements (200–800 °C), a nickel based rod electrode (Ø=9 mm) was placed on the sample surface while the substrate acted as the other electrode.

Dielectric breakdown strength (DBS) of a coating was calculated by dividing the breakdown voltage by the corresponding coating thickness at the painted electrode (Ø=11 mm) location. In the high temperature measurements (200–800 °C), the thickness was measured near the breakdown point after the measurement.

2.2.3 DC resistivity

Resistivity measurements were made using Keithley 6517B electrometer and a sample holder where the sample with substrate and silver painted electrode was placed in between two stainless steel electrodes (Ø=50 mm). The measuring electric field varied from 0.1 V/µm to 2.5 V/µm. The test voltage was maintained for a period of 300 s at each voltage step. Typically, the DC resistivity is determined from a stabilized current value (i.e. resistive current) but the current of the coatings did not reach a fully stabilized level at every applied field. However, the resistivity was defined from the average current value in the end of the measurement period. All the measuring arrangements were in accordance with the standard IEC 60093.

2.2.4 Relative permittivity and losses

Relative permittivity and losses of the material were studied by utilizing an insulation diagnosis analyzer device (IDA 200, U_{max}=200 V_{peak}) using the same sample holder as in the resistivity measurements. During the measurements, a sinusoidal voltage with varying frequency was applied over the sample. The measuring electric field strength was 0.3 V_{peak}/µm for all the coatings. All the test arrangements were performed in accordance with the IEC standard 60250.

The complex impedance of a sample was calculated from the measured test voltage and the current through a sample which was expressed by IDA device as the equivalent parallel RC circuit model. The real part of the relative permittivity (ε_r') is defined as:

$$\mathrm{Re}\left\{\varepsilon_r^*\right\} = \varepsilon_r' = \frac{C_p}{C_0} - \frac{C_e}{C_0} \qquad (2)$$

where C_p is measured parallel capacitance of the equivalent circuit. C_0 is the so-called geometric capacitance of the test sample (vacuum in place of the insulation) and ω is the angular frequency. The edge field correction (C_e) was not used since the shield electrode was utilized in the measurements. As indicated by Eq. 1, conductivity of a material will also contribute to the relative permittivity ($|\varepsilon_r^*|$).

However, in this paper ε_r' values are reported, which in authors' opinion better reflect the dielectric behavior of the materials.

Imaginary part of the relative permittivity indicates the total losses of a material, both polarization and conduction losses. It can be defined as:

$$\mathrm{Im}\left\{\varepsilon_r^*\right\} = \varepsilon_r'' + \frac{\sigma}{\omega\varepsilon_0} = \frac{1}{\omega R_p C_0} \quad (3)$$

where R_p is the parallel resistance of the equivalent circuit. In this paper, the total loss contribution is expressed. The conductivity related component can be estimated by using the measured conductivities but since the conductivity is shown to be dependent on several factors (e.g. field), an exact determination of the loss components would require more detailed studies. However, at the driest conditions the conductivity component is negligible (e.g. ~0.3% for HVOF at 20 °C/RH 20%) but it is totally dominating at the highest absolute humidities, see Figure 6.

3 RESULTS AND DISCUSSION

3.1 DC BREAKDOWN STRENGTH

The DC breakdown strengths (BDS) of the studied coatings at each conditions are presented in Table 3, where the results are based on 10–15 parallel breakdown measurements. In addition, Figure 2 shows the BDS of the coatings at 20, 60 and 180 °C. The highest BDS is noticed for HVOF at all the ambient conditions and the lowest one for Flexicord. The deviation between parallel samples was the highest for Plasma coatings, as indicated by the lowest Weibull β values in Table 3.

At 20–40 °C, the BDS of HVOF alumina remains at very similar level (α=34–39 V/µm) but at 60 °C/RH 45% it decreased slightly (α=28 V/µm). However, similar decrease cannot be seen for Plasma and Flexicord since at 20–60 °C the BDS for Plasma is 17–21 V/µm and for Flexicord 12–18 V/µm. The obtained breakdown strengths are at similar level with breakdown strengths of HVOF and plasma sprayed alumina coatings reported in the literature [5, 12–14, 18] as well as with our previous studies [6, 19, 32, 33]. Although the higher absolute humidity conditions seemed to decrease the BDS of HVOF alumina, similar effect is not seen for other coatings and it may be concluded that humidity did not directly affect the breakdown strength.

At 120 and 180 °C, the breakdown strength of HVOF does not change in comparison to the 20 °C/RH 20% results (α=34 V/µm at 120 °C and 35 V/µm at 180 °C). However, at 120 °C the BDS of Plasma is obviously higher (α= 27 V/µm) than at 20–60 °C but at 180 °C the BDS (α=18 V/µm) is again at a similar level with the low temperature results. It should be noted that the deviation in breakdown data of Plasma is very high (low β values in Table 3).

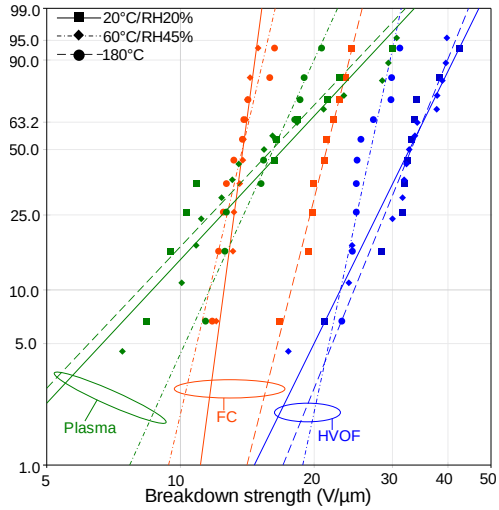

Figure 2. DC breakdown strenghts of the studied coatings at 20°C, 60°C and 180°C (FC is Flexicord).

The breakdown strength of Flexicord is 22 V/µm at 120 and 180 °C which is higher than the BDS at the low temperatures. It may be speculated especially for Flexicord that at the higher temperatures (120 and 180 °C), moisture is partially escaped from the porous coating, and thus the BDS increases compared to 20–60 °C results. Pawlowski [11] noticed that the dielectric constant of plasma sprayed alumina decreased after a long (48 h) period at 120 °C which was linked to the hygroscopic nature of the coatings which enables the moisture to penetrate into the coating easily. In this study, although the samples were in oven for a shorter period (1–2 hours) than in [11], the heat treatment most probably removed part of the moisture from the porous coating. This can explain the higher breakdown strengths of Flexicord at 120 and 180 °C.

Pawlowski [11] also noticed that high porosity decreased the breakdown strength of the plasma sprayed alumina coating. Toma *et al.* [12] made similar observation since HVOF sprayed alumina coating had a lower porosity and correspondingly a higher BDS than a plasma sprayed alumina coating. Our own previous studies have shown that high porosity of HVOF sprayed MgO-Al_2O_3 coatings (as indicated

Table 3. The breakdown fields of the studied coatings at the breakdown probabilities of 10%, 63.2% and 90% at 20°C–180°C and Weibull β. The statistical analysis of the breakdown data was performed using Weibull++® software and the least-square regression method was used in parameter estimation. The goodness of the fit results can be expressed by correlation coefficient, λ. The closer to 1 λ is, the better the fit is. λ was 0.91–0.97 for HVOF, 0.93–0.98 for Plasma and 0.93–0.98 for Flexicord.

	HVOF				Plasma				Flexicord			
	E_{bd} (V/µm)			β	E_{bd} (V/µm)			β	E_{bd} (V/µm)			β
	10 %	α, 63.2 %	90 %		10 %	α, 63.2 %	90 %		10 %	α, 63.2 %	90 %	
20°C/RH 20%	22.9	35.1	41.2	5.3	8.6	19.4	26.2	2.8	12.5	14.1	14.7	19.3
20°C/RH 45%	29.5	39.2	43.5	7.9	8.7	18.7	24.8	3.0	11.8	13.8	14.7	14.3
40°C/RH 20%	27.2	38.7	44.1	6.4	17.2	21.2	22.9	10.8	16.3	17.6	18.1	30.2
40°C/RH 45%	29.0	35.6	38.5	10.9	8.8	16.8	21.3	3.5	10.7	12.4	13.1	15.4
60°C/RH 45%	22.9	27.6	29.6	12.0	11.6	17.3	20.0	5.7	11.6	14.2	15.3	11.1
120°C	24.1	33.9	38.5	6.6	18.8	27.0	30.9	6.2	17.7	21.7	23.4	11.0
180°C	24.6	35.0	39.9	6.4	8.1	18.4	24.9	2.7	17.7	22.1	24.0	10.3

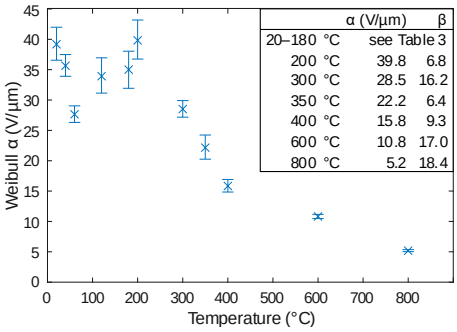

Figure 3. BDS of HVOF alumina as a function of temperature. The error bars represent the 90% confidence bounds. The relative humidity was 45% in 20°C, 40°C and 60°C results.

by relatively high gas permeability) decreased the breakdown strength [6], although for some of the HVOF alumina coatings similar decrease was not noticed [33]. Although the effect of porosity on the breakdown strength is not always so straightforward, in this study the most porous alumina coating (Flexicord) had also the lowest BDS while the lowest porosity alumina coating (HVOF) exhibited the highest BDS.

Since the ceramic coating may be used also at notably higher temperatures than 180 °C, the breakdown measurements were extended to higher temperatures (200–800 °C). Figure 3 presents the breakdown strength of the HVOF coating as a function of temperature. The BDS is at quite similar level from 20 to 200 °C although the deviation between the parallel samples is quite large in many cases. Interestingly, the deviation between parallel samples is remarkably lower at higher temperatures (above 350 °C) which can be seen as a high β in Figure 3. Above 300 °C the breakdown strength starts to decrease reaching the value of 5.2 V/µm at 800 °C which is 14% of the BDS at 20 °C/RH 20%. Yoshimura and Bowen [20] made almost similar observation since the breakdown strength of polycrystalline alumina decreased gradually from room temperature (90–100 V/µm) to 900 °C (~25 V/µm). Above 900 °C, the BDS of alumina decreased at much higher rate reaching 2 V/µm at 1400 °C [20].

3.2 DC RESISTIVITY

Figure 4 presents the DC resistivity of the coatings as a function of electric field at all the studied ambient conditions. At 20 °C/RH 20%, the DC resistivities of all the coatings are at the level of ~10^{12} Ωm from 0.1 to 0.5 V/µm. Above 0.5 V/µm, the resistivities start to decrease gradually indicating a non-ohmic behavior which has also been observed in our previous studies [30, 31, 33, 34]. In [33], a detailed analysis of DC conduction mechanisms up to breakdown fields was made for HVOF and plasma sprayed Al_2O_3 coatings and for several HVOF sprayed Al_2O_3-MgO coatings. It was speculated [33], that the conductivity of the coatings follows only partly the space charge limited conduction (SCLC) mechanism unlike the sintered bulk alumina [22], [36]. The microstructure of the ceramic coating, which consists of amorphous and crystalline regions as well as voids and unmelted particles, can be thought as an insulation system in which the conductivity of the amorphous regions is most probably higher than that of the crystalline regions. The differences in the conductivities and the resulting non-

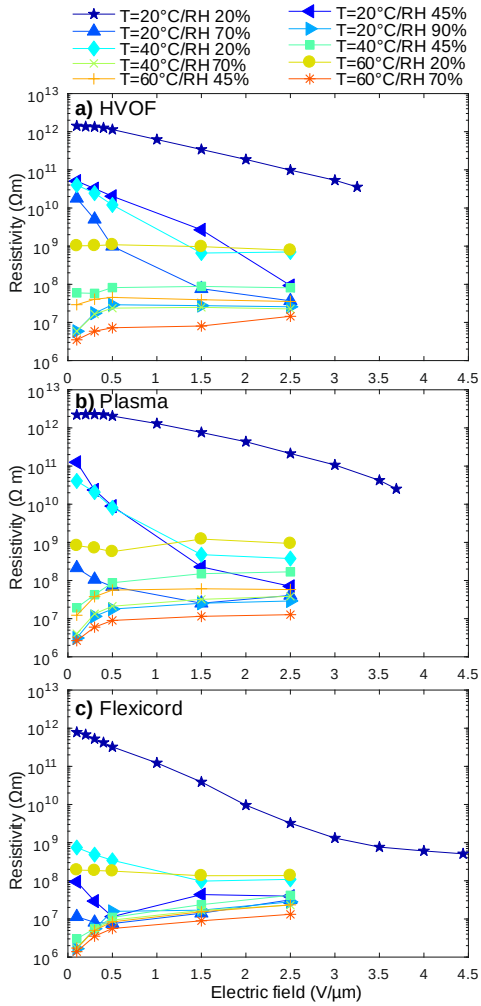

Figure 4. DC resistivity of the coatings as a function of electric field.

uniform electric field distribution are most probably the reasons why the coatings exhibit non-linear conductivity already at rather low electric fields in comparison to crystalline bulk alumina [33].

When the humidity and temperature increase above 20 °C/RH 20%, the non-ohmic conductivity cannot be seen for Flexicord (Figure 4). However, it can be noticed for HVOF and Plasma at 20 °C/RH 45% and at 40 °C/RH 20% but not at higher temperatures or humidities. It can be speculated that the conductivity caused by observed moisture most probably overrun the non-ohmic behavior of the coatings at high absolute humidities.

The resistivities of the coatings at the electric field of 0.3 V/µm are listed in Table 4. It can be noticed that Flexicord has evidently lower resistivity at all conditions in comparison to HVOF and Plasma which exhibit very similar resistivities. The differences of DC resistivities at various conditions between the coating types may be linked to their different microstructural features since the spraying parameters (e.g. flame temperature, particle velocity) affect the coating microstructure. The interfaces, thicknesses of the amorphous and crystalline layers, etc. differ between the coating types

Table 4. The DC resistivity at the electric field of 0.3 V/μm for the studied coatings as well as the real part of permittivity (ε_r') at frequency of 50 Hz and the imaginary part of permittivity ($\varepsilon_r''+\sigma/\omega\varepsilon_0$) indicating total losses at 50 Hz and 1 kHz.

		HVOF				Plasma				Flexicord			
T (°C)	RH (%)	ρ (Ωm)	ε_r' (50Hz)	$Im\{\varepsilon_r^*\}$ (50Hz)	$Im\{\varepsilon_r^*\}$ (1kHz)	ρ (Ωm)	ε_r' (50Hz)	$Im\{\varepsilon_r^*\}$ (50Hz)	$Im\{\varepsilon_r^*\}$ (1kHz)	ρ (Ωm)	ε_r' (50Hz)	$Im\{\varepsilon_r^*\}$ (50Hz)	$Im\{\varepsilon_r^*\}$ (1kHz)
20	20	1.3×10^{12}	11.3	3.8	0.7	2.3×10^{12}	12.9	4.5	0.7	5.3×10^{11}	13.0	5.4	1.1
20	45	3.2×10^{10}	25.0	21.8	4.1	2.4×10^{10}	26.6	22.5	4.1	2.9×10^{7}	33.5	51.8	7.2
20	70	5.1×10^{9}	44.5	60.2	9.3	1.1×10^{8}	40.0	216.9	17.4	8.2×10^{6}	42.7	92.5	10.8
20	90	1.8×10^{7}	53.2	253.6	22.6	1.2×10^{7}	68.8	997.7	60.6	5.6×10^{6}	54.3	216.3	18.1
40	20	2.4×10^{10}	14.8	6.9	1.6	2.1×10^{10}	15.2	6.6	1.2	4.9×10^{8}	16.6	9.3	2.0
40	45	5.8×10^{7}	39.2	30.2	6.8	4.3×10^{7}	37.9	31.0	7.0	5.6×10^{6}	34.0	61.4	7.8
40	70	1.7×10^{7}	53.5	116.5	14.8	1.3×10^{7}	43.3	271.1	21.0	5.4×10^{6}	42.5	160.6	14.9
60	20	1.0×10^{9}	18.8	10.0	2.5	7.1×10^{8}	18.3	8.6	1.9	1.9×10^{8}	18.4	10.3	2.5
60	45	4.1×10^{7}	49.4	47.1	9.9	3.8×10^{7}	41.0	34.9	8.2	5.0×10^{6}	47.1	74.4	11.1
60	70	5.9×10^{6}	49.3	155.5	15.9	6.0×10^{6}	55.7	266.2	22.8	3.5×10^{6}	46.7	248.2	19.7

and these differences can partly explain the differences in the DC resistivities.

It may be speculated that porosity partly affects the DC resistivity since the highest porosity alumina coating (Flexicord) exhibits the lowest resistivities at all conditions while HVOF exhibits the highest resistivity and correspondingly the lowest porosity. Plasma has slightly lower resistivity and higher porosity than HVOF. Pawlowski [11] noticed that the most porous plasma sprayed alumina coating exhibited the lowest DC resistivity which is well in line with the results in this study. Also, the DC resistivities of plasma sprayed alumina coatings were 5×10^{9}–3×10^{12} Ωm in [11] which is comparable to the results obtained in this study.

As can be seen from Table 4, increasing the relative humidity from 20 to 90% decreased the DC resistivity of the studied coatings five orders of magnitude at 0.3 V/μm. Toma *et al.* made similar observation in [12] when increasing the relative humidity from 30 to 95% decreased the DC resistivity of HVOF sprayed alumina coating from 1×10^{11} Ωm to 3×10^{5} Ωm. For the plasma sprayed (APS) alumina coating the decrease was from 3×10^{11} to 2×10^{4} Ωm.

In our previous study [30], the DC resistivity of spinel ($MgAl_2O_4$) coatings deposited by HVOF, Plasma and Flexicord techniques were studied at 20–60 °C at RH 20% and 45%. When comparing the DC resistivities of the spinel coatings to the resistivity of alumina coatings in this study, the values are at very similar level at 20 °C/RH 20%. However, when the temperature or humidity was increased above 20 °C/RH 20%, the resistivities of these alumina coatings decreased more than those of spinel coatings in [30] although the porosities of the spinels coatings in [30] were slightly higher. It can be speculated that the alumina together with water forms to aluminum hydroxide which can have a decreasing effect on the resistivity of alumina coatings. According to Toma *et al.* [12], the HVOF and plasma sprayed spinel coatings exhibit higher resistivities at RH 30% and RH 90% in comparison to the alumina coatings. In our previous study [6], the DC resistivity of HVOF sprayed Al_2O_3-MgO coatings decreased correspondingly to the DC resistivities in here (five orders of magnitude) when the humidity increased from 20% to 90%. However, the DC resistivities of the Al_2O_3-MgO coatings [6] were at a higher level at 20 °C/RH 20% than the resistivities of Al_2O_3 coatings in here. It was also noticed in [6] that the high porosity (as indicated by relatively high gas permeability) did not affect the resistivity although the humidity increased from 20 to 90%.

As it was discussed in [12] and as the resistivity results indicate in this study, the thermally sprayed alumina coatings exhibit sensitivity to absorbed moisture due to the nature of the coating, the microstructure, and the phase composition. However, as indicated by the above analysis, it is very difficult to clearly distinguish between exact effects of various microstructural or other details on the resistivity with increasing humidity, -only above like speculations may be made. However, it can be seen that all the coatings can absorb notable amount of moisture which can significantly decrease the resistivity, seemingly stabilizing to the range of 10^{7}–10^{8} Ωm. At the same time, the resistivity seems to turn from originally field dependent behavior to linear behavior.

3.3 RELATIVE PERMITTIVITY AND LOSSES

Figure 5 and Figure 6 present the relative permittivities and the total loss contributions of the studied Al_2O_3 coatings as a function of frequency at 20–60°C. As can be seen from the figures, at the low frequencies (below 1 Hz) the permittivities and the losses increase 3–5 orders of magnitude, indicating the notable conduction at increased humidities, as seen also in the resistivity results. At higher frequencies, the increase is much lower. However, it shall be remembered that the given permittivity values are the real parts of the complex permittivity (see Eq. 1) and do not thus include the loss related component, only the real polarizability related component. It can be speculated that main part of the increased permittivity is most probably originating from water content (H_2O: $\varepsilon_r\approx80$ at 20°C). Interestingly, the permittivity increases at lower frequencies also at driest conditions which may be due to the hypothesized interfacial polarization due to the coating microstructure with varying conductivities.

The increase in the real part of relative permittivity is well in line with the literature since Brown *et al.* noticed [15] that the dielectric constant of plasma sprayed alumina coating increased from 8.3 to 9.8 at 100 kHz when the relative humidity increased from 0% to 95%. In this study, the dielectric constant of plasma sprayed alumina coating increased from 9.8 to 30.6 at 1 kHz when the humidity increased from 20 to 90%. In our previous studies [30], the dielectric constants of HVOF, plasma and Flexicord sprayed $MgAl_2O_4$ coatings were found to increase with increasing temperature (20 to 60°C) when relative humidity was either 20 or 45%. The dielectric constants of the spinel coatings in [30] were at lower level than those of alumina coatings in this

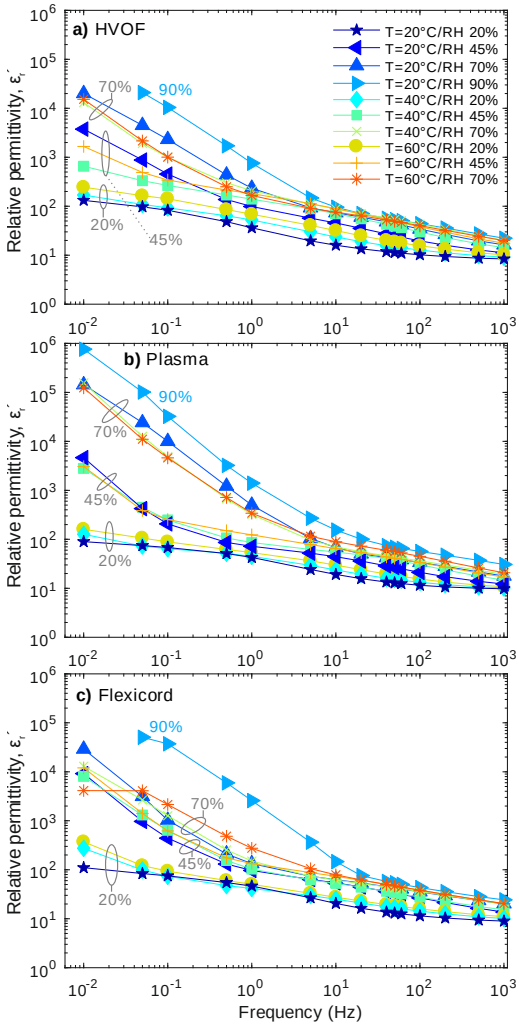

Figure 5. Relative permittivity (indicated as Re{ε_r*}) as a function frequency when the measuring electric field was 0.3 V_{peak}/µm. In RH 90% measurements, the high losses caused measurement problems and due to this the permittivity data at lowest frequencies are missing.

study. This is well in line with the DC resistivity results since the spinel coatings exhibited also higher DC resistivities in [30] than the alumina coatings in this study. In general, the lamellar microstructure with interfaces and regions of different dielectric properties enhance the permittivity of the coatings.

At 20 °C/RH 20% at the frequency of 1 kHz, the dielectric constants of HVOF, Plasma and Flexicord alumina are 8.4, 9.8 and 8.9, respectively. In [35], the dielectric constant of HVOF alumina coatings varied from 5.9 to 8.2 at 10 kHz which is quite well in line with the results obtained in this study. Brown *et al*. noticed [15] that the dielectric constant of plasma alumina coating was 11–23 at 1 kHz when the highest value was obtained for the coating which exhibited the lowest powder particle size. Correspondingly, the lowest dielectric constant was obtained for the highest particle size coating. These values are quite well in line with the real part of relative permittivity of Plasma at 20 °C/RH 45% and 20 °C/RH 70% where the permittivity was 12.2 and 17.8, respectively. Pawlowski reported in [11] that the dielectric constant of plasma sprayed alumina coatings was 6–8 at 1 kHz, which is slightly lower than reported in here. The differences in the dielectric constants can be partly explained by the different sample preparation since in [15] the coating samples were baked for 13 hours at 135 °C and in [11] for 1–3 days at 120°C while in here the samples were heat-treated in 120 °C for 2 hours. Longer baking time removes more completely moisture from a porous coating which can be seen as lower dielectric constant.

It should be noted that the measuring voltage was 1 V_{rms} in [11] while in this study the measuring voltage depends on the coating thickness varying from 57 V_{rms} to 69 V_{rms} corresponding to the electric field of 0.3 V_{peak}/µm. Although the measuring field might affect the relative permittivity, we noticed in [32] that at the frequency of 100 Hz the real part of relative permittivity of HVOF alumina and spinel coatings was not dependent on the measuring electric field (0.1–5 V/µm). However, at 0.1 Hz small increase in the real part of relative permittivity can be seen for some of the samples when the electric field was above 0.5 V/µm which is similar non-linear behavior as noticed for DC conductivity in [32].

As it can be seen from Figure 6, the losses increase with increasing humidity. The effect of increasing humidity on the losses at various temperatures can be seen in detail in Figure 7 where the losses are presented at the frequency of 50 Hz. It needs to be emphasized that the presented values indicate total measured losses including the contributions of both DC conductivity and polarization (see Eq. 3). At high humidities, the DC conduction part of the losses is more dominant limiting and preventing the charging phenomena, which can be seen obviously in Figure 6. HVOF alumina coating has the lowest losses while the Flexicord exhibits the highest values, see Figure 7 and Table 4. This similar trend was also noticed in the DC resistivity results.

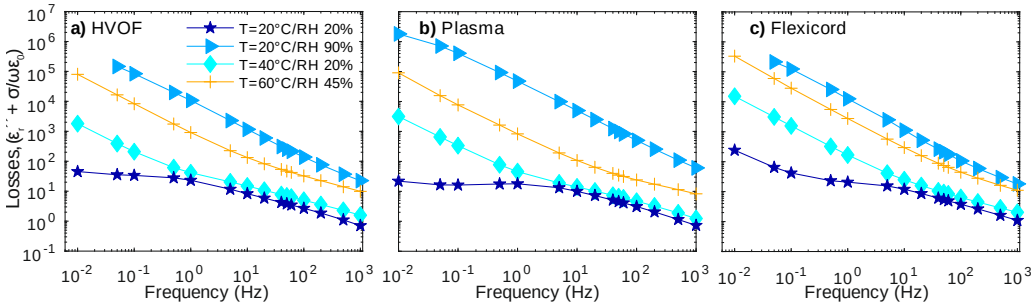

Figure 6. Losses (indicated as Im{ ε_r*}) as a function frequency when the measuring electric field was 0.3 V_{peak}/µm.

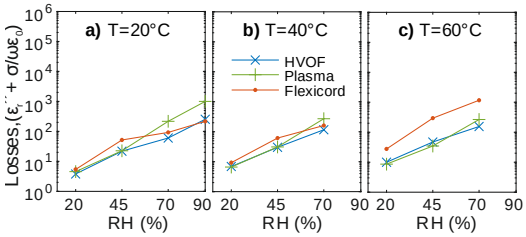

Figure 7. a)–c) The losses of the coatings at the frequency of 50 Hz.

3.4 FURTHER DISCUSSION

The results indicate that the dielectric properties of thermally sprayed alumina coatings clearly differ from that of bulk alumina, and thus lamellar microstructure and porosity most probably affect the dielectric properties. Furthermore, the properties of alumina change during thermal spraying process since varying amount of metastable γ-Al_2O_3, which is more hygroscopic than the stable α-Al_2O_3 [11, 12, 14], may form. Brown *et al.* [15] and Pawlowski [11] proposed that high dielectric constant of plasma sprayed alumina coating is related to high γ-Al_2O_3 content. Toma *et al.* [12] noticed that HVOF sprayed alumina coating had higher α-phase content than plasma alumina coating and correspondingly at high humidities (>RH 75%) the HVOF alumina coating had higher resistivity than plasma alumina but at low humidities (<RH 45%) the HVOF and plasma alumina exhibited similar resistivities. Anyhow, for both coating types the resistivity decreased approximately five orders of magnitude when the relative humidity increased from 30 to 95% [12] which is a similar decrease as obtained in this study. Toma *et al.* suggested in [14] that the higher DC resistivity of suspension HVOF alumina coating can be due to lower porosity and higher α-Al_2O_3 content in comparison to the conventional HVOF alumina coatings

However, Favre *et al*. [38] noticed that the DC resistivity of α-Al_2O_3 powder decreased approximately five orders of magnitude when the relative humidity increased from 20% to 80%. Thus, high γ-content of thermally sprayed alumina coatings cannot explain completely their sensitivity to the humidity. Although thermally sprayed spinel coatings exhibit more stable form also in coating [12, 15], their dielectric properties are also sensitive to the humidity [6, 12, 30, 39]. Thus, the nature of thermally sprayed ceramic coatings is moisture sensitive. If the operation temperatures of a thermally sprayed coatings are low enough, it is possible to impregnate a coating with an organic or inorganic sealant in order to make it more insensitive against the moisture penetration [40]. This also affects the dielectric properties of the impregnated coating.

4 CONCLUSIONS

Dielectric properties of thermally sprayed alumina coatings were studied at various conditions. It was found that spraying technique, temperature and humidity affected notably the dielectric properties. However, temperature had only a minor effect on the breakdown strength of the alumina coatings in the range of 20–180°C although the deviation in the breakdown data was quite high. The breakdown strength of alumina coatings decreased gradually from 300 to 800 °C reaching a value which was only 14% of the breakdown strength measured at 20 °C/RH 20%.

DC resistivity, permittivity and losses of the studied alumina coatings were at quite similar level at low temperatures and humidities. However, increasing the relative humidity from 20 to 90% decreased DC resistivity five orders of magnitude while AC losses increased correspondingly. In all coating types, permittivity increased at low frequencies also at dry conditions, possibly indicating interfacial type of polarization.

These major changes with humidity are attributable to the highly hygroscopic nature of the coatings, which, for alumina coatings, can partly be explained by the notable amount of metastable γ-phase. Moreover, the lamellar microstructure consisting of amorphous and crystalline regions with interfaces and voids in between can be speculated to enhance the moisture sensitive nature of the coatings.

In the potential applications for thermally sprayed ceramic insulations, the insulating layers are subjected to demanding conditions (e.g. high temperature, challenging geometries, mechanical or chemical stress, etc.). Thus, careful consideration of the effect of demanding conditions on dielectric properties of thermally sprayed ceramic coatings is of great importance in order to enable their reliable operation in final applications. Furthermore, it is necessary to evaluate the long-term ageing and degradation behavior of the coatings.

REFERENCES

[1] B. Basu and K. Balani, *Advanced Structural Ceramics*. Wiley-American Ceramic Society Inc, 2011.

[2] J. R. Davis, *Handbook of Thermal Spray Technology*. United States of America: ASM International, 2004.

[3] L. Pawlowski, *The Science and Engineering of Thermal Spray Coatings*, 2nd ed. Chichester, West Sussex, England: John Wiley & Sons Ltd, 2008.

[4] A. Piqué *et al.*, "Chapter 9 – Direct-Write Thermal Spraying of Multilayer Electronics and Sensor Structures," in *Direct-Write Technologies for Rapid Prototyping*, A. Pique and D. Chrisey, Eds. Academic Press, 2002, pp. 261–302.

[5] E. E. J. Young, E. Mateeva, J. J. Moore, B. Mishra, and M. Loch, "Low pressure plasma spray coatings," *Int. Conf. Metall. Coatings Thin Film.*, vol. 377–378, pp. 788–792, 2000.

[6] M. Niittymäki, I. Rytöluoto, K. Lahti, J. Metsäjoki, and T. Suhonen, "Role of microstructure in dielectric roperties of thermally sprayed ceramic coatings," in *IEEE International Conference on Dielectrics (ICD)*, 2016, pp. 1102–1105.

[7] N. H. Menzler, F. Tietz, S. Uhlenbruck, H. P. Buchkremer, and D. Stöver, "Materials and manufacturing technologies for solid oxide fuel cells," *J. Mater. Sci.*, vol. 45, no. 12, pp. 3109–3135, Feb. 2010.

[8] A. Kulkarni *et al.*, "Studies of the microstructure and properties of dense ceramic coatings produced by high-velocity oxygen-fuel combustion spraying," *Mater. Sci. Eng. A*, vol. 369, no. 1–2, pp. 124–137, Mar. 2004.

[9] R. McPherson, "Formation of metastable phases in flame- and plasma-prepared alumina," *J. Mater. Sci.*, vol. 8, no. 6, pp. 851–858, 1973.

[10] R. McPherson, "A review of microstructure and properties of plasma sprayed ceramic coatings," *Surf. Coatings Technol.*, vol. 39, pp. 173–181, 1989.

[11] L. Pawlowski, "The relationship between structure and dielectric properties in plasma-sprayed alumina coatings," *Surf. Coatings Technol.*, vol. 35, no. 3–4, pp. 285–298, 1988.

[12] F. L. Toma, S. Scheitz, L. M. Berger, V. Sauchuk, M. Kusnezoff, and S. Thiele, "Comparative study of the electrical properties and characteristics of thermally sprayed alumina and spinel coatings," *J. Therm. Spray Technol.*, vol. 20, no. 1–2, pp. 195–204, 2011.

[13] J. Kotlan, R. C. Seshadri, S. Sampath, P. Ctibor, Z. Pala, and R. Musalek, "On the dielectric strengths of atmospheric plasma sprayed Al_2O_3, Y_2O_3, ZrO_2–7% Y_2O_3 and (Ba,Sr)TiO_3 coatings," *Ceram. Int.*,

vol. 41, no. 9, pp. 11169–11176, Nov. 2015.
[14] F. L. Toma *et al.*, "Comparison of the microstructural characteristics and electrical properties of thermally sprayed Al_2O_3 coatings from aqueous suspensions and feedstock powders," *J. Therm. Spray Technol.*, vol. 21, no. 3–4, pp. 480–488, 2012.
[15] L. Brown, H. Herman, and R. K. MacCrone, "Plasma-sprayed insulated metal substrates," in *Proceedings of the Elevent International Thermal Spray Conference*, 1986, pp. 507–512.
[16] S. Sampath, "Thermal spray applications in electronics and sensors: past, present, and future," *J. Therm. Spray Technol.*, vol. 19, no. 5, pp. 921–949, Feb. 2010.
[17] S. Deshpande, A. Kulkarni, S. Sampath, and H. Herman, "Application of image analysis for characterization of porosity in thermal spray coatings and correlation with small angle neutron scattering," *Surf. Coatings Technol.*, vol. 187, no. 1, pp. 6–16, Oct. 2004.
[18] H. L. Filmer, J. Hochstrasser, A. R. . Nicoll, and S. Rangaswamy, "Plasma spray deposition of alumina-based ceramic coatings," *Am. Ceram. Soc. Bull.*, vol. 69, no. 12, pp. 1955–1958, 1990.
[19] M. Niittymäki, K. Lahti, T. Suhonen, and J. Metsäjoki, "Dielectric breakdown strength of thermally sprayed ceramic coatings: effects of different test arrangements," *J. Therm. Spray Technol.*, vol. 24, no. 3, pp. 542–551, Jan. 2015.
[20] M. Yoshimura and H. K. Bowen, "Electrical breakdown strength of alumina at high temperatures," *J. Am. Ceram. Soc.*, vol. 64, no. 7, pp. 404–410, 1981.
[21] I. O. Owate and R. Freer, "Ac breakdown characteristics of ceramic materials," *J. Appl. Phys.*, vol. 72, no. 6, pp. 2418–2422, 1992.
[22] F. Talbi, F. Lalam, and D. Malec, "DC conduction of Al_2O_3 under high electric field," *J. Phys. D. Appl. Phys.*, vol. 40, no. 12, pp. 3803–3806, 2007.
[23] L. Haddour, N. Mesrati, D. Goeuriot, and D. Tréheux, "Relationships between microstructure, mechanical and dielectric properties of different alumina materials," *J. Eur. Ceram. Soc.*, vol. 29, no. 13, pp. 2747–2756, Oct. 2009.
[24] D. Malec, V. Bley, F. Talbi, and F. Lalam, "Contribution to the understanding of the relationship between mechanical and dielectric strengths of alumina," *J. Eur. Ceram. Soc.*, vol. 30, no. 15, pp. 3117–3123, 2010.
[25] C. Neusel, H. Jelitto, D. Schmidt, R. Janssen, F. Felten, and G. A. Schneider, "Thickness-dependence of the breakdown strength: Analysis of the dielectric and mechanical failure," *J. Eur. Ceram. Soc.*, vol. 35, no. 1, pp. 113–123, Jan. 2015.
[26] F. Talbi, F. Lalam, and D. Malec, "Dielectric breakdown characteristics of alumina," in *Proceedings of the International Conference on Solid Dielectrics (ICSD)*, 2010, pp. 1–4.
[27] D. Malec, V. Bley, T. Lebey, F. Talbi, and F. Lalam, "Investigations on dielectric breakdown of ceramic materials," in *Annual Report Conference on Electrical Insulation and Dielectric Phenomena, 2005.*, 2005, pp. 63–66.
[28] C. Neusel and G. A. Schneider, "Size-dependence of the dielectric breakdown strength from nano- to millimeter scale," *J. Mech. Phys. Solids*, vol. 63, no. February, pp. 201–213, 2014.
[29] J. Luth, M. Cichosz, M. Lehmann, S. Hartmann, and F. Trenkle, "High velocity oxygen fuel sprayed insulation coatings for applications in high power electronics," in *Proceedings of the International Thermal Spray Conference*, 2015, pp. 1026–1030.
[30] M. Niittymäki, T. Suhonen, J. Metsäjoki, and K. Lahti, "Influence of humidity and temperature on the dielectric properties of thermally sprayed ceramic $MgAl_2O_4$ coatings," in *Annual Report Conference on Electrical Insulation and Dielectric Phenomena*, 2014, pp. 94–97.
[31] M. Niittymäki, T. Suhonen, J. Metsäjoki, and K. Lahti, "DC dielectric breakdown behavior of thermally sprayed ceramic coatings," in *Proceedings of the 14th Nordic Insulation Symposium on Materials, Components and Diagnostics*, 2015, pp. 80–85.
[32] M. Niittymäki, T. Suhonen, J. Metsäjoki, and K. Lahti, "Electric field dependency of dielectric behavior of thermally sprayed ceramic coatings," in *Proceedings of the IEEE 11th International Conference on the Properties and Applications of Dielectric Materials (ICPADM)*, 2015, pp. 500–503.
[33] M. Niittymäki, K. Lahti, T. Suhonen, and J. Metsäjoki, "DC conduction and breakdown behavior of thermally sprayed ceramic coatings," *IEEE Trans. Dielectr. Electr. Insul.*, vol. 24, no. 1, pp. 499–510, 2017.
[34] M. Niittymäki, K. Lahti, T. Suhonen, U. Kanerva, and J. Metsäjoki, "Dielectric properties of HVOF sprayed ceramic coatings," in *Proceedings of the IEEE International Conference on Solid Dielectrics*, 2013, pp. 389–392.
[35] E. Turunen *et al.*, "On the role of particle state and deposition procedure on mechanical, tribological and dielectric response of high velocity oxy-fuel sprayed alumina coatings," *Mater. Sci. Eng.* A, vol. 415, no. 1–2, pp. 1–11, Jan. 2006.
[36] C. Neusel, H. Jelitto, and G. A. Schneider, "Electrical conduction mechanism in bulk ceramic insulators at high voltages until dielectric breakdown," *J. Appl. Phys.*, vol. 117, no. 15, p. 154902, 2015.
[37] K.-C. Kao, *Dielectric Phenomena in Solids: With Emphasis on Physical Concepts of Electronic Processes*. Academic Press, 2004.
[38] F. Favre, F. Villieras, Y. Duval, E. Mcrae, and C. Rapin, "Influence of relative humidity on electrical properties of α-Al_2O_3 powders: resistivity and electrochemical impedance spectroscopy," *J. Colloid Interface Sci.*, vol. 286, no. 2, pp. 615–620, 2005.
[39] K. Ahn, B. W. Wessels, and S. Sampath, "Spinel humidity sensors prepared by thermal spray direct writing,", *Sensors Actuators B Chem.*, vol. 107, no. 1, pp. 342–346, 2005.
[40] J. Knuuttila, P. Sorsa, and T. Mäntylä, "Sealing of thermal spray coatings by impregnation," *J. Therm. Spray Technol.*, vol. 8, no. 2, pp. 249–257, Jun. 1999.

Minna Niittymäki (S'13) was born in Sahalahti, Finland, in 1984. She received the M.Sc. degree in electrical engineering from Tampere University of Technology in 2012. Since then she has been working as Researcher in the high voltage research group of the Laboratory of Electrical Energy Engineering at TUT, with the aim towards Ph.D. degree. Her current research interests are in the area of insulation materials focusing on the dielectric characterization of thermally sprayed insulating ceramic coatings.

Kari Lahti (M'01) was born in Hämeenlinna, Finland in 1968. He received the M.Sc. and Doctoral degrees in electrical engineering from Tampere University of Technology in 1994 and 2003, respectively. Since then he has worked at the Laboratory of Electrical Energy Engineering at TUT, currently as a Research Manager and Adjunct Professor. He is the head of TUT's research group on high voltage insulation systems. He has also been responsible for the high voltage laboratory services at TUT since 2002. His research interests are in the area of high voltage engineering including surge arresters, nanocomposite insulation systems, environmental testing of high voltage materials and apparatus, high voltage testing methods and dielectric characterization of insulating materials

Tomi Suhonen was born in Helsinki, Finland, in 1978. He is a Senior Scientist and Manager of multiscale materials modelling activities at VTT Technical Research Centre of Finland. He has 13 years' experience in scientific research related to advanced materials and has published more than 70 scientific papers and holds several international patents.

Jarkko Metsäjoki was born in Rauma, Finland, in 1982. He received M.Sc. degree in materials science from Tampere University of Technology (TUT) in 2008. He has worked at TUT, Braunschweig University of Technology, and since 2012 he has been working at VTT Technical Research Centre of Finland as Research Scientist. He is currently also a PhD student at Aalto University. His research interests include material characterization of thermally sprayed ceramic coatings.